

Hydrodynamics of impinging liquid jets used in cleaning

Melissa Wei Li Chee

Department of Chemical Engineering and Biotechnology
University of Cambridge

This thesis is submitted for the degree of

Doctor of Philosophy

Newnham College

September 2021

Preface

This thesis is the result of my own work and includes nothing which is the outcome of work done in collaboration except as declared in the Preface and specified in the text. It is not substantially the same as any that I have submitted, or, is being concurrently submitted, for a degree, diploma or other qualification at the University of Cambridge or any other University or similar institution. I further state that no substantial part of my thesis has already been submitted, or, is being concurrently submitted, for any such degree, diploma or other qualification at the University of Cambridge or any other University or similar institution. It does not exceed the prescribed word limit for the Engineering Degree Committee.

Some of the material presented in this thesis has been published in the following journal and conference papers:

1. CHEE, M. W. L. and WILSON, D. I. (2021). Cleaning viscous soil layers off walls by intermittent impinging jets. *J. Clean. Prod.*, **283**, 124660.
2. CHEE, M. W. L., AHUJA, T. V., BHAGAT, R. K., TAESOPAPONG, N., WAN, S. A., WIGMORE, R. L., and WILSON, D. I. (2019). Impinging jet cleaning of tank walls: Effect of jet length, wall curvature and related phenomena. *Food Bioprod. Process.*, **113**, 142–153.
3. BHAGAT, R. K., CHEE, M. W. L., AHUJA, T. V., WIGMORE, R. L., WAN, S. A., TAESOPAPONG, N., FERNANDES, R. R., and WILSON, D. I. (2018). Effect of jet length and surface curvature on cleaning of tank walls. In *Fouling and Cleaning in Food Processing 2018*, Lund, Sweden, pp. 333–340.

Melissa Wei Li Chee
September 2021

Abstract

Hydrodynamics of impinging liquid jets used in cleaning

Melissa Wei Li Chee

Impinging liquid jets are widely used in industrial cleaning-in-place (CIP) systems to remove residual product or soil layers from the internal surfaces of process equipment such as tanks and vessels. The optimisation of these cleaning operations is often done empirically as a large number of parameters are needed to define the problem. Three aspects of jet behaviour were investigated as a step towards enabling the systematic design and optimisation of CIP systems.

The effect of jet length and wall curvature were explored. The flow patterns generated by the impingement of a coherent, turbulent, horizontal water jet on a flat, vertical target were characterised as a benchmark and compared with existing models that predict the shape of the radial flow zone (RFZ). As the jet length increased, some liquid was lost to splatter through jet breakup into droplets and rebound of liquid droplets off the target. The shape of the RFZ agreed with existing models once the fraction of liquid lost to splatter was accounted for. Tests on horizontal and vertical cylinders with curvatures in the range 6.9 to 20 m⁻¹ showed that wall curvature did not have a significant effect on the shape of the RFZ unless the liquid film wrapped around the inside of the cylinder, observed at high jet flow rates. There was no appreciable effect of wall curvature on cleaning behaviour. Soaking a water-soluble soil prior to cleaning increased its cleaning rate.

In many CIP systems, the liquid jet impinges at an oblique angle to the target surface and an understanding of the liquid flow distribution created by inclined jets is needed to predict the cleaning behaviour. Tests with inclined jets were carried out to establish the shape of the hydraulic jump formed and their cleaning behaviour. Three flow distribution models were developed and compared with the experimental data, providing an insight into the liquid flow distribution, but further work remains to enable the liquid flow distribution to be predicted *a priori*.

The cleaning of viscous soil layers (petroleum jelly, tomato ketchup and two tooth-pastes) from vertical walls by an intermittent water jet was investigated by using a moving interrupter plate to periodically disrupt the impingement of a continuous water jet. The use of intermittent jets was found to provide no improvement in the cleaning of these soil layers in the absence of soaking.

Acknowledgements

First and foremost, I would like to thank my supervisor, Prof. Ian Wilson. His invaluable guidance, great intuition and insightful wisdom provided a solid foundation on which I could learn, grow and develop, not only as a researcher, but also as a person. This thesis would not have been possible without his constant encouragement and endless patience.

Financial support was provided by Newnham College, for which I am thankful.

I am also very grateful for all the friends that I have made throughout my time at Cambridge, from the Paste, Particle and Polymer Processing group (P⁴G), 3.17 office and beyond.

Finally, I would like to thank my parents who have never once doubted or questioned my chosen endeavours. I would not be where I am today without their steadfast love and unwavering support.

Table of contents

Preface	iii
Abstract	v
Acknowledgements	vii
Table of contents.....	ix
List of figures	xiii
List of tables	xxvii
Nomenclature	xxix
1 Introduction.....	1
1.1 Context	1
1.2 Project objectives	2
1.3 Thesis structure.....	4
2 Literature review	5
2.1 Cleaning in manufacturing and processing.....	5
2.2 Hydrodynamics of an impinging liquid jet	11
2.2.1 Hydraulic jump	11
2.2.2 Models.....	13
2.3 Related phenomena.....	19
2.3.1 Falling film	19
2.3.2 Flow in the rope	21
2.3.3 Jet breakup	22
2.3.4 Splatter.....	25
2.3.5 Wall curvature	27
2.3.6 Jet angle	27
2.4 Cleaning by impinging liquid jets.....	30
2.4.1 Overview	30
2.4.2 Models.....	32

	<i>Basic form</i>	32
	<i>Moving jets</i>	35
	<i>Inclined jets</i>	36
	<i>Yield stress materials</i>	37
2.4.3	Intermittent jets	38
2.5	Summary	40
3	Effect of jet length and wall curvature	41
3.1	Introduction	41
3.2	Methods and materials	42
3.2.1	Impinging jet apparatus	42
3.2.2	Flow patterns and image analysis	44
3.2.3	Jet length and splatter	45
3.2.4	Wall curvature	47
3.2.5	Cleaning	51
3.3	Models	53
3.3.1	Correction for refraction	53
	<i>Uncorrected for refraction</i>	53
	<i>Refraction: thin lens model</i>	54
	<i>Refraction: geometrical model</i>	56
3.3.2	Estimate of time taken to establish the hydraulic jump	59
3.4	Results and discussion	60
3.4.1	Jet hydrodynamics	60
	<i>Flow pattern formation</i>	60
	<i>Time taken to establish the hydraulic jump</i>	61
	<i>Steady state flow patterns</i>	62
3.4.2	Effect of jet length	65
	<i>Splatter</i>	65
	<i>Steady state flow patterns</i>	71
3.4.3	Correction for refraction	73
	<i>Second camera measurements and estimates</i>	73
	<i>Comparison between the models</i>	74
	<i>Empirical correlation</i>	76

3.4.4	Effect of wall curvature	78
	<i>Steady state flow patterns</i>	78
	<i>Other phenomena</i>	82
3.4.5	Cleaning	85
	<i>Impact of jet length</i>	85
	<i>Impact of wall curvature</i>	87
	<i>Impact of soaking</i>	88
3.5	Conclusions	89
4	Flow distribution of inclined jets	91
4.1	Introduction	91
4.2	Models	92
4.2.1	Geometric transformation	92
4.2.2	Flow distribution	96
	<i>Kate et al. (2007) model (KM)</i>	100
	<i>Circular model</i>	101
	<i>Moving stagnation point model</i>	102
	<i>Changing ellipse model</i>	104
4.3	Methods and materials	106
4.3.1	Hydrodynamic tests	106
	<i>Apparatus</i>	106
	<i>Flow patterns and image analysis</i>	109
4.3.2	Liquid flow rate measurements	110
4.3.3	Cleaning tests	112
	<i>Apparatus</i>	112
	<i>Soil material and target plate</i>	113
	<i>Imaging and image analysis</i>	114
4.3.4	Data processing	115
	<i>Hydrodynamic tests</i>	115
	<i>Liquid flow rate measurements</i>	116
	<i>Cleaning tests</i>	117
	<i>Quantifying the fit of the flow distribution models to experi-</i> <i>mental data</i>	118
4.4	Results and discussion	119

4.4.1	Hydrodynamic tests	119
	<i>Flow patterns</i>	119
	<i>Comparison between the flow distribution models</i>	120
	<i>Fitting the changing ellipse flow distribution model (CEM)</i>	123
4.4.2	Liquid flow measurements.....	127
	<i>Results in the literature</i>	129
4.4.3	Cleaning tests	131
	<i>Normally impinging jet</i>	131
	<i>Inclined jets</i>	134
	<i>Fitting the changing ellipse flow distribution model (CEM)</i>	136
4.4.4	Review of data sets.....	139
	<i>Hydrodynamic and cleaning tests</i>	139
	<i>Results in the literature</i>	142
4.5	Conclusions.....	148
5	Cleaning by intermittent jets	151
5.1	Introduction	151
5.2	Materials and methods	153
5.2.1	Intermittent jet apparatus	153
5.2.2	Soil materials	157
5.2.3	Target plate preparation	159
5.2.4	Cleaning.....	159
5.3	Results and discussion.....	160
5.3.1	Soil layer rheology	160
5.3.2	Continuous jet cleaning	164
5.3.3	Intermittent jet cleaning	172
5.3.4	Reconciliation with results in the literature	174
5.4	Conclusions.....	176
6	Conclusions and future work.....	179
6.1	Conclusions.....	179
6.2	Future work	181
	References.....	183

List of figures

1.1	Schematics of impinging liquid jet cleaning-in-place (CIP) systems: (a) spray ball and (b) rotary jet head. A spray ball can be static or rotated about its axis.	2
1.2	Schematic of (a) a circular hydraulic jump formed by the impingement of a vertical liquid jet on a horizontal surface, and (b) phenomena affecting the flow pattern and cleaning performance of a long liquid jet in an industrial CIP system, where L is the jet length and ϕ is the jet impingement angle.	3
2.1	Stages in the fouling-cleaning cycle (reproduced from Figure 1; Wilson, 2018). The solid material indicates a heat exchanger surface or vessel wall, and the porous material a membrane or filter.	6
2.2	Sinner's circle, illustrating the four key parameters for cleaning. The size of each sector in the circle will depend on the importance of each parameter.	8
2.3	Cleaning map of Fryer and Asteriadou (2009), reproduced from their Figure 1.	10
2.4	Schematics of the (a) side and (b) front views of a coherent horizontal jet impinging normally on a flat vertical wall, forming a hydraulic jump. In (b), O is the point of jet impingement. The grey arrows indicate the direction of the liquid flow.	12
2.5	Schematic of a coherent horizontal jet impinging on a flat vertical surface showing the geometry of the radial film, key parameters and the surface tension forces involved in termination of the radial flow. The inset shows the azimuthal angle θ . Adapted from Wang <i>et al.</i> (2013b).	13
2.6	Cross-section through the radial flow zone and hydraulic jump: (a) stagnation region, (b) boundary layer formation zone, shown by the dashed line, (c) start of the laminar zone, (d) laminar to turbulent transition, (e) hydraulic jump, and (f) rope. O is the point of jet impingement. The surface is drawn horizontal for convenience. Adapted from Bhagat and Wilson (2016).	16
2.7	Schematics of the falling film flow patterns: (a) gravity flow, (b) gravity flow with dry patch formation, and (c) rivulet flow. O is the point of jet impingement and the hydraulic jump is shown by the dashed locus. The grey arrows indicate the direction of the liquid flow. Adapted from Wang <i>et al.</i> (2013b).	19
2.8	Schematic showing the width of the rope, with the assumed rope cross-section shown in the inset. Adapted from Wang <i>et al.</i> (2013b). ..	21

2.9	Schematic of the effect of the jet velocity on its breakup length in the different jet breakup regimes. Before point (a), the liquid has insufficient momentum to form a continuous jet and the liquid drips out of the nozzle. (b) Rayleigh breakup, (c) first wind-induced, (d) second wind-induced and (e) atomisation regimes. Adapted from Lin and Reitz (1998).	24
2.10	Schematic of the splatter that occurs when a horizontal jet impinges normally on a vertical wall, reducing the liquid flow rate in the falling film from Q to Q_{eff}	25
2.11	Schematic of the Kate <i>et al.</i> (2007) model for the flow distribution in an inclined jet. The surface is drawn vertical for convenience. O is the axis of the jet and S is the source. There are two foci, S and S': S is nearest to the nozzle. ϕ_e is the angle that the jet axis makes with the wall.	27
2.12	Soil removal modes in cleaning by impinging jets. Mobile soils are removed by (a) dissolution or (b) roll-up, while immobile soils are removed by (c) erosion or (d) peeling. The arrows indicate the action of the liquid from the jet on the soil. Adapted from Bhagat <i>et al.</i> (2017).	30
2.13	Schematics of the (a) side and (b) front views of cleaning by a coherent horizontal jet impinging normally on a vertical wall. In (b), the white circular region indicates the cleaned area. The grey arrows indicate the direction of the liquid flow. δ is the thickness of the soil layer.	31
3.1	Schematic of the impinging jet apparatus used showing a horizontal jet impinging normally onto a flat vertical target.	42
3.2	Photograph of the steady flow pattern created by a horizontal jet impinging normally on a flat vertical Perspex [®] plate, $d_N = 2$ mm, $Q = 2.0$ L min ⁻¹ , and $L = 70$ mm. The key dimensions are shown. The subscript c refers to the external edge of the rope.	44
3.3	Schematic of the target cylinder mounted with its axis (a) vertical, and (b) horizontal.	47
3.4	Schematic of a vertical cylinder showing calibration lines: (a) side view, and (b) plan view. α and Ψ are the angles of liquid film and second camera from the point of impingement, respectively. Y is the length of interest. X is the axis of the cylinder. Position of calibration lines not drawn to scale: in this case the second camera is positioned at j	49
3.5	Schematic of a cross-section through a cylinder with outer diameter, D_o , and inner diameter, D_i , at the plane of impingement. X is the axis of the cylinder.	53

3.6	(a) Schematic of the cylinder wall modelled as a combined concave-convex thin lens where the focal lengths of the lenses are shown, and (b) schematic of the geometry and other parameters required to calculate the true arc length of the liquid film, A_i . X is the axis of the cylinder.	54
3.7	Schematic of the geometry and other parameters required to calculate A_i by Snell's law. X is the axis of the cylinder and the camera is located at T, a distance l away from X.....	56
3.8	Flow pattern evolution following the normal impingement of a horizontal jet on an initially dry flat vertical Perspex [®] plate, $d_N = 2$ mm, $Q = 2.0$ L min ⁻¹ , and $L = 70$ mm. Horizontal loci indicate steady state values.	60
3.9	Schematic of the flow pattern formation. (a) Initial formation of the hydraulic jump where $Z \approx R$, (b) steady state flow pattern where the rope at the top of the RFZ has been dragged downwards by gravity, giving $Z < R$, and (c) side view of the jet impingement showing both the initial hydraulic jump formed (dashed line) and the steady state flow pattern.....	61
3.10	Comparison of predictions of the time taken to establish the hydraulic jump, t_{jump} , with experimental data obtained for a coherent horizontal water jet impinging normally on a flat vertical Perspex [®] plate.	62
3.11	Effect of flow rate on the size of the radial flow zone. The predictions from the Wilson <i>et al.</i> (2012) and Bhagat and Wilson (2016) models, Equations 2.14 and 2.17, respectively, are shown.	63
3.12	Effect of flow rate on the shape of the flow pattern: relationship between (a) R_c and R , and (b) Z and R	63
3.13	Effect of flow rate on the shape of the flow pattern: relationship between (a) Z_c and Z , and (b) Z_c and R	64
3.14	Effect of flow rate on the rope width (a) directly above the point of impingement ($\theta = 0$), and (b) at the plane of impingement ($\theta = \pi/2$). The experimental data for (a) are from Figure 3.13(a), replotted in the form $B(0) = Z_c - Z$ while the experimental data for (b) are from Figure 3.12(a), replotted in the form $B(\pi/2) = R_c - R$	65
3.15	Effect of jet Reynolds number on the measured splatter fraction. The symbols are defined in the legend: colour indicates nozzle diameter, symbol shape indicates jet length and hollow symbols indicate that jet breakup was observed. The red asterisk data points are calculated from the data in Figure 16(c) of Kim <i>et al.</i> (2020) (rounded entry nozzle, $d_N = 2$ mm, $L = 750$ mm).	66

- 3.16 Splatter fraction from the Q_{eff}/Q data reported by Feldung Damkjær *et al.* (2017) for industrial scale nozzles. The symbols are defined in the legend: colour indicates nozzle diameter and symbol shape indicates jet length. Error bars are not shown as no attempt was made to quantify the errors. 67
- 3.17 Effect of jet length and velocity on the measured splatter fraction for $d_N = 2$ mm. (a) Data from Figure 18(b) of Kim *et al.* (2020) (rounded entry nozzle) and (b) data from Figure 3.15. Error bars in (b) are omitted for clarity but the errors were estimated to be $\xi \pm 0.02$ -0.05 and $L \pm 5$ -10 mm. 68
- 3.18 Data in Figure 3.15 plotted against L/d_N with the symbols representing (a) nozzle diameter and jet length, and (b) range of jet Weber numbers. Error bars are omitted for clarity. 68
- 3.19 Measured splatter fraction for the jets studied plotted against the Bhunia and Lienhard (1994) parameter Ω (Equation 2.33). (a) All the experimental data in this work. Hollow symbols indicate that jet breakup was observed. (b) The experimental data in this work where data with $\xi < 0.04$ and where jet breakup was observed have been omitted; the red asterisks denote data from Figure 7 of Bhunia and Lienhard (1994). The solid red line shows the Bhunia and Lienhard (1994) correlation (Equation 2.32) and the dashed black line shows the correlation obtained here (Equation 3.34). Note the \log_{10} scale for Ω 69
- 3.20 Onset of splattering experimental data in this work with (a) $\xi < 0.05$ and (b) $\xi \geq 0.05$. The solid line shows the Bhunia and Lienhard (1994) correlation (Equation 2.34) where points below the line are predicted to have $\xi < 0.05$ and points above the line $\xi \geq 0.05$. Note the \log_{10} scale for both L/d_N and We 70
- 3.21 Comparison of the measured half-width of the radial flow zone at the level of the point of impingement, R , with the measured (a) half-width of the wetted region at the level of the point of impingement, R_c and (b) height of the radial flow zone at the point of impingement, Z . The dashed line shows $R_c = 4R/3$ and $Z = 3R/4$ in (a) and (b), respectively. 71
- 3.22 Effect of nozzle diameter and jet length on the measured half-width of the radial flow zone at the level of the point of impingement, R , plotted against the flow rate in the falling film, Q_{eff} . The lines show the predictions from the Wilson *et al.* (2012) and Bhagat and Wilson (2016) models, Equations 2.14 and 2.17, respectively. 72
- 3.23 Flow patterns generated by a coherent horizontal liquid jet ($d_N = 2$ mm, $Q = 2.0$ L min^{-1}) impinging normally on Perspex[®] targets: (a) flat plate, (b) vertical cylinder ($\kappa = 9.1$ m^{-1}), and (c) horizontal cylinder ($\kappa = 9.1$ m^{-1}). 73

- 3.24 Comparison of the harmonic weighting and linear interpolation for measurements of (a) R and R_c on vertical cylinders, and (b) Z and Z_c on horizontal cylinders. The dashed line is the line of equality. Error bars are omitted for clarity. Filled symbols are used for R and R_c , hollow symbols are used for Z and Z_c , and colour indicates the cylinder used. At a given flow rate, $R_c > R$ and $Z_c > Z$ 74
- 3.25 Comparison of measurements from the main camera, uncorrected for refraction, with estimates from the second camera for (a) R and R_c on vertical cylinders, and (b) Z and Z_c on horizontal cylinders. The dashed line is the line of equality. Error bars are omitted for clarity. Filled symbols are used for R and R_c , hollow symbols are used for Z and Z_c , and colour indicates the cylinder used. At a given flow rate, $R_c > R$ and $Z_c > Z$ 74
- 3.26 Comparison of (a) R and R_c with Cylinder D placed vertically, and (b) Z and Z_c with Cylinder D placed horizontally. Error bars are omitted for clarity..... 75
- 3.27 Comparison of the estimates from the second camera with measurements from the main camera, corrected with the geometrical model, for (a) R and R_c on vertical cylinders, and (b) Z and Z_c on horizontal cylinders. The dashed line is the line of equality. Error bars are omitted for clarity. Filled symbols are used for R and R_c , hollow symbols are used for Z and Z_c , and colour indicates the cylinder used. At a given flow rate, $R_c > R$ and $Z_c > Z$ 76
- 3.28 Fit of the empirical correlations (Table 3.6) to the experimental data. Error bars are omitted for clarity. (V) – R and R_c on vertical cylinders, and (H) – Z and Z_c on horizontal cylinders. Filled symbols are used for R and R_c , hollow symbols are used for Z and Z_c , and colour indicates the cylinder used. At a given flow rate, $R_c > R$ and $Z_c > Z$.. 77
- 3.29 Experimental measurements of (a) R_c and R , (b) Z and R , and (c) Z_c and R for a horizontal water jet impinging normally on (i) vertical cylinders, and (ii) horizontal cylinders. The flat wall results from Section 3.4.1 are shown for comparison. Error bars are omitted for clarity: these are approximately ± 2 mm for R , R_c , Z and Z_c 79
- 3.30 Effect of curvature and flow rate on the rope width (a) directly above the point of impingement ($\theta = 0$), and (b) at the plane of impingement ($\theta = \pi/2$), on (i) vertical cylinders and (ii) horizontal cylinders. The flat wall results from Figure 3.14 in Section 3.4.1 are shown for comparison. Also plotted are the loci for the model for B presented by Wang *et al.* (Equation 2.28). Error bars are omitted for clarity. ... 80
- 3.31 Effect of flow rate on (a) Z , and (b) R , for a coherent horizontal water jet ($d_N = 2$ mm) impinging normally on (i) vertical cylinders, and (ii) horizontal cylinders. The flat wall results from Section 3.4.1 are shown for comparison. Error bars are omitted for clarity: these are approximately ± 2 mm for Z and R , and ± 0.1 L min⁻¹ for Q 81

- 3.32 Splatter in (a) horizontal, and (b) vertical cylinder under identical experimental conditions ($d_N = 2$ mm, $Q = 2.0$ L min⁻¹, $\kappa = 20$ m⁻¹). 82
- 3.33 (a) Shedding from the rope ($Q = 4.5$ L min⁻¹), (b) angle of the rope at the crown of the cylinder, ε , when wraparound occurs and the dashed line is the prediction from Equation 3.35, and (c) plan view of a horizontal jet impinging normally on a horizontal cylinder. Flow rate increases from (i) to (iv). $d_N = 4$ mm, $L = 30$ mm and $\kappa = 20$ m⁻¹. Vertical black line in (c) indicates the crown (top) of the cylinder. 83
- 3.34 Cleaning of a 0.2 mm thick petroleum jelly layer on a flat, vertical Perspex[®] plate over time. t is time elapsed after jet impingement. $d_N = 2$ mm, $Q_{\text{eff}} = 1.6$ L min⁻¹ and $L = 60$ mm. 85
- 3.35 Evolution of the cleaned region radius over time for 0.2 mm thick petroleum jelly layers on flat, vertical Perspex[®] plates. $d_N = 2$ mm, $Q_{\text{eff}} = 1.6$ L min⁻¹ for $L = 60, 245$ and 350 mm. Note the log₁₀ scale for time. Loci show fit to Equation 2.53. Error bars are omitted for clarity: these are approximately ± 2 mm for a 86
- 3.36 Effect of curvature on size of cleaned region for 1.3 mm thick ClearGlide[™] layers on vertical cylinders. $d_N = 2$ mm, $Q = 1.0$ L min⁻¹, $L = 60$ mm, no soaking. Note the log₁₀ scale for time. Error bars are omitted for clarity: these are approximately ± 2 mm for a 87
- 3.37 Effect of soaking time on the removal of 0.2 mm thick ClearGlide[™] layers on flat plates. A thin film of water covered the plate for 0 s (no soaking), 10 s or 60 s. In these tests the target plate was horizontal rather than vertical, and the jet was vertical rather than horizontal, as this allowed the soil to be cleaned immediately after soaking. $d_N = 2$ mm, $Q = 2.0$ L min⁻¹, $L = 245$ mm. Loci show fit to the expression $a = Kt^{0.2}$. Error bars are omitted for clarity: these are approximately ± 2 mm for a 88
- 4.1 Schematics of the (a) side and (b) plan views of an inclined jet, and (c) the resulting flow pattern formed, viewed from the dry side of the target. In (c), the solid locus denotes the location of the hydraulic jump, the dashed locus denotes the footprint of the jet, the arrow shows the principal flow direction and shading is used to indicate the major and minor flow regions. O is the point of impingement of the axis of the jet and S is the source of the flow. 93
- 4.2 Construction showing the effective jet angle ϕ^* as a combination of the angles ϕ and χ for a jet travelling from E and impinging on the vertical target ODGH at point O. 93

4.3	Schematic of an inclined jet with circular cross-section impinging on a target surface: (a) plan view and (b) angled view. O is the axis of the circular jet. The liquid flowing towards segment SAB marked in lilac (I) is assumed to leave radially across the boundary of the footprint region through the area marked in orange (II) of arc AB and height $h_{\theta, \text{model}}$, and thereafter through the area marked in green (III) of arc CD and height h_{θ}	96
4.4	Schematic of the Kate <i>et al.</i> (2007) model with the geometric transformation. O is the axis of the jet and S is the source.	100
4.5	Schematic of the circular flow distribution model. O is the axis of the jet and S is the source. S_k (as before) is shown.	101
4.6	Schematic of the moving stagnation point model. O is the axis of the jet and S is the source. S_k (as before) is shown.	103
4.7	Schematic of the changing ellipse model showing the true impingement angle, ϕ^* , and the modified angle, ϕ' , with the corresponding changes in footprint shape and source location. O is the axis of the jet and S is the source. S_k (as before) is shown.	104
4.8	(a) Schematic and (b) photograph of the inclined jet apparatus.	106
4.9	Image frames of the (a) initial flow pattern, before the formation of a steady rope and (b) steady state flow pattern for an inclined jet, at $t = 50$ ms and $t = 1$ s, respectively ($Q = 2.0$ L min ⁻¹ , $\phi = 120^\circ$, $\chi = 60^\circ$, $\phi_{\text{overall}}^* = 129.2^\circ$).	109
4.10	Schematic of the liquid flow measurement system showing separate tests with the target plate and reservoir lowered. O is the axis of the jet, T the top of the target plate, H the height of T above O, and H_{liq} the height of the liquid in the reservoir.	110
4.11	Photograph of the experimental setup and (b) schematic showing the liquid flow. $Q_{\text{collected, model}}$ is calculated between azimuthal angles θ_1 and θ_2 . θ_1 and θ_2 are determined by H	111
4.12	Schematic of the impinging jet apparatus used for inclined jet cleaning tests.	112
4.13	Cleaned region after 1.5 s of impingement by a normally impinging jet ($Q = 2.0$ L min ⁻¹). (a) Photograph, (b) processed image: the blue star indicates the point of jet impingement and the green locus the detected cleaned region, and (c) circle of radius $a_{\text{equiv}} = 20.8$ mm.	114
4.14	Schematic showing the location of the hydraulic jump for an inclined jet of ϕ_{overall}^* (solid black locus) and the corresponding locations of the hydraulic jumps for normally impinging jets of $Q_{\theta, \text{equiv}}$	115
4.15	Effect of jet flow rate on the local momentum flux for a jet of $d_N = 2$ mm, from the Wilson <i>et al.</i> (2012) hydrodynamic model (Equations 2.3, 2.7 and 2.10 combined)	117

- 4.16 Parameters used in quantifying the fit of the flow distribution models to the experimental data. 118
- 4.17 Location of the hydraulic jump during the initial formation and at steady state for $Q = 2.0 \text{ L min}^{-1}$ jets of varying orientations. The coordinate origin (0,0) is the point of jet impingement. (a) $\phi = 90^\circ$, $\chi = 60^\circ$, $\phi_{\text{overall}}^* = 60^\circ$, (b) $\phi = 60^\circ$, $\chi = 60^\circ$, $\phi_{\text{overall}}^* = 50.8^\circ$ and (c) $\phi = 120^\circ$, $\chi = 60^\circ$, $\phi_{\text{overall}}^* = 129.2^\circ$. The predictions from the KM model with the Wilson *et al.* (2012) hydrodynamic model, with and without the gravity term (Equations 4.13 and 4.18, respectively), and with the Bhagat and Wilson (2016) hydrodynamic model (Equations 2.41, 2.43 and 2.44), are shown by the solid, dashed and dashed-double dotted lines, respectively. 120
- 4.18 Location of the hydraulic jump for $Q = 2.0 \text{ L min}^{-1}$ jets: predictions from the (a) circular, (b) moving stagnation point and (c) changing ellipse models, compared with experimental data for (i) $\phi = 60^\circ$, $\chi = 60^\circ$, $\phi_{\text{overall}}^* = 50.8^\circ$ and (ii) $\phi = 120^\circ$, $\chi = 60^\circ$, $\phi_{\text{overall}}^* = 129.2^\circ$, respectively. 121
- 4.19 Hydraulic jumps predicted by the changing ellipse model for $Q = 2.0 \text{ L min}^{-1}$ with (a) $\phi = 30^\circ$, $\chi = 90^\circ$, $\phi_{\text{overall}}^* = 30^\circ$ and (b) $\phi = 135^\circ$, $\chi = 35^\circ$, $\phi_{\text{overall}}^* = 150.2^\circ$ 122
- 4.20 (a) CEM fitted to experimental data (Figure 4.17(b); $Q = 2.0 \text{ L min}^{-1}$, $\phi = 60^\circ$, $\chi = 60^\circ$, $\phi_{\text{overall}}^* = 50.8^\circ$) expressed as $Q_{\theta,\text{equiv}}$, (b) fitting parameter ψ (Equation 4.36) showing the optimal value of ω , and (c) predicted shape of the hydraulic jump with the optimal value of ω 124
- 4.21 (a) CEM fitted to experimental data ($Q = 2.0 \text{ L min}^{-1}$, $\phi = 135^\circ$, $\chi = 45^\circ$, $\phi_{\text{overall}}^* = 144.7^\circ$) expressed as $Q_{\theta,\text{equiv}}$, (b) fitting parameter ψ (Equation 4.36) showing the optimal value of ω , and (c) predicted shape of the hydraulic jump with the optimal value of ω 124
- 4.22 Variation of ψ (plotted as $\ln \psi$ for clarity) with ω across the different ϕ_{overall}^* values studied for (a) $Q = 1.0 \text{ L min}^{-1}$, (b) $Q = 2.0 \text{ L min}^{-1}$, and (c) $Q = 3.0 \text{ L min}^{-1}$, shown in (i) as a 3D plot and (ii) as a 2D plot with the colour scale indicating the value of $\ln \psi$. Different combinations of ϕ and χ that have the same ϕ_{overall}^* value (but different θ^* values; Table 4.3) are plotted offset by $\phi_{\text{overall}}^* = 0.1^\circ$, giving the dark vertical streaks in (ii). 125
- 4.23 Optimal values of ω for the CEM fitted to experimental data from hydrodynamic tests (measured $R_{\theta,\text{jump}}$ expressed as $Q_{\theta,\text{equiv}}$). Note that ω is undefined when $\phi_{\text{overall}}^* = 90^\circ$ (Equation 4.30). The parabolic lower bound is given by $\omega = -2 \times 10^{-4} (\phi_{\text{overall}}^* - 90^\circ) + 0.7$, where ϕ_{overall}^* is in degrees. 126

- 4.24 Measured liquid flow rate against the KM prediction for $Q = 2.0 \text{ L min}^{-1}$ jets with $\chi = 90^\circ$ and (a) $\phi = \phi_{\text{overall}}^* = 90^\circ$, (b) $\phi = \phi_{\text{overall}}^* = 60^\circ$, (c) $\phi = \phi_{\text{overall}}^* = 120^\circ$, and (d) $\phi = \phi_{\text{overall}}^* = 135^\circ$. The diagonal locus indicates the line of equality ($y = x$). The dashed lines indicate the locations of the top of the target plate as the target plate is lowered. At A, no liquid flows over the top of the target and all the liquid is collected. From B to C, an increasing amount of liquid flows over the top of the target and the remainder is collected. The shaded area indicates the region below the point of jet impingement where experimental values cannot be obtained. 128
- 4.25 Flow distributions measured by Taylor (1960), and the KM and CEM predictions (Equation 4.37) for (a) $\phi = 60^\circ$, (b) $\phi = 45^\circ$ and (c) $\phi = 30^\circ$. Taylor estimated the values of the hollow data points at $\theta = 180^\circ$ by assuming that the inertia and surface tension forces are balanced, giving $\rho u_T^2 h/2 = \gamma$. u_T is the liquid velocity given by $u_T = \sqrt{2gH_{\text{jet}}}$ where H_{jet} is the head of water used to generate the jet. Taylor used 2.27 mm diameter jets: a combined jet diameter of 3.21 mm ($= \sqrt{2} \times 2.27$) mm was used for the KM and CEM predictions. 130
- 4.26 Cleaning of NIVEA[®] cream by a normally impinging jet ($Q = 2.0 \text{ L min}^{-1}$) over time. t is time elapsed after jet impingement. 131
- 4.27 Evolution of the cleaned region over time, plotted on a (a) linear and (b) \log_{10} scale. Colour is used to indicate the jet flow rate and each test at a given jet flow rate is indicated by a different symbol. The symbol size is greater than or equal to the uncertainty in the data. ... 132
- 4.28 Cleaning rate data showing (a) the fit to the Glover *et al.* (2016) cleaning model (Equation 2.66), and (b) Equation 4.38. Note the \log_{10} scale on the axes in (b). The shaded region in (b) indicates data that were not used in the fitting. Colour is used to indicate the jet flow rate and each test at a given jet flow rate is indicated by a different symbol. 133
- 4.29 Cleaning of NIVEA[®] cream by an inclined jet ($Q = 2.0 \text{ L min}^{-1}$, $\phi = 135^\circ$, $\chi = 45^\circ$, $\phi_{\text{overall}}^* = 144.7^\circ$) over time. t is time elapsed after jet impingement. The yellow star indicates the point of jet impingement. 134
- 4.30 Evolution of the cleaned area over time, plotted on a (a) linear and (b) \log_{10} scale. Colour is used to indicate the jet flow rate and the symbols indicate jet orientation. Repeats of a test are shown by the same symbol. The symbol size is greater than or equal to the uncertainty in the data. 135

- 4.31 Data from an inclined jet cleaning test ($Q = 2.0 \text{ L min}^{-1}$, $\phi = 45^\circ$, $\chi = 90^\circ$, $\phi_{\text{overall}}^* = 45^\circ$). Colour is used to indicate the azimuthal angle, θ . (a) Evolution of the cleaned radius over time in different θ directions and the curves fitted to obtain an estimate of a cleaning rate, da_θ/dt . (b) Equation 4.38 was used to obtain a values of M for the da_θ/dt data from (a) and the cleaning data were compared with the curves from the Wilson *et al.* (2012) hydrodynamic model to obtain estimates of the volumetric flow rate in each θ direction, $Q_{\theta,\text{equiv}}$. 136
- 4.32 Fit of the CEM to $Q_{\theta,\text{equiv}}$ data from cleaning tests with a jet of $Q = 2.0 \text{ L min}^{-1}$: (a) $\phi = 60^\circ$, $\chi = 60^\circ$, $\phi_{\text{overall}}^* = 50.8^\circ$, and (b) $\phi = 135^\circ$, $\chi = 45^\circ$, $\phi_{\text{overall}}^* = 144.7^\circ$. The insets show the variation of the fitting parameter ψ with ω . The optimal value of ω (the best CEM fit to the data) is where ψ is a minimum. 137
- 4.33 Variation of ψ (plotted as $\ln \psi$ for clarity) with ω across the different ϕ_{overall}^* values studied with $Q = 2.0 \text{ L min}^{-1}$, shown in (a) as a 3D plot and (b) as a 2D plot with the colour scale indicating the value of $\ln \psi$. Different combinations of ϕ and χ that have the same ϕ_{overall}^* value (but different θ^* values; Table 4.3) are plotted offset by $\phi_{\text{overall}}^* = 0.1^\circ$, giving the dark vertical streaks in (b). 138
- 4.34 Optimal values of ω for the CEM fitted to experimental data from cleaning tests. Note that ω is undefined when $\phi_{\text{overall}}^* = 90^\circ$ (Equation 4.30). The parabolic lower bound is given by $\omega = -1 \times 10^{-4} (\phi_{\text{overall}}^* - 90^\circ) + 0.65$, where ϕ_{overall}^* is in degrees. 139
- 4.35 Combined results of the hydrodynamic and cleaning tests for $Q = 2.0 \text{ L min}^{-1}$ and (a) $\phi = 60^\circ$, $\chi = 60^\circ$, $\phi_{\text{overall}}^* = 50.8^\circ$ (Figures 4.20(a) and 4.32(a)), (b) $\phi = 135^\circ$, $\chi = 45^\circ$, $\phi_{\text{overall}}^* = 144.7^\circ$ (Figures 4.21(a) and 4.32(b)), (c) $\phi = 120^\circ$, $\chi = 60^\circ$, $\phi_{\text{overall}}^* = 129.2^\circ$ (Figure 4.17(c)), and (d) $\phi = 90^\circ$, $\chi = 60^\circ$, $\phi_{\text{overall}}^* = 60^\circ$ (Figure 4.17(a)). Optimal fits of the CEM to both hydrodynamic and cleaning tests are shown. 140
- 4.36 Distance of the source from the axis of the jet, S_{model} , scaled by the jet radius to give a non-dimensional term, S_{model}/r_0 , against the overall jet angle, ϕ_{overall}^* (Equation 4.7) for (a) hydrodynamic and (b) cleaning tests obtained with Equation 4.28 using the optimal value of ω from the CEM fits to the experimental data. The KM result (Equation 4.20) is shown by the solid black locus and the dashed line shows Equation 4.39. Only one jet radius ($r_0 = 1 \text{ mm}$) was used in all the tests. 141
- 4.37 Relationship between the overall modified jet angle, ϕ'_{overall} , from the CEM and the overall jet angle, ϕ_{overall}^* , from the geometric transformation (Equation 4.7) for (a) hydrodynamic and (b) cleaning tests. ϕ'_{overall} was obtained from Equations 4.30 and 4.32 with the optimal value of ω from the CEM fits to the experimental data. The KM result (recovered when $\omega = 1$, giving $\phi'_{\text{overall}} = \phi_{\text{overall}}^*$) is shown by the solid black locus and the dashed line shows Equation 4.40. 142

4.38	Data from Figure 12 of Baghel <i>et al.</i> (2020) interpreted and plotted in the form of Figure 4.36, showing the non-dimensional distance of the source from the axis of the jet for different jet angles and Reynolds numbers. The KM result (Equation 4.20) is shown by the solid black locus and the dashed line shows Equation 4.39.	143
4.39	Location of the hydraulic jump reported by Kate <i>et al.</i> (2007) in their Figure 7 compared with their scaling relation (Equation 2.37), the KM result (Equation 4.19) and the CEM result (Equation 4.31 with jet angle from Equation 4.40). (a) $r_0 = 3.5$ mm, $Q = 5.83 \times 10^{-5}$ m ³ s ⁻¹ (3.5 L min ⁻¹), $Re = 10\,600$, $\phi_e = 60^\circ$, $\phi_{\text{overall}}^* = 60^\circ$, $\phi'_{\text{overall}} = 69^\circ$; (b) $r_0 = 4.35$ mm, $Q = 8.33 \times 10^{-5}$ m ³ s ⁻¹ (5.0 L min ⁻¹), $Re = 12\,200$, $\phi_e = 45^\circ$, $\phi_{\text{overall}}^* = 45^\circ$, $\phi'_{\text{overall}} = 58^\circ$; and (c) $r_0 = 3.25$ mm, $Q = 5 \times 10^{-5}$ m ³ s ⁻¹ (3.0 L min ⁻¹), $Re = 9\,800$, $\phi_e = 35^\circ$, $\phi_{\text{overall}}^* = 35^\circ$, $\phi'_{\text{overall}} = 51^\circ$	144
4.40	Location of the hydraulic jump reported by Kate <i>et al.</i> (2008) in their Figure 12 for $d_N = 6.5$ mm, $\phi_e = 35^\circ$ and $6\,500 < Re < 29\,400$ compared with the (a) Kate <i>et al.</i> (2007) scaling relation (Equation 2.37), (b) KM result (Equation 4.19, $\phi_{\text{overall}}^* = 35^\circ$) and the CEM result (Equation 4.31 with jet angle from Equation 4.40, $\phi'_{\text{overall}} = 51^\circ$).	145
4.41	Location of the hydraulic jump reported by Kate <i>et al.</i> (2008) in their Figure 12 for $d_N = 6.5$ mm, $\phi_e = 45^\circ$ and $3\,300 < Re < 16\,300$ compared with the (a) Kate <i>et al.</i> (2007) scaling relation (Equation 2.37), (b) KM result (Equation 4.19, $\phi_{\text{overall}}^* = 45^\circ$) and the CEM result (Equation 4.31 with jet angle from Equation 4.40, $\phi'_{\text{overall}} = 58^\circ$).	146
4.42	Location of the hydraulic jump reported by Kate <i>et al.</i> (2008) in their Figure 12 for $d_N = 6.4$ mm, $\phi_e = 55^\circ$ and $3\,300 < Re < 19\,900$ compared with the (a) Kate <i>et al.</i> (2007) scaling relation (Equation 2.37), (b) KM result (Equation 4.19, $\phi_{\text{overall}}^* = 55^\circ$) and the CEM result (Equation 4.31 with jet angle from Equation 4.40, $\phi'_{\text{overall}} = 65^\circ$).	147
5.1	Schematic of different jet impingement conditions: (a) a coherent continuous jet, (b) a series of rectangular pulses, and (c) complete jet breakup into droplets.	152
5.2	Schematic of the modified impinging jet apparatus.	153
5.3	(a) Schematic of an interrupter plate; photographs showing the jet (b) passing through a slot in the plate, and (c) disrupted by the plate ($h_s = 9.5$ mm, $h_g = 20.5$ mm).	154
5.4	Volume-based particle size distributions of the Oral-B® and Colgate® toothpastes.	158

- 5.5 Oscillatory studies of soil material yielding behaviour. τ_a is the amplitude of the imposed oscillatory stress (frequency 1 Hz). (a) Ketchup, (b) Colgate[®], (c) Oral-B[®], and (d) PJ. Hollow symbols are used for G' and filled symbols are used for G'' . The vertical dashed lines on (a), (b) and (d) indicate the crossover stress τ_X . Note the different modulus scale on (d). 161
- 5.6 Flow behaviour of soil materials obtained from steady stress ramps. Note the different scale for the PJ data. Vertical dashed lines show τ_X values obtained in oscillatory stress testing (Figure 5.5) for PJ, ketchup and Colgate[®]. 162
- 5.7 Shear stress as a function of shear rate obtained from steady stress ramps of (a) ketchup and (b) PJ. The lines show the Bingham fits ($\tau = \tau_c + \mu_B \dot{\gamma}$, where $\dot{\gamma}$ is the shear rate) used in the viscous dissipation model. The Bingham parameters are reported in Table 5.3 163
- 5.8 Shear rate ramps for the Oral-B[®] toothpaste. Filled symbols indicate the increasing ramp and hollow symbols the decreasing ramp. The inset shows the shear rate ramps performed (note the y-axis is not to scale). 163
- 5.9 Example of the reproducibility of the continuous jet cleaning tests: cleaning of (a) ketchup and (b) Colgate[®] layers. Solid and dashed lines indicate different tests. The horizontal dashed line marked RFZ shows the location of the hydraulic jump observed with uncoated surfaces. . . 164
- 5.10 Cleaning of a Colgate[®] toothpaste soil layer by a continuous jet showing fingering and peeling. t is the time elapsed after jet impingement and a is the average cleaned radius. 165
- 5.11 Cleaning by continuous jet impingement. (a) Evolution of the average cleaned radius, a (note \log_{10} scales). Horizontal dashed line marked RFZ shows the location of the hydraulic jump observed with uncoated surfaces. Label F indicates fingering of the Colgate[®] soil layer. Symbol size greater than or equal to the uncertainty in measurement. (b) Cleaning rate data, plotted in the form of Equation 2.68: M calculated using the Bhagat and Wilson (2016) model (Equations 2.20, 2.23 and 2.26 in Table 2.1) and da/dt extracted from curve fitting to the data in (a). Error bars show the estimated uncertainty in the gradient from the fitting and are omitted where the symbol size is greater than or equal to the estimated uncertainty. Dashed lines show the fit of the data to Equation 2.68 with parameters k' and M_y given in Table 5.2. Hollow symbols indicate data that were not used in the fitting. 166
- 5.12 Cleaning profiles of (a) ketchup and (b) PJ fitted with Equation 2.68 from Figure 5.11(b) compared with the predictions from the Fernandes and Wilson (2020) viscous dissipation cleaning model for Bingham materials (Equation 2.69) for several values of δ_i 168

-
- 5.13 Cleaning of Oral-B[®] layer, with $t_{\text{on}} = 60$ ms, $t_{\text{off}} = 130$ ms: (a) cleaned radius detected from images, and (b) after removal of the stationary plateaus. The dashed line shows the cleaning profile for a continuous jet (Figure 5.11(a)). The interval labelled t_D in (a) indicates where the motor direction was reversed manually using its two-way switch. . 172
- 5.14 Cleaning profiles for each soil with the stationary plateaus removed. A reduced number of data points are plotted and error bars are omitted for clarity. The uncertainties in the measurements are approximately $a \pm 1$ mm and $t \pm 0.02$ s. The solid line indicates continuous jet cleaning. In (b), the half-shaded data points indicate tests where the area cleaned was not circular, and the label F and hollow data points indicate fingering. The label I indicates the time at which the inset image was taken. 173
- 5.15 Example cleaning profile from Fuchs *et al.* (2017). Cleaning rate data reproduced from Figure 4 in their paper: the cumulative mass removed was obtained by integrating the cleaning rate data. Label RFZ indicates the time at which the RFZ region was cleaned. The inset is Figure 3(d) from their paper, showing the two regions (Box 1 and Box 2) they used to evaluate cleaning. 175

List of tables

2.1	Key equations from the Bhagat and Wilson (2016) hydrodynamic model for the mean velocity, thickness and momentum flow rate per unit width of the liquid film in each region of the RFZ.	18
2.2	Criteria for the jet breakup regimes described by Lin and Reitz (1998). Schematics adapted from Kim <i>et al.</i> (2020).	23
3.1	Dimensions of the nozzles (adapted from Wang <i>et al.</i> , 2013b).	43
3.2	Summary of experimental conditions used to investigate the effect of jet length.	46
3.3	Dimensions of the Perspex [®] cylinders used.	47
3.4	Summary of experimental conditions used to investigate the effect of wall curvature.	48
3.5	Summary of experimental conditions used in the cleaning tests.	52
3.6	Empirical correlations used to correct for refraction, where $m = R, R_c, Z$ or Z_c	77
3.7	Summary of the cleaning parameters obtained from the experimental data shown in Figure 3.35.	87
4.1	Jet angles ϕ and χ and their resulting ϕ^* , ϕ^*_{overall} and θ^* values, ordered by increasing θ^* values.	95
4.2	Parameters in the flow distribution models.	100
4.3	Combinations of jet angles used in the inclined jet hydrodynamic tests and the corresponding ϕ^* , ϕ^*_{overall} and θ^* values.	108
4.4	Flow rates used in the inclined jet hydrodynamic tests.	108
4.5	Flow rates and combinations of jet angles used in the inclined jet cleaning tests.	113
4.6	Optimal values of ω for the CEM fitted to experimental data from hydrodynamic tests (measured $R_{\theta, \text{jump}}$ expressed as $Q_{\theta, \text{equiv}}$).	126
4.7	Optimal values of ω for the CEM fitted to experimental data from cleaning tests.	138
5.1	Key dimensions of the interrupter plates used and jet interruption periods studied.	156
5.2	Soil layer properties and rheological parameters (Figures 5.5 and 5.6), and cleaning model parameters obtained by fitting Equation 2.68 to data in Figure 5.11(b).	169

5.3	Bingham material parameters (Figure 5.7) and cleaning model parameters for different fits of Equation 2.69 to the data, shown in Figure 5.12.	169
5.4	Comparison of cleaning rate parameters obtained in this work to results in the literature.	170

Nomenclature

Symbols - Latin

a	Cleaned radius	m
a_0	Cleaned radius upon jet breakthrough at time t_0	m
a_{equiv}	Radius of a circle with equal area to the cleaned region	m
a_{max}	Maximum cleaned radius	m
a_X	Cleaned radius in the path of a moving jet	m
a_θ	Cleaned radius in azimuthal direction θ	m
A_1	True arc length of the curved liquid film	m
A_o	Measured arc length of the curved liquid film	m
B	Rope width	m
c	Lumped parameter ($c = 10\pi^2\rho\mu/3$)	$\text{kg}^2 \text{m}^{-4} \text{s}^{-1}$
C	Measured chord length of the curved liquid film	m
C_1	Constant ($C_1 = 0.3516$), Eq. 2.42	-
C_2	Constant ($C_2 = 1$), Eq. 2.42	-
C_3	Constant ($C_3 = 0.5$), Eq. 2.41 & Eq. 2.42	-
C_d	Nozzle discharge coefficient	-
$C_{\theta,\text{model}}$	Inclined jet liquid flow distribution constant, Eq. 4.11	$\text{m}^3 \text{s}^{-1}$
d_i	Nozzle internal diameter	m
d_N	Nozzle bore diameter	m
D_i	Cylinder inner diameter	m
D_o	Cylinder outer diameter	m
f	Combined focal length of the cylinder wall	m
f_{concave}	Concave lens focal length	m
f_{convex}	Convex lens focal length	m
f_{rope}	Rope width parameter, Eq. 2.29	-
g	Gravitational acceleration	m s^{-2}
G'	Elastic modulus	Pa
G''	Viscous modulus	Pa
h	Liquid film thickness	m
h_g	Interrupter plate gap height	m
h_s	Interrupter plate slot height	m
h_θ	Liquid film thickness in azimuthal direction θ	m
$h_{\theta,\text{model}}$	Liquid film thickness in azimuthal direction θ at the boundary of the source region	m

H	Height of the top of the target above the jet impingement point	m
H_{jet}	Head of water used to generate the liquid jet	m
H_{liq}	Height of the liquid in the reservoir	m
k'	Cleaning rate constant	m s kg^{-1}
k'_{B}	Cleaning rate constant (Bingham material)	m s kg^{-1}
$\overline{k'_{\text{B}}}$	Space-averaged cleaning rate constant (Bingham material)	m s kg^{-1}
K	Lumped cleaning rate constant ($K = \sqrt[5]{3k'\dot{m}^3/\pi c}$)	$\text{m s}^{-0.2}$
l	Distance of the camera from the cylinder axis	m
L	Jet length	m
L_{B}	Jet breakup length	m
L_{i}	Nozzle inlet length	m
L_{t}	Nozzle throat length	m
m	Refraction correction parameter, Table 3.6	m
\dot{m}	Jet mass flow rate	kg s^{-1}
\dot{m}_{eff}	Effective jet mass flow rate	kg s^{-1}
M	Momentum flow rate per unit width	N m^{-1}
M_{y}	Momentum flow rate per unit width required to cause yield of a viscoplastic fluid	N m^{-1}
$M_{\text{y,B}}$	Limiting momentum flow rate per unit width (Bingham material)	N m^{-1}
$\overline{M_{\text{y,B}}}$	Space-averaged limiting momentum flow rate per unit width (Bingham material)	N m^{-1}
M_{θ}	Momentum flow rate per unit width in azimuthal direction θ	N m^{-1}
ΔP	Pressure drop across the nozzle	Pa
Q	Jet volumetric flow rate	$\text{m}^3 \text{s}^{-1}$
$Q_{\text{collected,expt}}$	Average liquid volumetric flow rate in the falling film collected in the reservoir, measured experimentally	$\text{m}^3 \text{s}^{-1}$
$Q_{\text{collected,model}}$	Average liquid volumetric flow rate in the falling film collected in the reservoir, predicted by the model	$\text{m}^3 \text{s}^{-1}$
Q_{eff}	Liquid volumetric flow rate in the falling film	$\text{m}^3 \text{s}^{-1}$
Q_{wrap}	Jet volumetric flow rate above which the liquid film wraps around the internal surface of a horizontal cylinder	$\text{m}^3 \text{s}^{-1}$
$Q_{\theta,\text{equiv}}$	Equivalent volumetric flow rate in azimuthal direction θ from a normally impinging jet	$\text{m}^3 \text{s}^{-1}$

$Q_{\theta, \text{equiv, model}}$	Equivalent volumetric flow rate in azimuthal direction θ from a normally impinging jet, predicted by the model	$\text{m}^3 \text{s}^{-1}$
r	Radial distance	m
r_0	Jet radius	m
r_b	Boundary layer formation zone radius	m
r_c	Radius of the boundary of the source region (Circular model)	m
r_e	Radius of the boundary of the source region (Kate <i>et al.</i> (2007) model)	m
r_k	Radius of the boundary of the source region (Modified Kate <i>et al.</i> (2007) model)	m
r_t	Laminar-turbulent transition radius	m
r_θ	Radial distance in azimuthal direction θ	m
$r_{\theta, \text{model}}$	Radius of the boundary of the source region	m
r_λ	Radius of the boundary of the source region (Moving stagnation point model)	m
r_ω	Radius of the boundary of the source region (Changing ellipse model)	m
R	Half-width of the radial flow zone	m
R_c	Half-width of the wetted region	m
R_{jump}	Hydraulic jump radius	m
$R_{\theta, \text{jump}}$	Hydraulic jump radius in azimuthal direction θ	m
S	Distance of the source from the jet axis	m
S_c	Distance of the source from the jet axis (Circular model)	m
S_e	Distance of the source from the jet axis (Kate <i>et al.</i> (2007) model)	m
S_k	Distance of the source from the jet axis (Modified Kate <i>et al.</i> (2007) model)	m
S_{model}	Distance of the source from the jet axis for a given flow distribution model	m
S_λ	Distance of the source from the jet axis (Moving stagnation point model)	m
S_ω	Distance of the source from the jet axis (Changing ellipse model)	m
t	Time	s
t_0	Time at which jet breakthrough into the soil occurs	s

t_{breakup}	Jet breakup time associated with the Plateau-Rayleigh instability	s
t_c	Cylinder wall thickness	s
t_D	Time delay	s
t_{flow}	Characteristic timescale of the liquid flow	s
t_{jump}	Time taken for the hydraulic jump to be established	s
t_{on}	Length of time the jet is imposed on the target in each period	s
t_{off}	Length of time the jet is interrupted from impinging on the target in each period	s
t_{process}	Reaction or forcing timescale	s
Δt	Time since jet breakthrough into the soil ($\Delta t = t - t_0$)	s
T	Ratio of timescales ($T = t_{\text{flow}}/t_{\text{process}}$)	-
u	Liquid velocity parallel to the surface at distance z from the surface	m s^{-1}
u_1	Liquid velocity at the surface	m s^{-1}
u_T	Liquid velocity when a jet is generated by a head of H_{jet}	m s^{-1}
U	Mean velocity in the liquid film	m s^{-1}
U_0	Mean velocity of a jet with volumetric flow rate Q	m s^{-1}
$U_{0,\text{equiv}}$	Mean velocity of a jet with volumetric flow rate $Q_{\theta,\text{equiv}}$	m s^{-1}
$U_{0,\text{model}}$	Component of the jet velocity normal to the source region	m s^{-1}
U_R	Mean velocity in the liquid film at the hydraulic jump radius	m s^{-1}
U_θ	Mean velocity in the liquid film in azimuthal direction θ	m s^{-1}
w_c	Width of the region cleaned by a moving jet	m
x	Cartesian x -coordinate	m
x_{jet}	Horizontal distance travelled by the jet	m
y	Cartesian y -coordinate	m
y_{jet}	Vertical distance travelled by the jet	m
y'	Measurement of the curved liquid film from the second camera	m
Y	Estimate of the measurement of the curved liquid film from the second camera	m
z	Distance in the liquid film from the target surface	m
Z	Height of the hydraulic jump above the jet impingement point	m
Z_c	Height of the rope above the jet impingement point	m

Symbols - Greek

α	Angle of the curved liquid film from the cylinder axis	rad.
β	Soild-liquid contact angle	rad.
γ	Vapour-liquid surface tension	N m ⁻¹
$\dot{\gamma}$	Shear rate	s ⁻¹
Γ_{\min}	Minimum wetting rate in the falling film	kg m ⁻¹ s ⁻¹
δ	Soil layer thickness	m
δ_b	Liquid film boundary layer thickness	m
δ_i	Residual soil layer thickness after cleaning	m
ε	Angle of the rope at the crown of the cylinder	rad.
η_{air}	Air refractive index	-
η_{app}	Apparent viscosity	Pa s
η_{Perspex}	Perspex [®] refractive index	-
θ	Azimuthal angle	rad.
θ^*	Azimuthal angle of the jet projection onto the target	rad.
θ_c	Azimuthal angle from the source (Circular model)	rad.
θ_{model}	Azimuthal angle from the source	rad.
θ_λ	Azimuthal angle from the source (Moving stagnation point model)	rad.
κ	Cylinder wall curvature ($\kappa = 2/D_i$)	m ⁻¹
λ	Moving stagnation point model parameter ($0 \leq \lambda \leq 1$)	-
μ	Liquid dynamic viscosity	Pa s
μ_B	Bingham viscosity	Pa s
ν_{jet}	Moving jet nozzle traverse speed	m s ⁻¹
ξ	Splatter fraction	-
ρ	Liquid density	kg m ⁻³
ρ_g	Gas density	kg m ⁻³
σ	Lumped cleaning rate parameter ($\sigma = 3k'mU_0/5\pi$)	m ² s ⁻¹
τ	Steady shear stress	Pa
τ_a	Amplitude of the imposed oscillatory stress	Pa
τ_c	Bingham critical stress	Pa
τ_w	Wall shear stress	Pa
τ_X	Crossover stress	Pa
τ_y	Soil yield stress	Pa
ϕ	Jet impingement angle in the vertical plane	rad.
ϕ^*	Effective jet impingement angle	rad.
ϕ_{overall}^*	Overall jet impingement angle	rad.

ϕ'	Modified jet impingement angle (Changing ellipse model)	rad.
ϕ'_{overall}	Overall modified jet impingement angle (Changing ellipse model)	rad.
ϕ_e	Jet impingement angle (Kate <i>et al.</i> , 2007)	rad.
ϕ_{ramp}	Inclination angle of the wedge-shaped cleaning front	rad.
χ	Jet impingement angle in the horizontal plane	rad.
ψ	Parameter to quantify the fit of the flow distribution models to the experimental data, Eq. 4.36	-
Ψ	Angle of the second camera from the cylinder axis	rad.
ω	Changing ellipse model parameter ($0 \leq \omega \leq 1$)	-
Ω	Splatter fraction parameter, Eq. 2.33	-

Dimensionless groups

Oh	Jet Ohnesorge number ($Oh = \mu/\sqrt{\rho\gamma d_N}$)
Re	Jet Reynolds number ($Re = \rho U_0 d_N/\mu$)
We	Jet Weber number ($We = \rho U_0^2 d_N/\gamma$)
We_g	Gas Weber number ($We_g = \rho_g U_0^2 d_N/\gamma$)

Abbreviations

BLFZ	Boundary layer formation zone
CEM	Changing ellipse model
CIP	Cleaning-in-place
COP	Cleaning-out-of-place
FMCG	Fast moving consumer goods
GDP	Gross domestic product
KM	Kate <i>et al.</i> (2007) model
LAOS	Low amplitude oscillatory stress
LCA	Life cycle assessment
LED	Light-emitting diode
LZ	Laminar zone
PET	Polyethylene terephthalate
PIV	Particle image velocimetry
PJ	Petroleum jelly
PMMA	Polymethyl methacrylate
PVA	Polyvinyl acetate
RFZ	Radial flow zone
TZ	Turbulent zone

Chapter 1

Introduction

1.1 Context

Cleaning is an essential operation in any manufacturing process, and is critical in many industrial sectors such as fast moving consumer goods (FMCG), fine chemicals, food and pharmaceuticals to maintain hygienic operation and product quality. In a report published by the UK Food Standards Agency in 2017, 41% of food recalls between 2013 and 2016 were attributed to physical contamination, microbiological and hygiene issues, highlighting the importance of cleaning.

Large quantities of water, energy and chemicals are used daily for cleaning. For example, in the dairy industry, an estimated 0.5-5 L of water is required for cleaning per litre of milk processed, with a daily production downtime of 4-6 hours dedicated to cleaning (Alvarez *et al.*, 2010). Life cycle assessments (LCA) are a widely recognised quantitative method for evaluating the environmental impacts of industrial processes. An LCA study by Gésan-Guiziou *et al.* (2019) showed that cleaning operations accounted for nearly one-third of the total environmental impact of milk processing.

To improve efficiency and sustainability, industrial cleaning-in-place (CIP) operations have moved from traditional ‘fill and soak’ methods to the use of impinging liquid jets as the shear forces from impact can enhance soil removal rates, significantly reducing cleaning time and the volume of cleaning liquid required (Tamime, 2009). Impinging liquid jet CIP systems such as those based on rotary jet heads and spray balls are used to distribute cleaning solutions and rinsing liquid around the walls of tanks, reactors and other process vessels. A schematic is shown in Figure 1.1.

There are various factors that determine the effectiveness of cleaning operations. Sinner (1959) described cleaning as a balance between four key parameters: time, mechanical action (in CIP operations, the flow of the cleaning liquid), chemistry and temperature. This work focuses on mechanical action, investigating the hydrodynamics of impinging water jets used in cleaning.

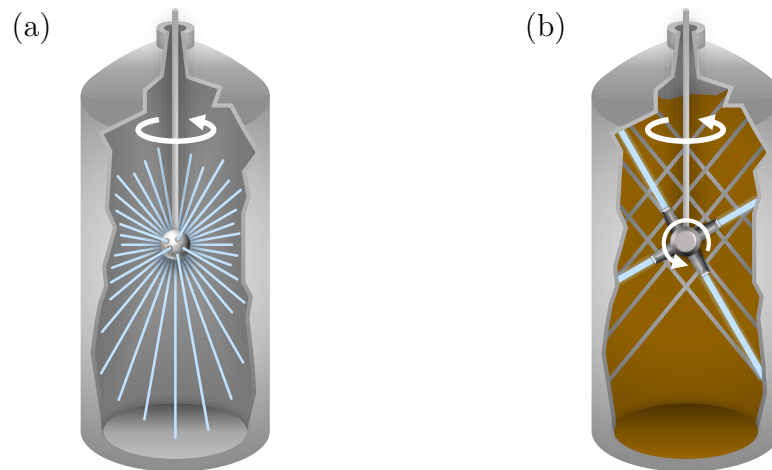


Figure 1.1: Schematics of impinging liquid jet cleaning-in-place (CIP) systems: a (a) spray ball and (b) rotary jet head. A spray ball can be static or rotated about its axis.

1.2 Project objectives

When a coherent vertical liquid jet impinges on a horizontal surface, as shown in Figure 1.2(a), it forms a circular hydraulic jump. This feature underpins jet cleaning methods and the topic has been studied extensively (*e.g.* Watson, 1964; Bohr *et al.*, 1993). Since 2012, quantitative models of the hydrodynamics of the flow generated by a coherent liquid jet impinging on a flat vertical wall have been developed and combined with cleaning models to predict the removal of soil layers from such walls (*e.g.* Wilson *et al.*, 2012; Bhagat *et al.*, 2017).

The jets employed in practice are subject to several phenomena which affect the transfer of those results to industrial systems. Figure 1.2(b) illustrates some of the considerations that need to be made in scaling up the results to industrial scales and conditions. Spray balls and rotary jet heads do not normally generate coherent jets and the jet is often subject to droop and breakup, which is promoted by the length that the jet travels before striking the wall. Droop and breakup can cause the angle of impingement to differ from that for a direct path. The surfaces of interest, internal surfaces of process equipment such as tanks and vessels, are often curved. Nozzle motion (usually rotation) and gravity mean that the jet will rarely impinge normally on a wall.

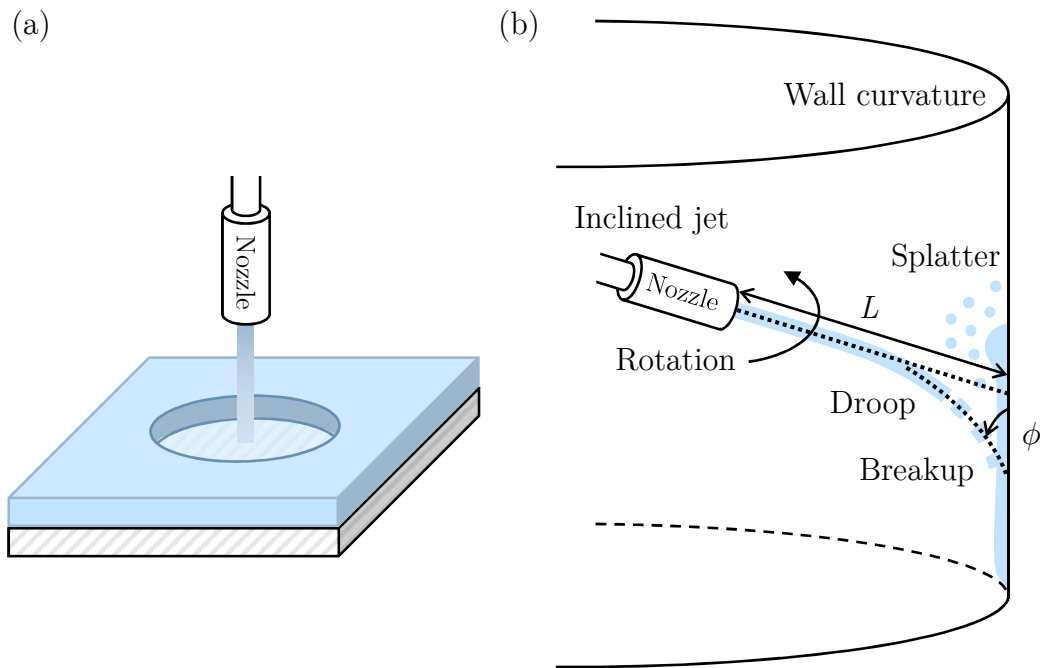


Figure 1.2: Schematic of (a) a circular hydraulic jump formed by the impingement of a vertical liquid jet on a horizontal surface, and (b) phenomena affecting the flow pattern and cleaning performance of a long liquid jet in an industrial CIP system, where L is the jet length and ϕ is the jet impingement angle.

The aim of this project was to extend the existing knowledge to industrial practice by investigating several of these phenomena. Three aspects were investigated, posing the following questions:

- I. How does jet length and wall curvature affect the flow pattern generated by a normally impinging liquid jet and thus its cleaning performance, and are the existing hydrodynamic models able to capture these effects?
- II. What is the liquid flow distribution in the film when a jet impinges at an angle to the target surface? How accurate is the existing Kate *et al.* (2007) model for the liquid flow distribution which has been used by previous workers and can this be improved?
- III. Does intermittent application of a liquid jet rather than continuous application allow the consumption of cleaning liquid to be reduced?

These questions were addressed primarily through experimental investigation, combined with modelling elements for question II. Tests on a small-scale in the laboratory are able to capture some aspects of large-scale industrial cleaning operations, such as the properties of the cleaning liquid, soil and target surface, while other aspects such

as the characteristic jet length vary depending on application. Droop and breakup of the jet are promoted by the length that the jet travels before striking the wall. An understanding of how this affects the jet behaviour would thus enable the results for fully coherent, steady jets from small-scale tests to be translated to those employed in practice.

1.3 Thesis structure

This thesis begins by introducing the field of cleaning by impinging liquids jets and defining the scope of the project.

Chapter 2 reviews the current knowledge on the hydrodynamics of impinging liquid jets. The key hydrodynamic models are outlined, followed by an overview of different aspects and phenomena related to liquid jet impingement. Recent studies where models have been developed to describe the cleaning of soils by impinging jets are summarised.

Chapter 3 explores three different aspects relevant to cleaning by impinging jets on industrial scales: jet length, wall curvature and soaking. Jet breakup occurs as the length of the jet increases and the amount of liquid lost to splatter was measured. The effect of jet length and wall curvature on the liquid flow pattern is investigated, followed by a study on how these aspects as well as soaking affect cleaning.

Chapter 4 investigates the liquid flow distribution when the jet is inclined. The shortcomings of the existing flow distribution model of Kate *et al.* (2007) are described and three alternative flow distributions models are proposed. The models are compared to experimental data obtained from three different types of tests: the shape of the hydraulic jump, measurements of the liquid flow rate and the cleaning of a model soil used as a probe to quantify the local jet flow rate from the observed motion of the cleaning front.

Chapter 5 describes the effect of applying a jet intermittently in the cleaning of layers of four soil materials: petroleum jelly, tomato ketchup and two toothpastes. Removal by an intermittent jet is compared to the cleaning by a continuous jet.

The key developments made in understanding the hydrodynamics of impinging liquid jets used in cleaning are summarised in Chapter 6. Suggested avenues for future research in this area are also identified.

Chapter 2

Literature review

2.1 Cleaning in manufacturing and processing

Cleaning is the process of removing unwanted material from a surface. In this thesis the surfaces of interest are the inner walls of processing equipment and fittings therein, and the term soil is used to refer to the unwanted material. The soil may be residual product remaining on the wall which needs to be removed in order to avoid contamination of a subsequent product, or after a storage container is emptied. These scenarios often arise in food plants that handle different products and in transport tankers.

The soil may also be a fouling layer or other deposit generated on the surface by interactions between the process stream and the wall under the conditions used in processing. Epstein (1983) provided a comprehensive review on the causes of fouling and classified these in terms of the formation mechanisms (crystallisation, particulate, chemical reaction, corrosion and biological fouling) and the five stages involved in the generation of a fouling deposit (initiation, transport, attachment, removal and ageing).

Crystallisation fouling is caused by the change of phase of a dissolved species in solution to a solid form (*e.g.* water scaling in hard water areas, wax deposition in crude oil transport). Particulate fouling occurs when fine solids suspended in the process fluid are deposited on the surface. These could have been generated by crystallisation in the bulk or corrosion upstream. Corrosion fouling occurs when the surface interacts with the process fluid, while in chemical reaction fouling, deposit is formed on the surface as a result of chemical reactions there in which the surface material itself is not a reactant. Biological fouling involves the attachment of macroorganisms or the colonisation and growth of microorganisms in biofilms. More than one mechanism can be involved in formation of fouling layers. A well-known example in the food sector is the formation of fouling layers in dairy plants (Wilson, 2005), where deposition arises from chemical reactions involving milk proteins alongside crystallisation of calcium

phosphate. The relative contribution of each fouling mechanism is dependent on the temperatures used and the milk composition.

Initiation is associated with the delay period often observed before any significant fouling occurs. Transport refers to mass transfer of the fouling precursor to the surface which is followed by its attachment. The fouling material may be removed after its deposition and fouling is often modelled as a balance between deposition and removal (Kern and Seaton, 1959). The freshly deposited material may also change in structure and properties as a result of extended exposure to the conditions at the surface, termed ageing. An example is the ‘cooking’ of dairy deposits on heat exchanger surfaces which renders the deposit harder to remove (Wilson, 2005).

Ageing links the processes of fouling and cleaning as this determines the properties and behaviour of the soil to be removed in any subsequent cleaning step. The symbiosis between fouling and cleaning, and the existence of fouling-cleaning cycles, shown in Figure 2.1, has been discussed by Wilson (2018).

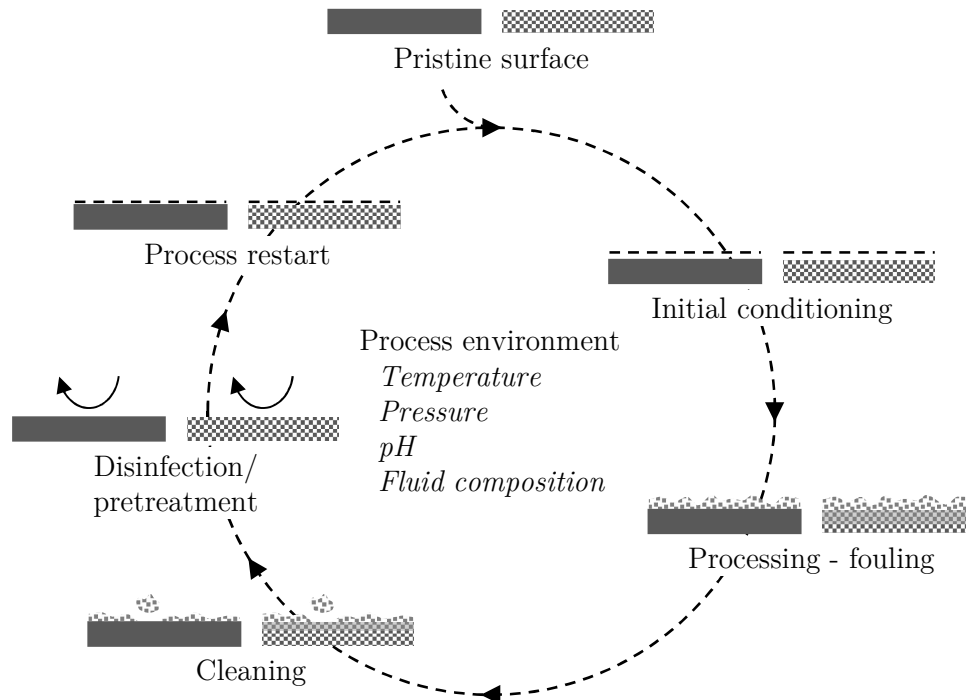


Figure 2.1: Stages in the fouling-cleaning cycle (reproduced from Figure 1; Wilson, 2018). The solid material indicates a heat exchanger surface or vessel wall, and the porous material a membrane or filter.

Fouling is a complex and costly problem. In industrial heat exchangers, the reduced heat transfer efficiency and downtime required for cleaning due to fouling has been estimated to cost approximately 0.25% of the gross domestic product (GDP) of industrialised countries, as well as contributing to 2.5% of the total equivalent anthropogenic emissions of carbon dioxide (Müller-Steinhagen *et al.*, 2005).

In the food sector, the relatively rapid rates of fouling experienced in units such as high temperature short time pasteurisation units, combined with the potential for microbiological contamination via fouling layers, leads to regular cleaning. The cost of cleaning has not been reviewed comprehensively but van Asselt *et al.* (2005) reported that the costs associated with fouling and cleaning constituted 80% of the production costs in the dairy industry. Pettigrew *et al.* (2015) reported that 35% of water used for beer production is used for cleaning, while Eide *et al.* (2003) conducted an LCA study of cleaning in dairies and reported that up to 30% of the energy used in dairy processing is linked to cleaning.

Given the various mechanisms that give rise to a soil layer, there is a wide range of approaches used to remove soils from a surface. When adhesion between the components of the soil and the surface is low, all that is required is some motive force to overcome the adhesive attraction and transport the soil matter away from the surface. An example is a slurry of fine particulates, which attaches to the surface when wet due to capillary action, but when dry, it can be blown off by application of dry air. When adhesion is strong and chemical in nature, cleaning agents need to be applied which react or otherwise interact with the soil and reduce its adhesion to the surface or the cohesion within the soil layer. When a force is applied, such as by a moving liquid, the soil is removed. The cleaning agent is often in liquid form in order to reduce aerosol formation, and can take the form of a solvent (particularly in the pharmaceutical sector) or a solution (*e.g.* sodium hydroxide solutions used in dairy cleaning as these promote the swelling and weakening of protein deposits; Alvarez *et al.*, 2007).

In sectors where the equipment is standardised and the source and behaviour of the soil is well understood, cleaning is also standardised (*e.g.* the removal of hard water scale from power station condensers; British Electricity International, 1992). In other sectors where the processes and products change regularly, cleaning methods and operations are subject to regular development and optimisation. Changes in legislation can require cleaning agents to be replaced, while the increasing need to reduce the environmental impact of processing operations and improve the sustainability

(environmental, financial and resource) of manufacturing mean that research into understanding cleaning mechanisms is an active area (*e.g.* Wilson and Chew, 2014; ModCaD workshop, 2021).

Three industrial sectors which are particularly active in cleaning research are the food, FMCG and pharmaceuticals sectors (*e.g.* ModCaD workshop, 2021). The products in these sectors include soft solids, complex fluids, viscous solutions and suspensions. In many automated and semi-automated manufacturing lines, cleaning-in-place (CIP) is employed over cleaning-out-of-place (COP) to reduce production downtime for cleaning and to minimise the risk of contaminants being introduced during the disassembly and transport of process equipment required for COP. CIP systems range from simple ‘fill and soak’ systems to systems that consist of a series of discrete stages, including flushing for the removal of gross debris, pre-rinse, recirculation of cleaning liquid(s), intermediate rinse, disinfection and final rinse (Tamime, 2009). It should be noted that the capital expenditure associated with a CIP system (several holding tanks, pumps, valve systems, sensors, computer control) can be large (Tamime, 2009).

Identification of the number of stages, identity of cleaning agents(s), operating conditions (temperature, composition, flow velocity and application method) and time represents a complex multiparameter optimisation task. The problem is often presented in the form of Sinner’s circle (Sinner, 1959), shown in Figure 2.2, with four key parameters for cleaning: time, mechanical action, chemistry and temperature.

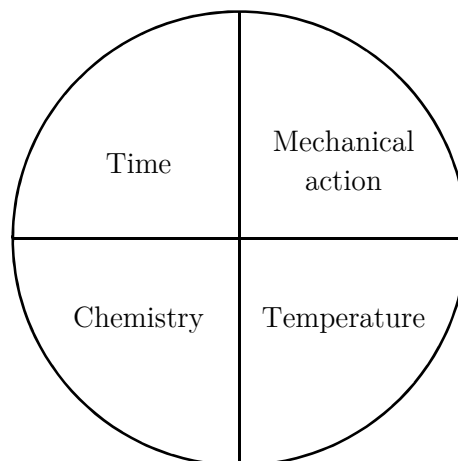


Figure 2.2: Sinner’s circle, illustrating the four key parameters for cleaning. The size of each sector in the circle will depend on the importance of each parameter.

Time refers to the contact time between the soil and the cleaning agent, and relates to chemical transformations as well as physical ones (*e.g.* swelling). Mechanical action relates to the mechanical force(s) applied to the soil, which in many CIP systems arises from hydraulic interactions but can also include ultrasound and ballistic contributions (*e.g.* via cavitation). Chemistry refers to the concentration and composition of the cleaning agent while temperature refers to the reaction kinetics as well as phase changes (*e.g.* melting of fats to render a food soil mobile).

Sinner's circle is often used to represent the relative importance of each parameter in the selection, design and optimisation of cleaning protocols, as well as how the parameters can be combined to achieve a desired level of cleaning (Tamime, 2009). The choice of temperature, chemistry and mechanical action are all determined by the composition and behaviour of the soil, and the surface to which it is attached. For any given soil-surface combination, there is likely to be more than one feasible combination.

Fryer and Asteriadou (2009) presented a qualitative cleaning map for food and FMCG products, shown in Figure 2.3, where they classified cleaning problems based on the type of cleaning fluid and the complexity of the soil. Water at ambient represented cases where the cleaning action derived from solubility of the soil components in water or simple hydraulic action, while hot chemical solutions represent cases where cleaning at acceptable rates required thermal and reactive contributions. Soil complexity was not defined, but the three types of deposits indicate that this metric relates to the number and strength of interactions between soil components (cohesion) and attraction to the surface (adhesion). The map does not include the contribution from hydraulic forces: a classification along these lines has been presented by Bhagat *et al.* (2017) and Joppa *et al.* (2019), and is discussed in Section 2.4. The map also does not cover all types of cleaning: for instance, ice-pigging (Quarini, 2002) is a mechanical operation wherein a viscoplastic ice slurry removes soil as it is pumped along a line or through a confined space.

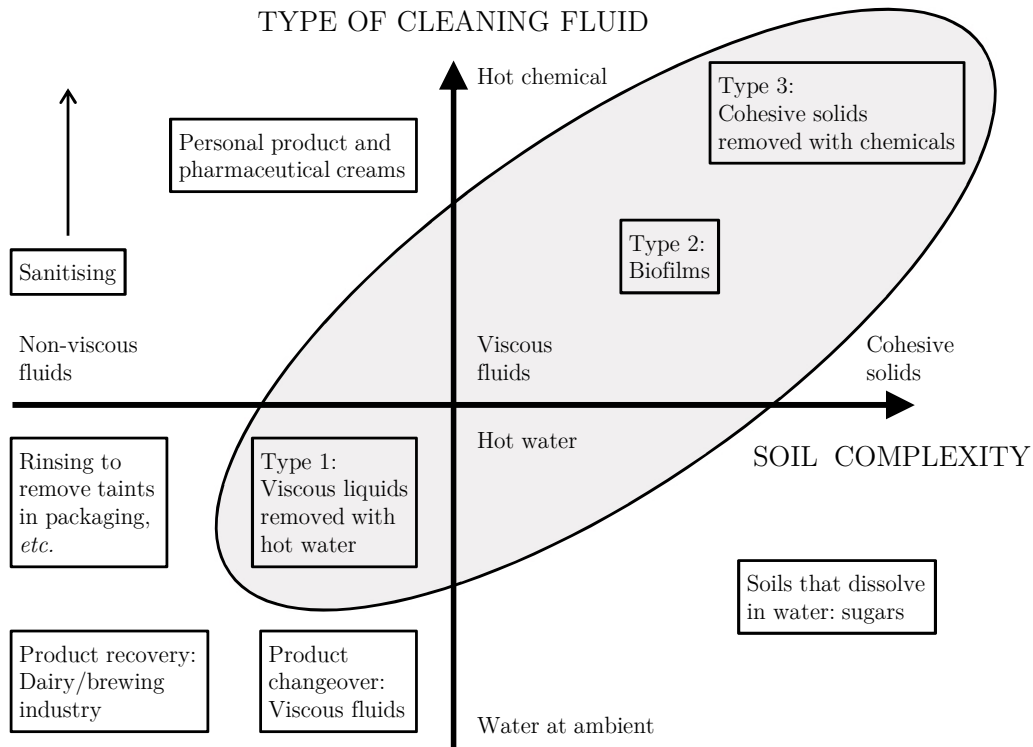


Figure 2.3: Cleaning map of Fryer and Asteriadou (2009), reproduced from their Figure 1.

CIP systems in the food, FMCG and pharmaceutical sectors employ solvents and solutions to deliver chemical agents to the soil and impose forces in the soil. A wide range of flow behaviours arise owing to the different geometries, flow rates and liquid properties. Landel and Wilson (2021) reviewed the range of fluid mechanics phenomena involved in cleaning. They classified flows as either confined, such as those arising in piping and heat exchangers, or free surface flows, such as those generated by jets and sprays. Liquid jets and sprays (*e.g.* Figure 1.1) are widely used to clean tanks and process vessels in CIP systems in these three sectors. The understanding of the jet hydrodynamics in relation to cleaning has been the subject of several research programmes in recent years (Wang, 2014; Köhler, 2018; Yang, 2018; Bhagat, 2019; Rodgers, 2019; Joppa, 2020).

2.2 Hydrodynamics of an impinging liquid jet

2.2.1 Hydraulic jump

When a liquid jet impinges on a solid surface, it gives rise to a rapid, radial flow away from the point of impingement that terminates with an abrupt increase in the height of the liquid film; this is known as a hydraulic jump. Some of the earliest work on hydraulic jumps is attributed to Rayleigh (1914), who developed a theoretical explanation for planar inviscid hydraulic jumps. The formation of a circular hydraulic jump by a coherent vertical liquid jet impinging on a horizontal surface has since been studied and discussed extensively in the fluid mechanics literature.

Bhagat *et al.* (2018) provided a comprehensive outline of the studies of circular hydraulic jumps to date. Key studies include those of Watson (1964) who first explained the formation of a hydraulic jump by a momentum balance. Bush and Aristoff (2003) added surface tension to Watson's theory and Bohr *et al.* (1993) obtained a scaling relation to predict the hydraulic jump radius by using shallow-water type equations and connecting the inner and outer solutions for radial flow through a shock. In these studies, gravity was considered to play a significant role in the formation of the hydraulic jump.

Bhagat *et al.* (2018) showed that at the jump, surface tension and viscous forces balanced the momentum in the liquid film, and gravity did not play a significant role. They showed in their tests that under the same flow conditions, normal impingement of a liquid jet gave a circular hydraulic jump of the same initial radius regardless of the surface orientation. Following this study, the role of gravity in the formation of the hydraulic jump has been debated (Askarizadeh *et al.*, 2019; Duchesne *et al.*, 2019; Wang and Khayat, 2019; Bhagat and Linden, 2020; Bohr and Scheichl, 2021). This line of investigation, examining the fundamental fluid dynamics behind the formation of the hydraulic jump, is not pursued further in this work.

Figure 2.4 shows the flow pattern generated when a coherent horizontal liquid jet impinges normally on a flat vertical wall. After impingement, the liquid from the jet spreads radially outwards from the point of impingement in the form of a thin, fast moving film until the hydraulic jump occurs, giving a transition to a slower moving, thicker film region. Above the point of impingement this gives rise to a hydraulic jump with a narrow band of liquid, termed the rope, which flows circumferentially

downwards beyond it. Below the point of impingement, gravity causes the initial hydraulic jump to evolve into a draining film, bounded by the rope which forms the boundary of the falling film (Aouad *et al.*, 2016; Bhagat *et al.*, 2018). The behaviour of the rope does not affect the location of the hydraulic jump.

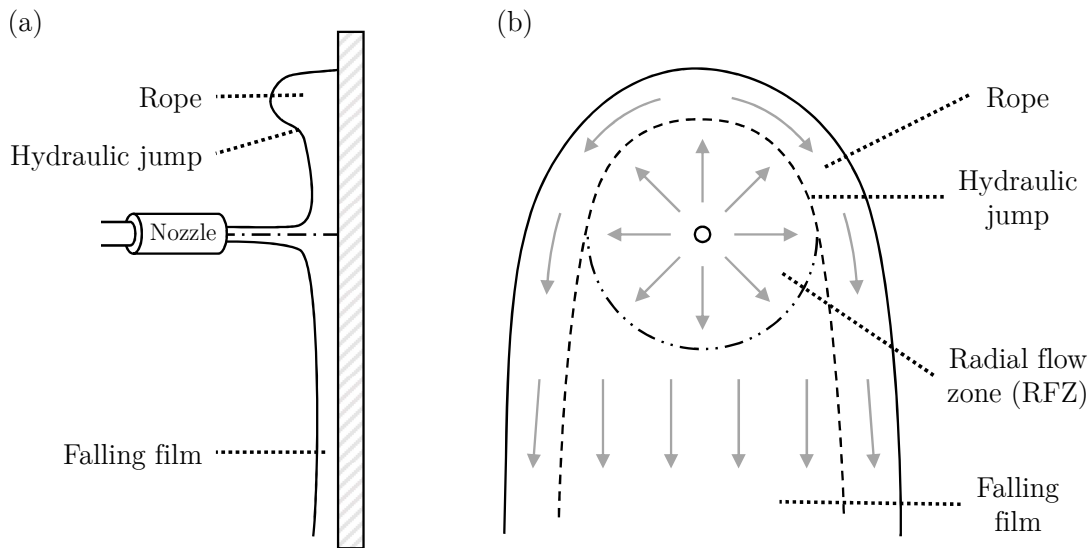


Figure 2.4: Schematics of the (a) side and (b) front views of a coherent horizontal jet impinging normally on a flat vertical wall, forming a hydraulic jump. In (b), O is the point of jet impingement. The grey arrows indicate the direction of the liquid flow.

Impinging jets therefore generate two regions of flow which can promote cleaning. In the area within the jump, here termed the radial flow zone (RFZ), the thin film of liquid is fast moving and exerts a high shear stress on the wall or any material attached to the wall, which can promote cleaning. In the falling film the shear stresses are smaller but the area is considerably larger, achieving contact of the soil with the cleaning liquid and promoting any weakening of the deposit associated with soaking. The wall shear stress exerted in the rope region is intermediate between the other two regions.

The first quantitative study of hydraulic jumps on vertical walls, representative of many cleaning applications, was that by Morison and Thorpe (2002) who reported experimental data for the wetting of vertical surfaces by a horizontal water jet from a spray ball. Wilson *et al.* (2012) presented a quantitative model for the formation of the hydraulic jump based on the work of Button *et al.* (2010) which was able to describe Morison and Thorpe's results. Wang *et al.* (2013b) refined the model by

including the effect of gravity on the flow of the liquid. The Wilson *et al.* model assumes a laminar liquid flow. Bhagat and Wilson (2016) revisited the treatment of the flow of the liquid film, incorporating the effect of turbulence in the film. The Wilson *et al.* (2012) and Bhagat and Wilson (2016) hydrodynamic models both give predictions for the location of the hydraulic jump and are outlined in the next section.

2.2.2 Models

Wilson *et al.* (2012) modelled the flow in the RFZ as a laminar film with a parabolic velocity profile similar to that in Nusselt's analysis of film condensation (Nusselt, 1916). A schematic is shown in Figure 2.5.

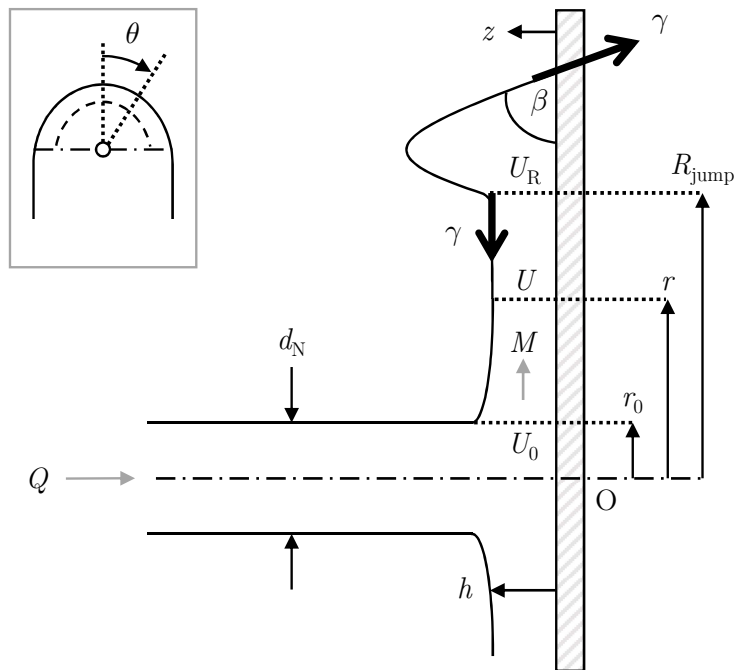


Figure 2.5: Schematic of a coherent horizontal jet impinging on a flat vertical surface showing the geometry of the radial film, key parameters and the surface tension forces involved in termination of the radial flow. The inset shows the azimuthal angle θ . Adapted from Wang *et al.* (2013b).

The coherent horizontal jet of volumetric flow rate Q impinges normally on a flat vertical surface. The jet is of radius r_0 , generated from a nozzle of diameter d_N ($d_N \approx 2r_0$). For a Newtonian liquid, the velocity profile of the liquid film is given by

$$\frac{u}{u_1} = \frac{2z}{h} - \frac{z^2}{h^2} \quad (2.1)$$

where u is the liquid velocity parallel to the surface at distance z from the surface, u_1 is the velocity at the liquid surface, h is the local thickness of the liquid film and the mean velocity in the liquid film, U , is given by

$$U = \frac{2}{3}u_1 \quad (2.2)$$

The momentum flow rate per unit width in the liquid film, M , is given by

$$M = \int_0^h \rho u^2 dz = \frac{6}{5}\rho U^2 h \quad (2.3)$$

where ρ is the liquid density.

A momentum balance on a streamline gives

$$\frac{d}{dr}(Mr) = -\tau_w r - rh\rho g \cos \theta \quad (2.4)$$

where r is the radial distance, τ_w is the wall shear stress, g is the gravitational acceleration ($g = 9.81 \text{ m s}^{-2}$) and θ is the azimuthal angle of the streamline measured from the upwards vertical (shown in the inset of Figure 2.5).

For a Newtonian fluid, the wall shear stress is given by Nusselt (1916) as

$$\tau_w = \frac{3\mu U}{h} \quad (2.5)$$

where μ is the liquid dynamic viscosity.

Substituting the expressions for M and τ_w from Equations 2.3 and 2.5, respectively, into Equation 2.4 gives

$$\frac{d}{dr} \left(\frac{6}{5}\rho U^2 hr \right) = -\frac{3\mu U r}{h} - rh\rho g \cos \theta \quad (2.6)$$

Conservation of volume gives

$$h = \frac{Q}{2\pi r U} \quad (2.7)$$

Substituting the expression for h from Equation 2.7 into Equation 2.6 gives, after simplification,

$$\frac{dU}{dr} = -\frac{10\pi^2\mu U^2 r^2}{\rho Q^2} - \frac{5}{6} \frac{g \cos \theta}{U} \quad (2.8)$$

Ignoring the gravity term so that an analytical solution can be obtained and setting the boundary condition $U = U_0$ at $r = r_0$, where U_0 is the mean jet velocity ($U_0 = Q/2\pi r_0^2$), gives

$$\int_{U_0}^U \frac{1}{U^2} dU = -\frac{10\pi^2\mu}{\rho Q^2} \int_{r_0}^r r^2 dr \quad (2.9)$$

which yields

$$\frac{1}{U} - \frac{1}{U_0} = \frac{10\pi^2\mu}{3\rho Q^2} (r^3 - r_0^3) \quad (2.10)$$

At the location of the hydraulic jump, R_{jump} , assuming $\frac{1}{U} \gg \frac{1}{U_0}$ and $r^3 \gg r_0^3$, the mean velocity in the liquid film, U_R , is given by

$$U_R = \frac{3\rho Q^2}{10\pi^2\mu} \frac{1}{R_{\text{jump}}^3} \quad (2.11)$$

The hydraulic jump occurs at radial distance R_{jump} when the outward flow of momentum in the liquid is matched by the surface tension force opposing wetting. A force balance gives

$$M = \gamma(1 - \cos \beta) \quad (2.12)$$

where γ is the vapour-liquid surface tension and β is the solid-liquid contact angle. This is termed the termination criterion.

Substituting the expressions for M and h from Equations 2.3 and 2.7, respectively, into Equation 2.12 gives, at the location of the hydraulic jump,

$$\frac{6}{5}\rho U_R^2 \left(\frac{Q}{2\pi R_{\text{jump}} U_R} \right) = \gamma(1 - \cos \beta)$$

$$U_R = \frac{5\pi\gamma(1 - \cos \beta)}{3\rho Q} R_{\text{jump}} \quad (2.13)$$

Combining Equations 2.11 and 2.13 gives the estimated location of the hydraulic jump, *viz.*

$$R_{\text{jump}} = \left[\frac{9}{50\pi^3} \frac{\rho^2 Q^3}{\mu\gamma(1 - \cos \beta)} \right]^{1/4} = 0.276 \left[\frac{\rho^2 Q^3}{\mu\gamma(1 - \cos \beta)} \right]^{1/4} \quad (2.14)$$

If the gravity term in Equation 2.8 is included, Equation 2.8 has to be integrated numerically to obtain $U = f(r)$ and combined with Equation 2.13 to identify the location of the hydraulic jump.

Bhagat and Wilson (2016) employed a more rigorous treatment of the flow in the RFZ, following an analysis similar to that of Azuma and Hoshino (1984). They modelled the thin film in the RFZ by subdividing it into three zones, shown in Figure 2.6: the boundary layer formation zone (BLFZ), the laminar zone (LZ), and the turbulent zone (TZ).

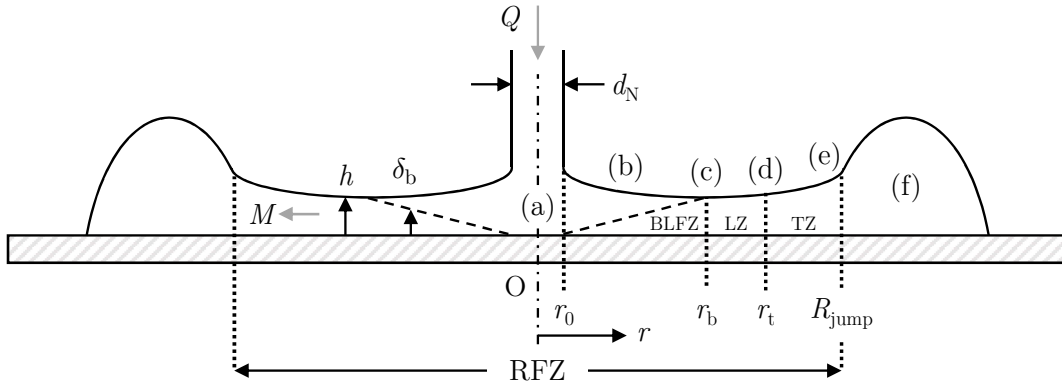


Figure 2.6: Cross-section through the radial flow zone and hydraulic jump: (a) stagnation region, (b) boundary layer formation zone, shown by the dashed line, (c) start of the laminar zone, (d) laminar to turbulent transition, (e) hydraulic jump, and (f) rope. O is the point of jet impingement. The surface is drawn horizontal for convenience. Adapted from Bhagat and Wilson (2016).

The BLFZ extends from $r_0(= d_N/2)$ to r_b , where r_b is the radius at which the boundary layer of thickness δ_b reaches the surface:

$$r_b = 0.24Re^{1/3}d_N \quad (2.15)$$

Here Re is the jet Reynolds number ($Re = \rho U_0 d_N / \mu$).

The LZ spans $r_b < r \leq r_t$, where r_t is the radius at which the laminar to turbulent transition occurs, at

$$r_t = 0.2964Re^{1/3}d_N \quad (2.16)$$

The TZ spans $r_t < r \leq R_{\text{jump}}$. R_{jump} is given by the value of r that satisfies Equation 2.17:

$$r \left[\frac{0.167}{Re^{1/4}} \left(\frac{r}{d_N} \right)^{9/4} + (2.37 - 0.0108Re^{1/2}) \right] = \gamma(1 - \cos \beta) \quad (2.17)$$

Equation 2.17 was obtained from the termination criterion in Equation 2.12, where the term on the left of Equation 2.17 is the expression for M in the TZ.

The equations from the Bhagat and Wilson (2016) hydrodynamic model for U , h and M in each of the three zones are summarised in Table 2.1 (Equations 2.18 to 2.26). These analytical expressions were obtained at $\theta = 90^\circ$ where gravity has no effect. Solutions at other θ values require numerical integration, outlined in full by Bhagat and Wilson (2016).

The solution to Equation 2.17 gives the Bhagat and Wilson (2016) model estimate for the location of the hydraulic jump if it occurs in the TZ. The hydraulic jump could however occur in the BLFZ or LZ; it occurs once the termination criterion in Equation 2.12 is met so the appropriate expression for M (Equation 2.20, 2.23 or 2.26) is required (M decreases with r).

Wang *et al.* (2013a; 2013b) found the location of the hydraulic jump to be insensitive to nature of the wall material at higher flow rates. The contribution from the wall material in the models occur via the $\cos \beta$ term in the termination criterion (Equation 2.12). Bhagat and Wilson (2016) observed similar behaviour and attributed this to shape of the rope. An effective contact angle of $\beta = 90^\circ$ is thus used throughout this work alongside values of $\rho = 1000 \text{ kg m}^{-3}$, $\mu = 0.001 \text{ Pa s}$ and $\gamma = 0.073 \text{ N m}^{-1}$ for water at 20°C .

Table 2.1: Key equations from the Bhagat and Wilson (2016) hydrodynamic model for the mean velocity, thickness and momentum flow rate per unit width of the liquid film in each region of the RFZ.

Region	$U / \text{m s}^{-1}$	h / m	$M / \text{N m}^{-1}$
Boundary layer formation zone $r_0 \leq r \leq r_b$	$U = \frac{U_0}{8 \left(\frac{r}{d_N}\right) \left[0.125 \left(\frac{d_N}{r}\right) + \frac{1.06}{\sqrt{Re}} \left(\frac{r}{d_N}\right)^{1/2}\right]} \quad (2.18)$	$h = d_N \left[0.125 \left(\frac{d_N}{r}\right) + \frac{1.06}{\sqrt{Re}} \left(\frac{r}{d_N}\right)^{1/2}\right] \quad (2.19)$	$M = -1.3746 \rho^{1/2} U_0^{3/2} \sqrt{\mu r} + \rho U_0^2 d_N \left[0.125 \left(\frac{d_N}{r}\right) + \frac{1.06}{\sqrt{Re}} \left(\frac{r}{d_N}\right)^{1/2}\right] \quad (2.20)$
Laminar zone $r_b < r \leq r_t$	$U = \frac{U_0}{8 \left(\frac{r}{d_N}\right) \left[0.1975 \left(\frac{d_N}{r}\right) + \frac{3.792}{Re} \left(\frac{r}{d_N}\right)^2\right]} \quad (2.21)$	$h = d_N \left[0.1975 \left(\frac{d_N}{r}\right) + \frac{3.792}{Re} \left(\frac{r}{d_N}\right)^2\right] \quad (2.22)$	$M = \frac{0.3516 \rho U_0^2 d_N^3}{16r^2 \left[0.1975 \left(\frac{d_N}{r}\right) + \frac{3.792}{Re} \left(\frac{r}{d_N}\right)^2\right]} \quad (2.23)$
Turbulent zone $r_t < r \leq R_{\text{jump}}$	$U = \frac{U_0}{\frac{0.167}{Re^{1/4}} \left(\frac{r}{d_N}\right)^{9/4} + (2.37 - 0.0108 Re^{1/2})} \quad (2.24)$	$h = d_N \left[\frac{0.0209}{Re^{1/4}} \left(\frac{r}{d_N}\right)^{5/4} + (0.296 - 0.001356 Re^{1/2}) \left(\frac{d_N}{r}\right) \right] \quad (2.25)$	$M = \frac{\rho^{64} Q_c U_0}{r \left[\frac{0.167}{Re^{1/4}} \left(\frac{r}{d_N}\right)^{9/4} + (2.37 - 0.0108 Re^{1/2}) \right]} \quad (2.26)$

2.3 Related phenomena

2.3.1 Falling film

The flow pattern of the falling film is an important consideration in the design of impinging jet systems as it affects the coverage of the area wetted by the jet. Figure 2.7 illustrates the flow patterns described by Wang *et al.* (2013b): gravity flow, gravity flow with dry patch formation and rivulet flow. Downward momentum dominates surface tension in gravity flow. Both dry patch formation and rivulet flow occur when surface tension is significant. Dry patch formation occurs when the falling film splits, while in rivulet flow, the falling film width decreases and one or more narrow tails form. Both are undesirable for cleaning applications. Kim *et al.* (2020) observed an additional flow pattern, rivulet flow with outward streams, where the narrow tails formed flowed outwards, away from the point of jet impingement.

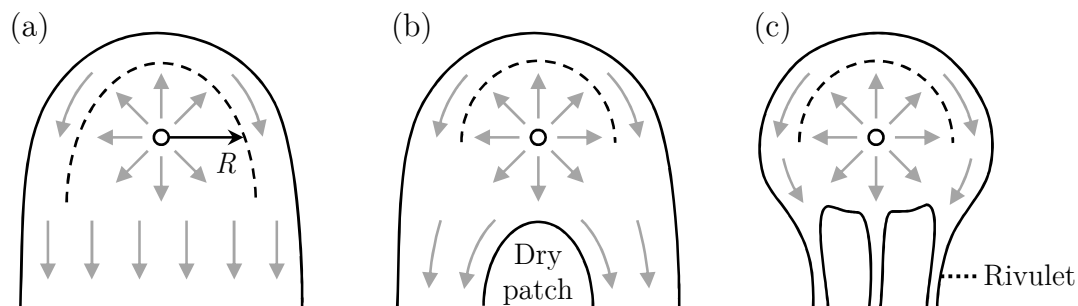


Figure 2.7: Schematics of the falling film flow patterns: (a) gravity flow, (b) gravity flow with dry patch formation, and (c) rivulet flow. O is the point of jet impingement and the hydraulic jump is shown by the dashed locus. The grey arrows indicate the direction of the liquid flow. Adapted from Wang *et al.* (2013b).

Wang *et al.* (2013a) found that the presence of a surfactant affected the flow pattern of the falling film although it had little influence on the location of the hydraulic jump. They attributed this to dynamic contact angle effects: in the falling film there was sufficient time for the surfactant to accumulate at the wetting line and influence the contact angle. Wilson *et al.* (2012) and Wang *et al.* (2013a; 2013b) found that rivulet flow was more prevalent on Perspex than on glass. Perspex has a higher contact angle (*i.e.* is less wetting) for water in air than glass, confirming that the contact angle affects the flow behaviour in the falling film.

Wilson *et al.* (2012) found that the occurrence of stable, wide films in gravity flow could be predicted using the Hartley and Murgatroyd (1964) criterion for the minimum wetting rate of a stable falling film, Γ_{\min} , where the wetting rate is defined as the mass flow rate per unit width, *viz.*

$$\Gamma_{\min} = 1.69 \left(\frac{\mu\rho}{g} \right)^{1/5} [\gamma(1 - \cos\beta)]^{3/5} \quad (2.27)$$

Wang *et al.* (2013b) proposed a simple two-stream model for falling film stability, where the falling film is modelled as a central stream bounded by an outer stream, the draining rope. The central stream is of width $2R$, where R is the half-width of the RFZ at the level of the point of impingement (see Figure 2.7(a)). The central stream and outer stream each have mass flow rate $\rho Q/2$. Dry patch formation occurs when the wetting rate in the central stream, $\rho Q/4R$, is lower than the Hartley and Murgatroyd wetting criterion. This simple model by Wang *et al.* provided a reasonable estimate of the onset of dry patch formation.

They also used the two-stream model to investigate the occurrence of rivulet flow, and reported that rivulet flow was observed in cases where the Hartley and Murgatroyd wetting criterion was satisfied in the central stream but violated in the outer stream. Mertens *et al.* (2005) modelled the braided patterns that can be formed by the tail in rivulet flow, and a revised model by Aouad *et al.* (2016) was found to give equally good or better agreement with the experimental data.

When a jet is inclined, the liquid flow distribution is altered. Wang *et al.* (2013b) observed rivulet flow with downward-inclined jets and dry patch formation with upward-inclined jets. The stability of the dry patches increased as the flow rate increased.

Another feature of the falling film is the presence of surface waves. These were investigated by Aouad *et al.* (2016).

2.3.2 Flow in the rope

The flow in the rope affects the flow pattern of the falling film and Wang *et al.* (2013a) reported that the width of the wetted region at the point of impingement, $2R_c$, is an important parameter for estimating the wetting rate in the falling film. Estimates for R can be obtained from the hydrodynamic models (Equations 2.14 and 2.17), and a model that predicts the width of the rope, B , would enable R_c to be estimated from $R_c = R + B$. A schematic is shown in Figure 2.8. Wang *et al.* (2013b) proposed a simple model to predict the width of the rope, B , at different azimuthal positions by assuming that the rope has a semi-circular cross-section, giving

$$B(\theta) = \frac{2}{\pi} \sqrt{\frac{Q}{\sqrt{2gR}}} \sqrt{\frac{\theta}{f_{\text{rope}}(\theta)}} \quad (2.28)$$

where

$$f_{\text{rope}}(\theta) = \frac{2 \sin \theta}{\theta} + \frac{2(\cos \theta - 1)}{\theta^2} - \cos \theta \quad (2.29)$$

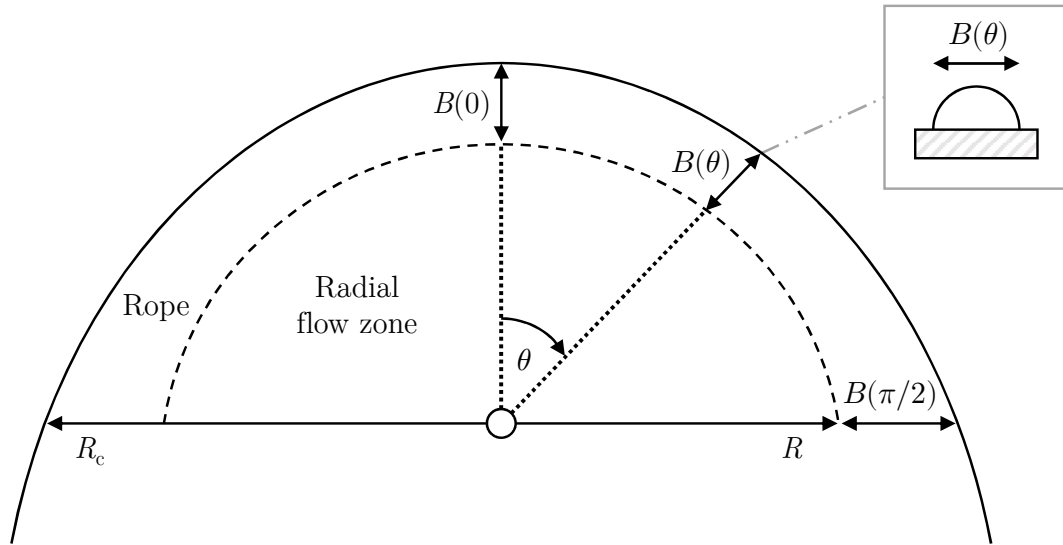


Figure 2.8: Schematic showing the width of the rope, with the assumed rope cross-section shown in the inset. Adapted from Wang *et al.* (2013b).

Wang *et al.* (2013b) found that the model provided a reasonable estimate of B directly above the point of impingement ($\theta = 0$), but not at the horizontal impingement plane ($\theta = \pi/2$) where it provided a lower bound. They noted that the flow in the rope is quite chaotic, so the assumption of a semi-circular cross-section is unlikely to be valid.

2.3.3 Jet breakup

Rayleigh (1879a; 1879b) showed that jet breakup occurs when disturbances on the jet surface promote hydrodynamic instabilities as a cylinder of liquid is thermodynamically less stable than a series of drops. The breakup of a liquid jet is a complex phenomenon and it is influenced by many parameters, including nozzle design, jet velocity, turbulence, and physical and thermodynamic properties of the liquid and surrounding environment. Reitz and Bracco (1986) identified four main regimes of jet breakup: Rayleigh breakup, first wind-induced, second wind-induced and atomisation. Lin and Reitz (1998) described the criteria for each of the regimes, summarised in Table 2.2, based on the jet Ohnesorge number, $Oh = \mu/\sqrt{\rho\gamma d_N}$; jet Weber number, $We = \rho U_0^2 d_N/\gamma$; and gas Weber number, $We_g = \rho_g U_0^2 d_N/\gamma$, where ρ_g is the density of the gas in the environment surrounding the liquid jet ($\rho_g = 1.2 \text{ kg m}^{-3}$ for air at 20°C and atmospheric pressure).

In the Rayleigh breakup regime, the growth of axisymmetric perturbations in the jet causes it to breakup into droplets, where the droplets are pinched off from the jet. In the first wind-induced regime, the perturbations and breakup into droplets are not as regular as in the Rayleigh breakup regime, resulting in additional smaller secondary droplets that are stripped off the liquid surface. The perturbations in the second wind-induced regime are very chaotic so the jet breaks up into large fragments and many secondary droplets are formed. In the atomisation regime, the jet disintegrates into droplets close to the nozzle, forming a spray with a small core of liquid near the nozzle. Kim *et al.* (2020) investigated the breakup of water jets and found the breakup regimes to be in agreement with the criteria given by Lin and Reitz (1998) (Table 2.2).

Table 2.2: Criteria for the jet breakup regimes described by Lin and Reitz (1998). Schematics adapted from Kim *et al.* (2020).

	Regime	Criteria
Rayleigh breakup		$We > 8$ and $We_g < 0.4$ or $1.2 + 3.41 Oh^{0.9}$
First wind-induced		$1.2 + 3.41 Oh^{0.9} < We_g < 13$
Second wind-induced		$13 < We_g < 40.3$
Atomisation		$We_g > 40.3$

Jet breakup can also be considered in terms of its breakup length, L_B , which is the length of the coherent portion of the jet before breakup. The jet breakup curve as a function of the mean jet velocity is shown in Figure 2.9.

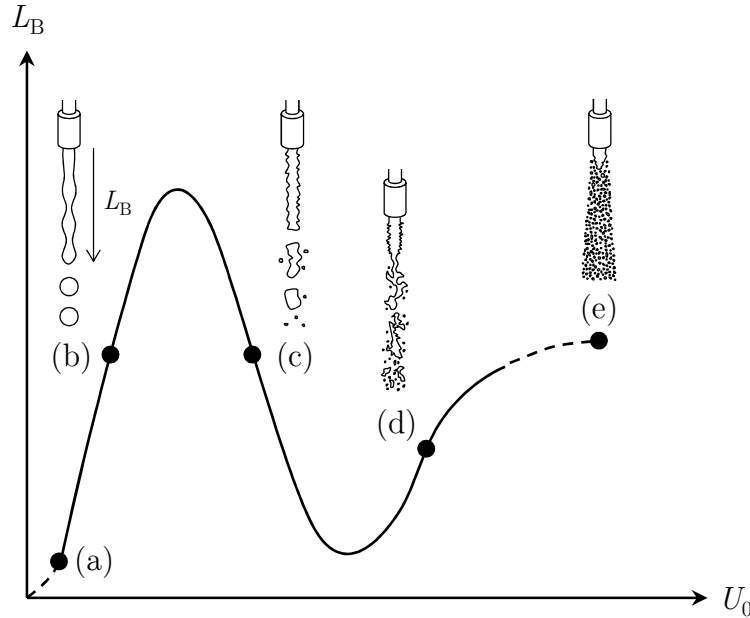


Figure 2.9: Schematic of the effect of the jet velocity on its breakup length in the different jet breakup regimes. Before point (a), the liquid has insufficient momentum to form a continuous jet and the liquid drips out of the nozzle. (b) Rayleigh breakup, (c) first wind-induced, (d) second wind-induced and (e) atomisation regimes. Adapted from Lin and Reitz (1998).

The shape of the breakup curve has been examined by many researchers including Grant and Middleman (1966), McCarthy and Malloy (1974), Leroux *et al.* (1996) and Lin and Reitz (1998). Due to the large number of parameters that influence jet breakup, variations are often reported in the shape of the breakup curve and quantitative predictions of L_B .

Grant and Middleman (1966) investigated the breakup of turbulent jets generated from long cylindrical nozzles and obtained a correlation for L_B :

$$L_B = 8.51d_N \left(\sqrt{We} \right)^{0.64} \quad (2.30)$$

Zhan *et al.* (2018) and Fuchs *et al.* (2019a; 2019b) obtained reasonable agreement of their measured values of L_B with Equation 2.30 in their investigations of jet breakup.

Fuchs *et al.* also found that jet breakup affected the impact force of the jet and the wetted area. Jet breakup decreased the impact force of the jet but increased the wetted area.

2.3.4 Splatter

Splatter occurs when a liquid jet impinges on a surface and liquid is lost from the main flow by rebound or shedding from the liquid film boundaries, reducing the volumetric flow rate in the falling film. A schematic is shown in Figure 2.10.

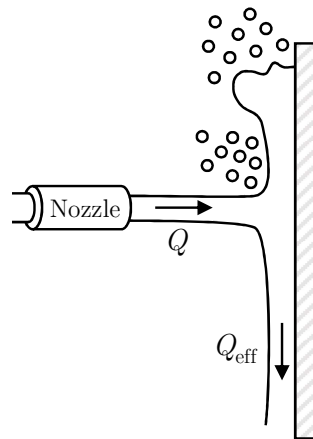


Figure 2.10: Schematic of the splatter that occurs when a horizontal jet impinges normally on a vertical wall, reducing the liquid flow rate in the falling film from Q to Q_{eff} .

Phenomena related to splatter caused by jets impinging on flat walls have been studied for well-defined coherent jets by Errico (1986), Lienhard *et al.* (1992) and Bhunia and Lienhard (1994). The review by Eggers and Villermaux (2008) highlighted the complexities of jet breakup and splatter, even for well-defined jets generated in carefully designed nozzles. Nozzles used in industrial practice are not usually designed to deliver coherent jets and an effective method of characterising these flows is therefore required.

The liquid lost to splatter can be quantified in terms of a splatter fraction, ξ , defined as

$$\xi = 1 - \frac{Q_{\text{eff}}}{Q} \quad (2.31)$$

where Q_{eff} is the volumetric flow rate of the liquid in the falling film.

Bhunja and Lienhard (1994) studied the splatter of jets generated from a long cylindrical nozzle striking a rigid flat surface and obtained the following correlation for predicting ξ :

$$\xi = -0.258 + 7.85 \times 10^{-5} \Omega - 2.51 \times 10^{-9} \Omega^2 \quad (2.32)$$

for $4400 < \Omega < 10000$, where Ω is a dimensionless parameter

$$\Omega = We \exp\left(\frac{0.971 L}{\sqrt{We} d_N}\right) \quad (2.33)$$

and L is the length of the jet.

They also proposed a correlation to predict the onset of splattering, defined as the point where $\xi \geq 0.05$:

$$\frac{L}{d_N} = \frac{130}{1 + 5 \times 10^{-7} We^2} \quad (2.34)$$

Wang *et al.* (2013b) studied the splatter from short coherent horizontal jets and found that Equation 2.32 did not provide a good description of their results. They attributed this to their use of convergent nozzles and a relatively short pipe entry length. They also found that the angle of inclination of the jet affected splatter. Upward-inclined jets showed the most splatter, followed by horizontal jets, then downward-inclined jets. Wassenburg *et al.* (2019) found splatter to be dependent on the nozzle design, with cylindrical pipe nozzles leading to more splatter than convergent nozzles, and the addition of two 90° deflections before the inlet of the convergent nozzles also increased the amount of splatter.

Zhan *et al.* (2020; 2021) studied jet breakup and splatter, and developed a correlation for ξ based on the impact frequency of droplets from a broken up jet and the size of the droplets. Feldung Damkjær *et al.* (2017) investigated the impingement of water jets from industrial scale nozzles. They found that the size of the RFZ decreased as the jet length increased and attributed this to a combined increase in jet breakup and splatter. Kim *et al.* (2020) also investigated the effect of jet length on splatter and found that splatter increased as jet length increased.

2.3.5 Wall curvature

Industrial process tanks and vessels are often cylindrical and the wall curvature could affect the liquid flow pattern upon jet impingement, but the effect of wall curvature has not been widely explored in studies of impinging liquid jets. Saberi *et al.* (2019; 2020) investigated the impingement of laminar vertical ethylene glycol jets onto flat and convex target plates. They found that under identical flow conditions, the hydraulic jumps formed on the convex target plates were larger than on a flat plate. Increasing the curvature of the convex target plate led to an increase in the radius of the hydraulic jump.

2.3.6 Jet angle

When a jet with a circular cross-section impinges obliquely on a surface, the intersection of the jet and the surface takes the form of an ellipse. Kate *et al.* (2007) studied liquid jets impinging obliquely on a horizontal surface, forming a non-circular hydraulic jump, and proposed a model for the liquid flow distribution based on the geometry of the system. Kate *et al.* assumed that the stagnation point, S, the source of the flow as the liquid flows radially away from the point of impingement, lies at the focus of the ellipse nearest the nozzle. A schematic is shown in Figure 2.11.

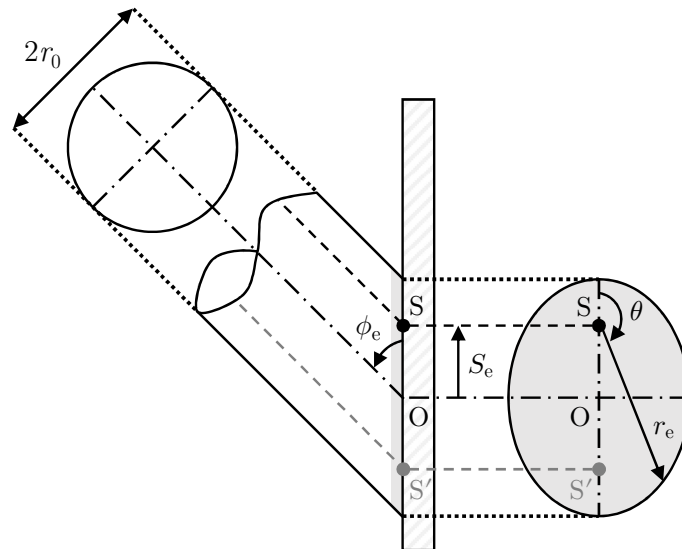


Figure 2.11: Schematic of the Kate *et al.* (2007) model for the flow distribution in an inclined jet. The surface is drawn vertical for convenience. O is the axis of the jet and S is the source. There are two foci, S and S': S is nearest to the nozzle. ϕ_e is the angle that the jet axis makes with the wall.

The radius of the source ellipse, r_e , is given by

$$r_e = r_0 \left(\frac{\sin \phi_e}{1 + \cos \phi_e \cos \theta} \right) \quad (2.35)$$

where ϕ_e is the angle that the jet axis makes with the wall (shown in Figure 2.11).

The distance of the source from the axis of the jet is

$$S_e = r_0 \cot \phi_e \quad (2.36)$$

Kate *et al.* (2007) also developed a scaling relation to predict the location of the hydraulic jump following an analysis similar to Bohr *et al.* (1993), giving

$$R_{\theta, \text{jump}} = 0.73 \left[\frac{r_0^2 \sin^3 \phi_e}{2 (1 + \cos \phi_e \cos \theta)^2} U_0 \right]^{5/8} \left(\frac{\mu}{\rho} \right)^{-3/8} g^{-1/8} \quad (2.37)$$

where $R_{\theta, \text{jump}}$ is the hydraulic jump radius in azimuthal direction θ . The coefficient of 0.73 is for a parabolic velocity profile; the value of the coefficient varies based on the velocity profile chosen.

Johnson and Gray (2011) followed a similar geometric argument to Kate *et al.* in their study of the flow of oblique jets of granular material. Beltaos (1976) investigated the oblique impingement of turbulent air jets.

Wang *et al.* (2013b) used the flow distribution proposed by Kate *et al.* to extend the Wilson *et al.* (2012) hydrodynamic model to liquid jets impinging obliquely on a vertical surface, using ϕ , the angle of the jet impingement in the vertical plane, in place of ϕ_e . Equation 2.8 becomes

$$\frac{dU}{dr} = -\frac{10\mu U^2 r^2}{\rho U_0^2 r_e^4 \sin^2 \phi} - \frac{5}{6} \frac{g \cos \theta}{U} \quad (2.38)$$

Ignoring the gravity term in Equation 2.38 and assuming the boundary condition $U = U_0$ at $r = r_e$, integrating Equation 2.38 yields the analytical result

$$\frac{1}{U} - \frac{1}{U_0} = \frac{10\mu}{3\rho U_0^2 r_e^4 \sin^2 \phi} (r^3 - r_e^3) \quad (2.39)$$

Following the analysis outlined in Section 2.2.2, the estimated location of the hydraulic jump is given by

$$R_{\theta, \text{jump}} = \left[\frac{9}{50} r_e^6 U_0^3 \sin^3 \phi \frac{\rho^2}{\mu \gamma (1 - \cos \beta)} \right]^{1/4} \quad (2.40)$$

where $r_e = f(\theta)$.

Bhagat and Wilson (2016) also combined the flow distribution proposed by Kate *et al.* with their hydrodynamic model to obtain predictions for jets impinging obliquely on a vertical surface. In the BLFZ, U is given by

$$U = \frac{\frac{1}{2} U_0 r_e^2 \sin \phi}{r \left(\frac{U_0 r_e^2 \sin \phi}{2r U_0} + (1 - C_3) \delta_b \right)} \quad (2.41)$$

where δ_b is given by

$$\frac{d(\delta_b^2)}{dr} = -\frac{2\delta_b^2}{r} - \frac{2\delta_b^2 g \cos \theta (1 - 2C_1 + C_3)}{U^2 (C_1 - C_3)} - \frac{2C_2 \mu}{\rho U (C_1 - C_3)} + \frac{\delta_b g r_e^2 \sin \phi \cos \theta}{(C_1 - C_3) U^2 r} \quad (2.42)$$

and C_1, C_2 and C_3 are constants ($C_1 = 0.3516, C_2 = 1, C_3 = 0.5$).

In the LZ,

$$\frac{dU}{dr} = -\frac{5.7\mu U^2 r^2}{\rho (U_0 r_e^2 \sin \phi)^2} - \frac{0.714g \cos \theta}{U} \quad (2.43)$$

and in the TZ

$$\frac{dU}{dr} = -\frac{0.04706 d_N^{1/4} r^{5/4} U^2}{\left(\frac{1}{2} U_0 r_e^2 \sin \phi\right) (4r_e^2 \sin \phi)^{1/4} Re^{1/4}} - \frac{63}{64} \frac{g \cos \theta}{U} \quad (2.44)$$

Numerical solutions are required to obtain values for U, h and M for the Bhagat and Wilson (2016) hydrodynamic model for inclined jets, following the procedure they outlined.

2.4 Cleaning by impinging liquid jets

2.4.1 Overview

The removal of a soil during cleaning is determined by its rheology, and its interaction with the surface and cleaning liquid. Bhagat *et al.* (2017) described four soil removal modes in cleaning by impinging liquid jets, shown in Figure 2.12.

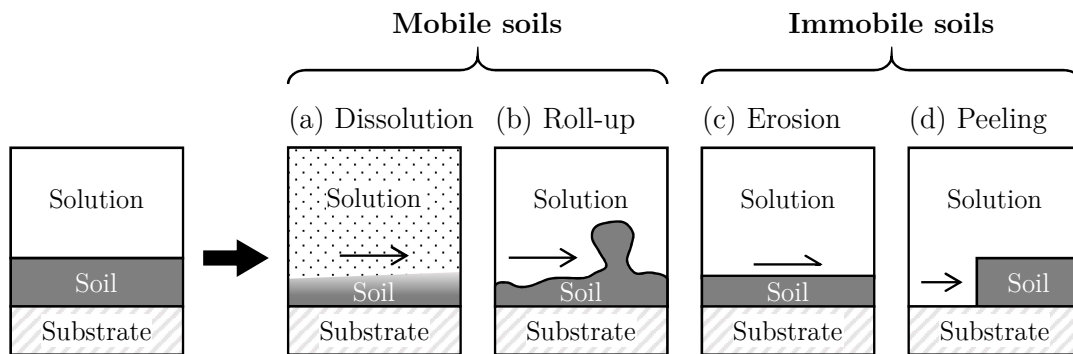


Figure 2.12: Soil removal modes in cleaning by impinging jets. Mobile soils are removed by (a) dissolution or (b) roll-up, while immobile soils are removed by (c) erosion or (d) peeling. The arrows indicate the action of the liquid from the jet on the soil. Adapted from Bhagat *et al.* (2017).

Mobile soils are readily displaced by the forces imposed by the cleaning liquid and are removed by dissolution or roll-up. Dissolution occurs if the soil is soluble in the cleaning liquid, where the cohesive interactions within the soil are less favourable than with the cleaning liquid, and if the timescale for diffusion is shorter than the timescale for cleaning. With roll-up, the soil is deformed and shifted by the fluid flow. Buoyancy forces may also play a role, and a residual layer may be left on the substrate, depending on the wetting behaviour and the dynamics of the three phase contact line.

Immobile soils do not deform considerably in response to the forces imposed by the cleaning liquid and are removed by erosion or peeling. Erosion occurs when the adhesion of the soil to the substrate is greater than the cohesive strength of the soil, so soil is removed by shear at the interface with the cleaning liquid. Peeling, also referred to as adhesive removal, occurs when the inverse is true: the adhesion of the soil to the substrate is weaker than the cohesive strength of the soil, so the soil detaches as a layer or as fragments.

The cleaning by an impinging liquid jet is also determined by location, shown in Figure 2.13. In the region beneath the impingement zone, sometimes referred to as the jet footprint, which is a circular region of radius $1-2 r_0$ for a circular jet of radius r_0 impinging normally on a flat substrate, removal is driven by dissipation of the jet's inertia, creating a crater in the soil layer by a combination of ballistic phenomena and flow displacement. This often occurs over short timescales in the range of microseconds to milliseconds (Kaye *et al.*, 1995). The penetration phenomenon is complex and is determined by the nature of the soil. Uth and Deshpande (2013) investigated the penetration of thick elastoplastic layers.

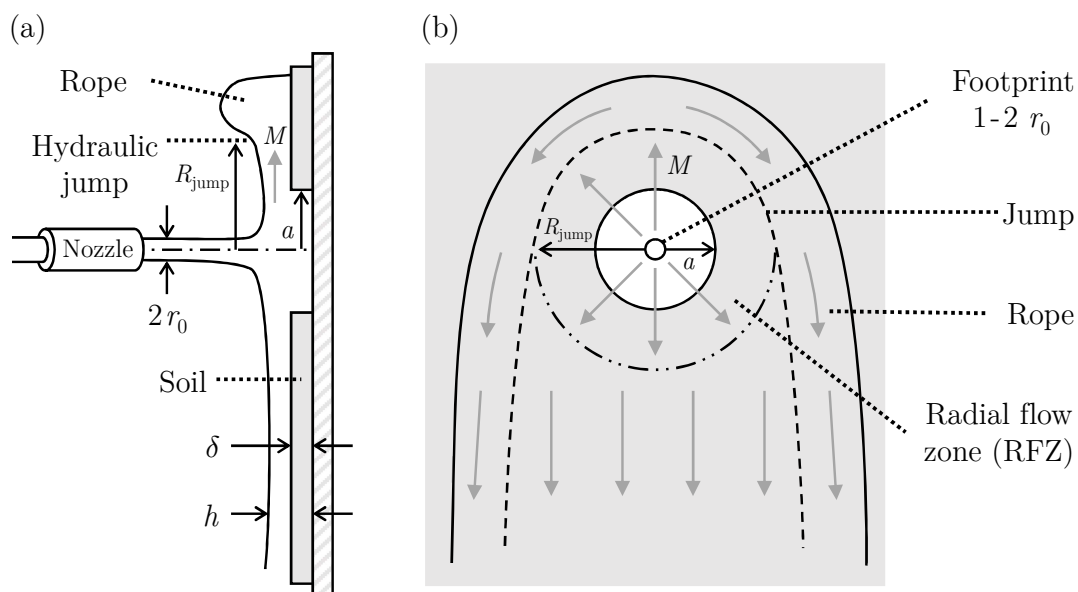


Figure 2.13: Schematics of the (a) side and (b) front views of cleaning by a coherent horizontal jet impinging normally on a vertical wall. In (b), the white circular region indicates the cleaned area. The grey arrows indicate the direction of the liquid flow. δ is the thickness of the soil layer.

Beyond the footprint and within the RFZ, the thin liquid film flow imposes relatively high shear stresses on the substrate and any soil layer on it. For a jet impinging normally, the cleaned area is usually circular with radius a as shown in Figure 2.13. The rate of cleaning then depends on the soil removal mode: removal of the layer by erosion is determined by the local shear stress while removal by peeling is determined by the momentum flow rate per unit width in the thin liquid film, M (*i.e.* the force imposed by the liquid in the radial direction).

Beyond the jump, the liquid film is thick and the average velocity is noticeably smaller than in the RFZ. Gravity promotes the formation of falling liquid films,

characterised by modest values of the shear stress and M . Studies such as those by Yang *et al.* (2019a; 2019b) have shown that removal of soils in these regions can be governed by soaking, where absorption of liquid from the falling film or reaction with the cleaning agent promotes softening of the soil until its strength (cohesive or adhesive) falls to a level where it can be eroded or peeled away from the substrate.

Yeckel and Middleman (1987) and Yeckel *et al.* (1990; 1994) investigated the removal of Newtonian oil layers, a mobile soil, from flat surfaces using impinging water jets. Recent studies (*e.g.* Wilson *et al.*, 2014) have focused on investigating the adhesive removal of soils by impinging liquid jets, developing models to describe the cleaning of soil layers after the point where the liquid jet had fully penetrated the soil layer and reached the substrate. These models are summarised in the next section.

Fernandes and Wilson (2020) discussed the effect of the thickness of the soil layer, δ , on the cleaning dynamics. They categorised soil layers as very thin ($\delta \ll h$), thin ($\delta \sim h$) and thick ($\delta \gg h$), and most studies have focused on the cleaning of thin soil layers. The cleaning of very thin and thick soil layers introduces additional complexities. Tuck *et al.* (2020) investigated the cleaning of a viscoplastic soil layer of varying thicknesses. With thick soil layers, upon penetration of the water jet into the soil layer, they observed the formation of a blister where the cleaning liquid was trapped within the soil layer.

2.4.2 Models

Basic form

Wilson *et al.* (2014) described the rate of growth of the area cleaned by an impinging liquid jet by a momentum-driven model

$$\frac{da}{dt} = k' M = k' \frac{3\dot{m} U}{5\pi a} \quad (2.45)$$

where a is the radius of the cleaned area, t is time, k' the cleaning rate constant, \dot{m} the mass flow rate of the jet ($\dot{m} = \rho Q$) and U the average velocity in the liquid film at radius a . M (and U) can be evaluated using the Wilson *et al.* (2012) hydrodynamic model (Equations 2.3, 2.7 and 2.8) or the Bhagat and Wilson (2016) hydrodynamic model (Table 2.1).

The value of k' is obtained by fitting to experimental data. Understanding how k' is affected by the properties of the soil such as its thickness and rheology, in order to be able to predict k' , is an active field of investigation (Fernandes, 2021). Values of k' that have been reported in the literature are given in Chapter 5 (Table 5.4).

Bhagat *et al.* (2017) employed the velocity profile of the Wilson *et al.* (2012) hydrodynamic model (Equation 2.10) and discussed three scenarios that can be expected to arise in cleaning.

(i) Strong soil (small a), where $U \approx U_0$:

$$\frac{da}{dt} = k' \frac{3\dot{m} U_0}{5\pi a} = \frac{\sigma}{a} \quad (2.46)$$

where σ is a lumped cleaning rate parameter ($\sigma = 3k'\dot{m}U_0/5\pi$). Integrating Equation 2.46 from the point where breakthrough of the jet through the soil occurs at time t_0 , giving a cleaned radius a_0 , gives

$$a^2 - a_0^2 = 2\sigma(t - t_0) \quad (2.47)$$

(ii) Weak soil (large a), where $1/U \gg 1/U_0$ so $1/U_0 \approx 0$ (validity discussed by Wang *et al.*, 2013b):

$$\frac{da}{dt} = k' \frac{3}{5\pi} \frac{\dot{m}^3}{c} \frac{1}{a(a^3 - r_0^3)} \quad (2.48)$$

where c is a lumped parameter dependent on the liquid properties ($c = 10\pi^2\rho\mu/3$). Integrating Equation 2.48 from the point where breakthrough of the jet occurs, at time t_0 and radius a_0 as above, gives

$$\left[\frac{a^5}{5} - \frac{a^2 r_0^3}{2} \right]_{a_0}^a = k' \frac{3}{5\pi} \frac{\dot{m}^3}{c} (t - t_0) \quad (2.49)$$

Assuming $a \gg a_0 > r_0$ such that $a^5 \gg a^2 r_0^3$,

$$a \approx \sqrt[5]{\frac{3k'}{\pi c} \dot{m}^3} \times (t - t_0)^{1/5} = K \Delta t^{0.2} \quad (2.50)$$

where K is a lumped cleaning rate constant dependent on the mass flow rate ($K = \sqrt[5]{3k'\dot{m}^3/\pi c}$) and $\Delta t = t - t_0$.

(iii) Intermediate strength soil, where the full form of Equation 2.10 is retained.

$$\frac{da}{dt} = k' \frac{3\dot{m}}{5\pi} \left[\frac{1}{U_0} + \frac{10\pi^2\mu}{3\rho Q^2} (a^3 - r_0^3) \right]^{-1} \frac{1}{a} \quad (2.51)$$

The weak soil case was considered by Wilson *et al.* (2014) and Wang *et al.* (2015). Glover *et al.* (2016) considered the weak soil case in a similar manner, assuming $a \gg r_0$, giving

$$\frac{da}{dt} = k' \frac{3}{5\pi} \frac{\dot{m}^3}{c} \frac{1}{a^4} = K^5 \frac{1}{5a^4} \quad (2.52)$$

$$a^5 - a_0^5 = K^5(t - t_0) \quad (2.53)$$

Feldung Damkjær *et al.* (2017) followed the approach of Glover *et al.* (2016) for the weak soil case and also assumed both a_0 and t_0 to be small, giving

$$a \approx \sqrt[5]{\frac{3k'}{\pi c} \dot{m}^3} \times t^{1/5} = Kt^{1/5} \quad (2.54)$$

In their study of cleaning by long jets, Feldung Damkjær *et al.* used a modified mass flow rate of the jet to account for jet breakup, *viz.*

$$a \approx \sqrt[5]{\frac{3k'}{\pi c} \dot{m}_{\text{eff}}^3} \times t^{1/5} \quad (2.55)$$

where \dot{m}_{eff} is the effective mass flow rate of the jet accounting for loss due to jet breakup ($\dot{m}_{\text{eff}} < \dot{m}$).

Moving jets

Wilson *et al.* (2015) extended the weak soil case given by Equation 2.52 to moving jets. A stationary point arises where the rate of cleaning is equal to the rate at which material is convected towards this point, at ν_{jet} . ν_{jet} is the nozzle traverse speed. They assumed $a \gg r_0$, giving

$$\frac{da_x}{dt} = \nu_{\text{jet}} = k' \frac{3}{5\pi} \frac{\dot{m}^3}{c} \frac{1}{a_x^4} \quad (2.56)$$

where a_x is the radial distance of the cleaning front directly ahead of the moving jet.

Integrating Equation 2.56 numerically gives

$$w_c = 2.94a_x = 2.94 \left(k' \frac{3}{5\pi} \frac{\dot{m}^3}{c} \frac{1}{\nu_{\text{jet}}} \right)^{0.25} = 2.94 \left(\frac{K^5}{5} \frac{1}{\nu_{\text{jet}}} \right)^{0.25} = 1.97 \frac{K^{1.25}}{\nu_{\text{jet}}^{0.25}} \quad (2.57)$$

where w_c is the width of the region cleared by the moving jet.

The mass flow rate through the nozzle is given by

$$\dot{m} = C_d \frac{\pi d_N^2}{4} \sqrt{2\rho\Delta P} \quad (2.58)$$

where C_d is the nozzle discharge coefficient and ΔP is the pressure drop across the nozzle.

Combining Equations 2.57 and 2.58 gives

$$w_c = k'^{0.25} \left(2.94 \left[\frac{9}{3200} \frac{d_N^6}{\rho\mu} C_d^3 (2\rho\Delta P)^{1.5} \frac{1}{\nu_{\text{jet}}} \right]^{0.25} \right) \quad (2.59)$$

Bhagat *et al.* (2017) presented an analytical solution to Equation 2.56, *viz.*

$$w_c = 3.04a_x = 3.04 \left(k' \frac{3}{5\pi} \frac{\dot{m}^3}{c} \frac{1}{\nu_{\text{jet}}} \right)^{0.25} \quad (2.60)$$

Fernandes *et al.* (2019) extended the strong soil case given by Equation 2.46 to moving jets and demonstrated its validity for the cleaning of a strong viscoplastic soil.

Inclined jets

Bhagat *et al.* (2017) extended the model proposed by Wilson *et al.* (2014) (Equation 2.45) to cleaning by inclined jets, yielding:

$$\frac{da}{dt} = k' M_\theta = \frac{3}{5} k' \rho U_0 r_e^2 \sin \phi \frac{U}{a} \quad (2.61)$$

where M_θ is the momentum flow per unit width in the liquid film in the θ direction.

Employing the velocity profile for inclined jets from the Wilson *et al.* (2012) hydrodynamic model (Equation 2.39), the three scenarios that can be expected to arise in cleaning become:

(i) Strong soil (small a), where $U \approx U_0$:

$$\frac{da}{dt} = \left[\frac{3}{5} k' \rho r_e^2 U_0^2 \sin \phi \right] \frac{1}{a} = \left[\sigma \frac{r_e^2}{r_0^2} \sin \phi \right] \frac{1}{a} \quad (2.62)$$

Integrating Equation 2.62 from the point where breakthrough of the jet into the soil occurs at time t_0 and a cleaned radius a_0 gives

$$a^2 - a_0^2 = 2 \left[\sigma \frac{r_e^2}{r_0^2} \sin \phi \right] (t - t_0) \quad (2.63)$$

which is of similar form to Equation 2.47.

(ii) Weak soil (large a), where $1/U \gg 1/U_0$ so $1/U_0 \approx 0$ and assuming $a^3 \gg r_e^3$:

$$\frac{da}{dt} = \left[\frac{9k' \rho^2}{50 \mu} r_e^6 U_0^3 \sin^3 \phi \right] \frac{1}{a^4} = \left[\frac{3\rho\sigma r_e^6}{10\mu r_0^2} U_0 \sin^3 \phi \right] \frac{1}{a^4} \quad (2.64)$$

(iii) Intermediate strength soil, where the full form of Equation 2.39 is retained.

$$\frac{da}{dt} = k' \frac{3}{5} \rho U_0 r_e^2 \sin \phi \left[\frac{1}{U_0} + \frac{10\mu}{3\rho U_0^2 r_e^4 \sin^2 \phi} (a^3 - r_e^3) \right]^{-1} \frac{1}{a} \quad (2.65)$$

Yield stress materials

Glover *et al.* (2016) proposed an alternative form of Equation 2.45 to describe the rate of cleaning of a yield stress material, *viz.*

$$\frac{da}{dt} = \begin{cases} k'(M - M_y) & M > M_y \\ 0 & M \leq M_y \end{cases} \quad (2.66a)$$

$$M \leq M_y \quad (2.66b)$$

where M_y is the momentum flow rate per unit width required to cause a viscoplastic fluid to yield.

They obtained an expression for M_y by assuming that at the cleaning front, the flow of liquid dislodging the material causes yield along a shear plane inclined at angle ϕ_{ramp} to the substrate surface, giving a wedge-shaped cleaning front:

$$M_y = \frac{\tau_y \delta}{(\tan \phi_{\text{ramp}} - \sin \phi_{\text{ramp}})} \quad (2.67)$$

Here τ_y is the yield stress of the soil and δ is the initial thickness of the soil layer.

Fernandes *et al.* (2019) extended the model proposed by Glover *et al.* (2016):

$$\frac{da}{dt} = \begin{cases} k' \left[M - M_y \underbrace{\left(\frac{M}{M + M_y/4} \right)^2}_{\text{creep}} \right] & M > \frac{M_y}{4} \\ 0 & M \leq \frac{M_y}{4} \end{cases} \quad (2.68a)$$

$$M \leq \frac{M_y}{4} \quad (2.68b)$$

They introduced the empirical factor labelled creep in Equation 2.68a to accommodate the behaviour observed as M approached M_y , reflecting the absence of a sharp transition between elastic and viscous behaviour in rheological testing.

Fernandes and Wilson (2020) derived expressions for the cleaning rate parameters in Equation 2.66a by assuming that the rate of cleaning is determined by the viscous dissipation occurring in the soil at the liquid-soil contact line. They obtained expressions for simple Newtonian, power law, Bingham and Herschel-Bulkley materials. For a Bingham material, the result is

$$\frac{da}{dt} = \frac{(\tan \phi_{\text{ramp}} - \sin \phi_{\text{ramp}})}{3\mu_B \ln \left(1 + \frac{h}{\delta_i} \right)} \left[M - \frac{3}{2} \frac{\tau_c h}{(\tan \phi_{\text{ramp}} - \sin \phi_{\text{ramp}})} \right] \quad (2.69)$$

where μ_B is the Bingham viscosity, δ_i is the thickness of the residual soil layer after cleaning and τ_c is the Bingham critical stress. The values of ϕ_{ramp} and δ_i were obtained by fitting to experimental data, and further fundamental work remains to be done in this area to predict these parameters *a priori*.

Equation 2.69 is of a similar form to Equation 2.66. This gives an expression for the cleaning rate constant

$$k'_B = \frac{(\tan \phi_{\text{ramp}} - \sin \phi_{\text{ramp}})}{3\mu_B \ln \left(1 + \frac{h}{\delta_i}\right)} \quad (2.70)$$

and the limiting momentum flow rate per unit width

$$M_{y,B} = \frac{3}{2} \frac{\tau_c h}{(\tan \phi_{\text{ramp}} - \sin \phi_{\text{ramp}})} \quad (2.71)$$

Since h varies with radial position (Equation 2.7) and thus changes over a cleaning test, Fernandes and Wilson defined space-averaged values of k'_B and $M_{y,B}$:

$$\overline{k'_B} = \frac{1}{a_{\text{max}} - a_0} \int_{a_0}^{a_{\text{max}}} k'_B(r) dr \quad (2.72)$$

$$\overline{M_{y,B}} = \frac{1}{a_{\text{max}} - a_0} \int_{a_0}^{a_{\text{max}}} M_{y,B}(r) dr \quad (2.73)$$

where a_{max} is the maximum cleaned radius observed.

2.4.3 Intermittent jets

Fuchs *et al.* (2017) reported that cleaning by impinging water jets could be enhanced while consuming less water by using intermittent jets, whereby the flow is repeatedly turned on and off, generating a series of regular accelerations. Cleaning by intermittent liquid flows through ducts, such as pipes and heat exchangers, has been studied in detail (*e.g.* Gillham *et al.*, 2000; Föste *et al.*, 2013), with significant enhancement observed under conditions where flow reversal occurs at the wall. Intermittent jetting has received less attention.

Fuchs *et al.* (2017) studied the use of intermittent and oscillating water jets to clean layers of dried xanthan gum and starch layers from vertical steel walls. Removal of the

soils extended beyond the RFZ and was quantified *in situ* by measuring fluorescence from ZnS crystals present in the soil layer. Intermittent jets were generated by successive opening and closing of a valve upstream of the nozzle to establish and then cut off the flow. Oscillating jets were produced by opening and closing a valve in a bypass stream back to the feed tank to vary the volumetric flow rate passing through the nozzle.

They varied the pulsation frequency of the intermittent and oscillating jets by varying the frequency at which the valves were opened and closed, and they conducted their tests at a fixed jet flow rate. They quantified cleaning in terms of the mass of soil removed per unit time and the mass of soil removed per unit volume of liquid. The performance of both intermittent and oscillating jets were found to be independent of the pulsation frequency. Oscillating jets gave similar performance to continuous ones, while intermittent jets gave better performance, with similar cleaning times for xanthan gum and longer cleaning times for starch, but consuming less liquid in both cases.

Werner *et al.* (2017) investigated the removal of dead yeast cells from woven filter cloths using pulsatile jet cleaning. The woven filter cloths were made of polyethylene terephthalate (PET) and the dead yeast cells were dyed with methylene blue. They quantified cleaning by measuring the contaminated area before and after cleaning. The pulsed jets were generated using a solenoid valve to reroute fluid flowing at a constant velocity in a bypass system to the cleaning nozzle periodically. They conducted tests at different jet velocities with a fixed pulsation frequency and found that cleaning improved as the jet velocity increased due to the increased kinetic energy of the jet. For a given amount of cleaning liquid, pulsatile cleaning gave better performance than continuous jet cleaning. This was attributed to the additional impulse delivered by the pulsed jets enabling yeast cells to be lifted from deeper regions in the filter.

Mitchell *et al.* (2018; 2019) compared the impulse force generated by a coherent water jet impinging normally on a flat plate for a continuous flow, and when the same flow was delivered as a series of droplets, achieved by imposing a disturbance at its Rayleigh frequency of 340 Hz. They found that delivering the flow as a series of droplets increased the initial impulse threefold and they suggested that this could enhance the rate of cleaning.

2.5 Summary

The location of the hydraulic jump formed by an impinging jet is a key parameter of interest for its application in cleaning. Hydrodynamic models that predict the location of the hydraulic jump have been developed by Wilson *et al.* (2012) and Bhagat and Wilson (2016). The Bhagat and Wilson model provides a more complete description of the flow in the liquid film over the Wilson *et al.* model, but is more complex and numerically involved so the Wilson *et al.* model is often used to obtain estimates.

Various aspects of cleaning by impinging jets have been investigated. The shape of the falling film and the flow in the rope determine the distribution of the liquid after the hydraulic jump is formed, and affect the total area that is wetted by a jet. Jet breakup and splatter are complex phenomena dependent on parameters such as nozzle design, and they affect the volume of liquid that is delivered by jet to the target. Wall curvature has not been widely explored in studies of impinging liquid jets and a gap in the literature has been identified to investigate the effect of concave walls on the location of the hydraulic jump.

To predict the location of the hydraulic jump when a jet is inclined, the Wilson *et al.* (2012) and Bhagat and Wilson hydrodynamic models employ the liquid flow distribution model proposed by Kate *et al.* (2007). The liquid flow distribution in an inclined jet is explored in depth in this work to assess the accuracy of the Kate *et al.* model.

Models to describe the cleaning of thin soil layers by impinging jets have been developed in recent studies. The models feature fitting parameters, and the prediction of these parameters based on the soil properties are a subject of ongoing work in the field.

The environmental sustainability of cleaning operations can be improved by reducing the resources required. At present, industrial CIP systems primarily employ continuous jets for cleaning, so the use of intermittent jets is investigated to assess their potential to reduce the consumption of liquid.

Chapter 3

Effect of jet length and wall curvature

3.1 Introduction

This chapter reports an experimental investigation of three different aspects that need to be considered for impinging jets used on industrial scales.

The effect of jet length and breakup on the shape of the radial flow zone (RFZ) and splatter is considered for long jets of lengths up to 1 m. The effect of jet length on cleaning is investigated briefly via testing on petroleum jelly, a hydrophobic soil.

A second aspect which has received little attention is the curvature of the wall. The effect of wall curvature on the shape of the RFZ and cleaning was investigated using vertical and horizontal cylinders. Whilst wall curvature is not expected to be large for many process tanks and vessels as curvature is related to radius⁻¹, its effect could be important for smaller items such as bottles or small fermenters.

The third aspect, which is considered briefly, is the effect of soil contact with the liquid before being exposed to the jet, *i.e.* soaking. This will occur in practice when a soil is contacted by liquid draining from above. Layers of ClearGlide™, a commercial wire pulling lubricant based on a polyacrylic acid gel (Carbopol®), were used for these tests.

Parts of this chapter have been published in the journal *Food and Bioproducts Processing* (Volume 113, pp. 142–153) in 2019 as ‘Impinging jet cleaning of tank walls: Effect of jet length, wall curvature and related phenomena’ with co-authors T. V. Ahuja, R. K. Bhagat, N. Taesopapong, S. A. Wan, R. L. Wigmore and D. I. Wilson. The experimental data in Section 3.4.2 were collected by MEng students T. V. Ahuja and R. L. Wigmore and the data for ClearGlide™ layers in Section 3.4.5 were collected by MEng students N. Taesopapong and S. A. Wan as part of their Chemical Engineering Tripos Part IIB research projects with the assistance of R. K. Bhagat.

3.2 Methods and materials

3.2.1 Impinging jet apparatus

The impinging jet apparatus used for the experimental work has previously been described by Wang *et al.* (2013b) and Glover *et al.* (2016). A schematic is shown in Figure 3.1.

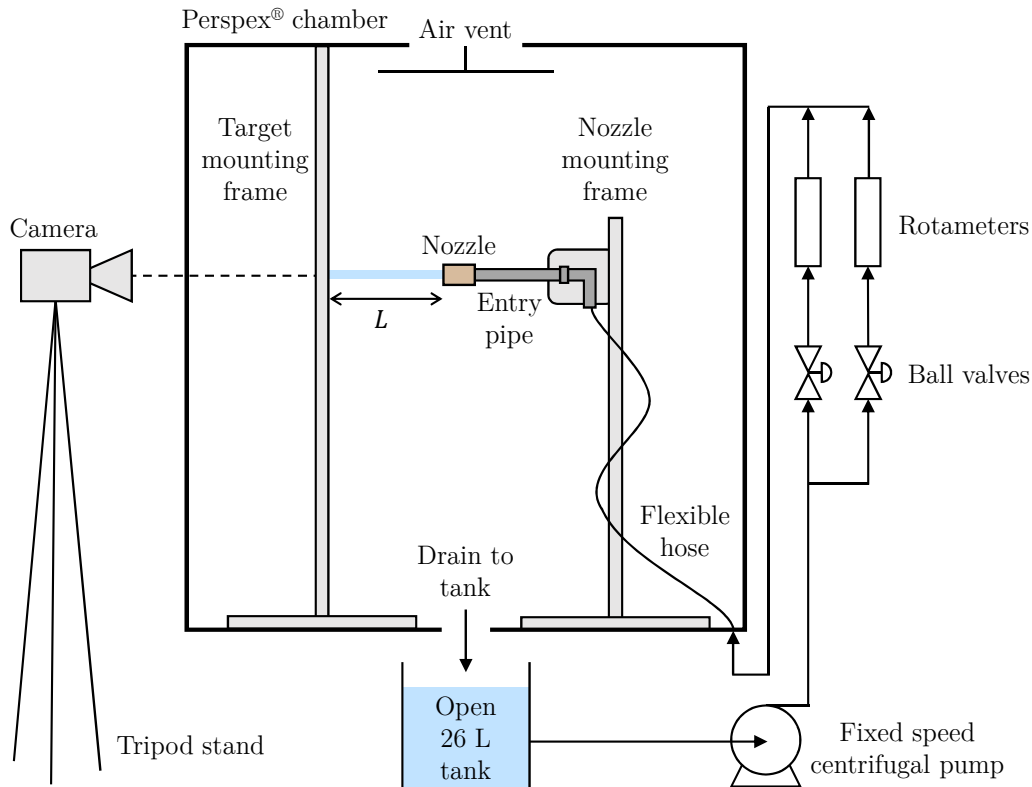
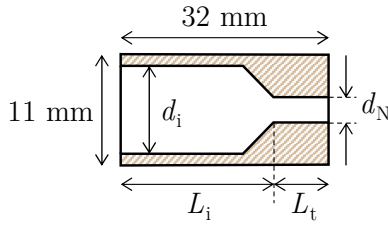


Figure 3.1: Schematic of the impinging jet apparatus used showing a horizontal jet impinging normally onto a flat vertical target.

The apparatus comprises of a $1.2 \times 1.2 \times 1.7$ m transparent Perspex® (polymethyl methacrylate, PMMA) walled chamber that the nozzle and target were mounted in. Tests were conducted with tap water at room temperature (20-22°C) for ease of operation and to avoid any temperature transients during cleaning tests. The water was pumped from an open 26 L tank by a fixed speed centrifugal pump (Clarke CEB103 230v 7230327, Clarke International, UK) through a rotameter and flow control valve before entering a 7.5 mm inner diameter steel pipe which served as a flow straightening section ahead of the nozzle. Pipes of lengths 150 mm and 350 mm were used. The nozzles used were the brass 55° convergent entry nozzles with bore

diameters, d_N , of 2, 3 and 4 mm employed by Wang *et al.* (2013b). The dimensions of the nozzles are summarised in Table 3.1.

Table 3.1: Dimensions of the nozzles (adapted from Wang *et al.*, 2013b).



Nozzle diameter, d_N / mm	Internal diameter, d_i / mm	Inlet length, L_i / mm	Throat length, L_t / mm
2	9	25	7
3	9	26	6
4	9	24	8

The volumetric flow rate through the nozzle, Q , was read from the rotameter which had been calibrated separately. In tests on flat targets, an interrupter plate was held between the nozzle and the target before the pump was turned on. Once the flow rate was set and the flow had stabilised, the interrupter plate was removed to allow the jet to impinge on the target.

Horizontal jets were used in the majority of tests. The nozzle was located at horizontal distance L from the target. At lower flow rates, jet droop could be significant and in some cases the jet did not reach the target: for others the inclination of the nozzle was adjusted to ensure that the jet impinged horizontally within $\pm 1^\circ$, verified against photographs of the jet taken from the side. Photographs of the jet from the side indicated that the midpoint of the jet followed the trajectory expected from gravity, namely $y_{\text{jet}} = -gx_{\text{jet}}^2/2U_0^2$, where y_{jet} is the vertical displacement, g the acceleration due to gravity, x_{jet} the horizontal distance travelled by the jet and U_0 the mean velocity of the jet ($U_0 = 4Q/\pi d_N^2$).

The targets used were transparent. Photographs and videos of the flow pattern at and near the point of impingement were taken from the dry side of the target with a Nikon D3300 or Sony Cyber-shot RX100V digital camera, aligned co-axially with the jet. A high speed camera (Photron FASTCAM SA3) was used to determine the time taken to for the hydraulic jump to be established, t_{jump} . Illumination was provided by an 800 W halogen lamp (Redhead PhotonBeam 800, Photon Beard, UK). Transparent graticule tape was placed on the dry side of the target to provide a length calibration for image processing.

3.2.2 Flow patterns and image analysis

Figure 3.2 shows the dimensions of the flow pattern extracted from photographs: the half-width of the RFZ at the level of the point of impingement, R , the half-width of the wetted region, R_c , the height of the hydraulic jump and the top of the rope, Z and Z_c , respectively, and the width of the rope B at azimuthal angle θ .

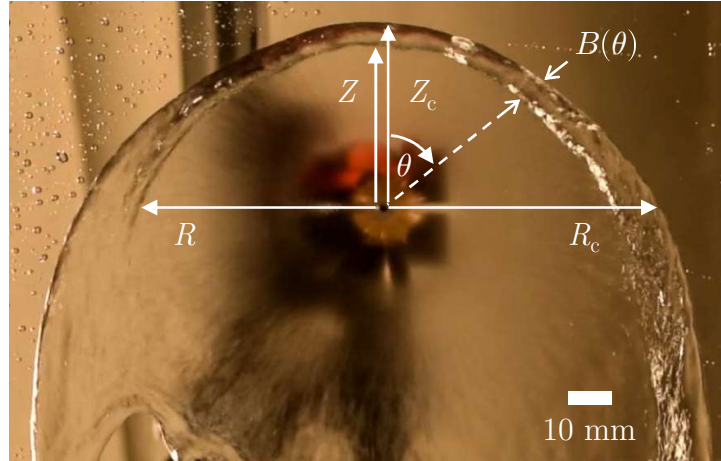


Figure 3.2: Photograph of the steady flow pattern created by a horizontal jet impinging normally on a flat vertical Perspex[®] plate, $d_N = 2$ mm, $Q = 2.0$ L min⁻¹, and $L = 70$ mm. The key dimensions are shown. The subscript c refers to the external edge of the rope.

The dimensions of interest were manually selected from the images using a script written in MATLAB[®] (MathWorks, USA). In tests to study the formation of steady flow patterns, an additional MATLAB[®] script was first used to split the videos into individual image frames. Multiple images were taken during steady state tests, and 10 image frames were analysed for each experimental condition. $B(\pi/2)$, R and R_c were measured on both sides of the point of impingement and the average value was used. The nature of the experimental setup meant that the alignment of the jet normal to the target had to be judged by eye, so the flow pattern was not always symmetrical about the vertical midplane.

All steady state tests were repeated twice, and the reported values of B , R , R_c , Z and Z_c are the average of 30 image frames. Many images were required in order to account for the dynamics of the rope. The rope was often unsteady and the target was subject to random wetting and de-wetting. At low flow rates, such as those studied by Wilson *et al.* (2012), these random fluctuations were not observed.

The main source of error lay in determining the locations of B , R , R_c , Z and Z_c by eye during image analysis, judged to give an error of ± 2 mm. The rotameters used to set the flow rate had been calibrated separately. The rotameter for lower flow rates (0.4 - 2.0 L min⁻¹) had divisions of 0.2 L min⁻¹, giving an error of ± 0.1 L min⁻¹, while the rotameter for higher flow rates (2.0 - 10.0 L min⁻¹) had divisions of 0.5 L min⁻¹, giving an error of ± 0.25 L min⁻¹.

3.2.3 Jet length and splatter

To investigate the effect of jet length, a $360 \times 600 \times 5$ mm (width \times height \times thickness) flat vertical Perspex[®] plate was used as the target. The jet lengths and flow rates tested for each nozzle, and the associated jet velocities, Reynolds, Weber and Ohnesorge numbers, expected breakup regimes and predicted breakup lengths are summarised in Table 3.2. All the jets studied were turbulent.

The jet breakup regime was determined using the correlations proposed by Lin and Reitz (1998) (Table 2.2) and the jets studied were expected to lie in the Rayleigh breakup and first wind-induced regimes. The predicted breakup lengths were determined using the correlation proposed by Grant and Middleman (1966) (Equation 2.30). The complete side profile of the jets could not be imaged with the experimental setup used so confirmation of the breakup regime and breakup length could not be obtained. In tests where the jets were longer than their predicted breakup length, jet breakup was not always observed. The correlations used were developed for well-defined jets from long cylindrical nozzles so their applicability to the short convergent entry nozzles employed here is expected to be limited.

The volumetric flow rate in the falling film, Q_{eff} , was determined by weighing the water collected in a wide reservoir located at the base of the target over a specified time. The reservoir was fitted with a slotted roof so that droplets originating from the jet due to breakup or droplets from rebound off the target were unlikely to be collected. The splatter fraction, ξ , was calculated using Equation 2.31.

Table 3.2: Summary of experimental conditions used to investigate the effect of jet length.

d_N / mm	L / mm	Q / L min ⁻¹	U_0 / m s ⁻¹	Re / -	W_e / -	We_g / -	Oh / -	Breakup regime (Table 2.2)	L_B (Equation 2.30) / mm
2	60	0.9 - 1.1	4.5 - 5.6	9 000 - 11 200	560 - 860	0.7 - 1.0	0.0026	Rayleigh breakup	130 - 150
		1.2 - 2.2	6.5 - 11.8	12 900 - 23 600	1 100 - 3 800	1.4 - 4.6		First wind-induced	160 - 240
	245	0.7 - 1.1	3.5 - 5.6	7 100 - 11 200	340 - 860	0.4 - 1.0		Rayleigh breakup	110 - 150
		1.2 - 2.2	6.5 - 11.8	12 900 - 23 600	1 100 - 3 800	1.4 - 4.6		First wind-induced	160 - 240
	350	0.9 - 1.1	4.5 - 5.6	9 000 - 11 200	560 - 860	0.7 - 1.0		Rayleigh breakup	130 - 150 ^a
		1.2 - 2.2	6.5 - 11.8	12 900 - 23 600	1 100 - 3 800	1.4 - 4.6		First wind-induced	160 - 240 ^b
	460	0.9 - 1.1	4.5 - 5.6	9 000 - 11 200	560 - 860	0.7 - 1.0		Rayleigh breakup	130 - 150 ^a
		1.2 - 2.2	6.5 - 11.8	12 900 - 23 600	1 100 - 3 800	1.4 - 4.6		First wind-induced	160 - 240 ^b
	1000	1.1	5.6	11 200	860	1.0		Rayleigh breakup	150 ^a
			6.5 - 11.8	12 900 - 23 600	1 100 - 3 800	1.4 - 4.6		First wind-induced	160 - 240 ^b
3	60	0.8 - 2.1	2.0 - 4.9	5 900 - 14 800	160 - 1 000	0.2 - 1.2	0.0021	Rayleigh breakup	130 - 230
		2.3 - 3.9	5.4 - 9.2	16 300 - 27 600	1 200 - 3 500	1.5 - 4.2		First wind-induced	250 - 350
	245	1.0 - 2.1	2.4 - 4.9	7 100 - 14 800	230 - 1 000	0.3 - 1.2		Rayleigh breakup	150 - 230
		2.3 - 3.9	5.4 - 9.2	16 300 - 27 600	1 200 - 3 500	1.5 - 4.2		First wind-induced	250 - 350
	350	1.2 - 2.1	2.9 - 4.9	8 600 - 14 800	340 - 1 000	0.4 - 1.2		Rayleigh breakup	160 - 230 ^b
		2.3 - 3.9	5.4 - 9.2	16 300 - 27 600	1 200 - 3 500	1.5 - 4.2		First wind-induced	250 - 350
	460	1.2 - 2.1	2.9 - 4.9	8 600 - 14 800	340 - 1 000	0.4 - 1.2		Rayleigh breakup	160 - 230 ^a
		2.3 - 3.9	5.4 - 9.2	16 300 - 27 600	1 200 - 3 500	1.5 - 4.2		First wind-induced	250 - 350
	1000	2.1	4.9	14 800	1 000	1.2		Rayleigh breakup	230 ^a
			5.4 - 9.2	16 300 - 27 600	1 200 - 3 500	1.5 - 4.2		First wind-induced	250 - 350 ^b
4	60	1.0 - 3.2	1.3 - 4.3	5 300 - 17 100	100 - 1 000	0.1 - 1.2	0.0019	Rayleigh breakup	150 - 310
		3.6 - 5.8	4.8 - 7.7	19 000 - 30 700	1 200 - 3 200	1.5 - 3.9		First wind-induced	330 - 450
	245	1.7 - 3.2	2.2 - 4.3	9 000 - 17 100	270 - 1 000	0.3 - 1.2		Rayleigh breakup	210 - 310
		3.6 - 5.8	4.8 - 7.7	19 000 - 30 700	1 200 - 3 200	1.5 - 3.9		First wind-induced	330 - 450
	350	4.1 - 5.8	5.5 - 7.7	21 900 - 30 700	1 600 - 3 200	2.0 - 3.9		First wind-induced	360 - 450
		2.4 - 3.2	3.2 - 4.3	12 600 - 17 100	550 - 1 000	0.7 - 1.2		Rayleigh breakup	260 - 310 ^b
	460	4.1 - 5.8	5.5 - 7.7	21 900 - 30 700	1 600 - 3 200	2.0 - 3.9		First wind-induced	360 - 450
		4.1 - 5.8	5.5 - 7.7	21 900 - 30 700	1 600 - 3 200	2.0 - 3.9		First wind-induced	360 - 450

^a Jet breakup observed in all tests^b Jet breakup observed in some tests

3.2.4 Wall curvature

The effect of wall curvature on the flow pattern was investigated using Perspex[®] cylinders. Four cylinders were tested with inner diameter, D_i , ranging from 100 to 290 mm and wall curvature, $\kappa = 2/D_i$, from 20 to 6.9 m^{-1} , summarised in Table 3.3. The flat plate served as a control with $\kappa = 0$.

Table 3.3: Dimensions of the Perspex[®] cylinders used.

Cylinder	Inner diameter, D_i / mm	Wall thickness, t_c / mm	Wall curvature, κ / m^{-1}
A	290	5	6.9
B	220	5	9.1
C	138	6	14
D	100	5	20

The feed pipe passed through a central 40×40 mm slot in the cylinder wall and the jets impinged normally on the inner wall. The target cylinder was mounted with its axis vertical or horizontal as shown in Figure 3.3.

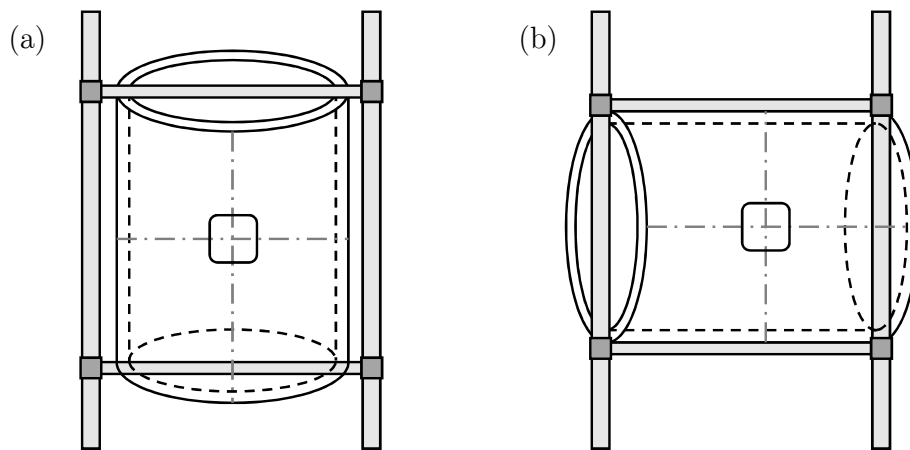


Figure 3.3: Schematic of the target cylinder mounted with its axis (a) vertical, and (b) horizontal.

The experimental conditions used are summarised in Table 3.4. Short jets were used to ensure that the jets were coherent.

Table 3.4: Summary of experimental conditions used to investigate the effect of wall curvature.

Target	d_N / mm	L / mm	Q / L min ⁻¹	U_0 / m s ⁻¹	Re / -	We / -	We_g / -	Oh / -	Breakup regime (Table 2.2)	L_B (Eq. 2.30) / mm
Flat plate	2	70	0.4 - 1.0	2.1 - 5.3	4 200 - 10 600	120 - 770	0.1 - 0.9	0.0026	Rayleigh breakup	80 - 140
			1.2 - 2.0	6.4 - 10.6	12 700 - 21 200	1 100 - 3 100	1.3 - 3.7			First wind-induced
Cylinders A - D	2	30	0.4 - 1.0	2.1 - 5.3	4 200 - 10 600	120 - 770	0.1 - 0.9	0.0026	Rayleigh breakup	80 - 140
			1.2 - 2.0	6.4 - 10.6	12 700 - 21 200	1 100 - 3 100	1.3 - 3.7			First wind-induced
Cylinder D	4	30	4.0 - 7.0	5.3 - 9.3	21 200 - 37 000	1 500 - 4 700	1.9 - 5.7	0.0019	First wind-induced	360 - 510

On a flat plate, the dimensions labelled in Figure 3.2, R , R_c , Z and Z_c , can easily be extracted from images. For the cylinders, the dimensions extracted from the images captured by the main camera, aligned co-axially with the jet, need to be corrected for refraction effects. The curvature of the cylinders affects measurement of dimensions R and R_c in vertical cylinders, and dimensions Z and Z_c in horizontal cylinders. Two models were tested; a thin lens model and a geometrical model. In the thin lens model, the wall of the cylinder was modelled as a combined concave-convex thin lens. The geometrical model was based on Snell's law of refraction. Detailed derivations of each model are provided in Section 3.3.1.

The model results were compared with measurements from a second camera which was moved around the apparatus to obtain refraction-free images so that the length of interest could be read directly from the graticule tape. To ensure that the camera was aligned normal to the surface of the cylinder, pairs of calibration lines showing the diameter of the cylinder were drawn at 10° intervals on the outer surface of the cylinder, shown in Figure 3.4.

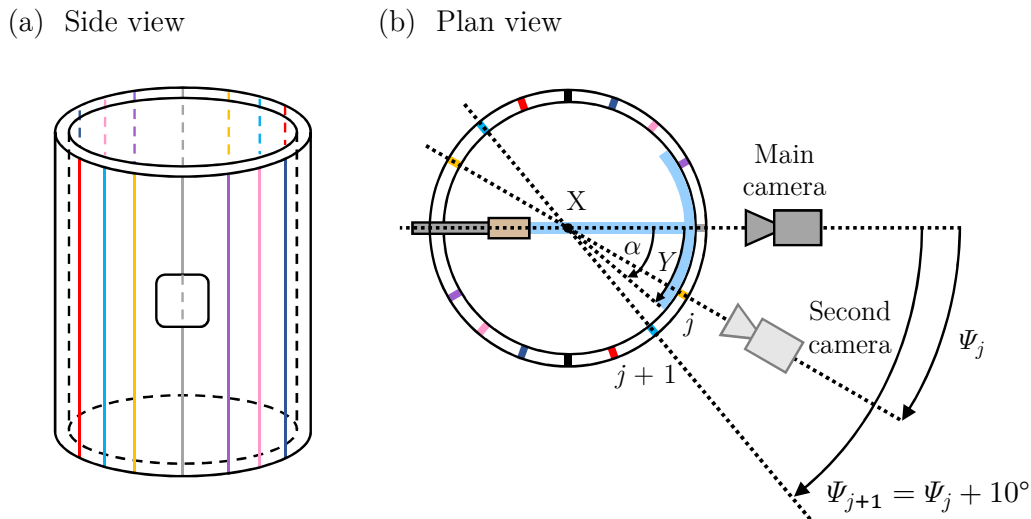


Figure 3.4: Schematic of a vertical cylinder showing calibration lines: (a) side view, and (b) plan view. α and Ψ are the angles of liquid film and second camera from the point of impingement, respectively. Y is the length of interest. X is the axis of the cylinder. Position of calibration lines not drawn to scale: in this case the second camera is positioned at j .

The experimental setup is limited in that the second camera can only be positioned accurately at 10° intervals, labelled Ψ , from the point of impingement. It does, however, remove the uncertainty in judging the exact position of the liquid film by

eye. To obtain an estimate of the measurement from the second camera, either a linear interpolation or harmonic weighting was used. The estimate of the length of interest, Y , and its angle α , are y'_j and α_j at position j , respectively; these are y'_{j+1} and α_{j+1} at the next position ($j + 1$).

The linear interpolation used is given by

$$Y = y'_j + \left[\frac{\left(\frac{\alpha_j + \alpha_{j+1}}{2} \right) - \Psi_j}{\Psi_{j+1} - \Psi_j} \times |y'_{j+1} - y'_j| \right] \quad (3.1)$$

while the harmonic weighting was

$$Y = \frac{\left[y'_j \times \frac{1}{|\alpha_j - \Psi_j|} \right] + \left[y'_{j+1} \times \frac{1}{|\alpha_{j+1} - \Psi_{j+1}|} \right]}{\left[\frac{1}{|\alpha_j - \Psi_j|} + \frac{1}{|\alpha_{j+1} - \Psi_{j+1}|} \right]} \quad (3.2)$$

3.2.5 Cleaning

Short sets of cleaning tests were performed on targets coated with thin layers of petroleum jelly (Atom Scientific GPS5220, provided by APC Pure, UK), a hydrophobic yield stress fluid, or ClearGlide™ (IDEAL Industries 31-388). ClearGlide™ is a commercial wire pulling lubricant based on an aqueous solution of Carbopol®. Carbopol® gels are suspensions of crosslinked polyacrylic acid polymer in water and are often used as model viscoplastic fluids (Dinkgreve *et al.*, 2018). Its yield stress depends on the volume fraction of polymer and pH, so extended contact with water is expected to reduce the yield stress and promote liquid-like behaviour.

Fernandes *et al.* (2019) studied the rheological properties of the petroleum jelly using a Kinexus Lab+ controlled-stress rheometer (Malvern Instruments, UK) and reported a critical stress, often taken to be the yield stress, of approximately 220 Pa. The yield stress of the ClearGlide™, measured using a vane tool, decreased from approximately 20 Pa to 5 Pa when diluted 1:1 with water (Douglas Gibson, internal communication). The cleaning behaviour of a viscoplastic soil is determined by its yield stress. If the stress imposed by the liquid film on the soil layer does not result in the yield stress being reached, the soil will not deform or move. In such cases, cleaning will not be observed until the yield stress changes, *e.g.* due to soaking or other processes reducing the cohesion in the soil layer.

Layers of the required thickness were prepared on an initially dry target using the spreading tool described by Glover *et al.* (2016). Petroleum jelly layers were rested for 30 minutes before cleaning to allow any residual stress from coating to dissipate (Fernandes *et al.*, 2019) while ClearGlide™ layers were cleaned immediately after preparation to avoid drying artefacts. A dark food grade dye was added to the ClearGlide™ to make it easier to determine when material had been removed from the target. With both materials the cleaned area took the form of a circle centred on the point of impingement which grew over time. The radius of the circle, a , was extracted from images using a script written in MATLAB® (MathWorks, USA). Edge detection was used to identify the visibly cleaned region in each image based on the difference in pixel intensity between the cleaned and uncleaned regions, enabling the cleaned area to be determined. a was then calculated as the radius of a circle with equal area to the cleaned region.

The experimental conditions used are summarised in Table 3.5.

Table 3.5: Summary of experimental conditions used in the cleaning tests.

Soil material	Soil layer thickness, δ / mm	Target	d_N / mm	L / mm	Q / L min ⁻¹	U_0 / m s ⁻¹	Re / -	We / -	We_g / -	Oh / -	Breakup regime (Table 2.2)	L_B (Eq. 2.30) / mm
Petroleum jelly	0.2	Flat plate (vertical)	2	60	1.6	8.5	17 000	2 000	2.4	0.0026	First wind-induced	190
				245	1.7	9.0	18 000	2 200	2.7	0.0026	First wind-induced	200
				350	2.0	10.6	21 200	3 100	3.7	0.0026	First wind-induced	220
ClearGlide™	1.3	Flat plate (vertical), Cylinders B - D (vertical)	2	60	1.0	5.3	10 600	770	0.9	0.0026	Rayleigh breakup	140
ClearGlide™	0.2	Flat plate (horizontal) ^a	2	245	2.0	10.6	21 200	3 100	3.7	0.0026	First wind-induced	220

^a Tests were conducted with a vertical jet

3.3 Models

3.3.1 Correction for refraction

The curvature of the cylinders affects the extraction of dimensions from photographs: R and R_c for vertical cylinders, and Z and Z_c with horizontal cylinders.

In the image analysis, C is the chord length of the liquid film on the outer surface of the cylinder with arc length A_o , shown in Figure 3.5. The parameter of interest is the true arc length of the liquid film on the inner surface of the cylinder, A_i .

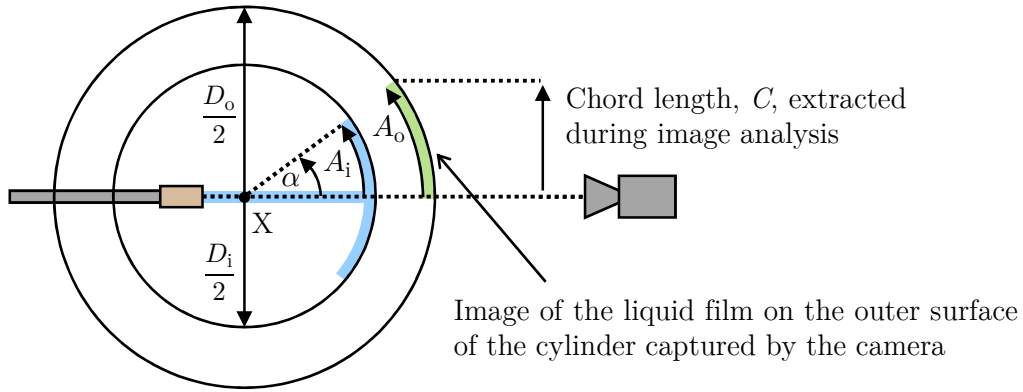


Figure 3.5: Schematic of a cross-section through a cylinder with outer diameter, D_o , and inner diameter, D_i , at the plane of impingement. X is the axis of the cylinder.

Uncorrected for refraction

Assuming no refraction occurs, the arc length of both the liquid film and its image on the outer surface of the cylinder are subtended by angle α from the axis of the cylinder. Angle α can be calculated from

$$C = \left(\frac{D_o}{2}\right) \sin \alpha \quad \Rightarrow \quad \alpha = \sin^{-1} \left(\frac{2C}{D_o}\right) \quad (3.3)$$

A_i can be calculated from

$$A_i = \alpha \left(\frac{D_i}{2}\right) = \frac{D_i}{2} \sin^{-1} \left(\frac{2C}{D_o}\right) \quad (3.4)$$

where α is in radians.

Refraction: thin lens model

The wall of the cylinder is modelled as a combined concave-convex thin lens, shown in Figure 3.6.

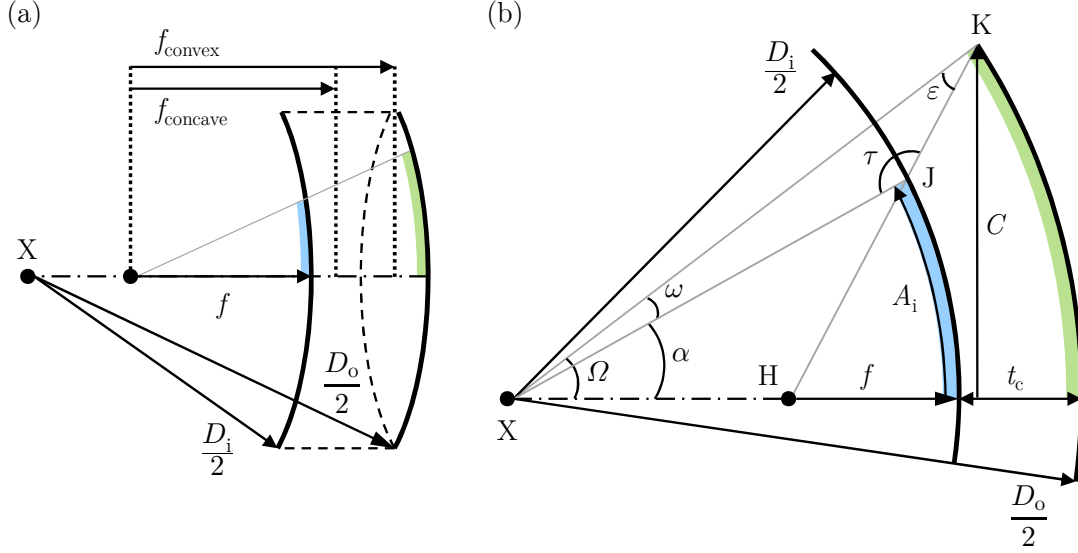


Figure 3.6: (a) Schematic of the cylinder wall modelled as a combined concave-convex thin lens where the focal lengths of the lenses are shown, and (b) schematic of the geometry and other parameters required to calculate the true arc length of the liquid film, A_i . X is the axis of the cylinder.

The focal length of the concave lens, f_{concave} , is related to the refractive index of Perspex[®], η_{Perspex} , and the diameters by

$$\frac{1}{f_{\text{concave}}} = (\eta_{\text{Perspex}} - 1) \left(-\frac{2}{D_i} - \frac{2}{D_i} \right) \quad (3.5)$$

The equivalent expression for the focal length of convex lens, f_{convex} , gives

$$\frac{1}{f_{\text{convex}}} = (\eta_{\text{Perspex}} - 1) \left(\frac{2}{D_i} - \frac{2}{D_o} \right) \quad (3.6)$$

The combined focal length of the cylinder wall, f , is

$$\frac{1}{f} = \frac{1}{f_{\text{concave}}} + \frac{1}{f_{\text{convex}}} \quad (3.7)$$

The arc length of the image of the liquid film is subtended by angle Ω from the axis of the cylinder. Angle Ω can be calculated from

$$\Omega = \sin^{-1} \left(\frac{2C}{D_o} \right) \quad (3.8)$$

Length XH is given by

$$\text{XH} = \frac{D_o}{2} - f - t_c \quad (3.9)$$

where t_c is the thickness of the cylinder wall

$$t_c = \frac{D_o}{2} - \frac{D_i}{2} \quad (3.10)$$

Applying the cosine rule to triangle XHK gives length HK:

$$\text{HK} = \sqrt{\left(\frac{D_o}{2}\right)^2 + (\text{XH})^2 - 2\left(\frac{D_o}{2}\right)(\text{XH})\cos\Omega} \quad (3.11)$$

Applying the sine rule to triangle XHK gives

$$\varepsilon = \sin^{-1} \left[\frac{\sin\Omega}{\text{HK}} \times \text{XH} \right] \quad (3.12)$$

Applying the sine rule to triangle XJK gives

$$\tau = \pi - \sin^{-1} \left[\left(\frac{\sin\varepsilon}{\left(\frac{D_i}{2}\right)} \right) \times \left(\frac{D_o}{2}\right) \right] \quad (3.13)$$

In triangle XJK

$$\omega = \pi - \varepsilon - \tau \quad (3.14)$$

and in triangle XHK

$$\alpha = \Omega - \omega \quad (3.15)$$

A_i can then be calculated from

$$A_i = \alpha \left(\frac{D_i}{2} \right) \quad (3.16)$$

Refraction: geometrical model

The geometrical model used to correct for refraction is based on Snell's law of refraction, shown in Figure 3.7.

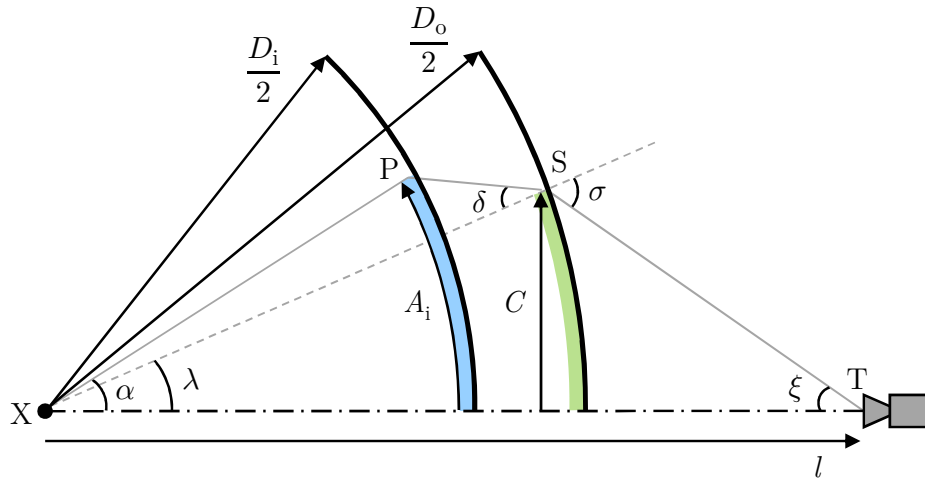


Figure 3.7: Schematic of the geometry and other parameters required to calculate A_i by Snell's law. X is the axis of the cylinder and the camera is located at T, a distance l away from X.

The arc length of the image of the liquid film is subtended by angle λ from the axis of the cylinder. Angle λ can be calculated from

$$\lambda = \sin^{-1} \left(\frac{2C}{D_o} \right) \quad (3.17)$$

Applying the sine rule to triangle XST gives

$$l \sin \xi = \left(\frac{D_o}{2} \right) \sin (\pi - \sigma) = \left(\frac{D_o}{2} \right) \sin \sigma \quad (3.18)$$

In triangle XST

$$\lambda + (\pi - \sigma) + \xi = \pi \quad \Rightarrow \quad \xi = \sigma - \lambda \quad (3.19)$$

Hence

$$l \sin (\sigma - \lambda) = \left(\frac{D_o}{2}\right) \sin \sigma \quad \Rightarrow \quad \sigma = \tan^{-1} \left(\frac{\sin \lambda}{\cos \lambda - \left(\frac{D_o}{2l}\right)} \right) \quad (3.20)$$

Applying Snell's law at S gives

$$\eta_{\text{Perspex}} \sin \delta = \eta_{\text{air}} \sin \sigma \quad \Rightarrow \quad \delta = \sin^{-1} \left(\frac{\eta_{\text{air}}}{\eta_{\text{Perspex}}} \times \sin \sigma \right) \quad (3.21)$$

where η_{air} is the refractive index of air.

Applying the sine rule to triangle XPS,

$$\begin{aligned} \left(\frac{D_o}{2}\right) \sin \delta &= \left(\frac{D_i}{2}\right) \sin [\pi - \delta - (\alpha - \lambda)] = \left(\frac{D_i}{2}\right) \sin (\delta + \alpha - \lambda) \\ \Rightarrow \alpha &= \lambda - \delta + \sin^{-1} \left[\left(\frac{D_o}{D_i}\right) \sin \delta \right] \end{aligned} \quad (3.22)$$

A_i can then be calculated from

$$A_i = \alpha \left(\frac{D_i}{2}\right) \quad (3.23)$$

A limiting case occurs when $\sigma \rightarrow \pi/2$, *i.e.* when $\tan \sigma \rightarrow \infty$:

$$\sigma = \tan^{-1} \left(\frac{\sin \lambda}{\cos \lambda - \left(\frac{D_o}{2l}\right)} \right) \quad \Rightarrow \quad \tan \sigma = \frac{\sin \lambda}{\cos \lambda - \left(\frac{D_o}{2l}\right)} \quad (3.24)$$

Therefore, at the limit,

$$\cos \lambda = \left(\frac{D_o}{2l}\right) \quad (3.25)$$

For a given value of l , the limiting value of λ is

$$\lambda = \cos^{-1} \left(\frac{D_o}{2l}\right) \quad (3.26)$$

At this value of λ , the light ray ST is tangential to the wall of the cylinder. Above this value, refraction of light into the cylinder will not occur. Hence, the geometrical model is only valid if

$$\lambda \leq \cos^{-1} \left(\frac{D_o}{2l} \right) \quad (3.27)$$

For a given value of λ , the limiting value of l is

$$l = \frac{D_o}{2 \cos \lambda} \quad (3.28)$$

At this value of l , the light ray ST is tangential to the wall of the cylinder. Below this value, refraction of light into the cylinder will not occur. Hence, the geometrical model is only valid if

$$l \geq \frac{D_o}{2 \cos \lambda} \quad (3.29)$$

3.3.2 Estimate of time taken to establish the hydraulic jump

Wilson *et al.* (2012) presented an approximate model for the liquid flow in the RFZ at steady state. The mean velocity in the film, U , at radial position r was given by Equation 2.10. Using this result to describe the mean velocity in the growing film and setting $U = dr/dt$ allows the time for the liquid to reach the location of the jump, t_{jump} , to be estimated from

$$\int_0^{t_{\text{jump}}} dt = \int_{r_0}^{R_{\text{jump}}} \frac{1}{U} dr \quad (3.30)$$

Substituting Equation 2.10 into Equation 3.30, assuming $1/U_0 \approx 0$ and $r^3 \gg r_0^3$, integrating, setting $R_{\text{jump}}^4 \gg r_0^4$ and using the expression for R_{jump} from Equation 2.14 gives

$$t_{\text{jump}} = \frac{0.276^4}{4} \frac{10\pi^2}{3} \frac{\rho Q}{\gamma(1 - \cos \beta)} \quad (3.31)$$

For high flow rate jets, the target surface has a weak influence on R_{jump} ($\cos \beta \approx 0$; Bhagat and Wilson, 2016), yielding

$$t_{\text{jump}} = 0.0477 \frac{\rho Q}{\gamma} \quad (3.32)$$

Bhagat and Wilson (2016) presented a more detailed model for the velocity in the thin film. Their model yields the following result

$$t_{\text{jump}} = \frac{8}{U_0} \left[0.125r + \frac{2.12r^{5/2}}{5d_N^{3/2}\sqrt{Re}} \right]_{r_0}^{r_b} + \frac{8}{U_0} \left[0.1975r + \frac{3.792r^4}{4d_N^3 Re} \right]_{r_b}^{r_t} + \frac{1}{U_0} \left[(2.37 - 0.0108\sqrt{Re})r + \frac{0.668r^{13/4}}{13d_N^{9/4} Re^{1/4}} \right]_{r_t}^{R_{\text{jump}}} \quad (3.33)$$

where r_b , r_t and R_{jump} are given by Equations 2.15, 2.16 and 2.17, respectively.

3.4 Results and discussion

3.4.1 Jet hydrodynamics

Flow pattern formation

The parameters of interest are the half-width of the RFZ at the plane of impingement, R , the half-width of the wetted region at the plane of impingement, R_c , the height of the hydraulic jump, Z , and the height of the top of the rope, Z_c . An example of the evolution of these parameters over time, t , for a jet impinging on an initially dry target is shown in Figure 3.8.

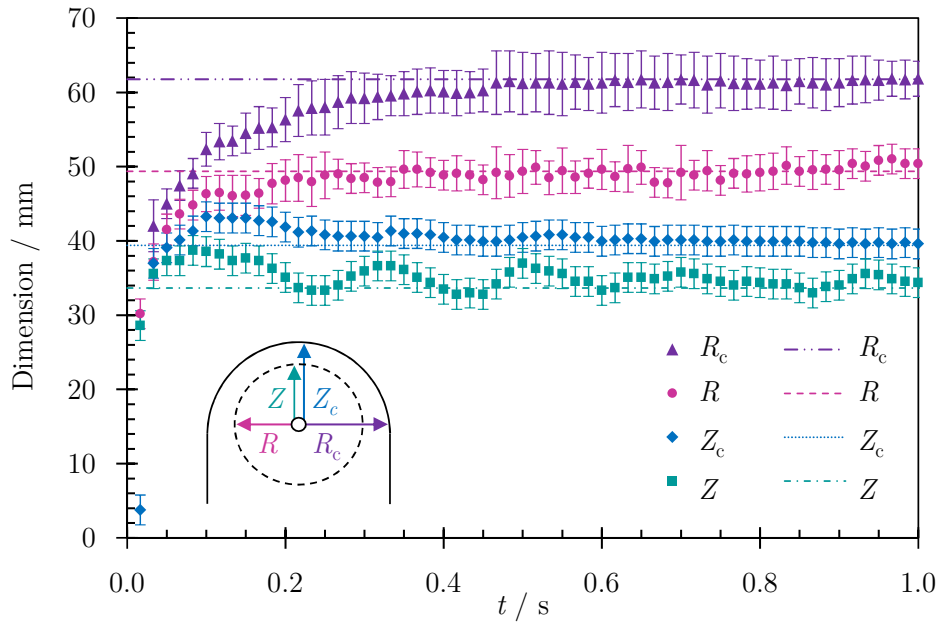


Figure 3.8: Flow pattern evolution following the normal impingement of a horizontal jet on an initially dry flat vertical Perspex[®] plate, $d_N = 2$ mm, $Q = 2.0$ L min⁻¹, and $L = 70$ mm. Horizontal loci indicate steady state values.

R and Z were initially almost equal, with Z slightly smaller due to gravity. After 0.1 s, the rapid growth stops and R increases while Z decreases as the rope is established over the next 0.2 s. R_c stabilised after a further 0.2 s, 0.5 s after the initial impact. A detailed account of the formation of the initial hydraulic jump is given in Bhagat *et al.* (2018): the changes in R and Z in the period 0.1 s $< t < 0.3$ s are associated with establishment of the boundary conditions downstream, *i.e.* as the rope develops, illustrated in Figure 3.9. At the top of the RFZ, the rope flows over the top of the thin film and is dragged downwards by gravity, giving $Z < R$.

Instabilities such as capillary waves in the jet also affect the flow in the rope and cause it to be unstable, giving rise to fluctuations in Z and R . The fluctuations are not seen in Z_c and R_c as the outer edge of the rope is pinned at the three-phase contact line.

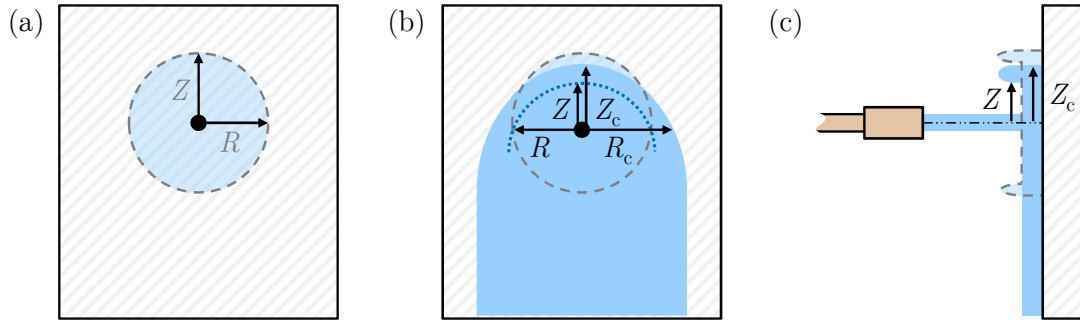


Figure 3.9: Schematic of the flow pattern formation. (a) Initial formation of the hydraulic jump where $Z \approx R$, (b) steady state flow pattern where the rope at the top of the RFZ has been dragged downwards by gravity, giving $Z < R$, and (c) side view of the jet impingement showing both the initial hydraulic jump formed (dashed line) and the steady state flow pattern.

Time taken to establish the hydraulic jump

The tests in this chapter are focused on continuous steady flows, which are directly related to continuous jets generated by static and moving nozzles in cleaning applications. Other workers such as Fuchs *et al.* (2017) have investigated the use of intermittent jets as a means of increasing cleaning efficiencies based on total water consumption. In these, a steady flow is applied for a period t_{on} , followed by a period where no jet impacts the target, and the cycle is repeated. The time taken to establish the hydraulic jump, t_{jump} (between 0.1 and 0.2 s in Figure 3.8), is a key timescale in the flow behaviour and is an important parameter in such applications as it constitutes a characteristic timescale for the periodicity of bursts: t_{on} shorter than t_{jump} would result in the liquid wetting a region smaller than the predicted hydraulic jump radius, while longer periods would mainly influence the cleaning of the wetted region below the point of impingement through effects such as soaking.

The use of intermittent jets for cleaning are investigated in Chapter 5. Here, a short series of tests was conducted to determine t_{jump} . The measured values of t_{jump} are compared with estimates based on the Wilson *et al.* (2012) and Bhagat and Wilson (2016) hydrodynamic models, given by Equations 3.32 and 3.33, respectively, in Figure 3.10.

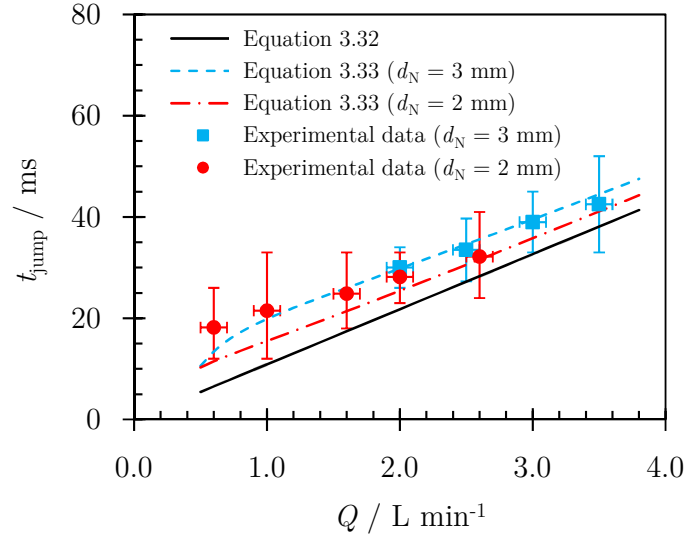


Figure 3.10: Comparison of predictions of the time taken to establish the hydraulic jump, t_{jump} , with experimental data obtained for a coherent horizontal water jet impinging normally on a flat vertical Perspex[®] plate.

Figure 3.10 shows that t_{jump} for these jets lay in the range 20–40 ms, so processes which might affect the formation of the jump such as diffusion are unlikely to be significant. Equation 3.32 gives a reasonable estimate of the magnitude of t_{jump} but does not capture the dependency on jet diameter (and thus jet velocity) for a given flow rate. Equation 3.33, from the more detailed model for the flow in the thin film by Bhagat and Wilson (2016), gives a more accurate description of the limited number of tests conducted. The experimental uncertainty is too large to confirm any effect of jet diameter.

Steady state flow patterns

The steady state flow patterns formed by horizontal jets of $d_N = 2 \text{ mm}$ impinging normally on a flat vertical Perspex[®] plate were investigated with a focus on the parameters Z , Z_c , R and R_c . The dynamics of the wetted region below the point of jet impingement were not explored in this work but would be important for applications where wetting by the draining liquid film is sufficient to achieve cleaning or promote cleaning via soaking.

Figure 3.11 shows the measured values of R for flow rates, Q , between 0.4 and 2.0 L min^{-1} compared with the predictions from the Wilson *et al.* (2012) and Bhagat and Wilson (2016) models, Equations 2.14 and 2.17, respectively. The Wilson *et al.* model underpredicts R while the Bhagat and Wilson model gives better agreement.

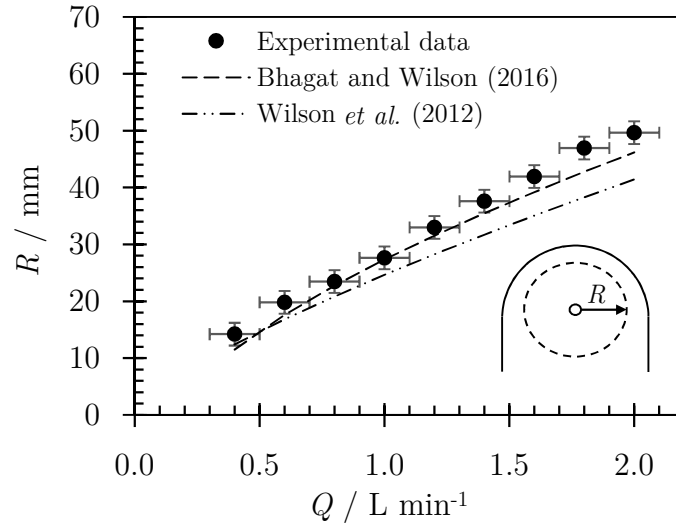


Figure 3.11: Effect of flow rate on the size of the radial flow zone. The predictions from the Wilson *et al.* (2012) and Bhagat and Wilson (2016) models, Equations 2.14 and 2.17, respectively, are shown.

Figure 3.12(a) shows that the half-width of the wetted area straddles the region between $R_c = 2R$ and $R_c = 4R/3$ at lower flow rates and moves towards the $R_c = 4R/3$ locus as the flow rate increases. Wilson *et al.* (2012) and Wang *et al.* (2013a; 2013b) reported similar trends. Figure 3.12(b) shows that the measured height of the RFZ lies close to the $Z = 3R/4$ locus. It should be noted that radial flow is expected to extend beyond Z : the measurement of Z is affected by the rope falling downwards to some degree.

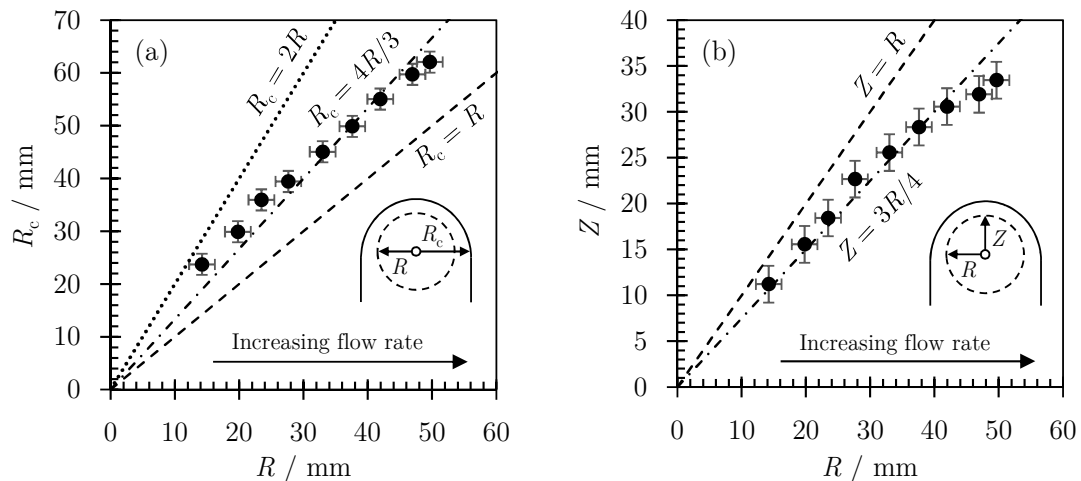


Figure 3.12: Effect of flow rate on the shape of the flow pattern: relationship between (a) R_c and R , and (b) Z and R .

The relationship between Z_c and Z was not reported in previous studies. The experimental data are shown in Figure 3.13(a). A linear trendline passing through the origin was fitted to the data, giving a relationship of $Z_c = 6Z/5$ (regression coefficient = 0.9778). Combining the relationships $Z_c = 6Z/5$ and $Z = 3R/4$ gives $Z_c = 9R/10$. Figure 3.13(b) shows that the experimental data lie close to the $Z_c = 9R/10$ locus. At lower flow rates, $Z_c \approx R$, and at higher flow rates, $Z_c < 9R/10$.

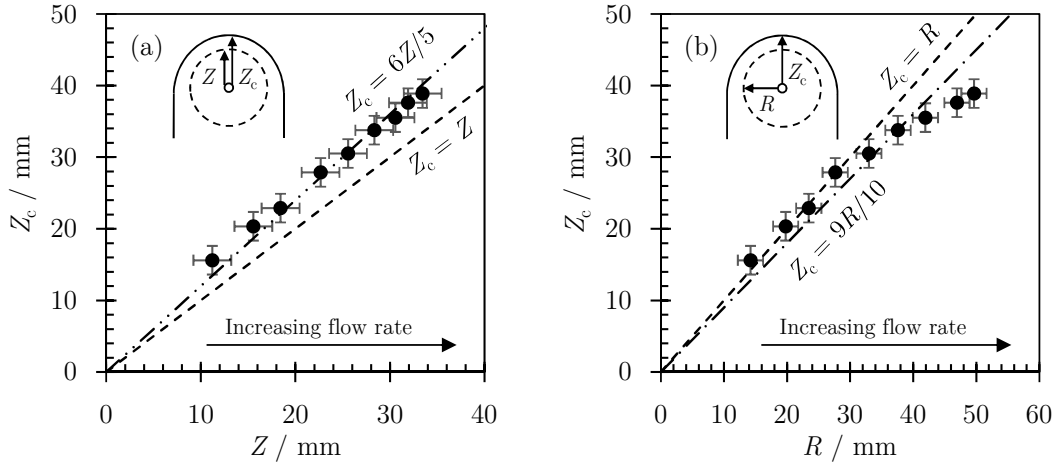


Figure 3.13: Effect of flow rate on the shape of the flow pattern: relationship between (a) Z_c and Z , and (b) Z_c and R .

The Wilson *et al.* (2012) (Equation 2.8) and Bhagat and Wilson (2016) models both predict $Z \approx 0.97R$ when the gravity term is considered in the velocity profiles used to predict the location of the hydraulic jump. The relationship between Z , Z_c and R seen here is thus consistent with the effect of gravity on the rope, causing the rope at the top to fall back over the thin film in the RFZ (Figure 3.9), and this effect is more pronounced at higher flow rates where the RFZ is larger.

The relationships $Z_c = 9R/10$ and $Z = 3R/4$ allow the width of the rope above the point of impingement to be estimated from $B(0) = Z_c - Z = 3R/20$. The relationship $R_c = 4R/3$ gives $B(\pi/2) = R_c - R = R/3$. The experimental values of B are shown in Figure 3.14. The data show a very weak dependence on Q . The data are compared with the relationships obtained for B and the Wang *et al.* (2013b) model (Equation 2.28), where the values of R were calculated using Equation 2.17. The Wang *et al.* model shows good agreement directly above the point of impingement ($\theta = 0$), but underpredicts B at the plane of impingement ($\theta = \pi/2$). Their model assumed that the cross-section of the rope is semi-circular and that the flow in the rope increases uniformly with angle θ from $\theta = 0$ to $\theta = \pi/2$. The shape assumption

is unlikely to be accurate so the rope is expected to be wider than that calculated by the model, which is seen here at $\theta = \pi/2$.

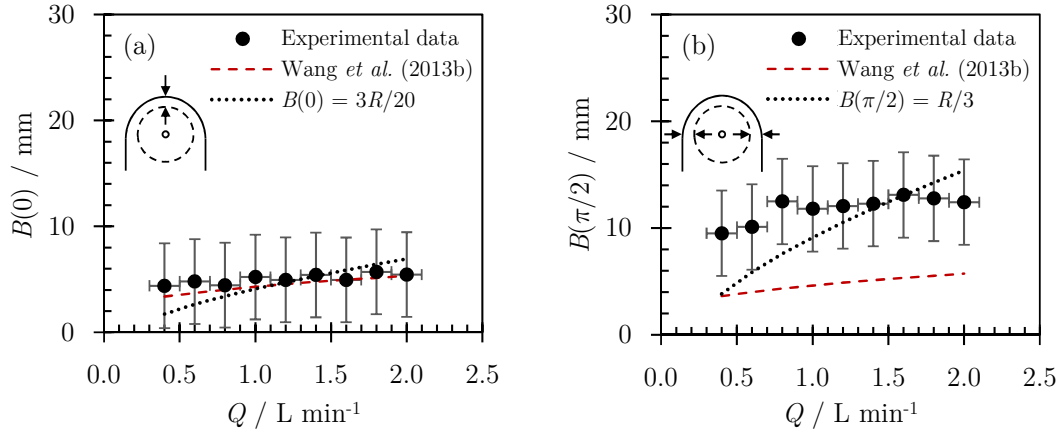


Figure 3.14: Effect of flow rate on the rope width (a) directly above the point of impingement ($\theta = 0$), and (b) at the plane of impingement ($\theta = \pi/2$). The experimental data for (a) are from Figure 3.13(a), replotted in the form $B(0) = Z_c - Z$ while the experimental data for (b) are from Figure 3.12(a), replotted in the form $B(\pi/2) = R_c - R$.

3.4.2 Effect of jet length

Splatter

Shorter jets ($L < 300$ mm) were coherent. Surface fluctuations were evident on all longer jets, and breakup was observed at lower Reynolds numbers with $L \geq 350$ mm. The splatter fraction, ξ , was determined and the data are shown in Figure 3.15. The data show a transition in splatter behaviour with increasing L , but this is not associated with a transition to jet breakup. For shorter jets, $\xi = f(Re)$ and for longer jets, $\xi \neq f(Re)$.

For shorter jets, $L < 300$ mm, there was little splatter at lower Re and data for all d_N exhibit an almost linear increase in ξ for $Re > 13000$, which is consistent with the behaviour reported by Wang *et al.* (2013b). For longer jets, $L \geq 350$ mm, there is a noticeable transition to ξ being independent of Re and strongly dependent on L , with a weak dependence on d_N . For a given Re , ξ increased as L increased.

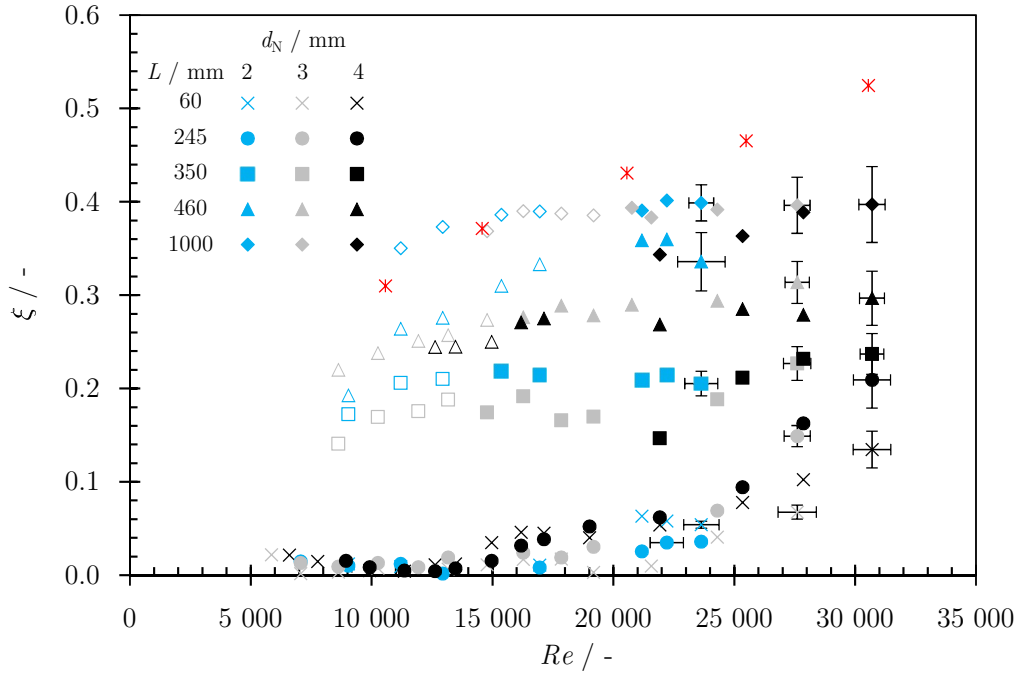


Figure 3.15: Effect of jet Reynolds number on the measured splatter fraction. The symbols are defined in the legend: colour indicates nozzle diameter, symbol shape indicates jet length and hollow symbols indicate that jet breakup was observed. The red asterisk data points are calculated from the data in Figure 16(c) of Kim *et al.* (2020) (rounded entry nozzle, $d_N = 2$ mm, $L = 750$ mm).

ξ approached 0.4 for the longest jets, indicating that a significant fraction of the liquid delivered by the nozzle did not appear in the draining film. For a given L , the value of ξ did not change appreciably when the jet breakup into droplets was observed (indicated by hollow symbols in Figure 3.15), so splatter was not determined solely by jet breakup. Splatter is attributed to the momentum of the drops formed as the jet breaks up and whether this is large enough for rebound to occur. It is also related to the stability of the film and rope, and whether surface tension is strong enough to prevent these shedding droplets. It was not possible to differentiate between water lost as a result of jet breakup, rebound and shedding with the apparatus used.

Zhan *et al.* (2021) studied the splatter from long vertical jets (up to $L = 500$ mm) impinging on a horizontal surface. The jets were generated using convergent entry nozzles similar to that used in this work ($d_N = 1, 2$ and 4 mm with $L_t = 10 d_N$) and tests were conducted with water, and 20 vol% and 40 vol% solutions of glycerin and ethanol. They measured the mass and size of the droplets that were splashed during jet impingement and developed a correlation to predict ξ . The predictions from their correlation did not match the ξ values obtained in this work.

Feldung Damkjær *et al.* (2017) studied long jets (up to $L = 2490$ mm) from industrial scale cylindrical nozzles (sharp entry, $d_N = 2, 3.8, 4.5$ and 5.5 mm with $L_t = 13$ mm). They did not measure ξ but instead measured R then estimated Q_{eff} using Equation 2.14. Their Q_{eff}/Q data are reported as ξ against Re in Figure 3.16. In their case, jets with $L \leq 300$ mm exhibited the trend of ξ increasing with Re but this trend was not evident for longer jets. The range of Re and ξ values were also noticeably larger than in this work.

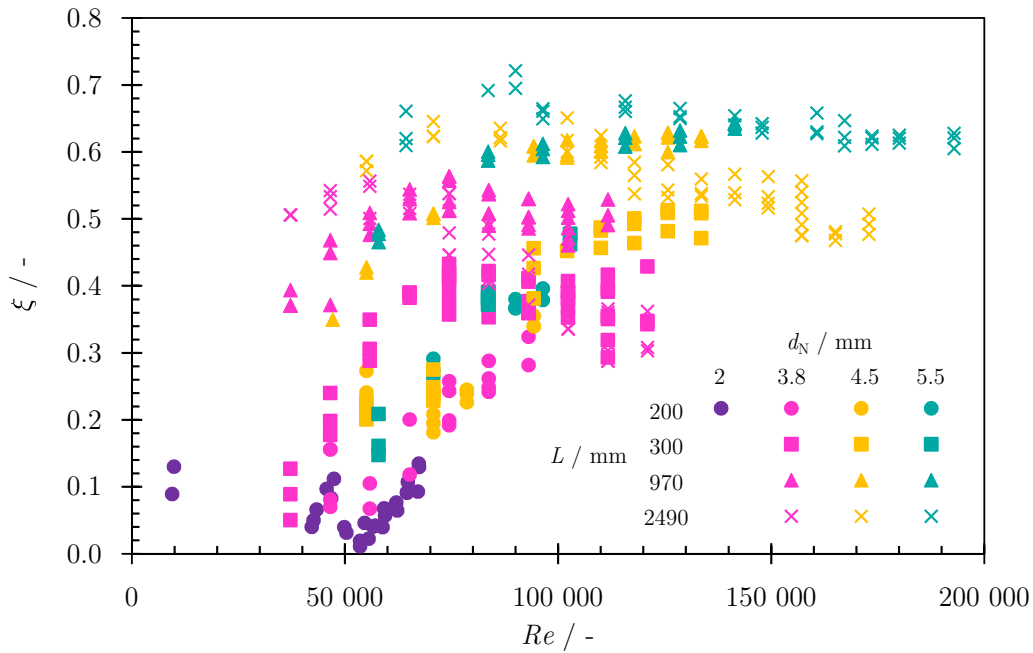


Figure 3.16: Splatter fraction from the Q_{eff}/Q data reported by Feldung Damkjær *et al.* (2017) for industrial scale nozzles. The symbols are defined in the legend: colour indicates nozzle diameter and symbol shape indicates jet length. Error bars are not shown as no attempt was made to quantify the errors.

Kim *et al.* (2020) studied the splatter behaviour of long water jets (up to $L = 1000$ mm; water temperature $19 \pm 2^\circ\text{C}$). They used cylindrical nozzles ($d_N = 1, 1.5$ and 2 mm with $L_t = 10$ mm) with rounded or sharp-edged entries. Their measured splatter fractions were larger than that in this work, shown by the dataset in Figure 3.15. Kim *et al.* obtained similar values of ξ for rounded and sharp-edged entry nozzles at similar conditions. The lower ξ values in this work could be attributed to the use of convergent entry nozzles, as a smoother transition in the flow through the nozzle is likely to improve the stability of the jet.

Figure 3.17(a) shows data reported by Kim *et al.* (2020). They reported an increase in ξ with both L and jet velocity for all jets studied. The increase in ξ with jet velocity did not match that observed in this work, shown in Figure 3.17(b).

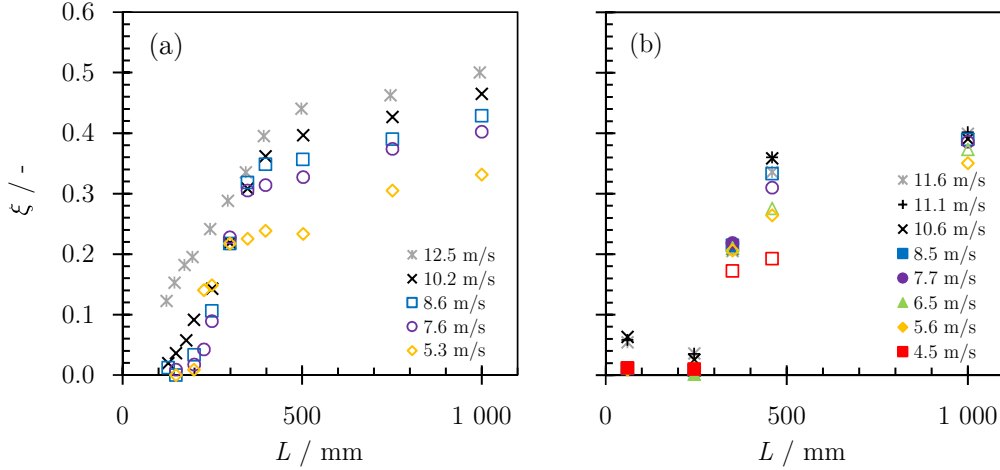


Figure 3.17: Effect of jet length and velocity on the measured splatter fraction for $d_N = 2$ mm. (a) Data from Figure 18(b) of Kim *et al.* (2020) (rounded entry nozzle) and (b) data from Figure 3.15. Error bars in (b) are omitted for clarity but the errors were estimated to be $\xi \pm 0.02$ -0.05 and $L \pm 5$ -10 mm.

The data in Figure 3.15 were plotted against L/d_N , shown in Figure 3.18(a), but this did not yield further insight. There was no apparent trend in the data when classified in terms of We , shown in Figure 3.18(b).

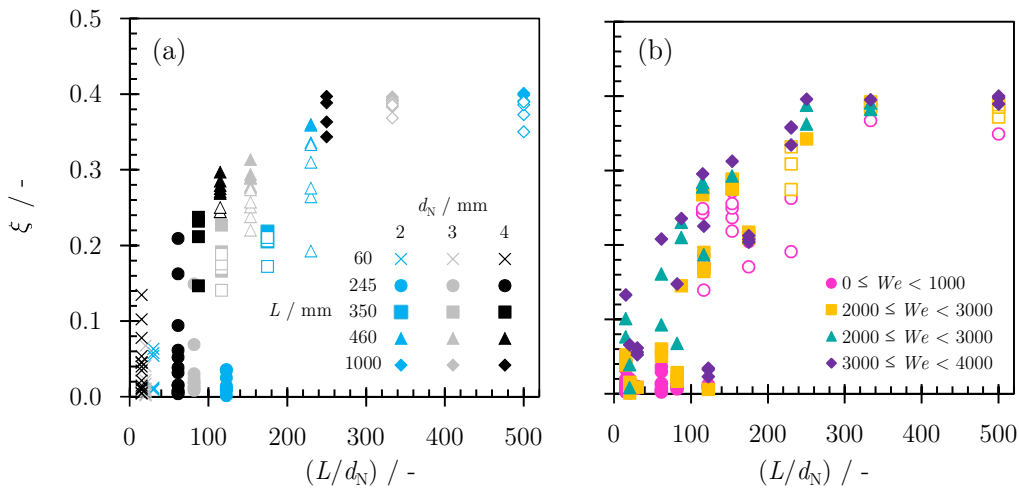


Figure 3.18: Data in Figure 3.15 plotted against L/d_N with the symbols representing (a) nozzle diameter and jet length, and (b) range of jet Weber numbers. Error bars are omitted for clarity.

Bhunia and Lienhard (1994) studied the splatter from water jets ($L = 2\text{--}300$ mm) generated by flow through long cylindrical nozzles ($d_N = 0.8\text{--}5.8$ mm with $L_t = 70\text{--}100 d_N$) striking a rigid flat surface. They presented a correlation relating ξ to Ω (Equation 2.32), where Ω is related to We and L/d_N (Equation 2.33). However, the correlation could not be used for comparison with the results in this work as the conditions used here were outside the range of their correlation ($1\,000 < We < 5\,000$, $L/d_N < 50$ and $4\,400 < \Omega < 10\,000$). Their chosen lower limit of Ω was to ensure that the predicted ξ was at least 4%, as below this level there was considerable scatter and high uncertainty in their measurements. For the tests in this work, their correlation gave ξ outside the range $0.04 < \xi < 1$.

The experimental data in this work lay in the range $90 < We < 4\,000$, $15 \leq L/d_N \leq 500$ and $400 < \Omega < 1.4 \times 10^{10}$, and are shown in Figure 3.19.

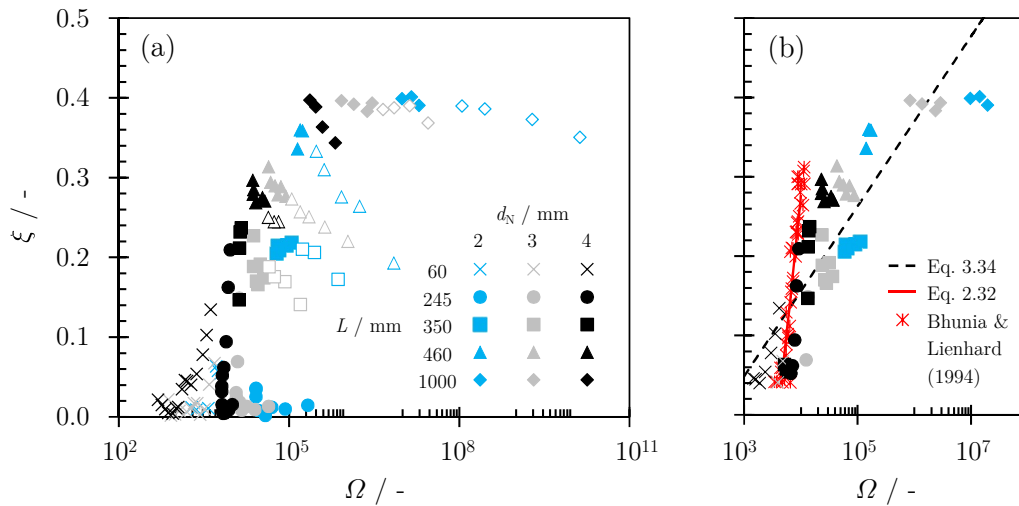


Figure 3.19: Measured splatter fraction for the jets studied plotted against the Bhunia and Lienhard (1994) parameter Ω (Equation 2.33). (a) All the experimental data in this work. Hollow symbols indicate that jet breakup was observed. (b) The experimental data in this work where data with $\xi < 0.04$ and where jet breakup was observed have been omitted; the red asterisks denote data from Figure 7 of Bhunia and Lienhard (1994). The solid red line shows the Bhunia and Lienhard (1994) correlation (Equation 2.32) and the dashed black line shows the correlation obtained here (Equation 3.34). Note the \log_{10} scale for Ω .

A trendline was fitted to the experimental data, giving

$$\xi = 0.0465 \ln \Omega - 0.2724 \quad (3.34)$$

Experimental data where $\xi < 0.04$ and where jet breakup was observed were omitted from the fitting and the regression coefficient was 0.7612.

Bhunia and Lienhard (1994) also proposed a correlation to predict the onset of splattering (Equation 2.34), defined as the point where $\xi \geq 0.05$. Figure 3.20 compares the experimental data in this work with their correlation.

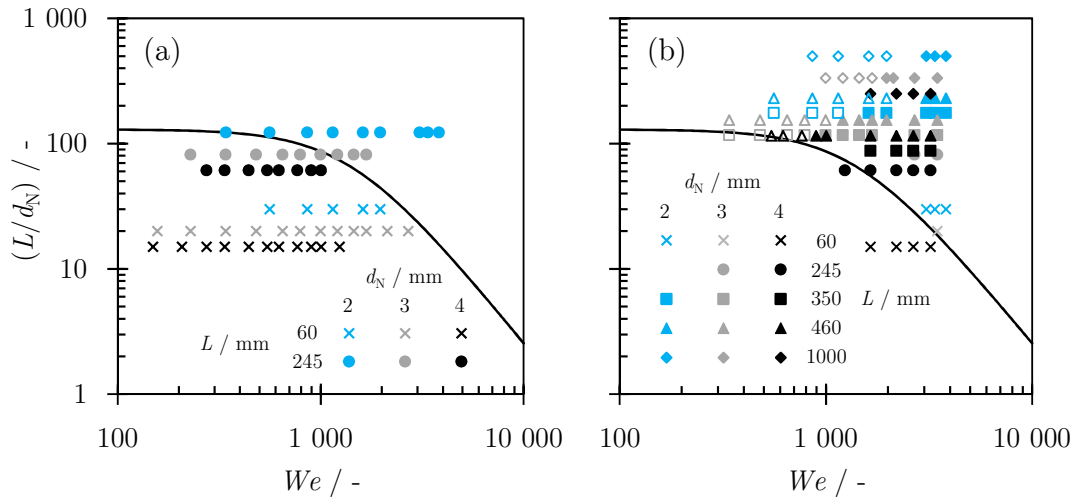


Figure 3.20: Onset of splattering experimental data in this work with (a) $\xi < 0.05$ and (b) $\xi \geq 0.05$. The solid line shows the Bhunia and Lienhard (1994) correlation (Equation 2.34) where points below the line are predicted to have $\xi < 0.05$ and points above the line $\xi \geq 0.05$. Note the \log_{10} scale for both L/d_N and We .

There is relatively good agreement between the correlation and the experimental data with the exception of the $d_N = 2$ mm, $L = 245$ mm data set (Figure 3.20(a)) and the $d_N = 4$ mm, $L = 60$ mm data set (Figure 3.20(b)). This indicates that at a given L/d_N , the onset of splatter is governed by We .

Steady state flow patterns

A short study was carried out to determine the effect of jet length on the steady state flow pattern. The shape of the steady state flow pattern, shown in Figure 3.21, follows the same trend seen in Figure 3.12 where $R_c = 4R/3$ and $Z = 3R/4$.

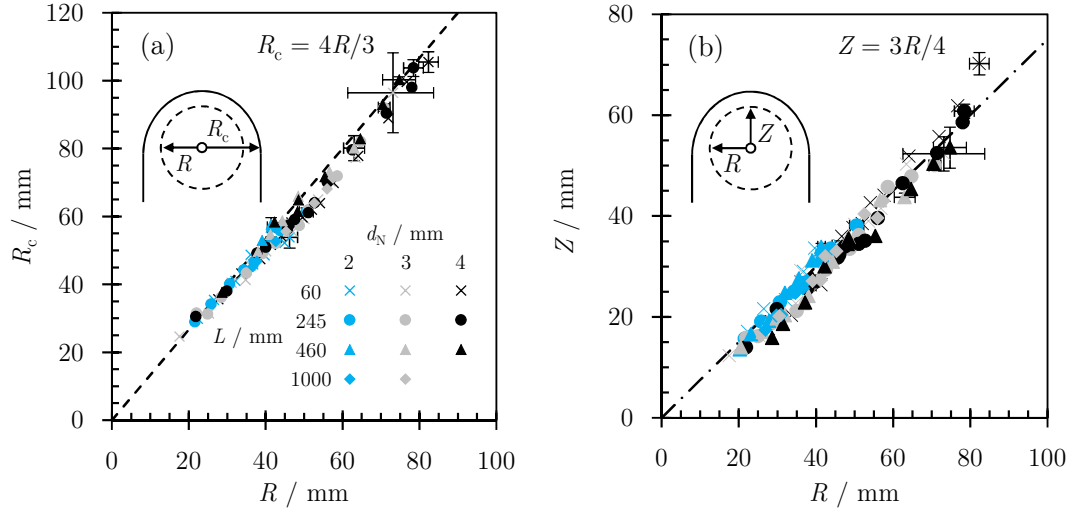


Figure 3.21: Comparison of the measured half-width of the radial flow zone at the level of the point of impingement, R , with the measured (a) half-width of the wetted region at the level of the point of impingement, R_c and (b) height of the radial flow zone at the point of impingement, Z . The dashed line shows $R_c = 4R/3$ and $Z = 3R/4$ in (a) and (b), respectively.

Figure 3.22 shows that the measured half-width of the radial flow zone at the level of the point of impingement, R , collapsed to a common trend when plotted against Q_{eff} . This indicates that the splatter fraction correction is partly able to account for the differences in fluid flow behaviour. There is still some variation, however, and this is evident when the data are compared with the predictions by the Wilson *et al.* (2012) and Bhagat and Wilson (2016) models, Equations 2.14 and 2.17, respectively.

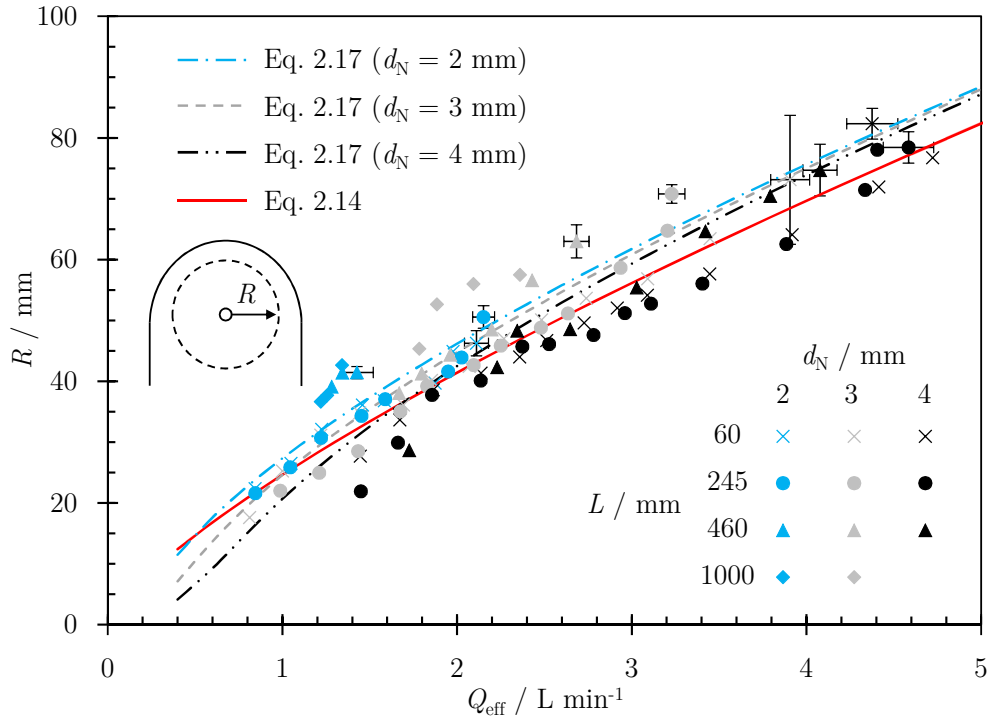


Figure 3.22: Effect of nozzle diameter and jet length on the measured half-width of the radial flow zone at the level of the point of impingement, R , plotted against the flow rate in the falling film, Q_{eff} . The lines show the predictions from the Wilson *et al.* (2012) and Bhagat and Wilson (2016) models, Equations 2.14 and 2.17, respectively.

3.4.3 Correction for refraction

The flow patterns generated by the impinging water jet on cylindrical targets were similar to those observed on a flat plate, namely radial flow near the impingement point, a hydraulic jump, and a confining rope of draining liquid, shown in Figure 3.23. Refraction was expected to affect the measurements of R and R_c on vertical cylinders, and the measurements of Z and Z_c on horizontal cylinders.

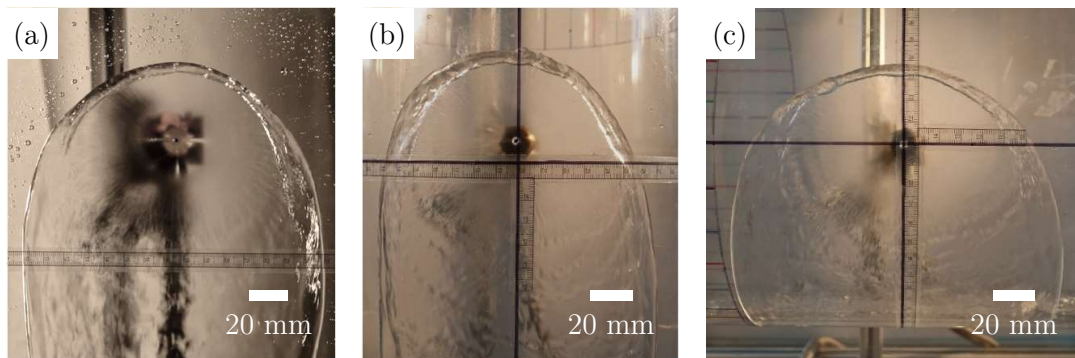


Figure 3.23: Flow patterns generated by a coherent horizontal liquid jet ($d_N = 2$ mm, $Q = 2.0$ L min^{-1}) impinging normally on Perspex[®] targets: (a) flat plate, (b) vertical cylinder ($\kappa = 9.1$ m^{-1}), and (c) horizontal cylinder ($\kappa = 9.1$ m^{-1}).

Second camera measurements and estimates

A second camera was moved around the apparatus at 10° intervals in order to obtain refraction-free images. To obtain an estimate of the measurement from the second camera, a linear interpolation was compared with a harmonic weighting. The results in Figure 3.24 show that there is no significant difference between the linear interpolation and the harmonic weighting. The harmonic weighting was used to obtain the second camera estimates in the following sections.

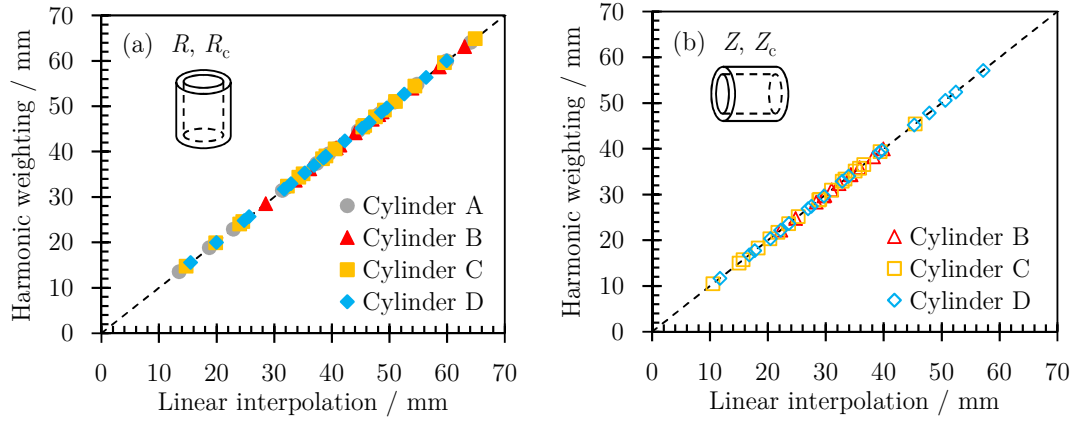


Figure 3.24: Comparison of the harmonic weighting and linear interpolation for measurements of (a) R and R_c on vertical cylinders, and (b) Z and Z_c on horizontal cylinders. The dashed line is the line of equality. Error bars are omitted for clarity. Filled symbols are used for R and R_c , hollow symbols are used for Z and Z_c , and colour indicates the cylinder used. At a given flow rate, $R_c > R$ and $Z_c > Z$.

Comparison between the models

The estimates from the second camera are compared with the measurements from the main camera in Figure 3.25. Refraction effects are significant.

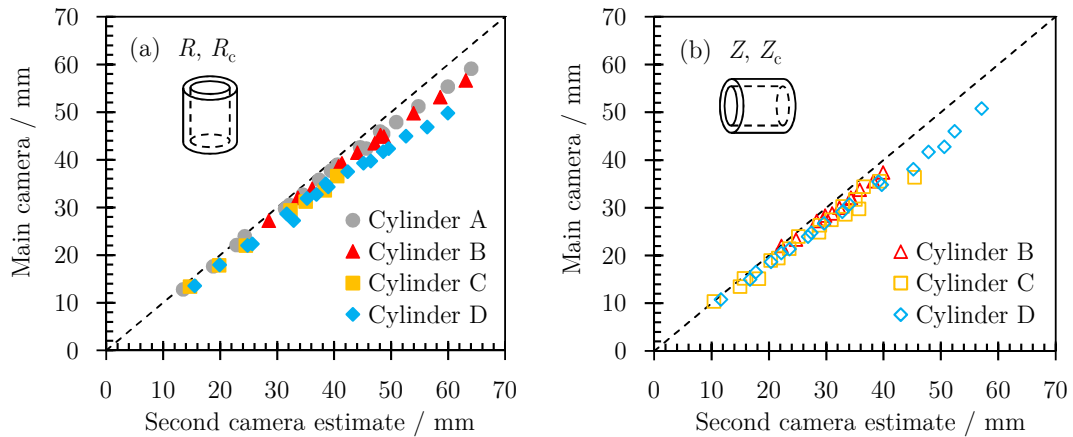


Figure 3.25: Comparison of measurements from the main camera, uncorrected for refraction, with estimates from the second camera for (a) R and R_c on vertical cylinders, and (b) Z and Z_c on horizontal cylinders. The dashed line is the line of equality. Error bars are omitted for clarity. Filled symbols are used for R and R_c , hollow symbols are used for Z and Z_c , and colour indicates the cylinder used. At a given flow rate, $R_c > R$ and $Z_c > Z$.

The measurements from the main camera were corrected for refraction using the thin lens and geometrical models described in Section 3.3.1 and compared with the estimates from the second camera. The results for Cylinder D, the cylinder with the highest curvature, are shown in Figure 3.26. Similar trends were seen with all the other cylinders tested.

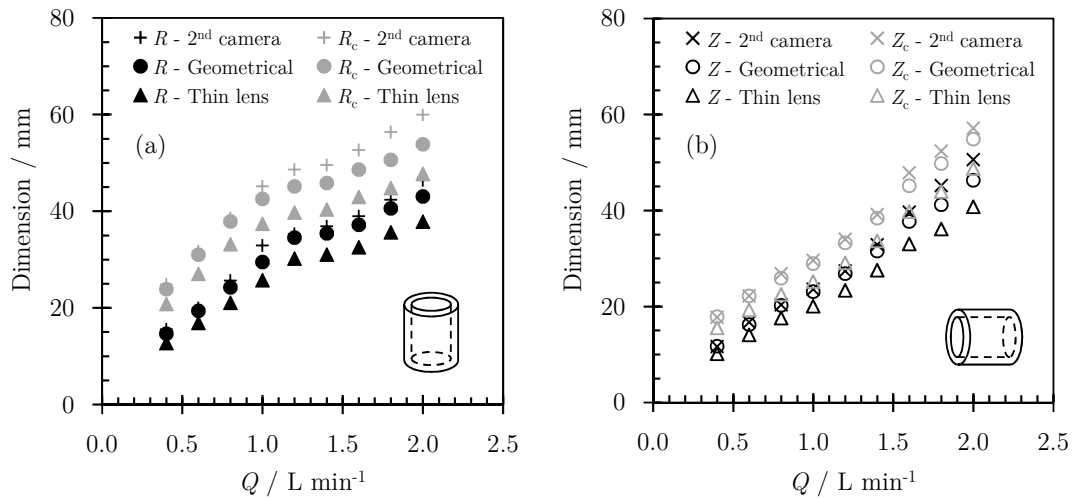


Figure 3.26: Comparison of (a) R and R_c with Cylinder D placed vertically, and (b) Z and Z_c with Cylinder D placed horizontally. Error bars are omitted for clarity.

The results from the thin lens model showed poor agreement with estimates from the second camera while the results from the geometrical model were much closer to the estimates from the second camera. Figure 3.27 shows the comparison of the results from the geometrical model with the second camera estimates. There is good agreement at lower flow rates, but an increasing deviation is evident as the flow rate increases and the film travels further around the surface of the cylinder away from camera. This indicates that the geometrical model does not capture all the physics of the problem: one parameter that is not accounted for is the focal length of the camera lens.

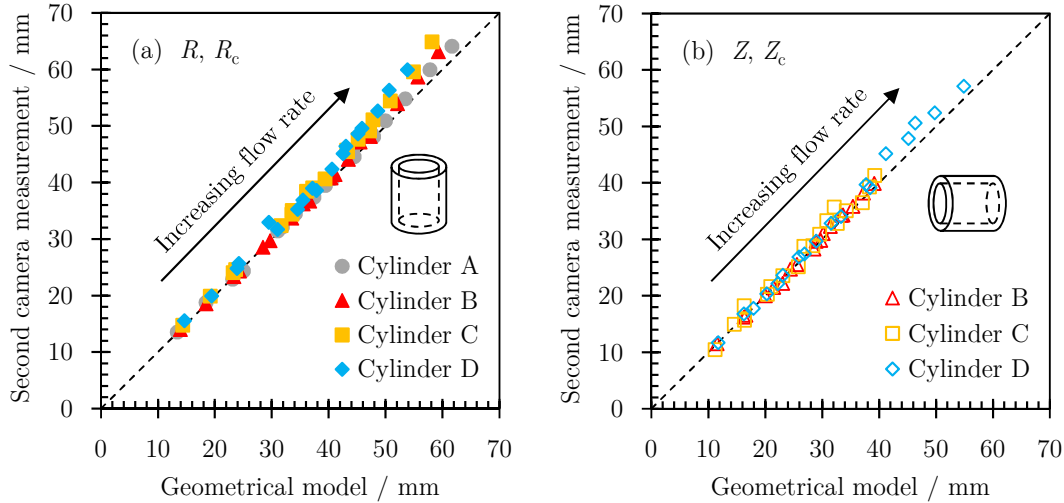


Figure 3.27: Comparison of the estimates from the second camera with measurements from the main camera, corrected with the geometrical model, for (a) R and R_c on vertical cylinders, and (b) Z and Z_c on horizontal cylinders. The dashed line is the line of equality. Error bars are omitted for clarity. Filled symbols are used for R and R_c , hollow symbols are used for Z and Z_c , and colour indicates the cylinder used. At a given flow rate, $R_c > R$ and $Z_c > Z$.

Empirical correlation

Both the thin lens and geometrical models were unable to correct for refraction completely. For simplicity, empirical correlations were used instead. The estimates from the second camera are plotted against the chord length measured using the main camera, C , scaled by the wall curvature, κ , in Figure 3.28. A second order polynomial was found to give the best fit to the experimental data, given in Table 3.6. Measurements of R and R_c on vertical cylinders and Z and Z_c on horizontal cylinders were obtained in subsequent tests using the main camera and this calibration.

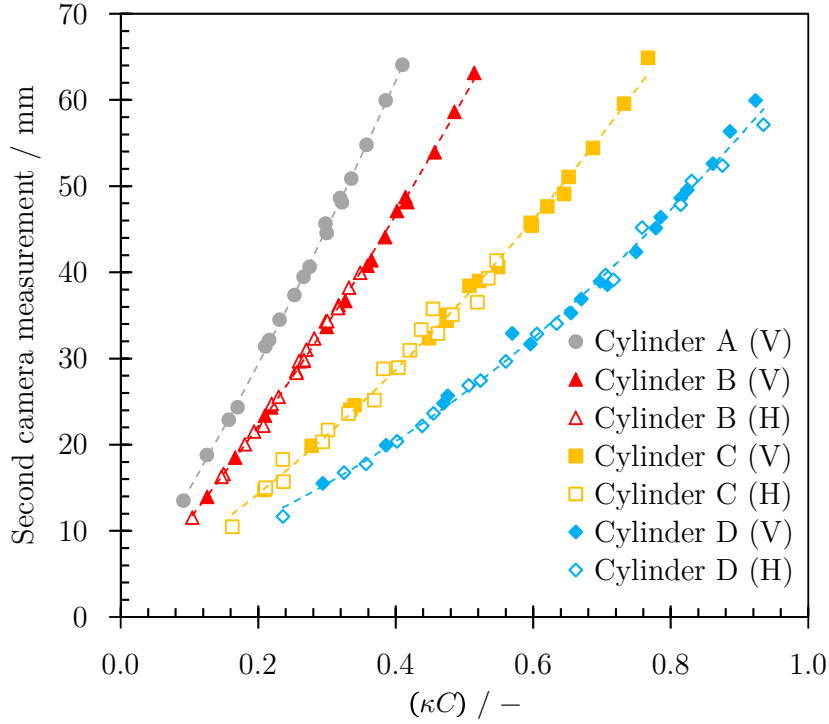


Figure 3.28: Fit of the empirical correlations (Table 3.6) to the experimental data. Error bars are omitted for clarity. (V) – R and R_c on vertical cylinders, and (H) – Z and Z_c on horizontal cylinders. Filled symbols are used for R and R_c , hollow symbols are used for Z and Z_c , and colour indicates the cylinder used. At a given flow rate, $R_c > R$ and $Z_c > Z$.

Table 3.6: Empirical correlations used to correct for refraction, where $m = R, R_c, Z$ or Z_c .

Cylinder	Curvature, κ / m^{-1}	Correlation	Regression coefficient
A	6.9	$m = 66.1(\kappa C)^2 + 124.9(\kappa C) + 1.74$	0.9992
B	9.1	$m = 49.2(\kappa C)^2 + 93.1(\kappa C) + 1.55$	0.9989
C	14	$m = 38.2(\kappa C)^2 + 49.0(\kappa C) + 2.97$	0.9944
D	20	$m = 36.2(\kappa C)^2 + 23.8(\kappa C) + 5.07$	0.9947

3.4.4 Effect of wall curvature

Steady state flow patterns

Figure 3.29 summarises the effect of wall curvature on the observed flow patterns generated by coherent horizontal jets ($d_N = 2$ mm). Figure 3.29(a) shows that there is little effect of wall curvature on the relationship between R_c and R . The experimental data for both vertical and horizontal cylinders show similar behaviour to that for flat plates where $R_c = 4R/3$ (Figure 3.12(a)).

Figure 3.29(b) shows that the experimental data lie close to the $Z = 3R/4$ locus for flat plates (Figure 3.12(b)). A deviation from the $Z = 3R/4$ locus is seen at higher flow rates when Cylinder D is placed vertically. Cylinder D has the smallest diameter of the cylinders studied and thus the highest curvature. At higher flow rates, the film travels further around the curved inner surface away from the camera.

A linear trendline passing through the origin was fitted to the experimental data of Z_c against Z , giving a relationship of $Z_c = 5Z/4$ for both vertical and horizontal cylinders (regression coefficient: vertical cylinders = 0.9530, horizontal cylinders = 0.9649), similar to the relationship of $Z_c = 6Z/5$ obtained for flat plates (Figure 3.13(a)).

Combining the relationships $Z_c = 5Z/4$ and $Z = 3R/4$ gives $Z_c = 15R/16$. Figure 3.29(c) shows that the experimental data lie close to the $Z_c = 15R/16$ locus. The $Z_c \approx R$ relationship is consistent with the effect of gravity on the rope, causing the rope at the top to fall back over the thin film in the RFZ (Figure 3.9), giving rise to $Z < R$ when measurements are made of the flow at steady state.

The relationships $Z_c = 15R/16$ and $Z = 3R/4$ allow the width of the rope above the point of impingement to be estimated from $B(0) = Z_c - Z = 3R/16$. The relationship $R_c = 4R/3$ gives $B(\pi/2) = R_c - R = R/3$. The experimental values of B are shown in Figure 3.30. The data show a very weak dependence on Q and there is no systematic variation with curvature. The data are compared with the relationships obtained for B and the Wang *et al.* (2013b) model (Equation 2.28), where the values of R were calculated using Equation 2.17. The Wang *et al.* model shows good agreement directly above the point of impingement ($\theta = 0$), but underpredicts B at the plane of impingement ($\theta = \pi/2$). The trends observed on curved walls are similar to those on flat plates (Figure 3.14).

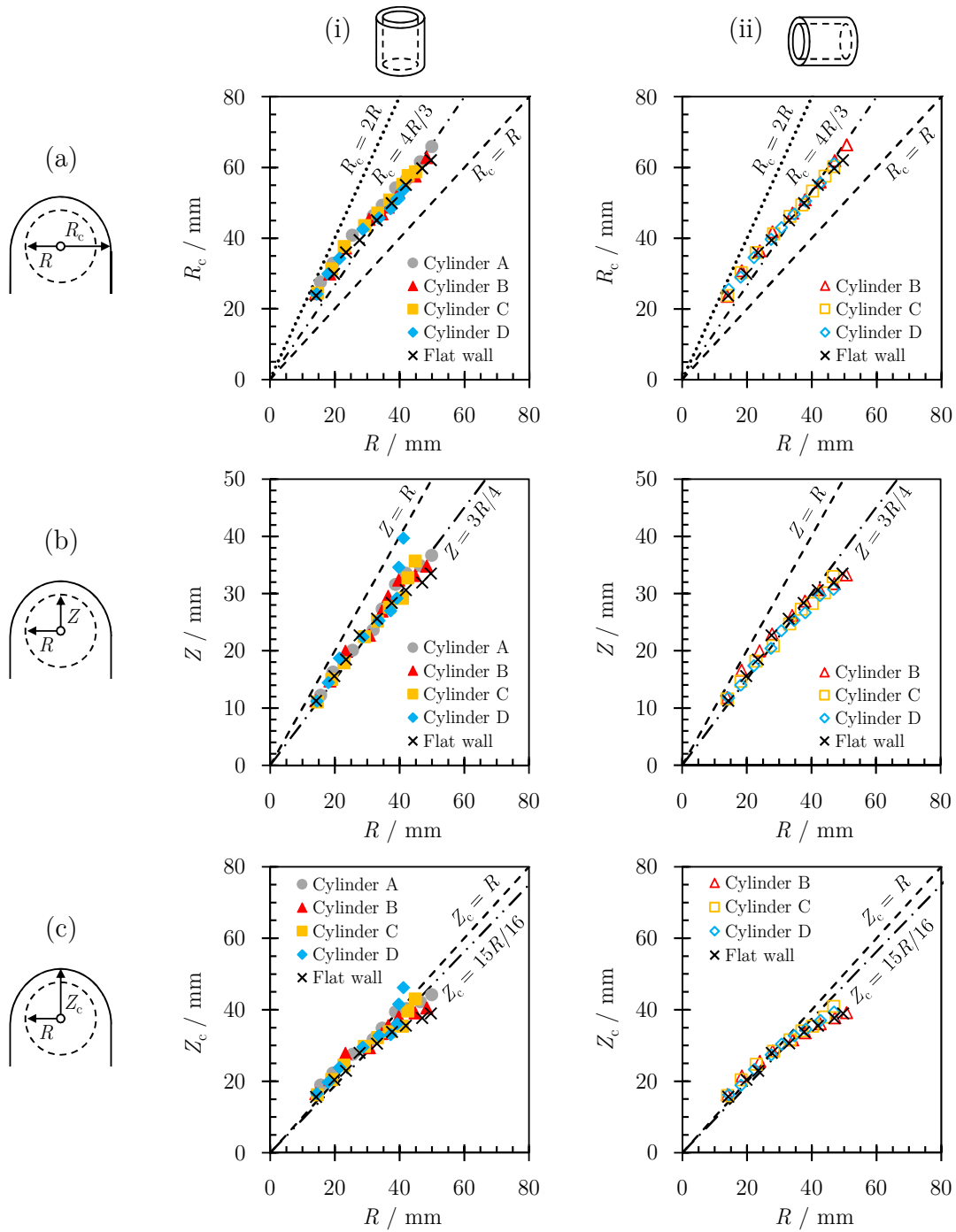


Figure 3.29: Experimental measurements of (a) R_c and R , (b) Z and R , and (c) Z_c and R for a horizontal water jet impinging normally on (i) vertical cylinders, and (ii) horizontal cylinders. The flat wall results from Section 3.4.1 are shown for comparison. Error bars are omitted for clarity: these are approximately ± 2 mm for R , R_c , Z and Z_c .

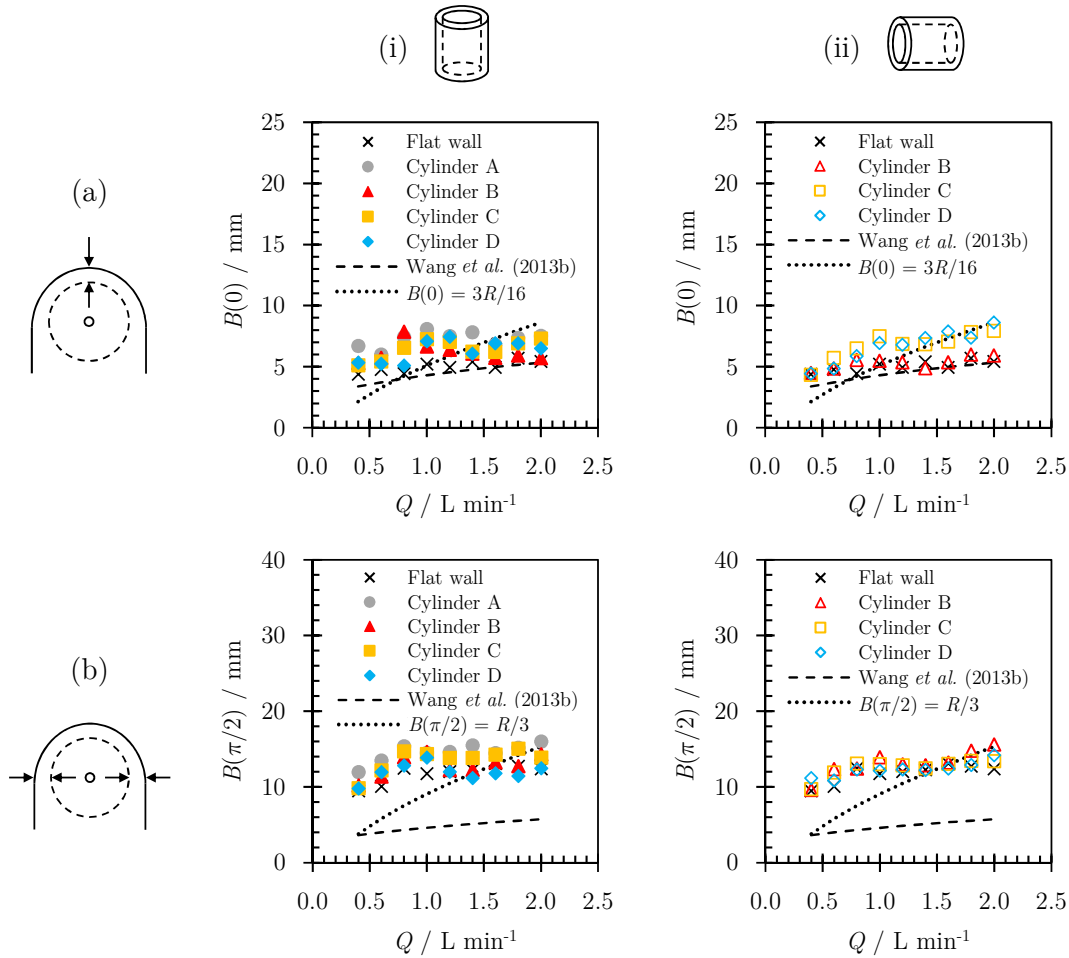


Figure 3.30: Effect of curvature and flow rate on the rope width (a) directly above the point of impingement ($\theta = 0$), and (b) at the plane of impingement ($\theta = \pi/2$), on (i) vertical cylinders and (ii) horizontal cylinders. The flat wall results from Figure 3.14 in Section 3.4.1 are shown for comparison. Also plotted are the loci for the model for B presented by Wang *et al.* (Equation 2.28). Error bars are omitted for clarity.

Figure 3.31 summarises the effect of wall curvature on the dimensions of the radial flow zone, Z and R , at different flow rates ($4\,200 \leq Re \leq 21\,000$). For vertical cylinders, the height of the hydraulic jump, Z , does not change appreciably with curvature at lower flow rates. As the flow rate increases, the variation that occurs is attributed to splatter as there was noticeable spray observed within the cylinders. Splatter was observed on a flat plate above a jet Reynolds number of 13 000 (Figure 3.15), corresponding to a flow rate of about 1.2 L min^{-1} with $d_N = 2 \text{ mm}$. The half-width of the radial flow zone, R , is similarly insensitive to curvature (within experimental error) at lower flow rates. At higher flow rates, there is a steady decrease in R with increasing curvature. In vertical cylinders, the flow in the direction of R is subject to

strong curvature effects, so the results suggest that the amount of splatter increases (so Q_{eff} , decreases and thus R decreases) as κ increases.

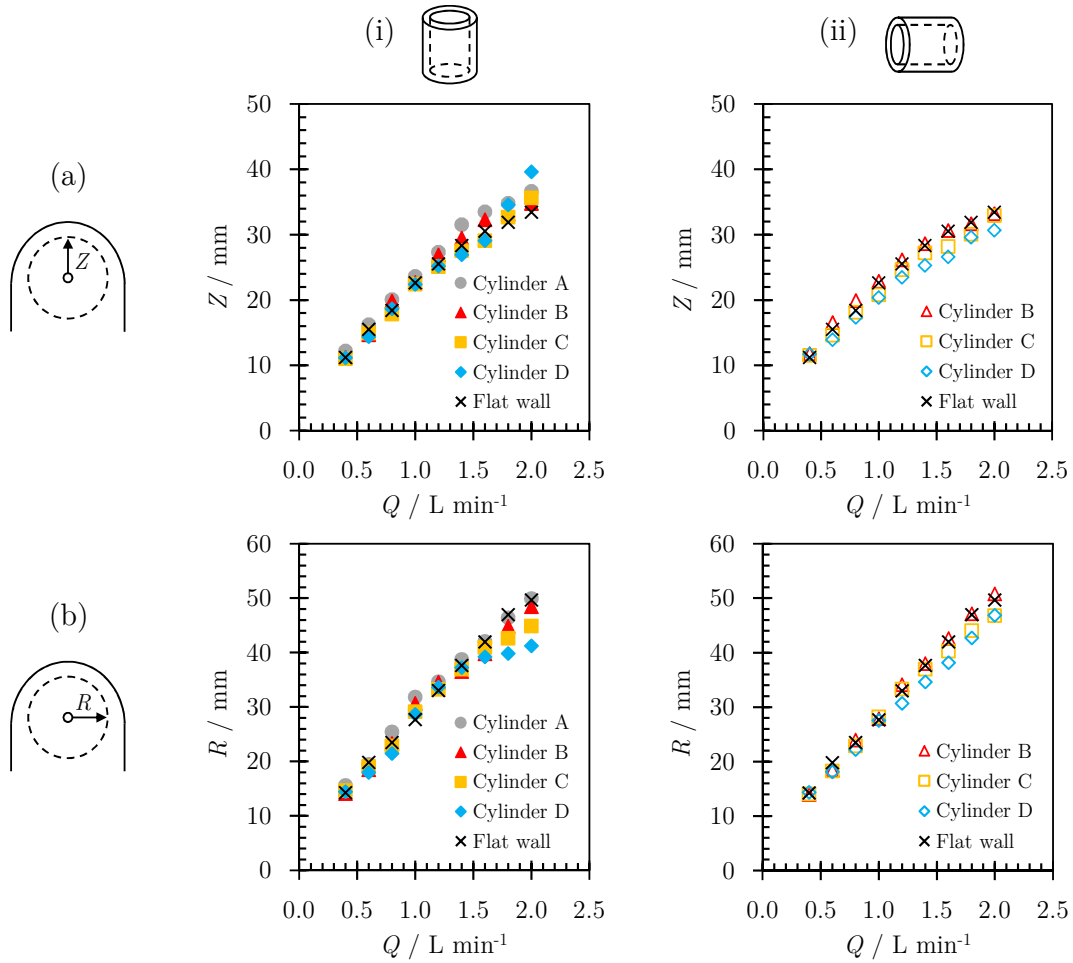


Figure 3.31: Effect of flow rate on (a) Z , and (b) R , for a coherent horizontal water jet ($d_N = 2$ mm) impinging normally on (i) vertical cylinders, and (ii) horizontal cylinders. The flat wall results from Section 3.4.1 are shown for comparison. Error bars are omitted for clarity: these are approximately ± 2 mm for Z and R , and ± 0.1 L min $^{-1}$ for Q .

For horizontal cylinders, little variation was observed at lower flow rates while a decrease with κ was observed at higher flow rates for both Z and R . The decrease at higher flow rates is attributed to splatter. The spray observed within the cylinders was noticeably stronger with horizontal cylinders than vertical cylinders, shown in Figure 3.32, demonstrating the complexity of these wall curvature effects. Quantitative measurements of splatter could not be made in the cylinder tests with the experimental setup used.

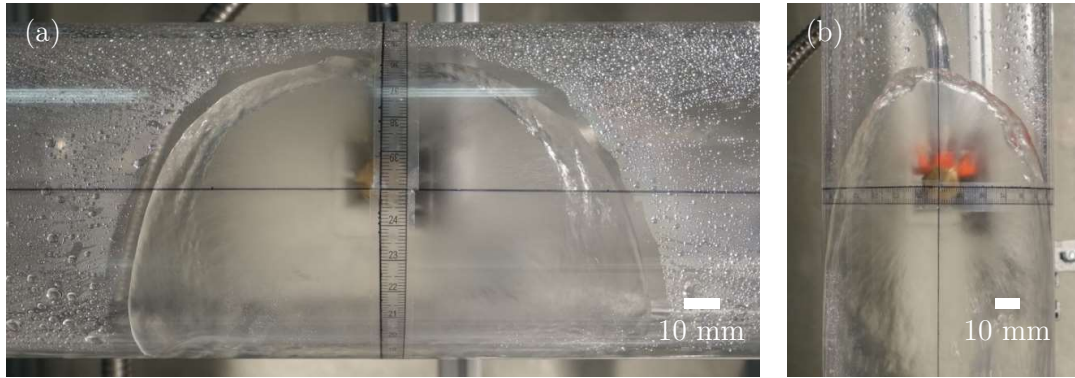


Figure 3.32: Splatter in (a) horizontal, and (b) vertical cylinder under identical experimental conditions ($d_N = 2 \text{ mm}$, $Q = 2.0 \text{ L min}^{-1}$, $\kappa = 20 \text{ m}^{-1}$).

These results demonstrate that a positive curvature of the wall, as arises with jets striking the internal wall of a cylinder, has a slight effect on the behaviour of the radial film pattern. The thickness of the liquid film, h , was observed visually and estimated to be $\sim 1\text{-}2 \text{ mm}$ in the RFZ and $\sim 4\text{-}5 \text{ mm}$ in the rope. The effect of wall curvature, κ , is likely to only become significant when $h\kappa > 1$, and the curvatures studied here give $h\kappa \leq 0.1$. The curvatures studied here are larger than those likely to be encountered in process tanks and vessels in many industrial applications, so the influence of curvature in practice is therefore expected to be small. The results presented here have been collected for concave walls: the impact of a convex wall on splatter has not been studied and represents an avenue for further work as these are often encountered in CIP applications as piping, fitting connections and other protuberances.

Other phenomena

Higher flow rates were also investigated with a jet of a larger diameter ($d_N = 4 \text{ mm}$). At higher flow rates the radial flow zone extended further around the cylinder inner wall. Two flow patterns not seen on flat plates were observed in tests with horizontal cylinders: shedding (Figure 3.33(a)) and wraparound (Figure 3.33(b)). These were not observed in tests with vertical cylinders.

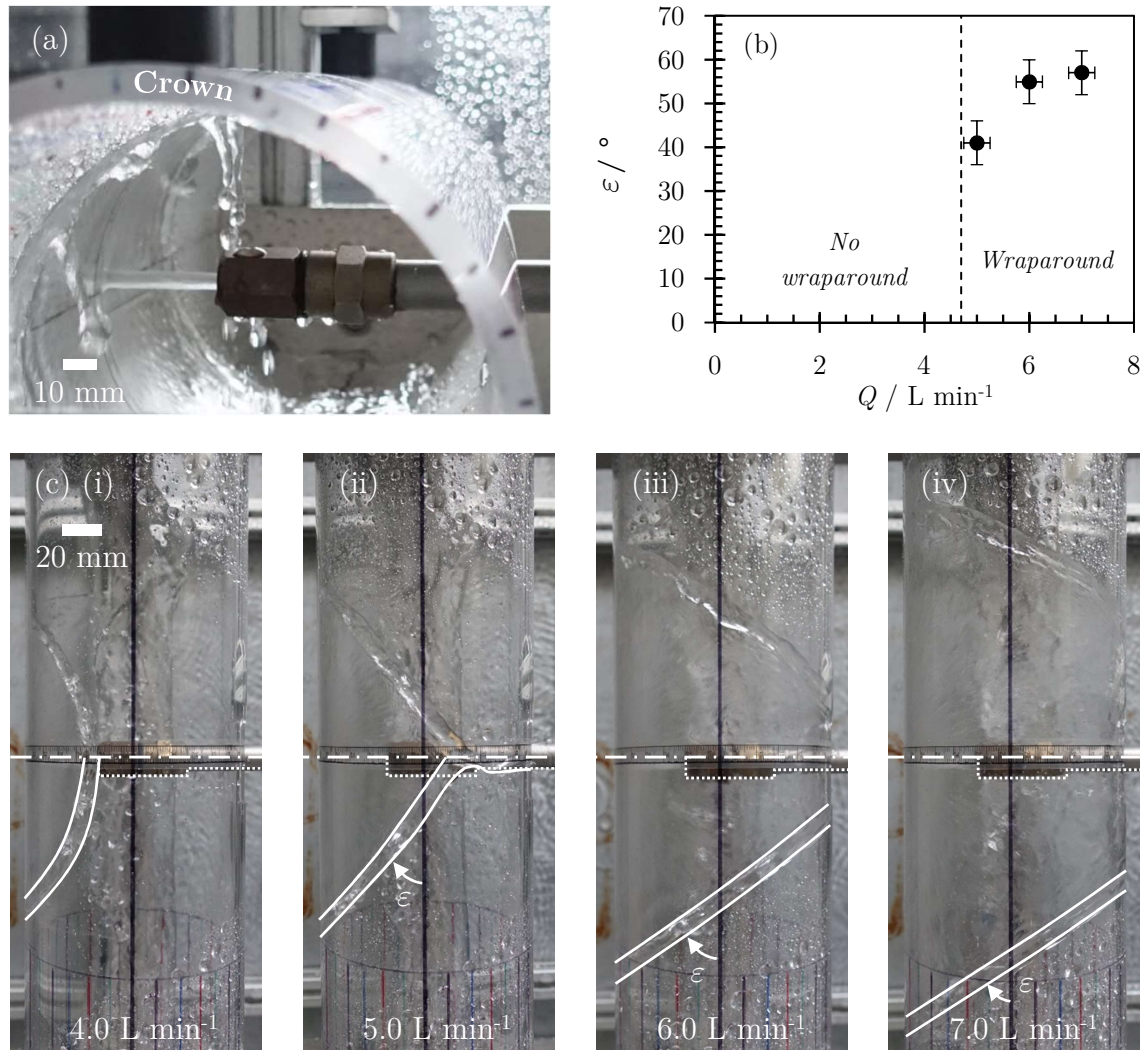


Figure 3.33: (a) Shedding from the rope ($Q = 4.5 \text{ L min}^{-1}$), (b) angle of the rope at the crown of the cylinder, ε , when wraparound occurs and the dashed line is the prediction from Equation 3.35, and (c) plan view of a horizontal jet impinging normally on a horizontal cylinder. Flow rate increases from (i) to (iv). $d_N = 4 \text{ mm}$, $L = 30 \text{ mm}$ and $\kappa = 20 \text{ m}^{-1}$. Vertical black line in (c) indicates the crown (top) of the cylinder.

Figure 3.33(a) shows an example in a horizontal cylinder where gravity causes water to be shed from the rope. Shedding is not expected to affect the liquid velocity in the RFZ, but it will reduce the flow rate in the rope. Shedding was not observed in tests with $d_N = 2 \text{ mm}$ ($0.4 \leq Q \leq 2.0 \text{ L min}^{-1}$, $L = 30 \text{ mm}$ and $\kappa = 6.9\text{-}20 \text{ m}^{-1}$) but was observed in all tests with $d_N = 4 \text{ mm}$ ($4.0 \leq Q \leq 7.0 \text{ L min}^{-1}$, $L = 30 \text{ mm}$ and $\kappa = 20 \text{ m}^{-1}$).

At sufficiently high flow rates, the flow pattern wrapped around the inside of horizontal cylinders. Figure 3.33(c) shows an example, photographed from above. The curved rope approaches the crown of the cylinder as the flow rate increases (Figure 3.33(c)(i)). At some critical flow rate, the crown is reached and some of the rope drains beyond the crown: the rope then forms a Y-shape (Figure 3.33(c)(ii)). At higher flow rates, wraparound extends with almost linear rope boundaries. The narrowing of the flow pattern after it wraps around shows that surface tension dominates over downward momentum. Figure 3.33(b) reports the angle of the rope at the crown of the cylinder, ε , marked in Figure 3.33(c), which increases as Q increases.

If curvature has no effect on the flow in the RFZ, wraparound in a horizontal cylinder is expected to occur if $Z_c \geq \pi D/4$ when the jet impinges normally at the midplane of the cylinder. Assuming $Z_c \approx R$ (Figure 3.29(c)(ii)), Equation 2.14 then predicts that wraparound will occur at flow rates above a critical value, Q_{wrap} , given by

$$Q_{\text{wrap}} = \left[\frac{\mu\gamma(1 - \cos\beta)}{\rho^2} \left(\frac{Z_c}{0.276} \right)^4 \right]^{1/3} \quad (3.35)$$

For the case shown in Figure 3.33(c), with $\beta = 90^\circ$, wraparound is expected where $Q \geq 4.7 \text{ L min}^{-1}$, which is consistent with the observed transition in rope behaviour.

When wraparound occurs, the area wetted by the cleaning liquid will be greater than that predicted by existing models. The increase in wetted area would be advantageous for applications where cleaning arises primarily from the chemical action of the cleaning liquid, and contact with the liquid is all that is required.

3.4.5 Cleaning

Impact of jet length

Figure 3.34 shows the growth of the cleaned region over time for a layer of petroleum jelly on a flat, vertical Perspex[®] plate.

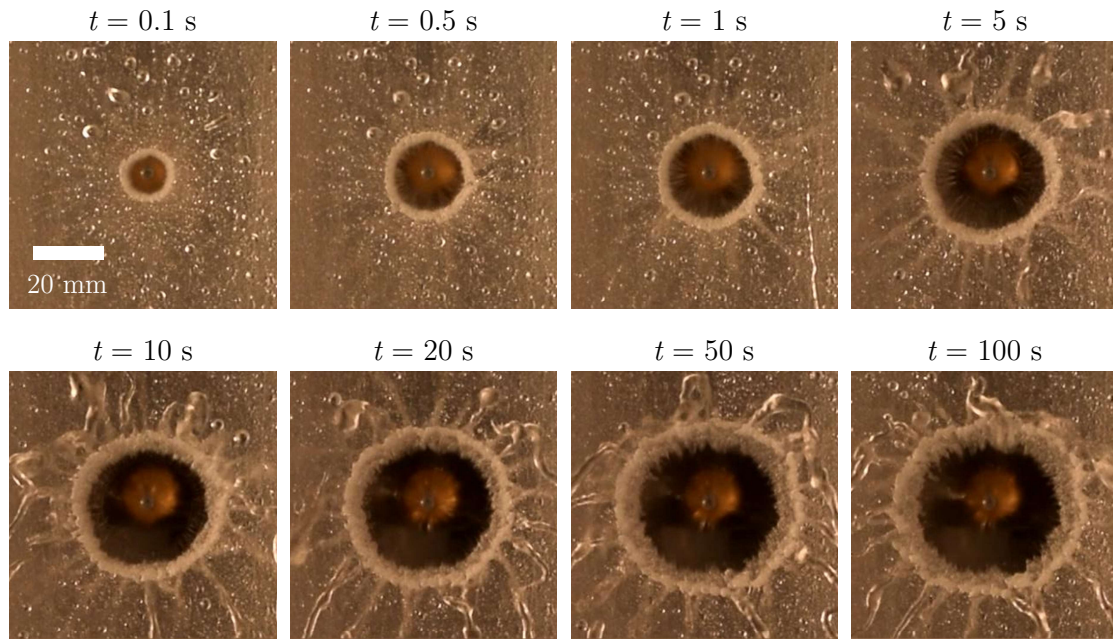


Figure 3.34: Cleaning of a 0.2 mm thick petroleum jelly layer on a flat, vertical Perspex[®] plate over time. t is time elapsed after jet impingement. $d_N = 2$ mm, $Q_{\text{eff}} = 1.6 \text{ L min}^{-1}$ and $L = 60$ mm.

The data for cleaning with jets of three different lengths are shown in Figure 3.35. The cleaned region was observed to be circular so the data were reported in terms of a , the radius of a circle with equal area to the cleaned region. The values of Q were chosen so that the jets had similar Q_{eff} values: Q_{eff} was estimated from measurements on clean plates. The presence of a soil layer affects the flow in the thin film beyond the cleaning front significantly: with the petroleum jelly a berm of dislodged soil collected at the cleaning front which deflected the thin film away from the surface and created a spray.

The cleaning profiles in Figure 3.35 are of similar form, with all data sets exhibiting rapid initial cleaning followed by an approach to an asymptote, denoted a_{max} , at 17-18 mm. The asymptotic behaviour is associated with the soil having a yield stress. In each case a_{max} was smaller than the size of the RFZ ($R = 36.9 \pm 2$ mm from experimental measurements on clean plates; Figure 3.22).

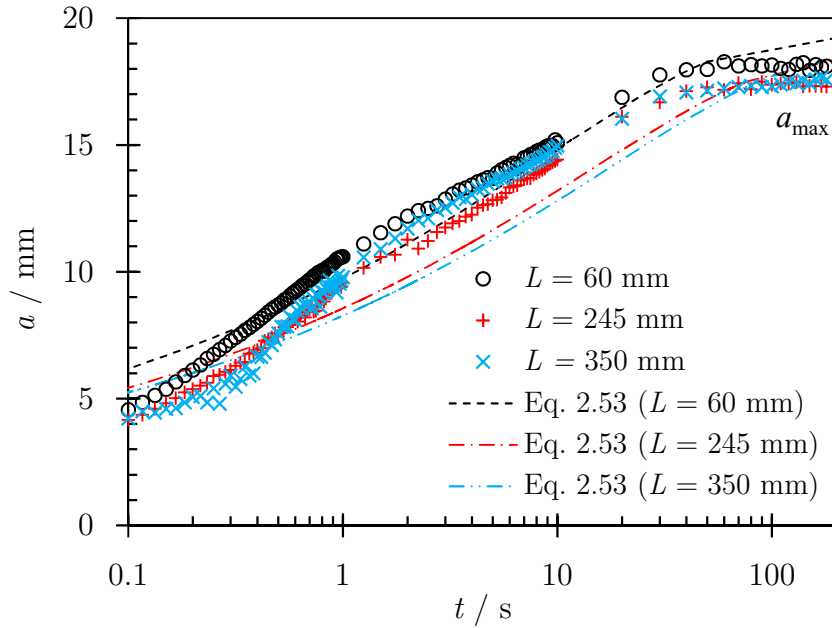


Figure 3.35: Evolution of the cleaned region radius over time for 0.2 mm thick petroleum jelly layers on flat, vertical Perspex[®] plates. $d_N = 2$ mm, $Q_{\text{eff}} = 1.6 \text{ L min}^{-1}$ for $L = 60, 245$ and 350 mm. Note the \log_{10} scale for time. Loci show fit to Equation 2.53. Error bars are omitted for clarity: these are approximately ± 2 mm for a .

Bhagat and Wilson (2016) presented a detailed model of the flow in the RFZ, and presented results for two key transitions: r_b , where the growing viscous boundary layer reaches the surface, and r_t , the transition from laminar to turbulent flow in the film, given by Equations 2.15 and 2.16, respectively. For a nozzle with $d_N = 2$ mm and $Q_{\text{eff}} = 1.6 \text{ L min}^{-1}$, $r_b = 12.3$ mm and $r_t = 15.2$ mm, so a_{max} lies in the region where the flow in the film is turbulent.

The data were fitted by eye to the simple cleaning model used by Glover *et al.* (2016) in their study of a different petroleum jelly (Equation 2.53) to obtain an estimate of the lumped cleaning parameter K . a_{max} was taken to be the largest observed value of $a + 1$ mm. All data sets had similar values of K and a_{max} , summarised in Table 3.7.

The fits from Equation 2.53 are shown in Figure 3.35. The plots show that the cleaning profiles are not described well by the model. Feldung Damkjær *et al.* (2017) also reported that cleaning profiles of a petroleum jelly with longer jets deviated from the model behaviour. These results indicate that whilst Q_{eff} captures the effect of breakup and splatter on hydrodynamics, it does not give a complete description

of the impact of the film dynamics on cleaning. Using Q_{eff} (based on ξ) tended to underestimate the rate: in this case it provides a useful engineering result and indicates that this topic requires further investigation.

Table 3.7: Summary of the cleaning parameters obtained from the experimental data shown in Figure 3.35.

L / mm	$K / \text{mm s}^{-0.2}$	$a_{\text{max}} / \text{mm}$
60	9.8 ± 1.1	19.3
245	8.6 ± 1.2	18.5
350	8.3 ± 1.9	18.6

Impact of wall curvature

Figure 3.36 shows the cleaning profiles obtained for ClearGlide™ layers applied to the inner wall of three of the vertical Perspex® cylinders alongside that obtained for a jet impinging on a similarly coated flat vertical plate.

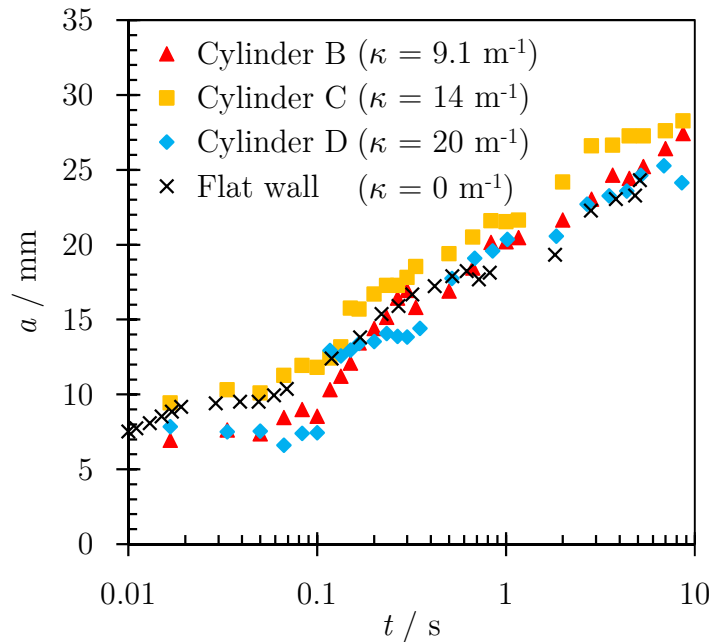


Figure 3.36: Effect of curvature on size of cleaned region for 1.3 mm thick ClearGlide™ layers on vertical cylinders. $d_N = 2 \text{ mm}$, $Q = 1.0 \text{ L min}^{-1}$, $L = 60 \text{ mm}$, no soaking. Note the \log_{10} scale for time. Error bars are omitted for clarity: these are approximately $\pm 2 \text{ mm}$ for a .

All four tests employed a coherent jet, so that the degree of splashing and jet breakup was similar. Under these conditions, wall curvature had little impact on cleaning

dynamics, which is consistent with the observations on flow patterns. Particular care had to be taken with the ClearGlide™ layers as the cleaning rate increased noticeably if they were left in contact with water, which is attributed to water diffusing into the layer and changing its rheology.

Impact of soaking

The effect of soaking is demonstrated in Figure 3.37, which shows that the approach to an asymptote, a_{\max} , was not observed at long times with the soaked layers.

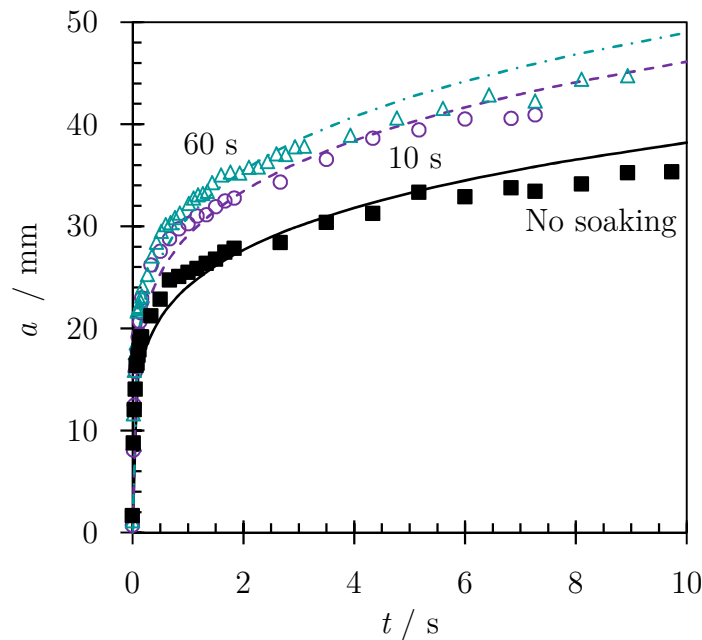


Figure 3.37: Effect of soaking time on the removal of 0.2 mm thick ClearGlide™ layers on flat plates. A thin film of water covered the plate for 0 s (no soaking), 10 s or 60 s. In these tests the target plate was horizontal rather than vertical, and the jet was vertical rather than horizontal, as this allowed the soil to be cleaned immediately after soaking. $d_N = 2$ mm, $Q = 2.0$ L min⁻¹, $L = 245$ mm. Loci show fit to the expression $a = Kt^{0.2}$. Error bars are omitted for clarity: these are approximately ± 2 mm for a .

The fit of all three data sets to the expression $a = Kt^{0.2}$, which Equation 2.53 collapses to when $a_{\max} \rightarrow \infty$, improves with soaking time. The K values (reflecting ease of cleaning) increased from 24.1 mm s^{-0.2} (no soaking) to 29.1 mm s^{-0.2} (after 10 s) and 30.9 mm s^{-0.2} (after 60 s), which is expected from the increased water content of the layer.

The observed change in K (and a_{\max}) on soaking is important for industrial application. Soil in the lower regions of a tank is often contacted with cleaning liquid for extended times as a result of the falling film created by jets striking the wall above. The width of the cleaned region created by the passage of a jet will therefore increase with soaking time and this would suggest that for soaking-sensitive materials the jet would not have to make as many passes over the lower regions of a tank in order to achieve cleaning.

3.5 Conclusions

An experimental investigation of some of the factors influencing impinging water jet cleaning of vessel walls was conducted. The time taken to establish a steady flow pattern is short and can be estimated with some confidence from simple flow theory.

The effect of jet length and wall curvature on the flow pattern and cleaning performance of impinging liquid jets was investigated. Splatter arising from jet breakup and related phenomena was significant for non-coherent jets. The splatter data showed a noticeable transition in behaviour as jet length increased. An existing correlation predicting the onset of splatter showed reasonable agreement with the data but the amount of splatter was not predicted well.

Correcting the jet flow rate for losses due to splatter in existing models gave reasonable predictions for the shape of the radial flow zone. Correcting the flow rate in the film was not able to account for the differences observed in cleaning behaviour, but the splatter correction does provide an engineering estimate of the cleaning rate.

Refraction through the curved walls was found to affect the collection of experimental data from the tests with cylinders. A thin lens model and a geometrical model to correct for refraction were constructed. The geometrical model showed better performance than the thin lens model but was unable to capture all aspects of the problem, so an empirical correlation based on the experimental data was used instead.

The flow patterns generated on curved walls shared several features to those on flat plates, namely the formation of a radial flow zone around the point of impingement followed by a rope after the hydraulic jump. Wall curvature was found to have little effect on the shape of the flow pattern formed unless wraparound occurred. The results obtained were insensitive to wall curvature regardless of cylinder orientation

and were consistent with previous studies on flat plates. It was found that $Z_c \approx R$, showing the effect of gravity on the rope.

The variations in the dimensions of the radial flow zone, Z and R , with wall curvature at higher flow rates were likely to be due to splatter. Splatter was observed visually within the cylinders, but quantitative measurements could not be made. Splatter increased with wall curvature, and more splatter was observed with horizontal cylinders than with vertical ones. Wall curvature also led to other complexities in the flow patterns: in horizontal cylinders, gravity caused drops to be shed from the rope and wraparound flow patterns were observed for larger jet diameters and higher flow rates.

The curvature of the wall had little effect on the RFZ hydrodynamics and cleaning. The cleaning behaviour of ClearGlide™ changed on extended contact with water, which highlighted the need to understand how the soil interacts with the cleaning liquid.

The effect of the shape of the nozzle has not been considered in this work but it is an avenue for further work as the nozzle design is expected to affect jet breakup and splatter. The work in this chapter encompassed steady continuous jets and jets that had started to breakup into a series of droplets. The effect of a continuous jet applied intermittently to a target in short, regular bursts, representing intermediate behaviour between a continuous jet and jet breakup into droplets, is examined in Chapter 5.

Chapter 4

Flow distribution of inclined jets

4.1 Introduction

This chapter examines the liquid flow distribution on a flat surface created by an inclined impinging jet. In many industrial applications of impinging liquid jets such as rotary jet heads and spray balls, the liquid jet impinges at an oblique angle to the target surface. Understanding the liquid flow distribution created by an inclined jet is needed to predict the cleaning behaviour of such devices. Most of the work in the academic literature to date has employed normally impinging jets, where the flow pattern is axisymmetric, whereas many applications involve some degree of inclination. Only short, coherent inclined jets are considered in this work. The effect of jet length and splatter is not considered.

The geometric model of the flow distribution of an inclined jet proposed by Kate *et al.* (2007) has been used by Wang *et al.* (2013b) and Bhagat *et al.* (2017). They coupled it with the Wilson *et al.* (2012) hydrodynamic model to predict the shape of the hydraulic jump formed when a jet impinges on a vertical target. Bhagat and Wilson (2016) followed a similar analysis, using the Kate *et al.* (2007) flow distribution coupled with their hydrodynamic model. In all the cases above, the jets were inclined only in the vertical plane. A geometric transformation is developed here to extend this approach to include inclination in the horizontal plane, to enable predictions to be made for jets inclined in both the horizontal and vertical planes. Particular attention is paid to targets where gravity is active, *i.e.* the liquid drains away from the impingement point rather than collecting as a slow moving film (the standard configuration in most cases in the fluid mechanics literature), as this arises in many practical applications.

Three different flow distribution models are developed as an alternative to the Kate *et al.* (2007) flow distribution for inclined jets, hereafter referred to as KM. The models are compared using three different types of experimental data. The shape of the hydraulic jump formed is compared with the model predictions. Separate measurements of the liquid flow are also attempted. There are several challenges in

measuring the hydraulic jump for inclined jets, as gravity can suppress a jump while the liquid films generated are very thin and fast moving. An alternative approach is therefore employed, inferring the flow distribution from the cleaning of a soft solid soil layer, NIVEA[®] cream. The cream was chosen for its reproducibility so it could be used as a reliable probe to investigate the jet behaviour. Its cleaning behaviour is characterised using a jet impinging normally to the target, and the patterns produced by inclined jets are used to estimate the local liquid flow distribution in an inverse calculation.

Some of the experimental data reported in Section 4.4.1 were collected by MEng students Panna Chauhan and Jason Georgiou as part of their Chemical Engineering Tripos Part IIB research project, co-supervised by the author.

4.2 Models

4.2.1 Geometric transformation

Flat surfaces and coherent cylindrical jets are considered. An inclined jet can be described by its angle of impingement in the vertical plane, ϕ , measured from the upward vertical, and its angle of impingement in the horizontal plane, χ . A schematic is shown in Figure 4.1.

The inclination and loss of symmetry result in a non-uniform distribution of liquid in different directions on the target plane. The direction of highest local flow is termed the principal flow direction. The region with higher local flow is termed the major flow region and the region with lower local flow is termed the minor flow region. The jet angles ϕ and χ can be combined to give an effective jet angle, ϕ^* . A schematic of the construction involved is shown in Figure 4.2.

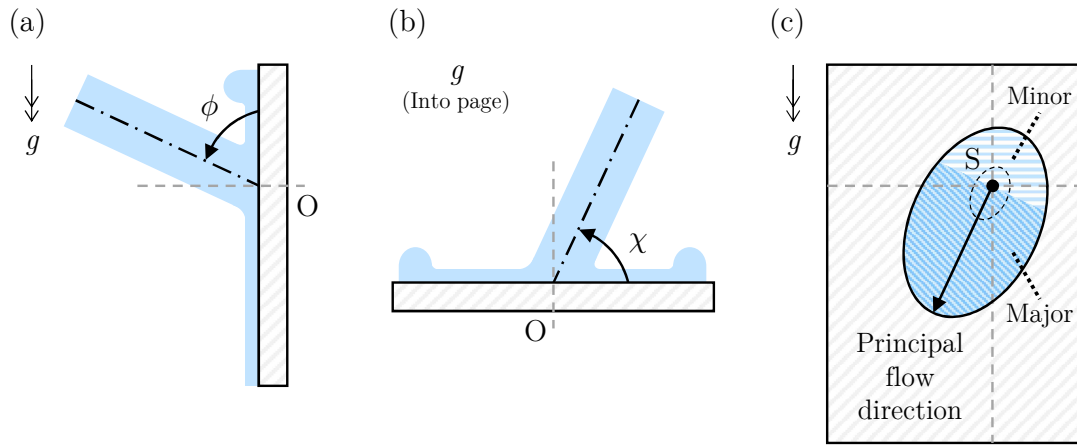


Figure 4.1: Schematics of the (a) side and (b) plan views of an inclined jet, and (c) the resulting flow pattern formed, viewed from the dry side of the target. In (c), the solid locus denotes the location of the hydraulic jump, the dashed locus denotes the footprint of the jet, the arrow shows the principal flow direction and shading is used to indicate the major and minor flow regions. O is the point of impingement of the axis of the jet and S is the source of the flow.

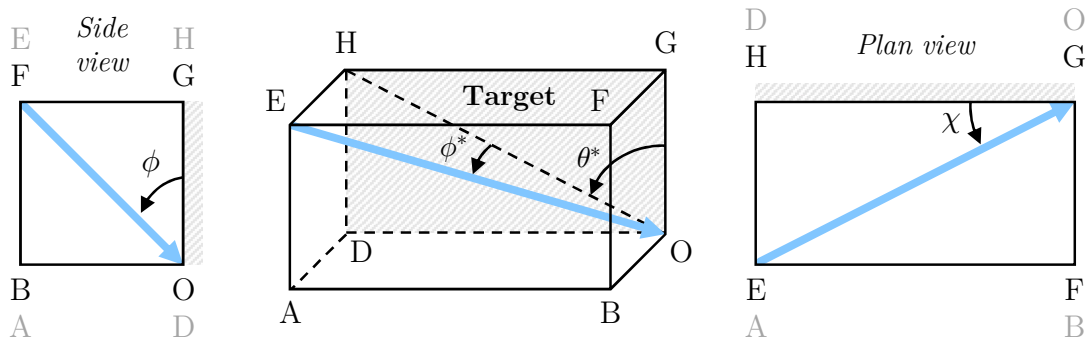


Figure 4.2: Construction showing the effective jet angle ϕ^* as a combination of the angles ϕ and χ for a jet travelling from E and impinging on the vertical target ODGH at point O.

From the construction in Figure 4.2,

$$HD = \frac{EH}{\tan \phi} \quad (4.1)$$

$$HG = \frac{EH}{\tan \chi} \quad (4.2)$$

$$\tan \phi^* = \frac{EH}{OH} = \frac{EH}{\sqrt{HD^2 + HG^2}} \quad (4.3)$$

$$\tan \theta^* = \frac{HG}{HD} \quad (4.4)$$

The effective jet angle is thus given by

$$\tan \phi^* = \frac{1}{\sqrt{\frac{1}{\tan^2 \phi} + \frac{1}{\tan^2 \chi}}} \quad (4.5)$$

and the azimuthal angle of the projection of the jet onto the target, θ^* , is

$$\tan \theta^* = \frac{\tan \phi}{\tan \chi} \quad (4.6)$$

The effective jet angle, ϕ^* , is the angle of projection of the jet onto the target. To indicate the direction of the jet, an overall jet angle, ϕ_{overall}^* , is defined as

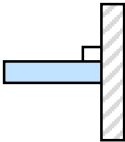
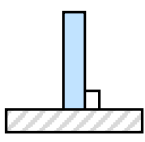
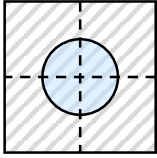
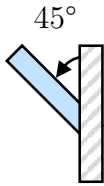
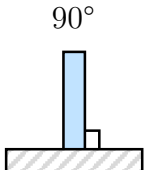
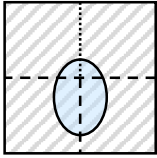
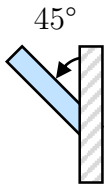
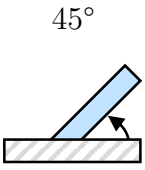
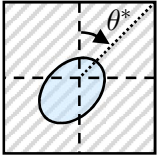
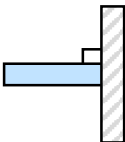
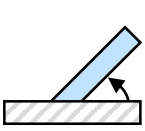
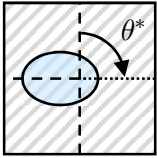
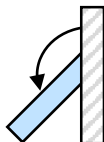
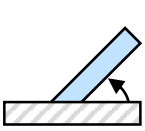
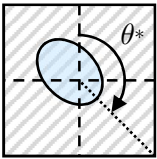
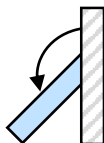
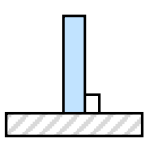
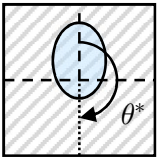
$$\phi_{\text{overall}}^* = \begin{cases} \phi^* & \phi \leq 90^\circ \\ 180^\circ - \phi^* & \phi > 90^\circ \end{cases} \quad (4.7a)$$

$$\phi > 90^\circ \quad (4.7b)$$

such that $\phi_{\text{overall}}^* < 90^\circ$ indicates a jet pointing downwards or sideways while $\phi_{\text{overall}}^* > 90^\circ$ indicates a jet pointing upwards. A normally impinging jet has $\phi_{\text{overall}}^* = 90^\circ$.

Azimuthal angles θ and θ^* are measured clockwise when viewed from the dry side of the target. Table 4.1 lists examples of combinations of jet angles ϕ and χ used in the tests and the resulting ϕ^* , ϕ_{overall}^* and θ^* values.

Table 4.1: Jet angles ϕ and χ and their resulting ϕ^* , ϕ^*_{overall} and θ^* values, ordered by increasing θ^* values.

ϕ <i>Side view</i>	χ <i>Plan view</i>	<i>View from the dry side</i>	ϕ^* (Eq. 4.5)	ϕ^*_{overall} (Eq. 4.7)	θ^* (Eq. 4.6)
90° 	90° 		90°	90°	-
45° 	90° 		45°	45°	0°
45° 	45° 		35.3°	35.3°	45°
90° 	45° 		45°	45°	90°
135° 	45° 		35.3°	144.7°	135°
135° 	90° 		45°	135°	180°

4.2.2 Flow distribution

Application of a hydrodynamic model to inclined jets requires a flow distribution model. Figure 4.3 shows an inclined jet impinging on a target surface. Only jets with circular cross-section are considered in this work.

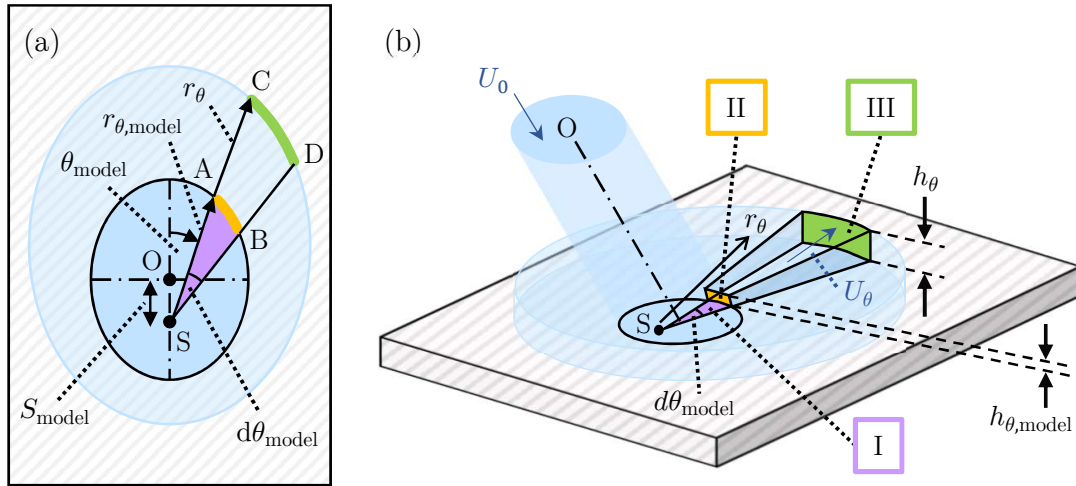


Figure 4.3: Schematic of an inclined jet with circular cross-section impinging on a target surface: (a) plan view and (b) angled view. O is the axis of the circular jet. The liquid flowing towards segment SAB marked in lilac (I) is assumed to leave radially across the boundary of the footprint region through the area marked in orange (II) of arc AB and height $h_{\theta,\text{model}}$, and thereafter through the area marked in green (III) of arc CD and height h_{θ} .

When a jet with circular cross-section impinges on a target surface at an angle, the footprint of the jet on the target surface is elliptical. This is based on the geometry of the system: when a horizontal plane cuts an inclined cylinder, the intersection takes the form of an ellipse. A flow distribution model quantifies the distribution of the liquid from the jet in each azimuthal direction on the target surface.

It is convenient to relate the flow pattern to a stagnation point, which acts as a source, S . The liquid moves radially away from S . S_{model} is the distance from S to the axis of the jet, O . For a given azimuthal direction, θ_{model} , the increment of volumetric flow rate, dQ , in direction θ_{model} to $\theta_{\text{model}} + d\theta_{\text{model}}$ is given by

$$\begin{aligned}
dQ &= \underbrace{\frac{1}{2} U_{0,\text{model}} r_{\theta,\text{model}}^2 d\theta_{\text{model}}}_{\text{I}} = \underbrace{U_0 r_{\theta,\text{model}} h_{\theta,\text{model}} d\theta_{\text{model}}}_{\text{II}} \\
&= \underbrace{U_{\theta} h_{\theta} r_{\theta} d\theta_{\text{model}}}_{\text{III}} \tag{4.8}
\end{aligned}$$

Term I is the source of the volumetric flow rate for $d\theta_{\text{model}}$, here a segment of the elliptical footprint of the jet, where $U_{0,\text{model}}$ is the component of the jet velocity normal to the segment.

The liquid flowing towards the segment is assumed to leave radially as a film across the boundary of the footprint region with volumetric flow rate given by term II. The boundary of the footprint region is at radial distance $r_{\theta,\text{model}}$ from S and the liquid film is of thickness $h_{\theta,\text{model}}$. It is assumed that the mean velocity in the liquid film is U_0 , *i.e.* there are no energy losses in the footprint due to the change in direction or wall friction. The inaccuracy introduced by this assumption is difficult to quantify without detailed numerical simulations of the free surface flow problem (Baghel *et al.*, 2020).

The liquid film continues to flow radially outwards and term III is the volumetric flow rate at radial distance r_{θ} from S, where U_{θ} and h_{θ} are the local velocity and thickness of the liquid film, respectively.

Equating terms I and II gives

$$h_{\theta,\text{model}} = \frac{1}{2} \frac{U_{0,\text{model}}}{U_0} r_{\theta,\text{model}} \tag{4.9}$$

Equating terms II and III, and substituting in the expression for $h_{\theta,\text{model}}$ from Equation 4.9 gives

$$U_{\theta} h_{\theta} r_{\theta} = \frac{1}{2} r_{\theta,\text{model}}^2 U_{0,\text{model}} \tag{4.10}$$

Assuming that the flow is radial (no azimuthal leakage), dQ is constant: let $U_\theta h_\theta r_\theta = C_{\theta,\text{model}}$,

$$C_{\theta,\text{model}} = U_\theta h_\theta r_\theta = \frac{1}{2} r_{\theta,\text{model}}^2 U_{0,\text{model}} \quad (4.11)$$

Equation 4.11 is the flow distribution term to be substituted into the equations for the hydrodynamic model.

For the Wilson *et al.* (2012) hydrodynamic model, the momentum flow rate per unit width in the liquid film (Equation 2.3) can be written as

$$M_\theta = \frac{6}{5} \rho U_\theta^2 h_\theta = \frac{6}{5} \frac{\rho C_{\theta,\text{model}} U_\theta}{r_\theta} \quad (4.12)$$

The momentum balance on a streamline (Equation 2.4) is now

$$\begin{aligned} \frac{d}{dr_\theta} \left(\frac{6}{5} \rho U_\theta^2 h_\theta r_\theta \right) &= - \frac{3 \mu U_\theta r_\theta}{h_\theta} - r_\theta h_\theta \rho g \cos \theta \\ \frac{d}{dr_\theta} \left(\frac{6}{5} \rho U_\theta C_{\theta,\text{model}} \right) &= - \frac{3 \mu U_\theta^2 r_\theta^2}{C_{\theta,\text{model}}} - \frac{C_{\theta,\text{model}}}{U_\theta} \rho g \cos \theta \\ \frac{dU_\theta}{dr_\theta} &= \frac{5}{2} \frac{\mu}{\rho} \frac{r_\theta^2 U_\theta^2}{C_{\theta,\text{model}}^2} - \frac{5}{6} \frac{\rho g \cos \theta}{U_\theta} \end{aligned} \quad (4.13)$$

Ignoring the gravity term so that an analytical solution can be obtained, Equation 4.13 gives

$$\int_{U_0}^{U_\theta} \frac{1}{U_\theta^2} dU_\theta = - \frac{5}{2} \frac{\mu}{\rho} \frac{1}{C_{\theta,\text{model}}^2} \int_{r_{\theta,\text{model}}}^{r_\theta} r_\theta^2 dr_\theta \quad (4.14)$$

which yields

$$\frac{1}{U_\theta} - \frac{1}{U_0} = \frac{5}{6} \frac{\mu}{\rho} \frac{1}{C_{\theta,\text{model}}^2} \left(r_\theta^3 - r_{\theta,\text{model}}^3 \right) \quad (4.15)$$

At the location of the hydraulic jump, $R_{\theta,\text{jump}}$, assuming $\frac{1}{U_\theta} \gg \frac{1}{U_0}$ and $r_\theta^3 \gg r_{\theta,\text{model}}^3$, the mean velocity in the liquid film, $U_{\theta,\text{jump}}$, is given by

$$U_{\theta,\text{jump}} = \frac{6}{5} \frac{\rho}{\mu} \frac{C_{\theta,\text{model}}^2}{R_{\theta,\text{jump}}^3} \quad (4.16)$$

The hydraulic jump occurs when the termination criterion $M_\theta = \gamma(1 - \cos \beta)$ (Equation 2.12) is met. Equation 4.12 then gives

$$\frac{6}{5} \frac{\rho C_{\theta,\text{model}} U_{\theta,\text{jump}}}{R_{\theta,\text{jump}}} = \gamma(1 - \cos \beta) \quad (4.17)$$

This ignores any additional curvature in the jump arising from the non-uniform flow distribution.

Combining Equations 4.16 and 4.17 gives the estimated location of the hydraulic jump for an inclined jet for any flow distribution model

$$R_{\theta,\text{jump}} = \left[\frac{36}{25} \frac{\rho^2 C_{\theta,\text{model}}^3}{\mu \gamma (1 - \cos \beta)} \right]^{1/4} \quad (4.18)$$

Equation 4.13 can be integrated numerically to obtain $U_\theta = f(r_\theta)$ and combined with the termination criterion in Equation 4.17 to obtain a prediction for the location of the hydraulic jump with the gravity term in Equation 4.13 included. The subscript θ has been used to emphasise that the parameters and location of the hydraulic jump vary with azimuthal angle θ .

Three different flow distribution models were developed as an alternative to the KM, the circular, moving stagnation point and changing ellipse models. The parameters for each of the flow distribution models are summarised in Table 4.2 and the models are discussed in the following sections.

Table 4.2: Parameters in the flow distribution models.

Model	$r_{\theta, \text{model}}$	θ_{model}	$U_{0, \text{model}}$	$h_{\theta, \text{model}}$	$C_{\theta, \text{model}}$
Kate <i>et al.</i> (2007) (KM)	r_k	θ	$U_0 \sin \phi^*$	$\frac{1}{2} r_k \sin \phi^*$	$\frac{1}{2} r_k^2 U_0 \sin \phi^*$
Circular	r_c	θ_c	U_0	$\frac{1}{2} r_c$	$\frac{1}{2} r_c^2 U_0$
Moving stagnation point	r_λ	θ_λ	$U_0 \sin \phi^*$	$\frac{1}{2} r_\lambda \sin \phi^*$	$\frac{1}{2} r_\lambda^2 U_0 \sin \phi^*$
Changing ellipse	r_ω	θ	$U_0 \sin \phi'$	$\frac{1}{2} r_\omega \sin \phi'$	$\frac{1}{2} r_\omega^2 U_0 \sin \phi'$

The location of S varies in each of the flow distribution models. Its location affects $r_{\theta, \text{model}}$, and this needs to be evaluated for each case.

Kate et al. (2007) model (KM): $r_{\theta, \text{model}} = r_k$

The KM stagnation point is located at the focus of the elliptical footprint of the jet on the target surface. A schematic is shown in Figure 4.4.

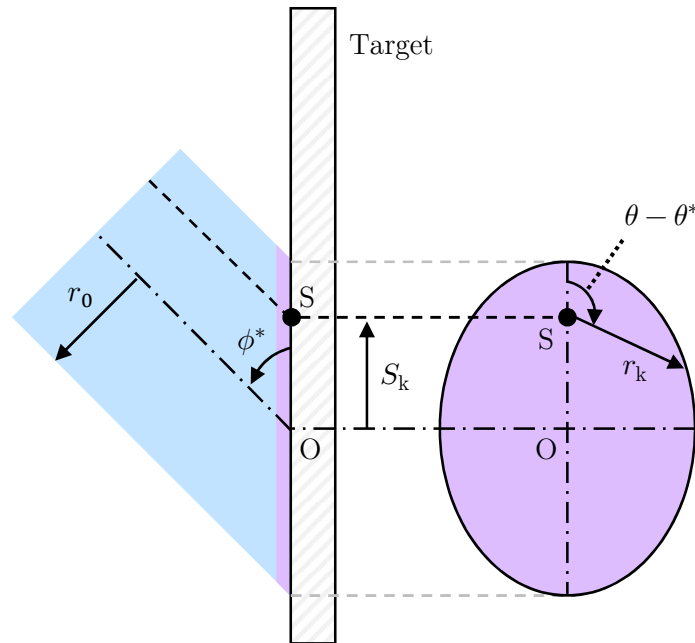


Figure 4.4: Schematic of the Kate *et al.* (2007) model with the geometric transformation. O is the axis of the jet and S is the source.

With the geometric transformation in Section 4.2.1, Equation 2.35 becomes

$$r_k = r_0 \left(\frac{\sin \phi^*}{1 + \cos \phi^* \cos (\theta - \theta^*)} \right) \quad (4.19)$$

and Equation 2.36 becomes

$$|S_k| = r_0 \cot \phi^* \quad (4.20)$$

Circular model: $r_{\theta, \text{model}} = r_c$

The circular flow distribution model is based on the KM but the source plane is taken to be a cross-section of the jet instead of the elliptical jet footprint. A schematic is shown in Figure 4.5.

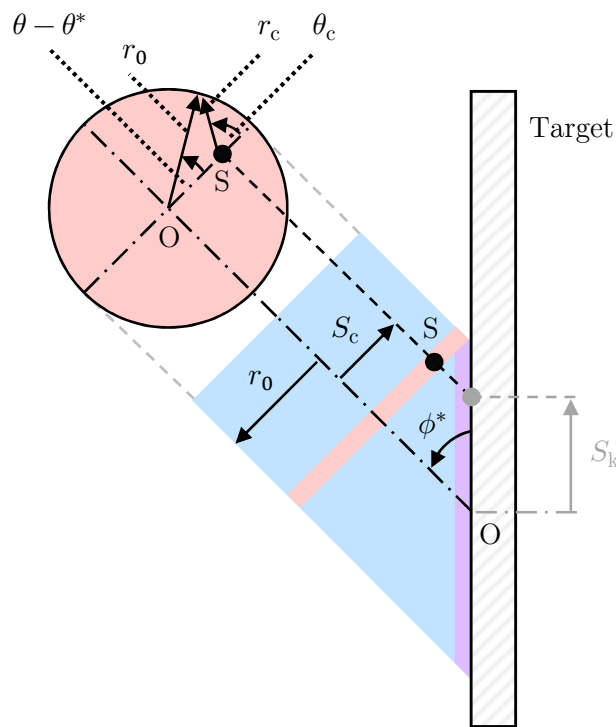


Figure 4.5: Schematic of the circular flow distribution model. O is the axis of the jet and S is the source. S_k (as before) is shown.

From the geometry in Figure 4.5,

$$\sin \phi^* = \frac{S_c}{S_k} \quad (4.21)$$

Substituting in the expression for S_k from Equation 4.20 into Equation 4.21 gives the distance of the source from the axis of the jet

$$|S_c| = r_0 \cos \phi^* \quad (4.22)$$

r_c can be found using the cosine rule

$$\begin{aligned} r_c^2 &= r_0^2 + (r_0 \cos \phi^*)^2 - 2(r_0)(r_0 \cos \phi^*) \cos(\theta - \theta^*) \\ r_c &= r_0 \sqrt{1 + \cos^2 \phi^* - 2 \cos \phi^* \cos(\theta - \theta^*)} \end{aligned} \quad (4.23)$$

θ_c can also be found by using the cosine rule again and substituting in the expression for r_c from Equation 4.23, giving

$$\begin{aligned} r_0^2 &= r_c^2 + (r_0 \cos \phi^*)^2 - 2(r_c)(r_0 \cos \phi^*) \cos(\pi - \theta_c) \\ r_0^2 &= r_c^2 + (r_0 \cos \phi^*)^2 + 2(r_c)(r_0 \cos \phi^*) \cos(\theta_c) \\ \cos \theta_c &= \frac{r_0^2 - r_c^2 - (r_0 \cos \phi^*)^2}{2(r_c)(r_0 \cos \phi^*)} \\ \cos \theta_c &= \frac{\cos(\theta - \theta^*) - \cos \phi^*}{\sqrt{1 + \cos^2 \phi^* - 2 \cos \phi^* \cos(\theta - \theta^*)}} \end{aligned} \quad (4.24)$$

Moving stagnation point model: $r_{\theta, \text{model}} = r_\lambda$

The moving stagnation point flow distribution model retains the KM impingement ellipse as the source plane. The source is shifted between O and the focus of the ellipse (the KM source) by a factor λ to give the new source at distance S_λ from O. This is an empirical attempt to capture the deviation from the geometrical result arising from energy losses. A schematic is shown in Figure 4.6.

The distance of the source from O, S_λ , is given by

$$|S_\lambda| = \lambda |S_k| = \lambda r_0 \cot \phi^* \quad (4.25)$$

The factor λ lies in the range $0 \leq \lambda \leq 1$ where $\lambda = 0$ gives a source coincident with O and $\lambda = 1$ recovers the KM result.

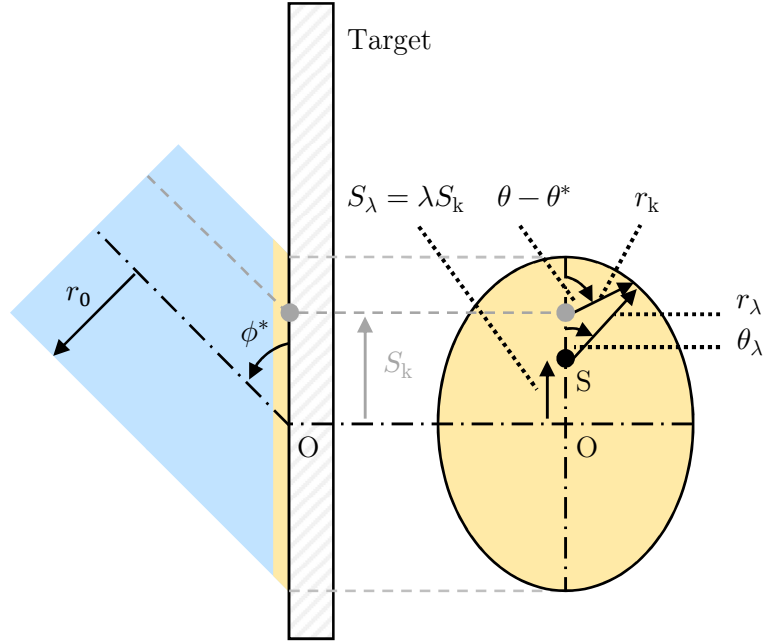


Figure 4.6: Schematic of the moving stagnation point model. O is the axis of the jet and S is the source. S_k (as before) is shown.

r_λ can be found using the cosine rule and substituting in the expressions for r_k and S_k from Equations 4.19 and 4.20, respectively, yielding

$$r_\lambda^2 = r_k^2 + [(1 - \lambda) S_k]^2 - 2(r_k)[(1 - \lambda) S_k] \cos[\pi - (\theta - \theta^*)]$$

$$r_\lambda = \sqrt{r_k^2 + [(1 - \lambda) S_k]^2 + 2(r_k)[(1 - \lambda) S_k] \cos(\theta - \theta^*)}$$

$$r_\lambda = r_0 \sqrt{\frac{\sin^2 \phi^*}{[1 + \cos \phi^* \cos(\theta - \theta^*)]^2} + (1 - \lambda)^2 \cot^2 \phi^* + \frac{2(1 - \lambda) \cos \phi^* \cos(\theta - \theta^*)}{1 + \cos \phi^* \cos(\theta - \theta^*)}} \quad (4.26)$$

θ_λ can also be found by using the cosine rule again. Substituting in the expressions for r_k , S_k and r_λ from Equations 4.19, 4.20 and 4.26, respectively, gives

$$r_k^2 = r_\lambda^2 + [(1 - \lambda) S_k]^2 - 2(r_\lambda)[(1 - \lambda) S_k] \cos \theta_\lambda$$

$$\cos \theta_\lambda = \frac{r_\lambda^2 + [(1 - \lambda) S_k]^2 - r_k^2}{2(r_\lambda)[(1 - \lambda) S_k]}$$

$$\cos \theta_\lambda = \frac{(1 - \lambda) \cot \phi^* (1 + \cos \phi^* \cos(\theta - \theta^*)) + \sin \phi^* \cos(\theta - \theta^*)}{\sqrt{\frac{\sin^2 \phi^* + (1 - \lambda)^2 \cot^2 \phi^* [1 + \cos \phi^* \cos(\theta - \theta^*)]^2}{+ 2(1 - \lambda) \cos \phi^* \cos(\theta - \theta^*) [1 + \cos \phi^* \cos(\theta - \theta^*)]}}} \quad (4.27)$$

Changing ellipse model: $r_{\theta, \text{model}} = r_{\omega}$

This model takes the source to be the focus of a shifted impingement ellipse, corresponding to the footprint of a jet with a modified effective jet angle, ϕ' . The distance of the source from O is S_{ω} . A schematic is shown in Figure 4.7.

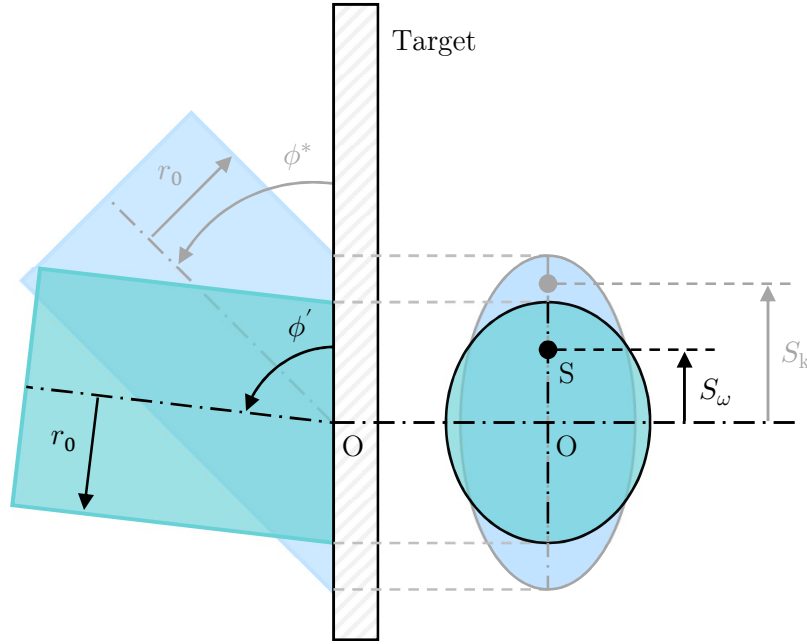


Figure 4.7: Schematic of the changing ellipse model showing the true impingement angle, ϕ^* , and the modified angle, ϕ' , with the corresponding changes in footprint shape and source location. O is the axis of the jet and S is the source. S_k (as before) is shown.

The distance of the source from O, S_{ω} , is given by

$$|S_{\omega}| = \omega |S_k| = \omega r_0 \cot \phi^* \quad (4.28)$$

The factor ω lies in the range $0 \leq \omega \leq 1$. When $\omega = 0$, the shifted impingement ellipse is a circle and S and O are coincident (the modified angle is $\phi' = 90^\circ$, *i.e.* a normally impinging jet). When $\omega = 1$, the KM result is recovered.

S_{ω} is the focus of the impingement ellipse of a jet with a modified effective jet angle, ϕ' , giving

$$|S_{\omega}| = r_0 \cot \phi' \quad (4.29)$$

Combining Equations 4.28 and 4.29 gives the modified effective jet angle

$$r_0 \cot \phi' = \omega r_0 \cot \phi^*$$

$$\tan \phi' = \frac{\tan \phi^*}{\omega} \quad (4.30)$$

ϕ' can then be used in Equation 4.19 in place of ϕ^* , giving

$$r_\omega = r_0 \left(\frac{\sin \phi'}{1 + \cos \phi' \cos (\theta - \theta^*)} \right) \quad (4.31)$$

To account for the direction of the jet, the overall modified jet angle, ϕ'_{overall} , is defined as

$$\phi'_{\text{overall}} = \begin{cases} \phi' & \phi \leq 90^\circ \\ 180^\circ - \phi' & \phi > 90^\circ \end{cases} \quad (4.32a)$$

$$(4.32b)$$

such that $\phi'_{\text{overall}} < 90^\circ$ indicates a modified jet pointing downwards or sideways while $\phi'_{\text{overall}} > 90^\circ$ indicates a modified jet pointing upwards. A normally impinging jet has $\phi'_{\text{overall}} = 90^\circ$.

4.3 Methods and materials

4.3.1 Hydrodynamic tests

Apparatus

Hydrodynamic tests with inclined jets were performed using the apparatus shown in Figure 4.8. The apparatus was adapted from that used by Wang *et al.* (2013a).

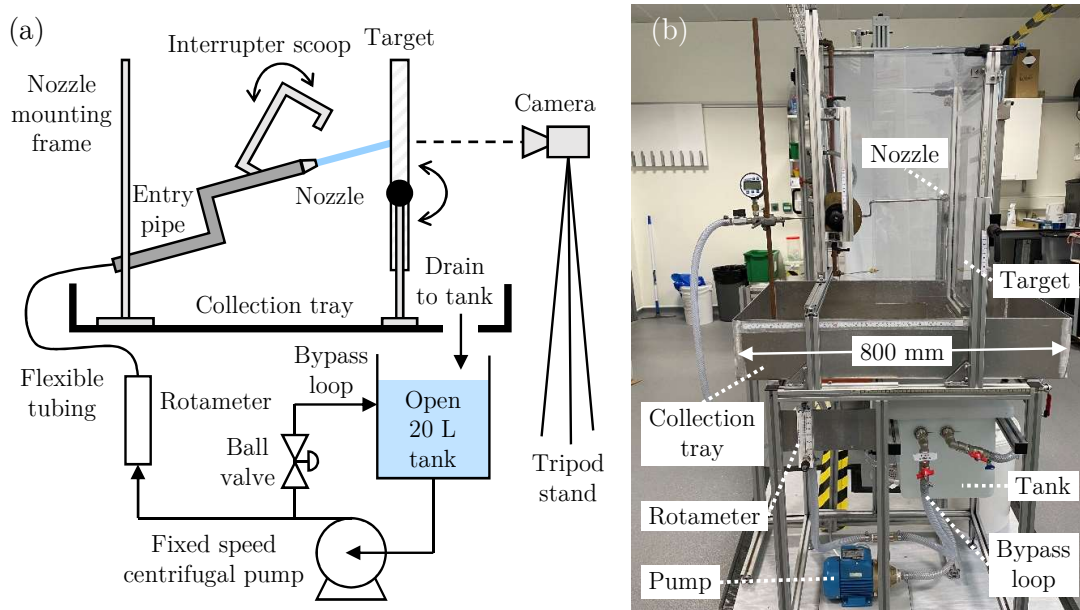


Figure 4.8: (a) Schematic and (b) photograph of the inclined jet apparatus.

A fixed speed centrifugal pump (Clarke CEB103 230v 7230327, Clarke International, UK) was used to pump softened tap water at room temperature (20-22°C) from an open 20 L tank through either a bypass loop back to the tank or through a rotameter towards the nozzle. A stainless steel nozzle with a 56° convergent entry and bore diameter $d_N = 2$ mm was used. The nozzle was preceded by a 4 mm inner diameter stainless steel pipe of 685 mm total length with two 90° bends. The stainless steel pipe was mounted on a frame that enabled the jet angles in the horizontal and vertical planes to be set. The jet angles were measured with a digital spirit level and verified against photographs of the jet taken from the top and side with Logitech Brio 4K webcams.

The jet length was set at 50 mm to ensure that the jet was coherent. For the flow rates studied, the jet did not droop. The volumetric flow rate through the nozzle was set by varying the flow through the bypass loop. The flow rate was read from the rotameter, which had been calibrated separately. Flow rates in the range of 1.0-3.0 L min⁻¹ were used ($U_0 = 5.3$ -15.9 m s⁻¹, $Re = 10\,600$ -31 800, $We = 770$ -6 900). Under these conditions the jet dynamics lie in the Rayleigh breakup and first wind-induced regimes (Lin and Reitz, 1998) (Table 2.2) with an expected breakup length of 140-290 mm (Grant and Middleman, 1966) (Equation 2.30).

An interrupter scoop was placed between the nozzle and the target to divert the jet away from the target while the pump was allowed to run for at least 30 s after being turned on to ensure that a stable jet had formed. A transparent 360 × 600 × 5 mm (width × height × thickness) flat Perspex[®] plate was used as the target, mounted vertically. Graticule tape was placed on the dry side of the target to provide a length calibration for image processing. Photographs and videos of the flow patterns formed were taken from the dry side of the target with a Sony Cyber-shot RX100V digital camera aligned with the point of impingement of the jet. Videos were recorded at 1000 frames per second. Illumination was provided by an 800 W halogen lamp (Redhead PhotonBeam 800, Photon Beard, UK) and two light-emitting diode (LED) standing lamps (Neewer 1500W Photography Studio Softbox Lighting Kit, Shenzhen Neewer Technology, China).

The combinations of jets angles and the corresponding values of ϕ^* , ϕ_{overall}^* and θ^* , and the flow rates used in the hydrodynamic tests are summarised in Tables 4.3 and 4.4, respectively.

Table 4.3: Combinations of jet angles used in the inclined jet hydrodynamic tests and the corresponding ϕ^* , ϕ_{overall}^* and θ^* values.

χ	45°	60°	75°	90°	45°	60°	75°	90°	45°	60°	75°	90°
ϕ	$\phi^*/^\circ$ (Equation 4.5)				$\phi_{\text{overall}}^*/^\circ$ (Equation 4.7)				$\theta^*/^\circ$ (Equation 4.6)			
45°	35.3	-	-	45	35.3	-	-	45	45	-	-	0
60°	-	50.8	57.5	60	-	50.8	57.5	60	-	45	24.9	0
75°	44	57.5	69.2	75	44	57.5	69.2	75	75	65.1	45	0
90°	45	60	75	90	45	60	75	90	90	90	90	-
105°	44	57.5	69.2	75	136	122.5	110.8	105	105	114.9	135	180
120°	-	50.8	57.5	60	-	129.2	122.5	120	-	135	155.1	180
135°	35.3	-	-	45	144.7	-	-	135	135	-	-	180

Table 4.4: Flow rates used in the inclined jet hydrodynamic tests.

ϕ	χ	45°	60°	75°	90°
		$Q / \text{L min}^{-1}$			
45°	45°	1.0, 1.5, 2.0, 2.5, 3.0	-	-	1.0, 1.5, 2.0, 2.5, 3.0
60°	45°	-	1.0, 1.5, 2.0, 2.5, 3.0	2.0	1.0, 2.0, 3.0
75°	45°	2.0	2.0	1.0, 2.0, 3.0	2.0
90°	45°	1.0, 2.0, 3.0	1.0, 2.0, 3.0	1.0, 2.0, 3.0	1.0, 1.5, 2.0, 2.5, 3.0
105°	45°	2.0	2.0	1.0, 2.0, 3.0	2.0
120°	45°	-	1.0, 1.5, 2.0, 2.5, 3.0	1.0, 2.0, 3.0	1.0, 2.0, 3.0
135°	45°	1.0, 1.5, 2.0	-	-	1.0, 1.5, 2.0, 2.5, 3.0

Flow patterns and image analysis

Figure 4.9 shows an example of the flow pattern for an inclined jet with the initial formation of the hydraulic jump before the rope and falling film had fully developed (Figure 4.9(a)) and where a steady state had been reached (Figure 4.9(b)). Scripts written in MATLAB® (MathWorks, USA) were used to split the videos into individual image frames and extract the location of the hydraulic jump. The location of the hydraulic jump was extracted for both initial formation and steady state images to provide insight into the effect of the dynamics of the rope and falling film on the shape of the hydraulic jump.

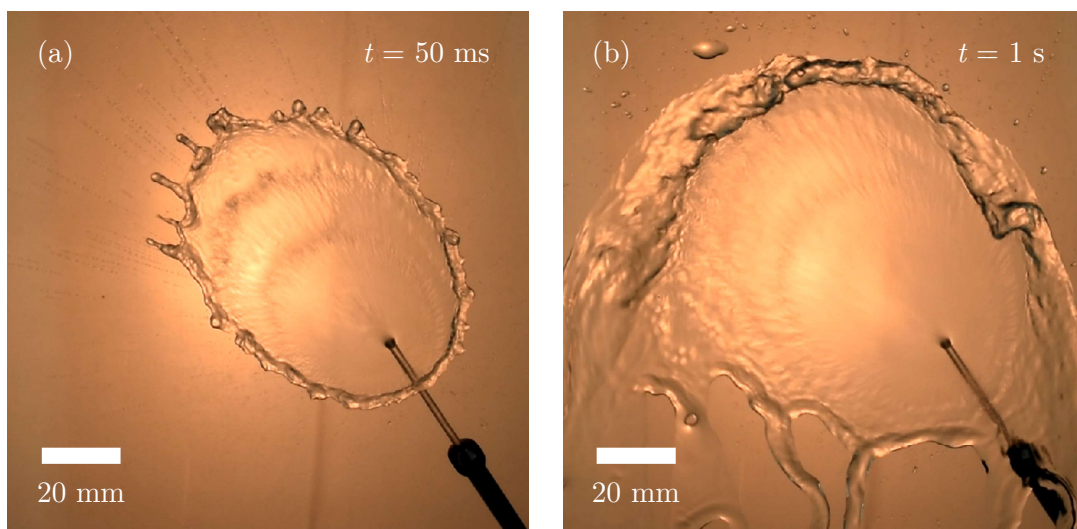


Figure 4.9: Image frames of the (a) initial flow pattern, before the formation of a steady rope and (b) steady state flow pattern for an inclined jet, at $t = 50$ ms and $t = 1$ s, respectively ($Q = 2.0$ L min^{-1} , $\phi = 120^\circ$, $\chi = 60^\circ$, $\phi_{\text{overall}}^* = 129.2^\circ$).

At steady state, the location of the hydraulic jump could only be extracted above the point of impingement due to the falling film below (Figure 4.9(b)). The rope was often unsteady, causing random wetting and de-wetting of the target and shedding of droplets.

All tests were repeated twice and the average values are reported. The main source of error lay in determining the location of the hydraulic jump by eye during image analysis due to refraction of light through the liquid, judged to give an error of ± 2 mm. The rotameter used had been calibrated separately and had divisions of 0.1 L min^{-1} , giving an error of ± 0.05 L min^{-1} .

4.3.2 Liquid flow rate measurements

The impinging jet apparatus described in Section 3.2.1 was used to measure the liquid flow rate. A $360 \times 600 \times 5$ mm (width \times height \times thickness) flat vertical Perspex[®] plate was used as the target. A reservoir of internal dimensions $290 \times 210 \times 55$ mm (width \times height \times depth) was located at the base of the target. A schematic is shown in Figure 4.10. The angle and location of the jet were kept fixed in each test while the target plate was lowered by a known distance, thus changing the amount of liquid collected in the reservoir as any liquid that flowed over the top of the plate was not collected. The reservoir was fitted with a slotted roof so that any droplets caused by the splashing as the liquid flows over the top of the target plate were unlikely to be collected.

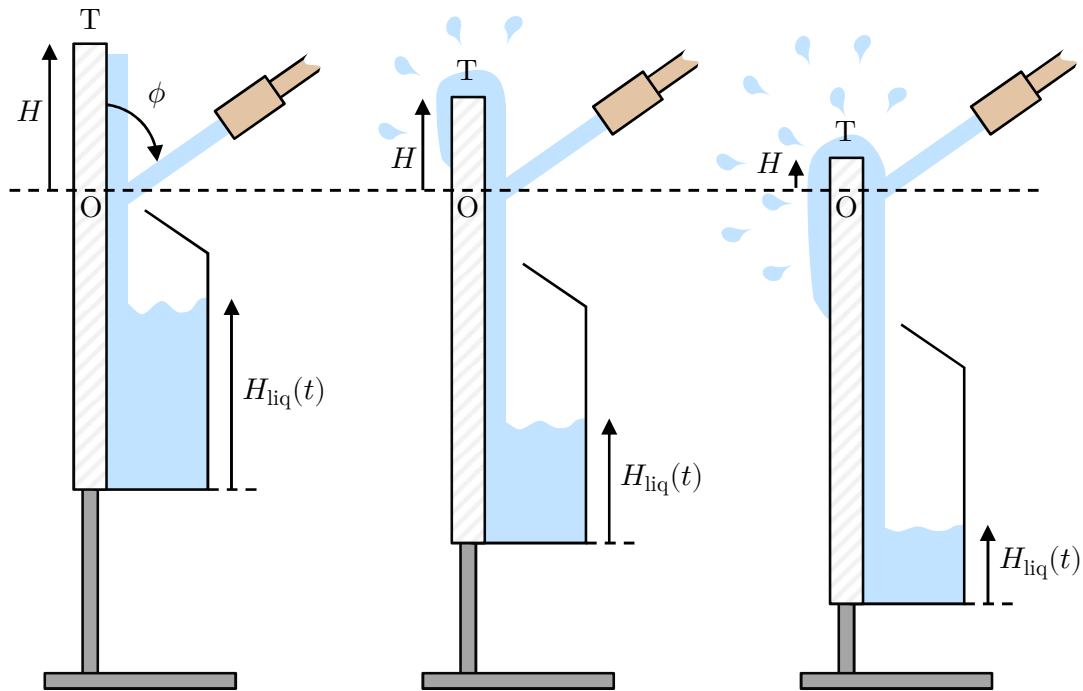


Figure 4.10: Schematic of the liquid flow measurement system showing separate tests with the target plate and reservoir lowered. O is the axis of the jet, T the top of the target plate, H the height of T above O, and $H_{\text{liq}}(t)$ the height of the liquid in the reservoir.

Figure 4.11(a) shows a photograph of the setup. Tests were carried out for jets of angles $\phi = 60^\circ, 90^\circ, 120^\circ$ and 135° with $d_N = 2$ mm, $Q = 2.0 \text{ L min}^{-1}$, $\chi = 90^\circ$ and a jet length of 60 mm to ensure that the jet was coherent. The tests with a normally impinging jet allowed the accuracy of the technique to be assessed. The average liquid flow rate, $Q_{\text{collected,expt}}$, was determined by the change in the height of the

liquid in the reservoir, H_{liq} , over time. The height of the top of the plate (T) above the point of jet impingement (O), H , was also measured. $Q_{\text{collected,expt}}$ was compared to the volumetric flow rate predicted by the model, $Q_{\text{collected,model}}$. A schematic is shown in Figure 4.11(b).

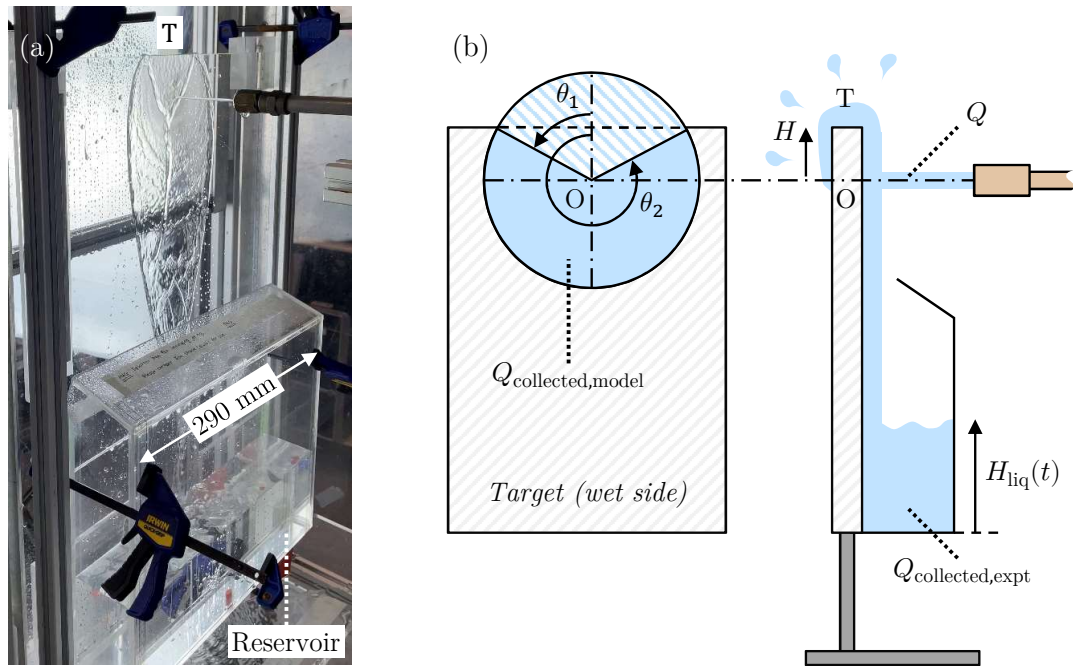


Figure 4.11: Photograph of the experimental setup and (b) schematic showing the liquid flow. $Q_{\text{collected,model}}$ is calculated between azimuthal angles θ_1 and θ_2 . θ_1 and θ_2 are determined by H .

4.3.3 Cleaning tests

Apparatus

Modifications were made to the impinging jet apparatus described in Section 3.2.1 for the cleaning tests with inclined jets. A schematic is shown in Figure 4.12.

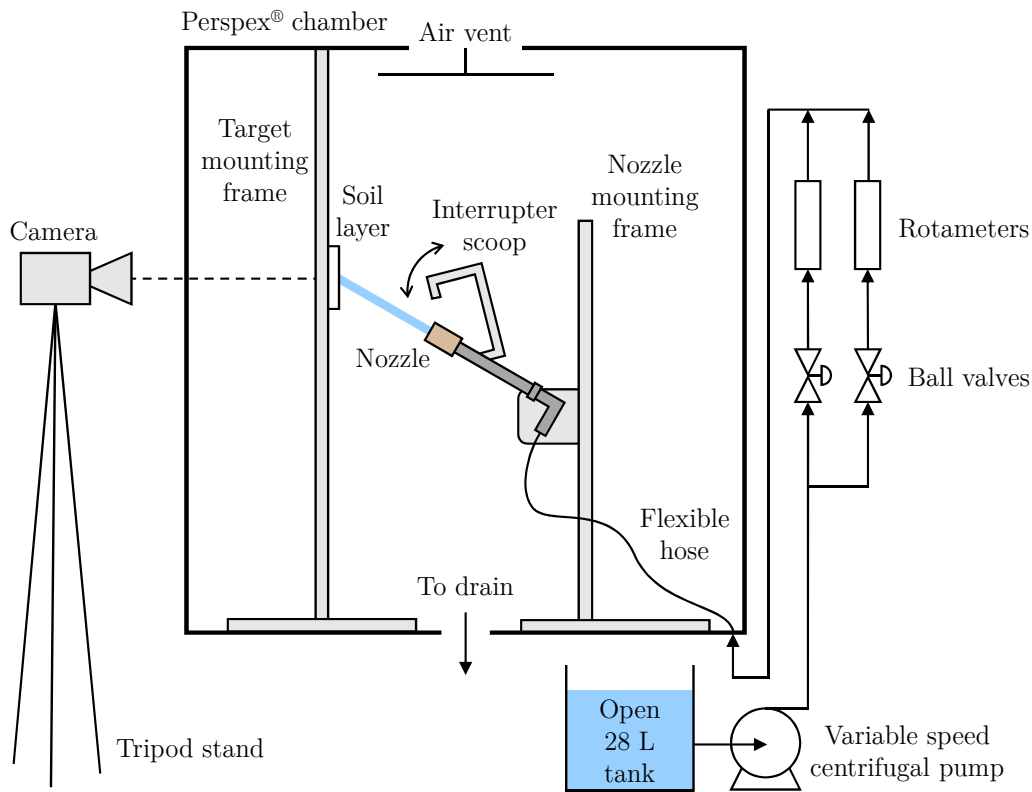


Figure 4.12: Schematic of the impinging jet apparatus used for inclined jet cleaning tests.

Tests were performed at room temperature (20–22°C), using softened tap water as the test liquid. The water was pumped from an open 28 L tank by a variable speed centrifugal pump (Cole-Parmer 316 SS Magnetic Drive Pump, Cole-Parmer, UK). The brass 55° convergent entry nozzle with bore diameter $d_N = 2$ mm was used and the nozzle was preceded by a straight pipe (150 mm length, 7.5 mm inner diameter) that served as a flow straightening section. The jet length was set at 60 mm to ensure that the jet was coherent.

The volumetric flow rate through the nozzle was set by changing the pump speed. The pump was allowed to run for at least 30 s before cleaning was started to ensure that a stable jet had formed. An interrupter scoop was placed over the end of the

nozzle during this initial period to divert the jet away from the target. The softened tap water was not recirculated. Illumination was provided by two light-emitting diode (LED) standing lamps (Neewer 1500W Photography Studio Softbox Lighting Kit, Shenzhen Neewer Technology, China).

The combinations of jets angles and flow rates used in the cleaning tests are summarised in Table 4.5.

Table 4.5: Flow rates and combinations of jet angles used in the inclined jet cleaning tests.

ϕ	45°		60°		90°	
	ϕ_{overall}^* (Eq. 4.7)	$Q /$ L min ⁻¹	ϕ_{overall}^* (Eq. 4.7)	$Q /$ L min ⁻¹	ϕ_{overall}^* (Eq. 4.7)	$Q /$ L min ⁻¹
45°	35.3°	2.0	-	-	45°	1.5, 2.0, 2.5
60°	-	-	50.8°	2.0	60°	2.0
75°	-	-	-	-	75°	2.0
90°	45°	2.0	60°	2.0	90°	1.0, 1.5, 2.0, 2.5
105°	-	-	-	-	105°	2.0
120°	-	-	129.2°	2.0	120°	2.0
135°	144.7°	2.0	-	-	135°	1.5, 2.0, 2.5

Soil material and target plate

A commercial moisturising cream (NIVEA® Soft Moisturising Cream, Beiersdorf AG, Germany), an oil-in-water emulsion, was used as the soil material. A transparent Perspex® plate with dimensions 150 × 150 × 10 mm (width × height × thickness) was used as the target and the plate was mounted vertically for the cleaning tests. A centred square recess of side length 110 mm and depth 1 mm was machined into the plate and an area measuring 80 × 80 mm was marked out within the recess using tape. Soil layers were prepared by applying the soil to the recessed area and scraping excess soil away before removing the tape. This method enabled soil layers to be generated with consistent depth. Cleaning was performed immediately after coating to avoid drying artefacts. After each test, the plate was cleaned with soap and warm tap water, wiped with isopropyl alcohol then allowed to dry before a new layer of soil was applied.

Imaging and image analysis

The target plate was mounted on a rigid frame located close to one wall of the chamber so that the camera could focus on the soil layer. The cleaning pattern was videoed at 60 frames per second with a Nikon D3300 digital camera located outside the chamber, behind the target, aligned with the point of jet impingement. Graticule tape was placed on the dry side of the target to provide a length scale for image processing. The videos were split into individual image frames using a script written in MATLAB[®] (MathWorks, USA).

Edge detection was used in a separate MATLAB[®] script to identify the visibly cleaned region in each image based on the difference in pixel intensity between the cleaned and uncleaned regions. It is acknowledged that visual cleanliness does not guarantee that all the layer has been removed as a thin, colourless layer of residual or adsorbed material could remain, but visual cleanliness is an important part of the acceptance criteria for cleaning validation (European Commission, 2015).

Figure 4.13(a) shows an example of the cleaned region formed after 1.5 s of cleaning by a normally impinging jet. For normally impinging jets where the cleaned region is approximately circular, the cleaning results are reported as a_{equiv} , where a_{equiv} is the radius of a circle with equal area to the cleaned region. Figure 4.13(b) shows the processed image with the detected cleaned region and Figure 4.13(c) shows the circle of radius a_{equiv} . For inclined jets, the cleaned radius was extracted at $\Delta\theta = 30^\circ$ intervals. Additional measurements were made at $\Delta\theta = 10^\circ$ intervals close to the principal flow direction.

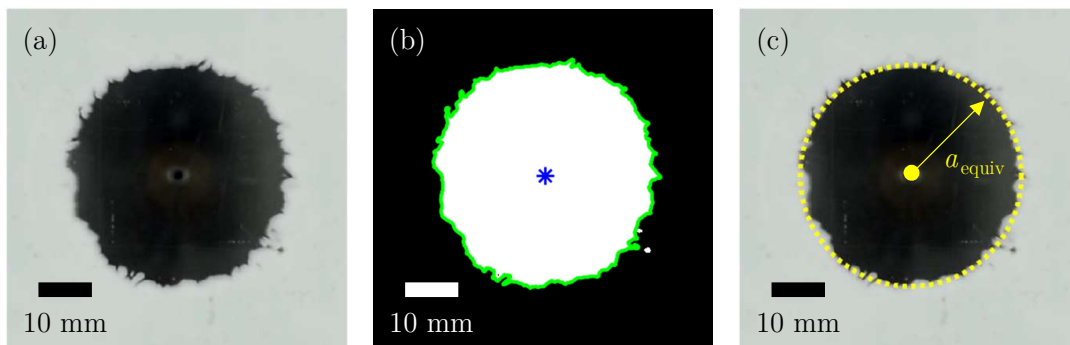


Figure 4.13: Cleaned region after 1.5 s of impingement by a normally impinging jet ($Q = 2.0 \text{ L min}^{-1}$). (a) Photograph, (b) processed image: the blue star indicates the point of jet impingement and the green locus the detected cleaned region, and (c) circle of radius $a_{\text{equiv}} = 20.8 \text{ mm}$.

4.3.4 Data processing

To enable the experimental data from the hydrodynamic, liquid flow rate measurement and cleaning tests to be compared to the model predictions, the data were expressed in the form of an equivalent volumetric flow rate, $Q_{\theta,\text{equiv}}$. $Q_{\theta,\text{equiv}}$ is the equivalent volumetric flow rate arising in azimuthal direction θ from a normally impinging jet.

Hydrodynamic tests

The location of the hydraulic jump, $R_{\theta,\text{jump}}$, can be used to determine $Q_{\theta,\text{equiv}}$ as follows: $Q_{\theta,\text{equiv}}$ is the volumetric flow rate of a normally impinging jet of the same jet diameter which gives a hydraulic jump at location $R_{\theta,\text{jump}}$. A schematic is shown in Figure 4.14.

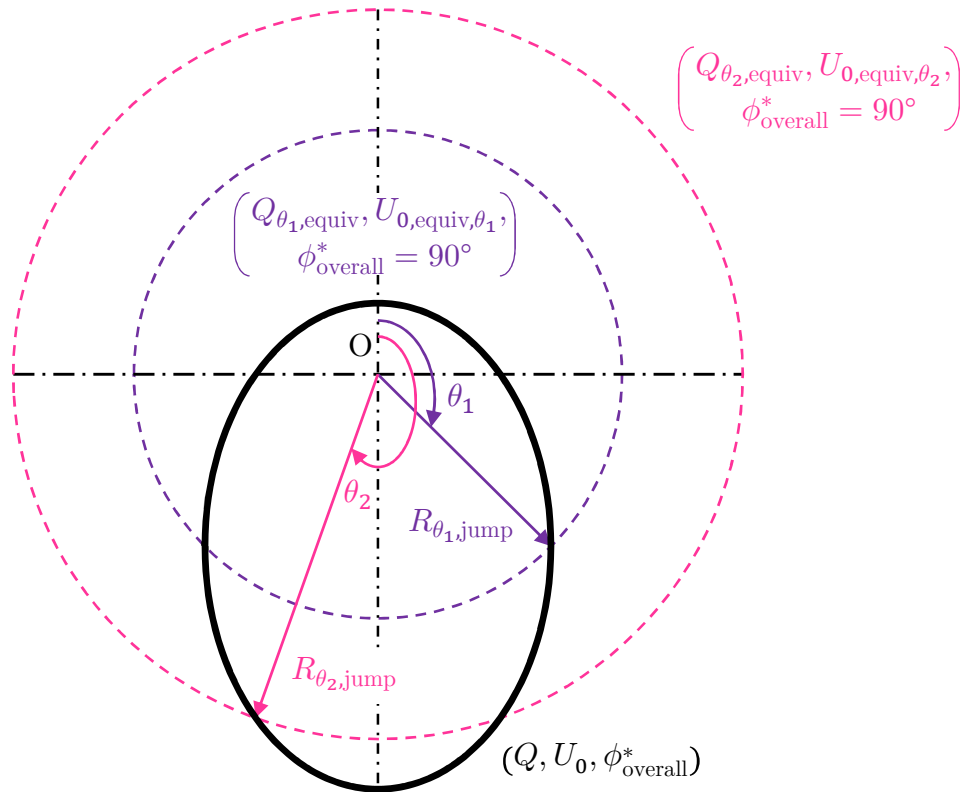


Figure 4.14: Schematic showing the location of the hydraulic jump for an inclined jet of ϕ_{overall}^* (solid black locus) and the corresponding locations of the hydraulic jumps for normally impinging jets of $Q_{\theta,\text{equiv}}$.

If $\phi_{\text{overall}}^* = 90^\circ$, the hydraulic jump is almost circular (the deviation from a circular shape is due to the effect of gravity) and $Q_{\theta,\text{equiv}} = Q$ (the actual jet flow rate) for all θ .

Equation 2.14 gives the Wilson *et al.* (2012) prediction of the location of the hydraulic jump for a normally impinging jet and this is used to determine $Q_{\theta,\text{equiv}}$:

$$U_{0,\text{equiv}} = \left[\frac{50 \mu \gamma (1 - \cos \beta)}{9 \rho^2 r_0^6} R_{\theta,\text{jump}}^4 \right]^{1/3}$$

$$\therefore Q_{\theta,\text{equiv}} = \pi r_0^2 U_{0,\text{equiv}} = \pi r_0^2 \left[\frac{50 \mu \gamma (1 - \cos \beta)}{9 \rho^2 r_0^6} R_{\theta,\text{jump}}^4 \right]^{1/3} \quad (4.33)$$

where $U_{0,\text{equiv}}$ is the velocity of the jet with volumetric flow rate $Q_{\theta,\text{equiv}}$.

It is expected that

$$\frac{1}{2\pi} \int_0^{2\pi} Q_{\theta,\text{equiv}} d\theta = Q \quad (4.34)$$

Liquid flow rate measurements

$Q_{\text{collected,expt}}$ from the tests is compared with $Q_{\text{collected,model}}$. To obtain $Q_{\text{collected,model}}$, a flow distribution model combined with Equation 4.18 gives $R_{\theta,\text{jump}}$ and $Q_{\theta,\text{equiv}}$ is obtained from Equation 4.33. $Q_{\text{collected,model}}$ is then given by

$$Q_{\text{collected,model}} = \frac{\int_{\theta_1}^{\theta_2} Q_{\theta,\text{equiv}} d\theta}{Q \times 2\pi} \times Q$$

$$Q_{\text{collected,model}} = \frac{1}{2\pi} \times \int_{\theta_1}^{\theta_2} Q_{\theta,\text{equiv}} d\theta \quad (4.35)$$

where $\theta_1 \leq \theta \leq \theta_2$ is the azimuthal angle range over which the liquid flows into the reservoir (Figure 4.11(b)).

Cleaning tests

Normally impinging jets were used to characterise the cleaning of the NIVEA[®] cream. Polynomial or logarithmic trendlines were fitted to the data of a_{equiv} against t and the results were differentiated to obtain an estimate of the cleaning rate, da/dt . The cleaning rate was then plotted against M , calculated using the Wilson *et al.* (2012) hydrodynamic model (Equations 2.3, 2.7 and 2.10 combined), yielding a relationship between da/dt and M .

Tests with inclined jets were carried out and the cleaning rate, da_{θ}/dt , was estimated from data of a_{θ} against t following the same procedure used for the tests with normally impinging jets. a_{θ} is the cleaned radius in azimuthal direction θ . da_{θ}/dt was used to infer the local value of M using the relationship obtained between da/dt and M from the tests with normally impinging jets.

Figure 4.15 shows how the local value of M varies with jet flow rate Q for a fixed jet radius r_0 according to the Wilson *et al.* (2012) hydrodynamic model (Equations 2.3, 2.7 and 2.10 combined). This was compared with the experimental data in a given azimuthal direction θ to obtain an estimate for $Q_{\theta,\text{equiv}}$.

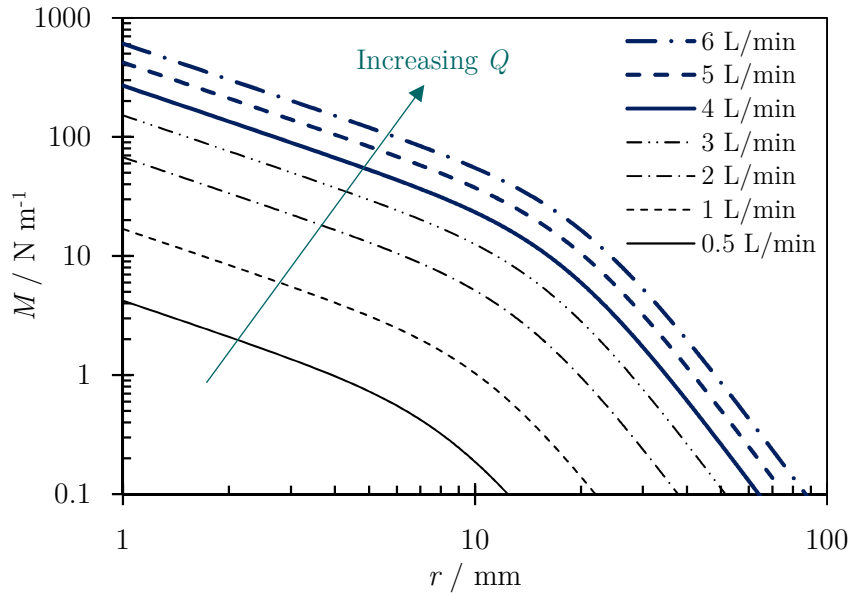


Figure 4.15: Effect of jet flow rate on the local momentum flux for a jet of $d_N = 2$ mm, from the Wilson *et al.* (2012) hydrodynamic model (Equations 2.3, 2.7 and 2.10 combined)

Quantifying the fit of the flow distribution models to experimental data

With the experimental data from the hydrodynamic and cleaning tests expressed as $Q_{\theta,\text{equiv}}$, these values could be compared to the predictions from the different flow distribution models, $Q_{\theta,\text{equiv,model}}$. The fit of the models to the data was quantified using a parameter ψ , the least squares difference between the model predictions and experimental values of $Q_{\theta,\text{equiv}}$, scaled by the volumetric flow rate of the jet, Q . ψ is given by

$$\psi = \sum_i \left[\underbrace{\frac{\Delta\theta_i}{360^\circ}}_I \times \underbrace{\frac{\left(\frac{Q_{\theta,\text{equiv},i}}{\Delta Q_{\theta,\text{equiv},i}}\right)}{\sum_i \left(\frac{Q_{\theta,\text{equiv},i}}{\Delta Q_{\theta,\text{equiv},i}}\right)}}_{II} \times \underbrace{\left(\frac{Q_{\theta,\text{equiv},i} - Q_{\theta,\text{equiv,model},i}}{Q}\right)^2}_{III} \right] \quad (4.36)$$

where i is a given experimental data point, $\Delta\theta_i$ is its azimuthal angle range and $\Delta Q_{\theta,\text{equiv},i}$ its range of equivalent volumetric flow rates. These parameters are illustrated in Figure 4.16.

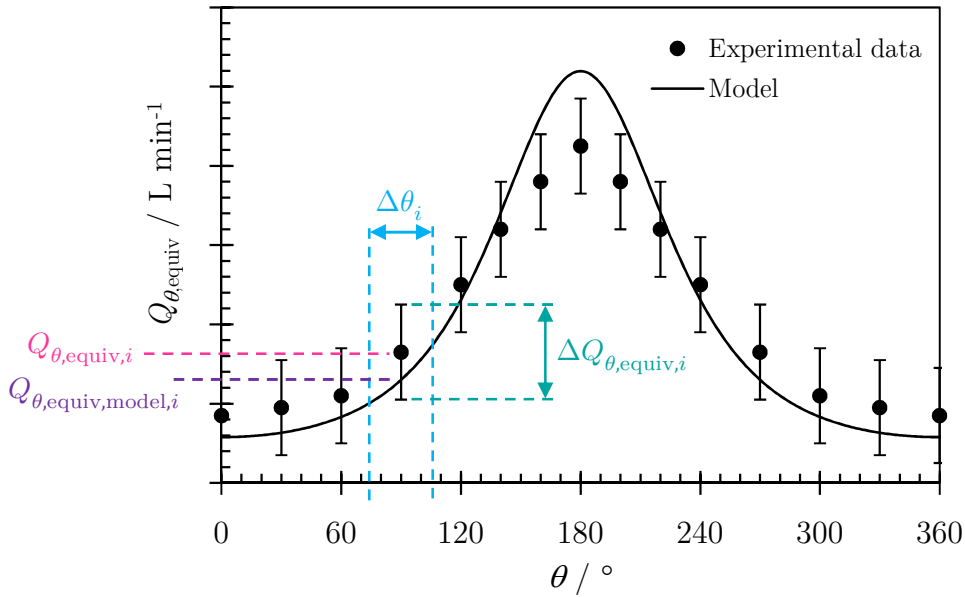


Figure 4.16: Parameters used in quantifying the fit of the flow distribution models to the experimental data.

Term III in Equation 4.36 is the least squares difference and Terms I and II are the weightings used. Term I accounts for the spread of the experimental data over θ while term II accounts for the uncertainty in the values of $Q_{\theta,\text{equiv}}$ obtained from the tests.

4.4 Results and discussion

4.4.1 Hydrodynamic tests

Flow patterns

The hydrodynamic tests established the location of the hydraulic jump when an inclined jet impinges on a target. The location of the hydraulic jump was extracted during the initial formation of the jump (Figure 4.9(a)) and once a steady state flow pattern had been reached (Figure 4.9(b)). Figure 4.17 shows the results obtained for a small set of jet orientations. The results are compared to the predictions from the KM with Equations 4.13 and 4.18, with and without the gravity term in the velocity profile of the Wilson *et al.* (2012) hydrodynamic model, respectively, and using the Bhagat and Wilson (2016) hydrodynamic model (Equations 2.41, 2.43 and 2.44).

The location of the hydraulic jump during its initial formation and at steady state were similar. The steady state values could only be extracted above the point of jet impingement. Gravity caused the rope to fall back over the RFZ under its own weight so the location of the hydraulic jump extracted from the images may be lower than its true position. The effect of gravity on the rope was more apparent as the distance of the hydraulic jump above the point of impingement increased (Figure 4.17(c)), and similar behaviour was observed across all the other jet orientations and jet flow rates studied. The location of the hydraulic jump extracted from the initial formation stage was used in all subsequent analyses.

The KM coupled with the Wilson *et al.* (2012) and Bhagat and Wilson (2016) hydrodynamic models gave similar predictions. The models overpredicted the flow in the major flow region and underpredicted the flow in the minor flow region, regardless of jet orientation. The principal flow direction (direction of greatest flow) predicted by the models was also not co-linear with that of the experimental data. This could be due to the effect of gravity on the flow pattern, reflecting further considerations that need to be made in the geometric transformation (Section 4.2.1).

The Wilson *et al.* (2012) hydrodynamic model without the gravity term (Equation 4.18) was used for consistency and simplicity in all subsequent analyses to illustrate the different flow distribution models as it allowed an analytical solution to be obtained. Some variation in numerical values is expected if the gravity term is included and if the Bhagat and Wilson (2016) hydrodynamic model is used instead.

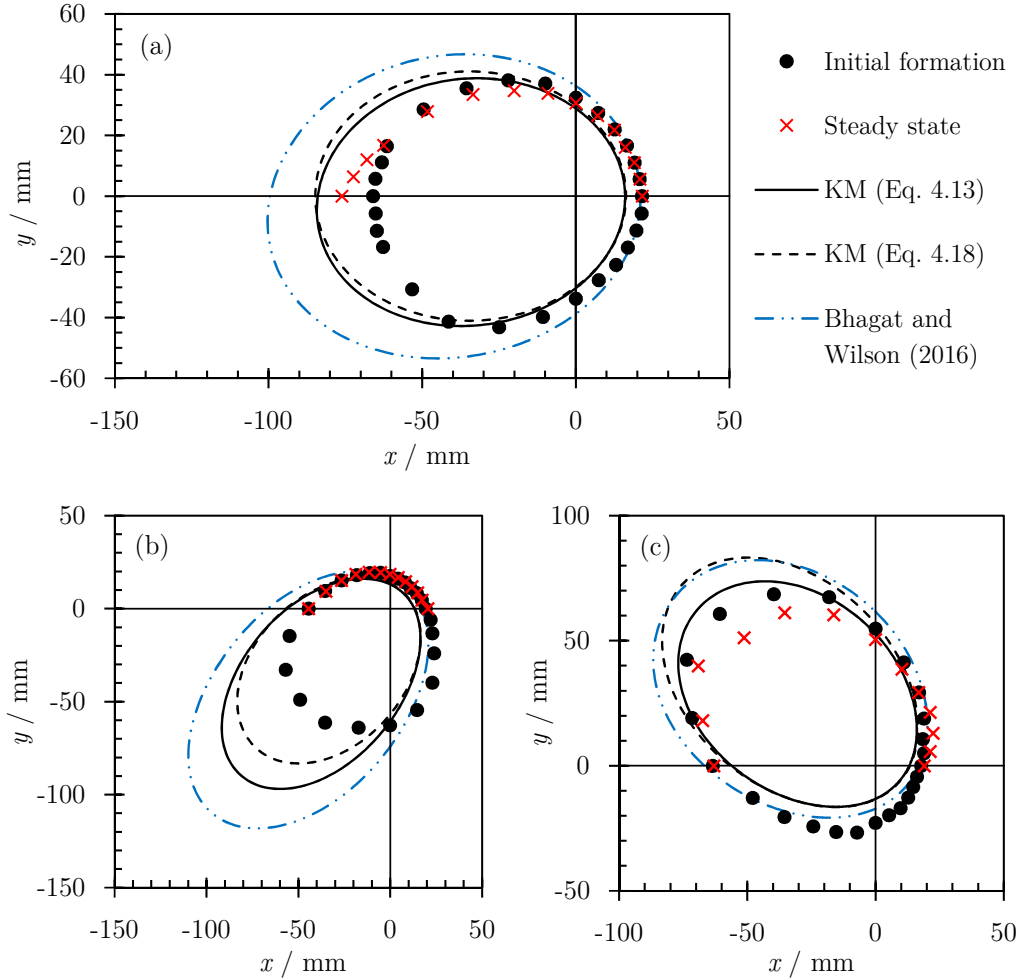


Figure 4.17: Location of the hydraulic jump during the initial formation and at steady state for $Q = 2.0 \text{ L min}^{-1}$ jets of varying orientations. The coordinate origin (0,0) is the point of jet impingement. (a) $\phi = 90^\circ$, $\chi = 60^\circ$, $\phi_{\text{overall}}^* = 60^\circ$, (b) $\phi = 60^\circ$, $\chi = 60^\circ$, $\phi_{\text{overall}}^* = 50.8^\circ$ and (c) $\phi = 120^\circ$, $\chi = 60^\circ$, $\phi_{\text{overall}}^* = 129.2^\circ$. The predictions from the KM model with the Wilson *et al.* (2012) hydrodynamic model, with and without the gravity term (Equations 4.13 and 4.18, respectively), and with the Bhagat and Wilson (2016) hydrodynamic model (Equations 2.41, 2.43 and 2.44), are shown by the solid, dashed and dashed-double dotted lines, respectively.

Comparison between the flow distribution models

Figure 4.18 shows the experimental data from Figures 4.17(b) and (c) compared with the predictions from the three proposed flow distributions: the circular, moving stagnation point and changing ellipse models. The KM results are also shown for comparison (recovered when $\lambda = 1$ in the moving stagnation point model and when $\omega = 1$ in the changing ellipse model).

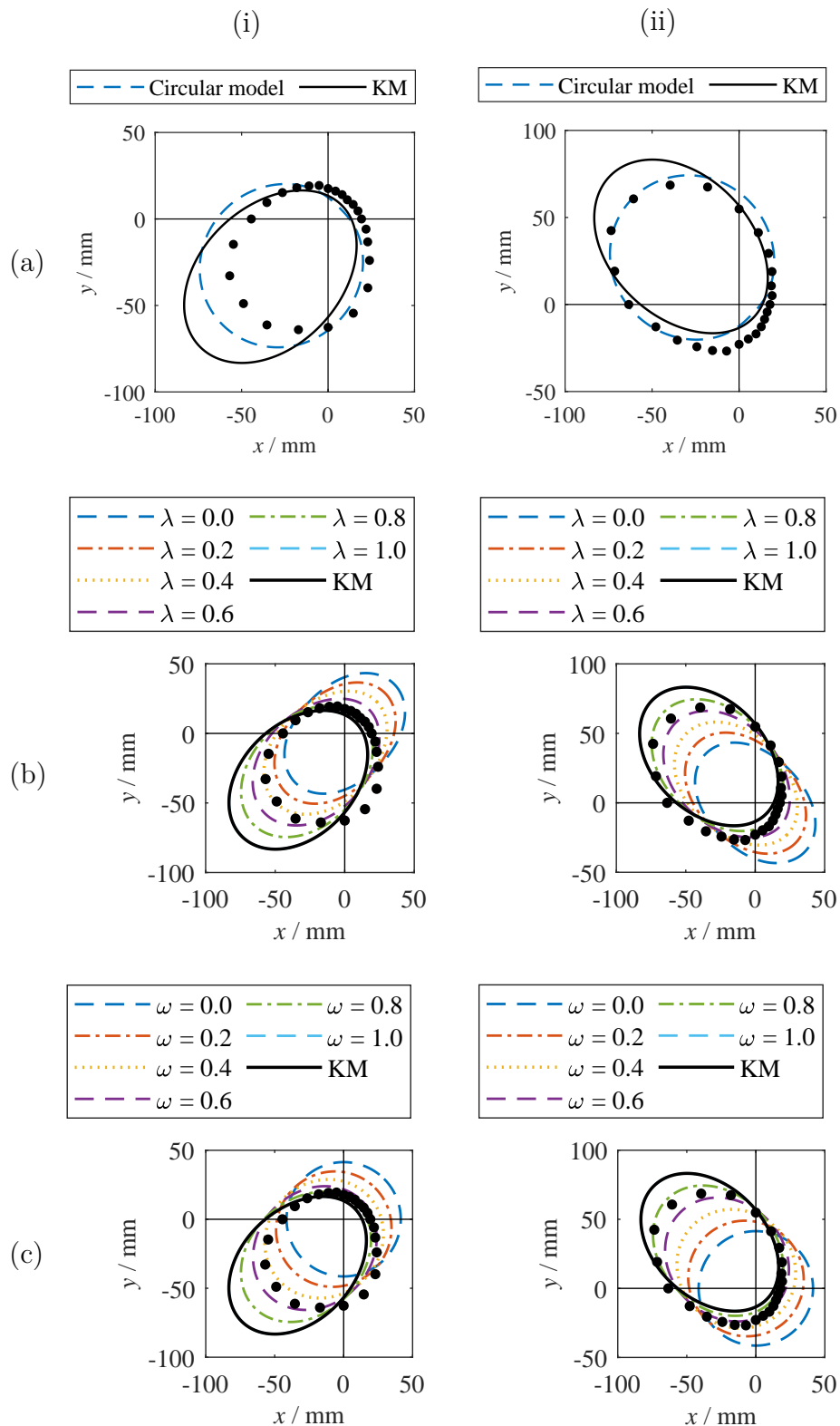


Figure 4.18: Location of the hydraulic jump for $Q = 2.0 \text{ L min}^{-1}$ jets: predictions from the (a) circular, (b) moving stagnation point and (c) changing ellipse models, compared with experimental data for (i) $\phi = 60^\circ$, $\chi = 60^\circ$, $\phi_{\text{overall}}^* = 50.8^\circ$ and (ii) $\phi = 120^\circ$, $\chi = 60^\circ$, $\phi_{\text{overall}}^* = 129.2^\circ$, respectively.

Across all the jet flow rates and jet orientations studied, the circular model was found to provide a poor fit to the experimental data. It predicts a hydraulic jump with a much rounder shape than that observed experimentally. The circular flow distribution was therefore not considered further.

The moving stagnation point and changing ellipse model employ parameters λ and ω , respectively. Figures 4.18(b) and (c) show that both models were able to describe the shape of the hydraulic jump by fitting of the respective parameter.

However, the moving stagnation point model was found to predict unrealistic shapes for combinations of ϕ and χ where the jet is very strongly inclined with respect to the target ($\phi_{\text{overall}}^* \rightarrow 30^\circ$ or $\phi_{\text{overall}}^* \rightarrow 150^\circ$). At these jet angles, lower values of λ give a hydraulic jump that is pinched at the point of impingement. Examples are shown in Figure 4.19.

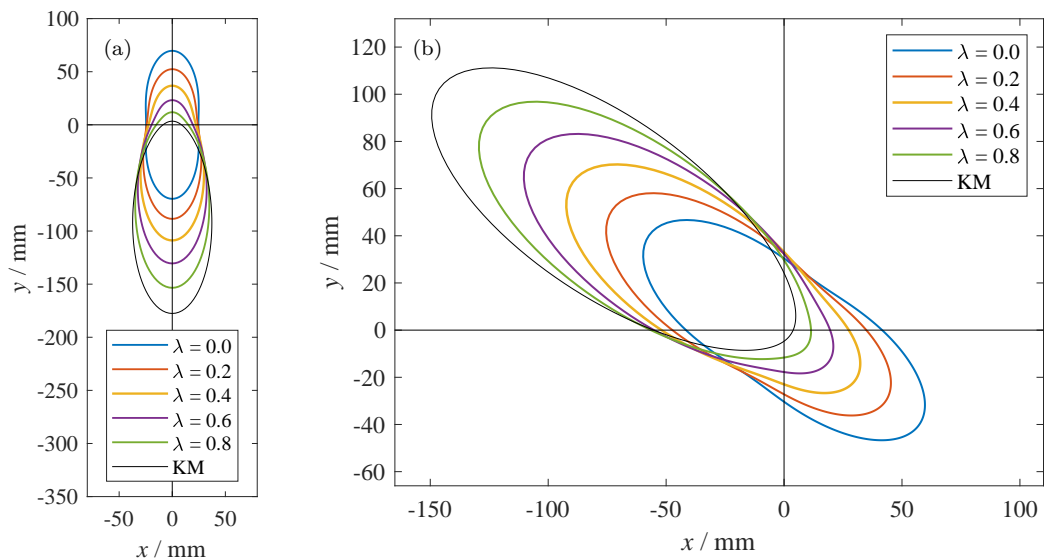


Figure 4.19: Hydraulic jumps predicted by the changing ellipse model for $Q = 2.0 \text{ L min}^{-1}$ with (a) $\phi = 30^\circ$, $\chi = 90^\circ$, $\phi_{\text{overall}}^* = 30^\circ$ and (b) $\phi = 135^\circ$, $\chi = 35^\circ$, $\phi_{\text{overall}}^* = 150.2^\circ$.

The changing ellipse flow distribution appeared to be a suitable candidate model so was taken forward for further consideration. It is hereafter referred to as CEM.

In studies of inclined circular water jets impinging on a horizontal glass target, Kate *et al.* (2007; 2008) found that jet angles in the range $25^\circ \leq \phi_e \leq 90^\circ$ (equivalent to $25^\circ \leq \phi_{\text{overall}}^* \leq 155^\circ$ in this work) gave hydraulic jumps bounded by smooth curves. If the jets were inclined more obliquely, hydraulic jumps with distinct corners

were observed. Jalil and Rajaratnam (2006) observed little to no flow in the minor flow region in their study of high Re ($380\,000 \leq Re \leq 720\,000$) inclined circular water jets impinging on a horizontal aluminium target when $\phi_e < 45^\circ$ (equivalent to $\phi_{\text{overall}}^* < 45^\circ$ or $\phi_{\text{overall}}^* > 135^\circ$ in this work). Superhydrophobic surfaces have also been found to affect the shape of the hydraulic jump, such as a sharp corner caused by the rebound of the liquid from the surface, and this has been studied by workers such as Kibar (2018).

These complex jump shapes have not been considered in this work as the focus is on the flow distribution in inclined jets that form a hydraulic jump bounded by a smooth curve. The jets used in this work were inclined in the range $35.3^\circ \leq \phi_{\text{overall}}^* \leq 144.7^\circ$ and formed hydraulic jumps bounded by a smooth curve.

Fitting the changing ellipse flow distribution model (CEM)

The data from the hydrodynamic tests were expressed in terms of $Q_{\theta, \text{equiv}}$ using Equation 4.33. The CEM fit to the data was quantified using the fitting parameter ψ (Equation 4.36) and the minimum value of ψ gave the optimal value of ω , the best fit. Figures 4.20 and 4.21 show the results for two data sets. The KM result is shown for comparison and is recovered with the CEM when $\omega = 1$.

The CEM was consistently found to provide a better fit to the experimental data than the KM result. Figure 4.22 shows the variation in ψ with ω for different jet orientations and flow rates. The optimal values of ω are given in Table 4.6 and shown in Figure 4.23. There was no consistent optimum in ω . The ω values appear to lie in a band between a parabolic lower bound and an upper bound of about 0.9. Most (51 out of 59) of the optimal ω values lay in the range $0.5 \leq \omega \leq 0.85$.

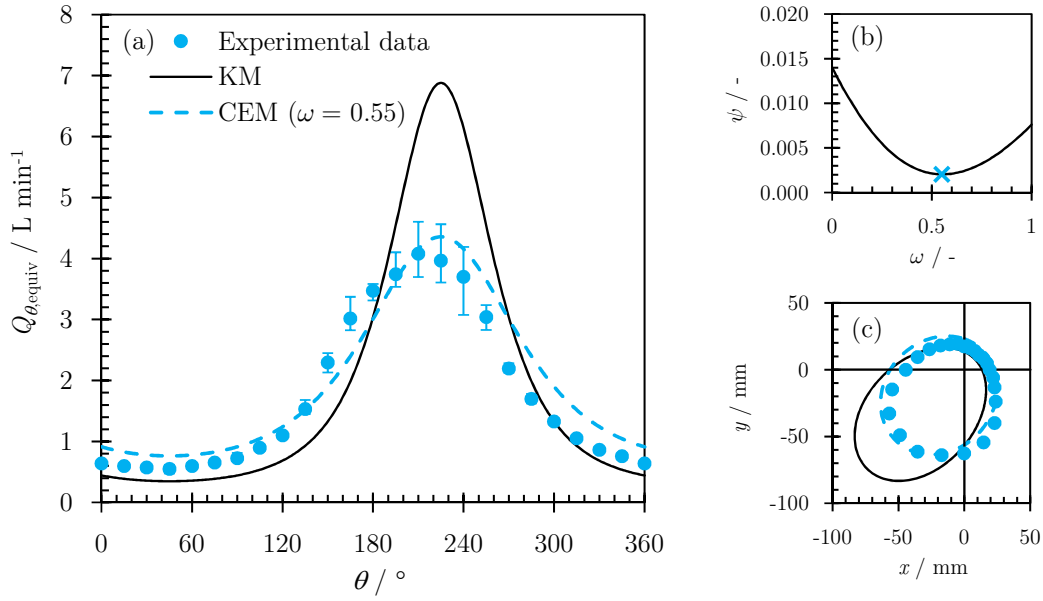


Figure 4.20: (a) CEM fitted to experimental data (Figure 4.17(b); $Q = 2.0 \text{ L min}^{-1}$, $\phi = 60^\circ$, $\chi = 60^\circ$, $\phi_{\text{overall}}^* = 50.8^\circ$) expressed as $Q_{\theta,equiv}$, (b) fitting parameter ψ (Equation 4.36) showing the optimal value of ω , and (c) predicted shape of the hydraulic jump with the optimal value of ω .

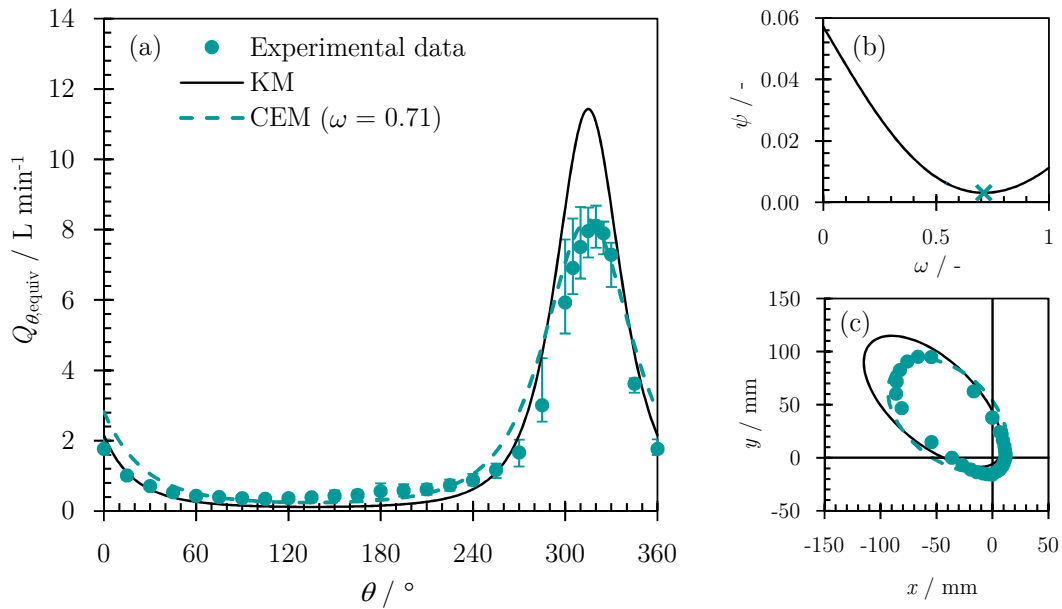


Figure 4.21: (a) CEM fitted to experimental data ($Q = 2.0 \text{ L min}^{-1}$, $\phi = 135^\circ$, $\chi = 45^\circ$, $\phi_{\text{overall}}^* = 144.7^\circ$) expressed as $Q_{\theta,equiv}$, (b) fitting parameter ψ (Equation 4.36) showing the optimal value of ω , and (c) predicted shape of the hydraulic jump with the optimal value of ω .

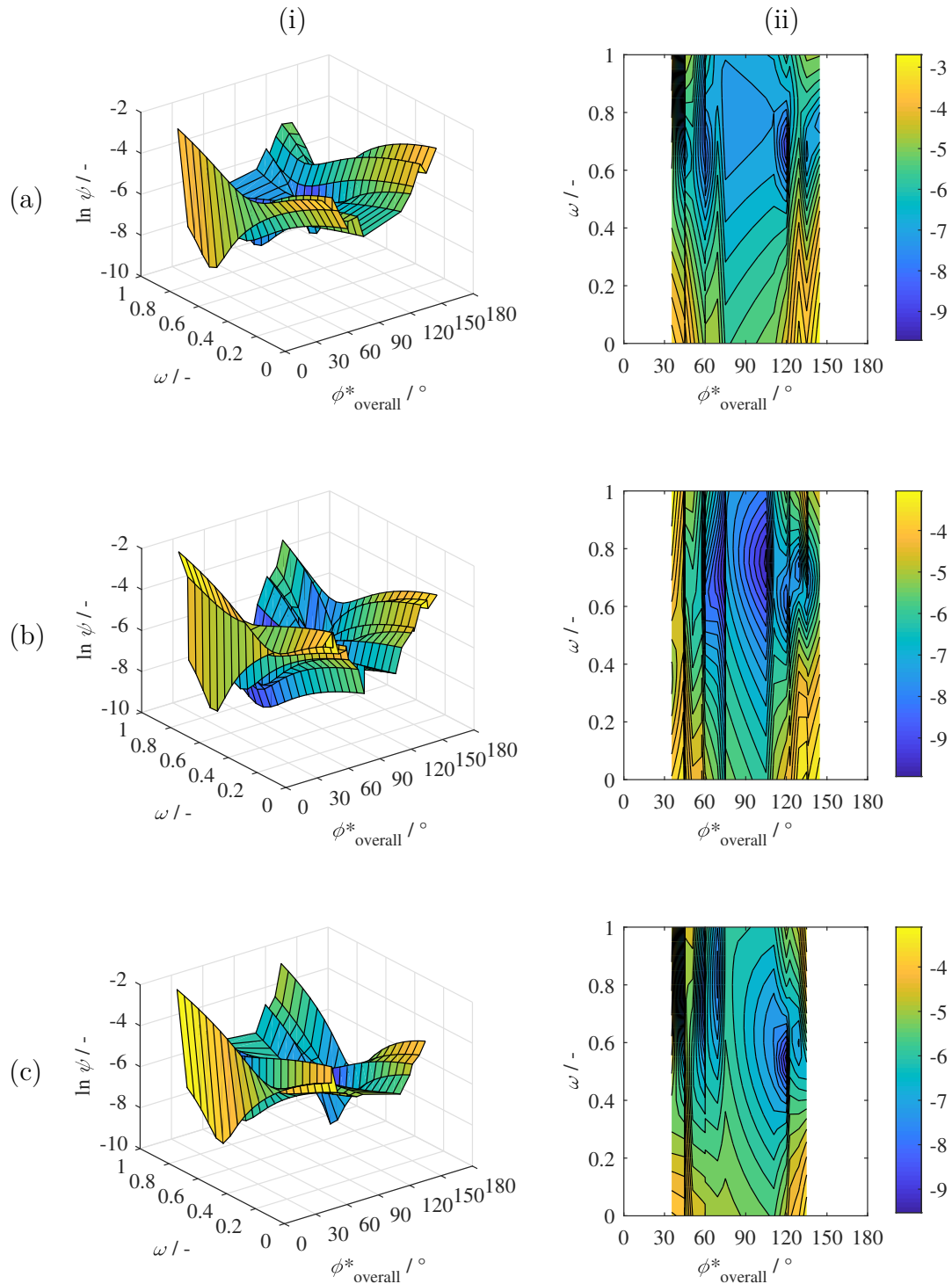


Figure 4.22: Variation of ψ (plotted as $\ln \psi$ for clarity) with ω across the different ϕ_{overall}^* values studied for (a) $Q = 1.0 \text{ L min}^{-1}$, (b) $Q = 2.0 \text{ L min}^{-1}$, and (c) $Q = 3.0 \text{ L min}^{-1}$, shown in (i) as a 3D plot and (ii) as a 2D plot with the colour scale indicating the value of $\ln \psi$. Different combinations of ϕ and χ that have the same ϕ_{overall}^* value (but different θ^* values; Table 4.3) are plotted offset by $\phi_{\text{overall}}^* = 0.1^\circ$, giving the dark vertical streaks in (ii).

Table 4.6: Optimal values of ω for the CEM fitted to experimental data from hydrodynamic tests (measured $R_{\theta, \text{jump}}$ expressed as $Q_{\theta, \text{equiv}}$).

χ	$Q = 1.0 \text{ L min}^{-1}$			$Q = 1.5 \text{ L min}^{-1}$			$Q = 2.0 \text{ L min}^{-1}$			$Q = 2.5 \text{ L min}^{-1}$			$Q = 3.0 \text{ L min}^{-1}$			
ϕ	45°	60°	75°	90°	45°	60°	75°	90°	45°	60°	75°	90°	45°	60°	75°	90°
45°	0.50	-	-	0.84 ^a	0.46	-	-	0.79	0.35	-	-	0.83 ^a	0.36	-	-	0.77 ^a
60°	-	0.62	-	0.74 ^b	-	0.50	-	-	-	0.55	0.76 ^d	-	-	0.50	-	0.75 ^b
75°	-	-	1.00	-	-	-	-	-	0.66	0.78 ^d	0.71	0.73 ^c	-	-	-	0.84
90°	0.66 ^a	0.64 ^b	0.77	N/A	-	-	N/A	-	0.73 ^a	0.61 ^b	0.92 ^c	N/A	-	0.77 ^a	0.61 ^b	0.96
105°	-	-	0.78	-	-	-	-	-	0.69	0.73 ^e	0.76	0.76	-	-	-	0.61
120°	-	0.82	0.81	0.68	-	0.85	-	-	-	0.73	0.65 ^e	0.62	-	0.67	-	0.60
135°	0.76	-	-	0.66	0.72	-	-	0.73	0.71	-	-	0.60	-	-	-	0.55

^{a, b, c, d, e} Combinations of ϕ and χ that have the same ϕ_{overall}^* value (but different θ^* values; Table 4.3)

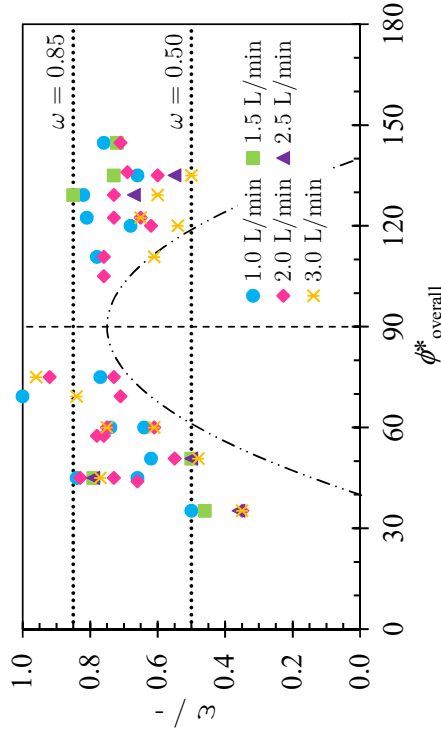


Figure 4.23: Optimal values of ω for the CEM fitted to experimental data from hydrodynamic tests (measured $R_{\theta, \text{jump}}$ expressed as $Q_{\theta, \text{equiv}}$). Note that ω is undefined when $\phi_{\text{overall}}^* = 90^\circ$ (Equation 4.30). The parabolic lower bound is given by $\omega = -2 \times 10^{-4} (\phi_{\text{overall}}^* - 90^\circ) + 0.7$, where ϕ_{overall}^* is in degrees.

4.4.2 Liquid flow measurements

Tests were carried out to measure the liquid flow rate over a range of θ for a given jet by allowing some of the liquid to flow over the top of the vertical target and collecting the remaining liquid that drained down the target plate in a reservoir (Figures 4.10 and 4.11), giving $Q_{\text{collected,expt}}$. $Q_{\text{collected,expt}}$ was compared with the KM prediction, $Q_{\text{collected,model}}$ (Equation 4.35), and the results are shown in Figure 4.24.

For all the tests conducted, the data lie close to the line of equality ($y = x$), but there were large uncertainties in the data. Calculation of $Q_{\text{collected,model}}$ required the θ range over which the liquid flows down the target and into the reservoir, so the uncertainty in the measurements of θ gave rise to uncertainties in $Q_{\text{collected,model}}$. $Q_{\text{collected,expt}}$ was determined by the change in the height of the liquid in the reservoir over time. Measurements of the height of the liquid were subject to large uncertainties due to surface waves caused by liquid entering the reservoir.

The flow of the liquid over the top of the target was observed to cause a slight distortion in the shape of the hydraulic jump. Liquid could be seen to be pinned at the top of the target as the target used was 5 mm thick. As the liquid flowed over the top of the target, a spray of liquid droplets was also generated. These phenomena may affect the measurements of the liquid flow rate.

With the hydrodynamic tests, the KM was observed to overpredict the flow in the major flow region and underpredict the flow in the minor flow region (Figure 4.17). This was not seen with the data from these liquid flow rate measurements. If KM overpredicts the flow in the major flow region and underpredicts the flow in the minor flow region, the data in Figure 4.24(b) ($\phi_{\text{overall}}^* < 90^\circ$ so the minor flow region is above the point of impingement) are expected to lie above the line of $y = x$ while the data in Figures 4.24(c) and (d) ($\phi_{\text{overall}}^* > 90^\circ$ so the major flow region is above the point of impingement) are expected to lie below the line of $y = x$. Given the uncertainties associated with the data, it was not possible to draw any firm conclusions and no attempts were made to fit the CEM to the data.

This measurement technique is also limited in that measurements can only be made up to the point where the top of the target and the point of jet impingement are level, so few data points can be obtained for jets that point downwards (Figure 4.24(b); $\phi_{\text{overall}}^* < 90^\circ$). The accuracy of the technique could be improved by the addition of baffles to the reservoir to minimise the surface waves that affect the measurements of

the liquid height, or the liquid flow rate could instead be determined by the change in weight of the liquid in the reservoir over time. The use of a thinner target combined with chamfering of its top edge could minimise pinning and the generation of a spray.

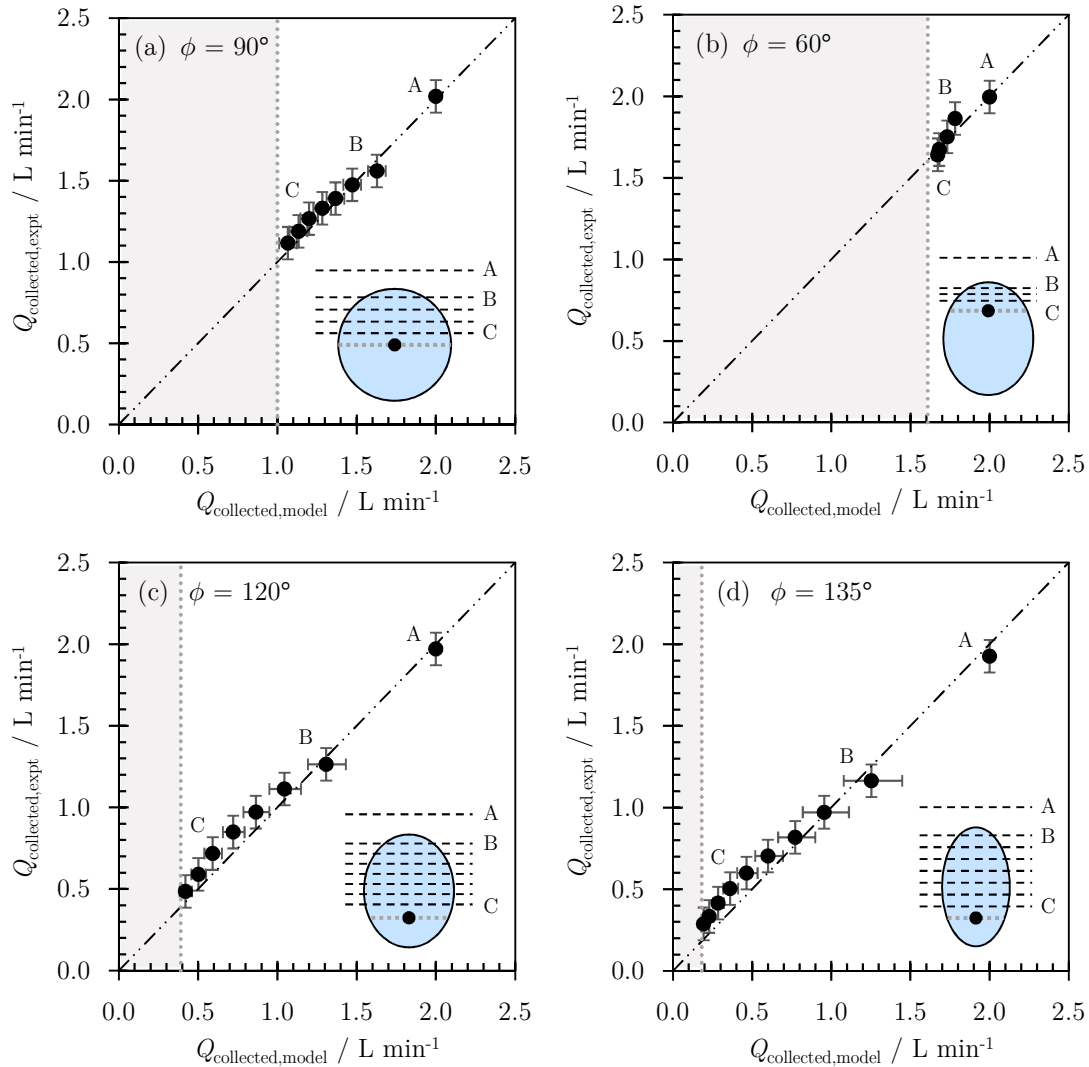


Figure 4.24: Measured liquid flow rate against the KM prediction for $Q = 2.0 \text{ L min}^{-1}$ jets with $\chi = 90^\circ$ and (a) $\phi = \phi_{\text{overall}}^* = 90^\circ$, (b) $\phi = \phi_{\text{overall}}^* = 60^\circ$, (c) $\phi = \phi_{\text{overall}}^* = 120^\circ$, and (d) $\phi = \phi_{\text{overall}}^* = 135^\circ$. The diagonal locus indicates the line of equality ($y = x$). The dashed lines indicate the locations of the top of the target plate as the target plate is lowered. At A, no liquid flows over the top of the target and all the liquid is collected. From B to C, an increasing amount of liquid flows over the top of the target and the remainder is collected. The shaded area indicates the region below the point of jet impingement where experimental values cannot be obtained.

Results in the literature

Taylor (1960) studied the formation of thin horizontal flat sheets of water generated by the collision of two identical inclined jets (see inset in Figure 4.25(a)). Taylor measured the flow distribution in the sheets of water by collecting the water in a given θ direction passing through the gap between two razor blades into a box. Taylor reported the distribution in terms of the product rh , where r is the radial distance and h is the height of the liquid film.

From Equation 4.10, at the boundary of the jet footprint where it is assumed that $U_\theta = U_0$,

$$r_\theta h_\theta = \frac{1}{2} r_{\theta, \text{model}}^2 \frac{U_{0, \text{model}}}{U_0} \quad (4.37)$$

$r_{\theta, \text{model}}$ and $U_{0, \text{model}}$ for the KM and CEM flow distributions are given in Table 4.2.

Figure 4.25 shows the data reported by Taylor compared with the KM and CEM predictions. The optimal value of ω for the CEM fit to Taylor's data was the ω value that resulted in the minimum sum of the least squares difference between the experimental data and model values. Equation 4.37 is independent of jet flow rate (the velocity terms cancel as $U_{0, \text{model}} = f(U_0)$) and is only dependent on the jet angle and jet diameter. For the KM and CEM predictions, the jet diameter was taken to be the diameter of a single jet with area equal to the combined area of the two jets used by Taylor as this gives the correct total flow rate.

The data from Taylor lie below or are equal the KM predictions at all values of θ , and the KM again overpredicts the flow in the major flow region. The CEM predictions alter the shape of the distribution from the KM result, where there is more flow in the minor region and the flow in the major region decreases as the value of ω is decreased from 1 to 0. The CEM was thus unable to accurately describe Taylor's data. The flow conditions for the data reported by Taylor, with two jets colliding to form a liquid sheet, are unlikely to be identical to that in this work where a single jet impinges on a solid target. There is no friction in the midplane, owing to symmetry, whereas there will be viscous losses and a growing boundary layer at the wall when it is solid.

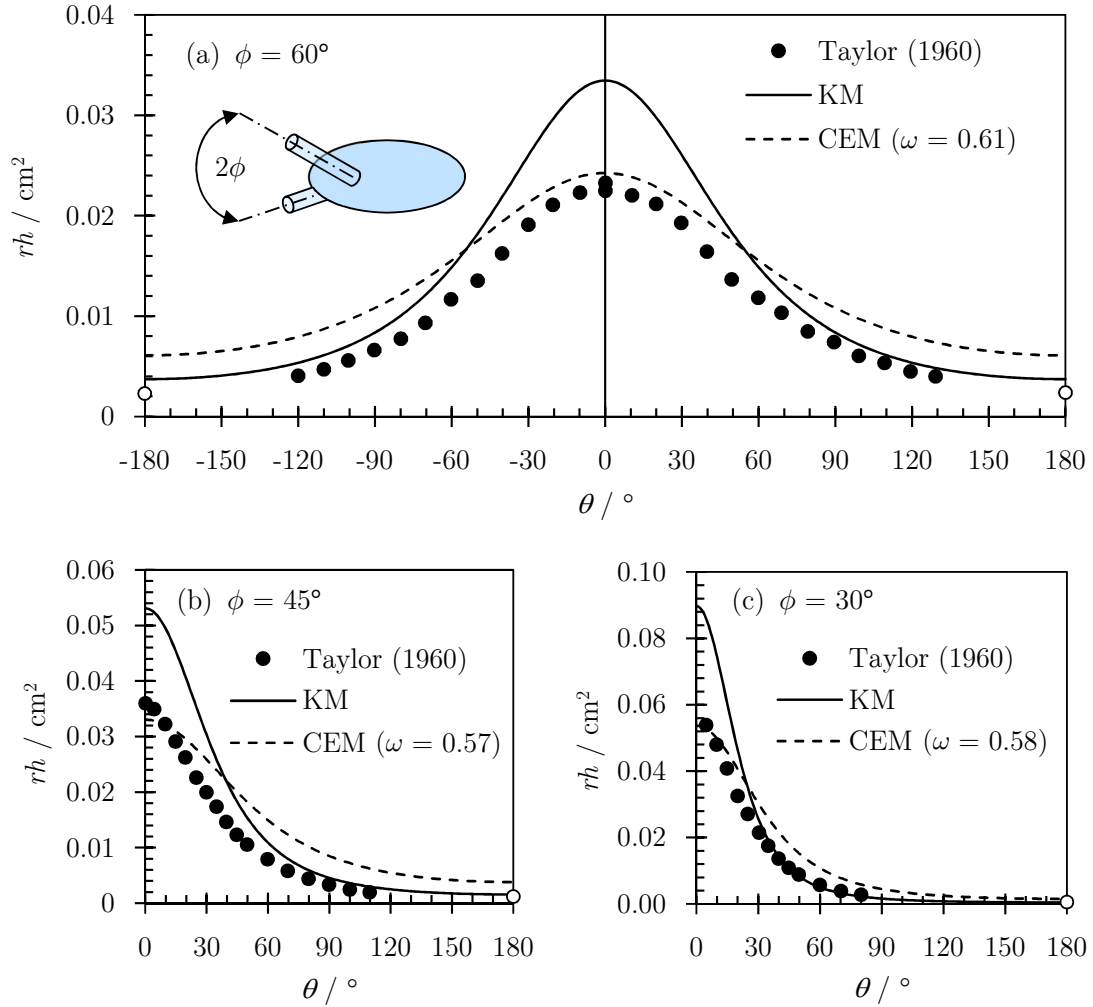


Figure 4.25: Flow distributions measured by Taylor (1960), and the KM and CEM predictions (Equation 4.37) for (a) $\phi = 60^\circ$, (b) $\phi = 45^\circ$ and (c) $\phi = 30^\circ$. Taylor estimated the values of the hollow data points at $\theta = 180^\circ$ by assuming that the inertia and surface tension forces are balanced, giving $\rho u_T^2 h / 2 = \gamma$. u_T is the liquid velocity given by $u_T = \sqrt{2gH_{\text{jet}}}$ where H_{jet} is the head of water used to generate the jet. Taylor used 2.27 mm diameter jets: a combined jet diameter of 3.21 mm ($= \sqrt{2} \times 2.27$) mm was used for the KM and CEM predictions.

4.4.3 Cleaning tests

Cleaning tests were carried out as a separate means of determining the flow distribution for inclined jets.

Normally impinging jet

Cleaning by a normally impinging horizontal jet was used to characterise the cleaning of the NIVEA[®] cream. Figure 4.26 shows the growth of the cleaned region over time for the reference case.

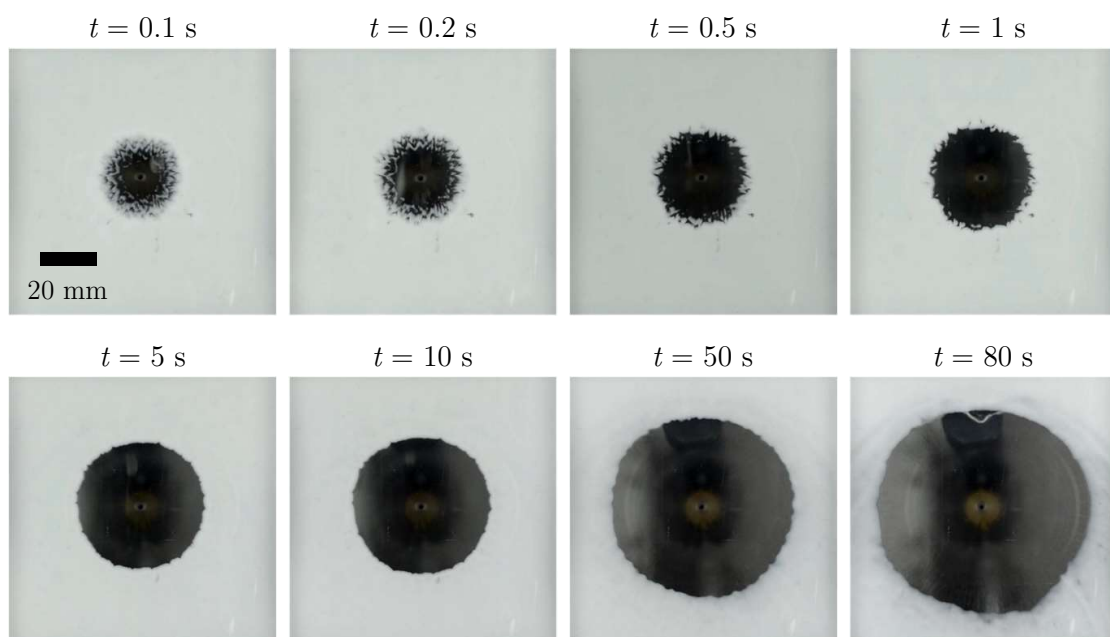


Figure 4.26: Cleaning of NIVEA[®] cream by a normally impinging jet ($Q = 2.0 \text{ L min}^{-1}$) over time. t is time elapsed after jet impingement.

Patches of uncleaned material were observed close to the cleaning front at early times across the jet flow rates studied, when $t < 0.5 - 1 \text{ s}$, but a smooth cleaning front was observed thereafter. Glover *et al.* (2016) reported the presence of similar patches of uncleaned material at early times in their study of the cleaning of polyvinyl acetate (PVA) glue.

With a normally impinging jet, the cleaned region was observed to be circular so the data were reported in terms of a_{equiv} , the radius of a circle with equal area to the cleaned region, shown in Figure 4.27.

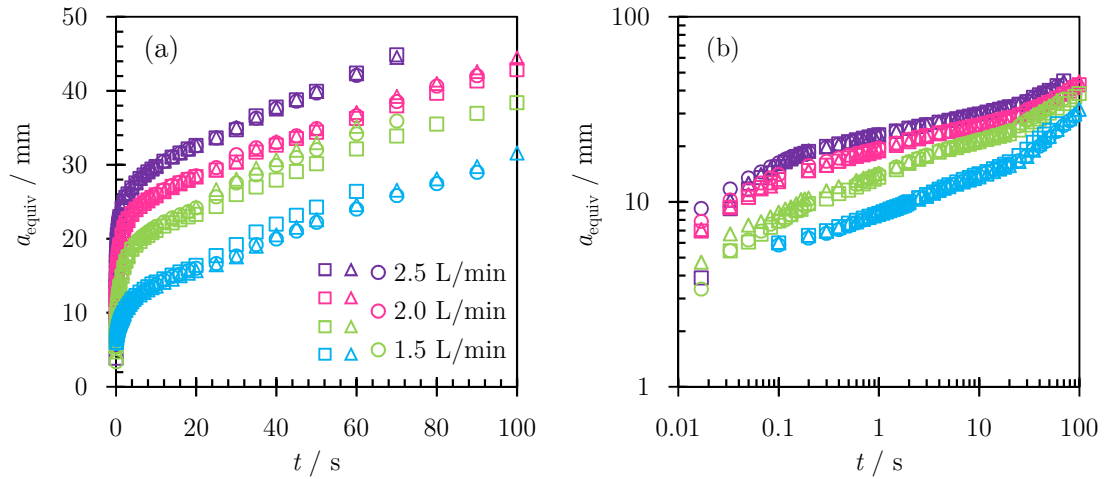


Figure 4.27: Evolution of the cleaned region over time, plotted on a (a) linear and (b) \log_{10} scale. Colour is used to indicate the jet flow rate and each test at a given jet flow rate is indicated by a different symbol. The symbol size is greater than or equal to the uncertainty in the data.

Three tests were carried out at a given flow rate to establish the repeatability, and the cleaning profiles were found to be similar. The variation observed at later times ($t > 20$ s) was attributed to the effect of soaking on the soil layer by the draining liquid film. Two distinct stages in cleaning were observed across the jet flow rates studied; namely a rapid initial growth of the cleaned region when $t < 5$ s, followed by a slower rate. Figure 4.28 shows the data plotted as cleaning rates, where M was calculated using the Wilson *et al.* (2012) hydrodynamic model (Equations 2.3, 2.7 and 2.10 combined).

Figure 4.28(a) shows the fit of the data to the simple Glover *et al.* (2016) cleaning model (Equation 2.66). The fitting was performed by eye, yielding $k' = 0.02 \text{ m s kg}^{-1}$ and $M_y = 2 \text{ N m}^{-1}$. These values of the cleaning model parameters are compared with the values obtained for other soils reported in the literature in Chapter 5 (Table 5.4).

The aim of the cleaning tests with normally impinging jets was to provide a relationship between da/dt and M to enable the rate of cleaning with inclined jets to be used to infer the local flow rate and thus the flow distribution, in an inverse calculation. With the Glover *et al.* (2016) cleaning model, $da/dt = 0$ when $M \leq M_y$, which limits the use of the model as a significant fraction of the data featured $M \leq 2 \text{ N m}^{-1}$.

A trendline was instead fitted to the cleaning rate data, shown in Figure 4.28(b), giving

$$\ln\left(\frac{da}{dt}\right) = 2.2 \ln M + 0.9 \quad 0.5 \text{ mm s}^{-1} \leq \frac{da}{dt} \leq 200 \text{ mm s}^{-1} \quad (4.38)$$

The kink observed in the data at low values of M was due to artefacts in the fitting of the curves to the data in Figure 4.27 to obtain estimates of the cleaning rate. The data in this region were excluded from the fitting as it did not provide a one-to-one mapping of da/dt to M .

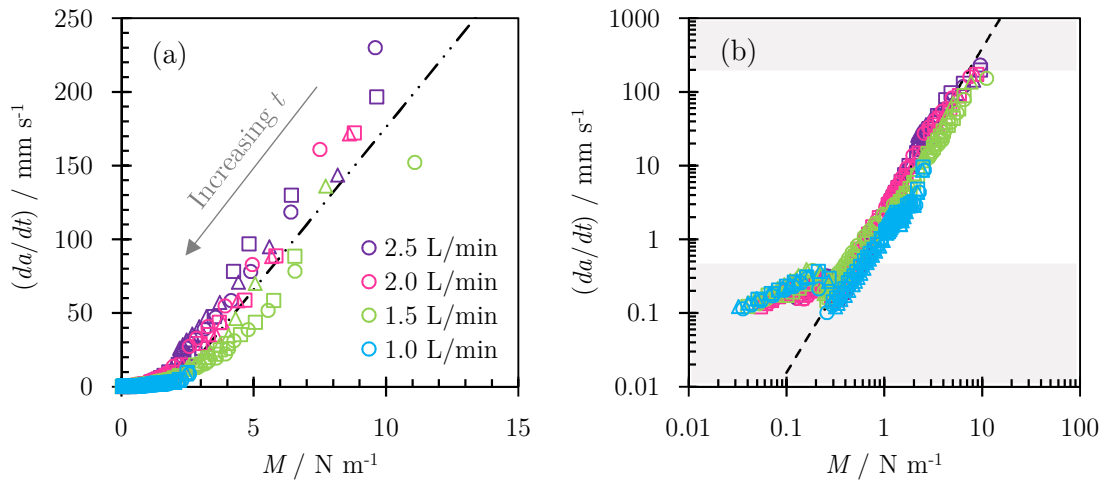


Figure 4.28: Cleaning rate data showing (a) the fit to the Glover *et al.* (2016) cleaning model (Equation 2.66), and (b) Equation 4.38. Note the \log_{10} scale on the axes in (b). The shaded region in (b) indicates data that were not used in the fitting. Colour is used to indicate the jet flow rate and each test at a given jet flow rate is indicated by a different symbol.

Inclined jets

Figure 4.29 shows an example of the growth of the cleaned region formed by an inclined jet. The cleaned region is no longer circular. Similar patches of uncleaned material were observed close to the cleaning front at early times when $t < 0.5$ -1 s. At later times, the shape of the cleaned region was not as smooth as in Figure 4.26, but is representative of the degree of variation observed with cleaning by inclined jets.

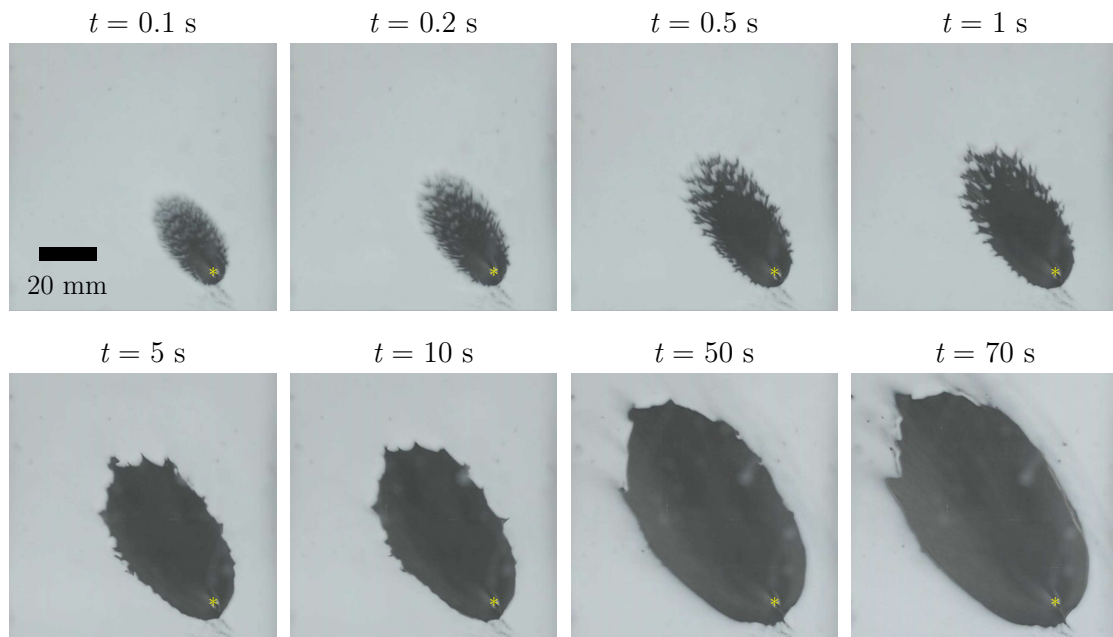


Figure 4.29: Cleaning of NIVEA[®] cream by an inclined jet ($Q = 2.0 \text{ L min}^{-1}$, $\phi = 135^\circ$, $\chi = 45^\circ$, $\phi_{\text{overall}}^* = 144.7^\circ$) over time. t is time elapsed after jet impingement. The yellow star indicates the point of jet impingement.

The growth of the cleaned region over time for all the cleaning tests conducted is shown in Figure 4.30. The cleaning profiles of inclined jets were similar to those for normally impinging jets, with initial rapid growth of the cleaned area followed by a slower increase. The variation at later times is again attributed to the effect of soaking. For a given jet flow rate, there was little effect of the jet orientation on the cleaned area. This has different implications for the design of cleaning by static and moving nozzles. For static nozzles, changing the jet orientation would have little effect on the total area cleaned. For moving nozzles, however, the jet orientation could be optimised to maximise the width of the region cleaned by the jet, thus minimising the number of passes required over the surface for cleaning.

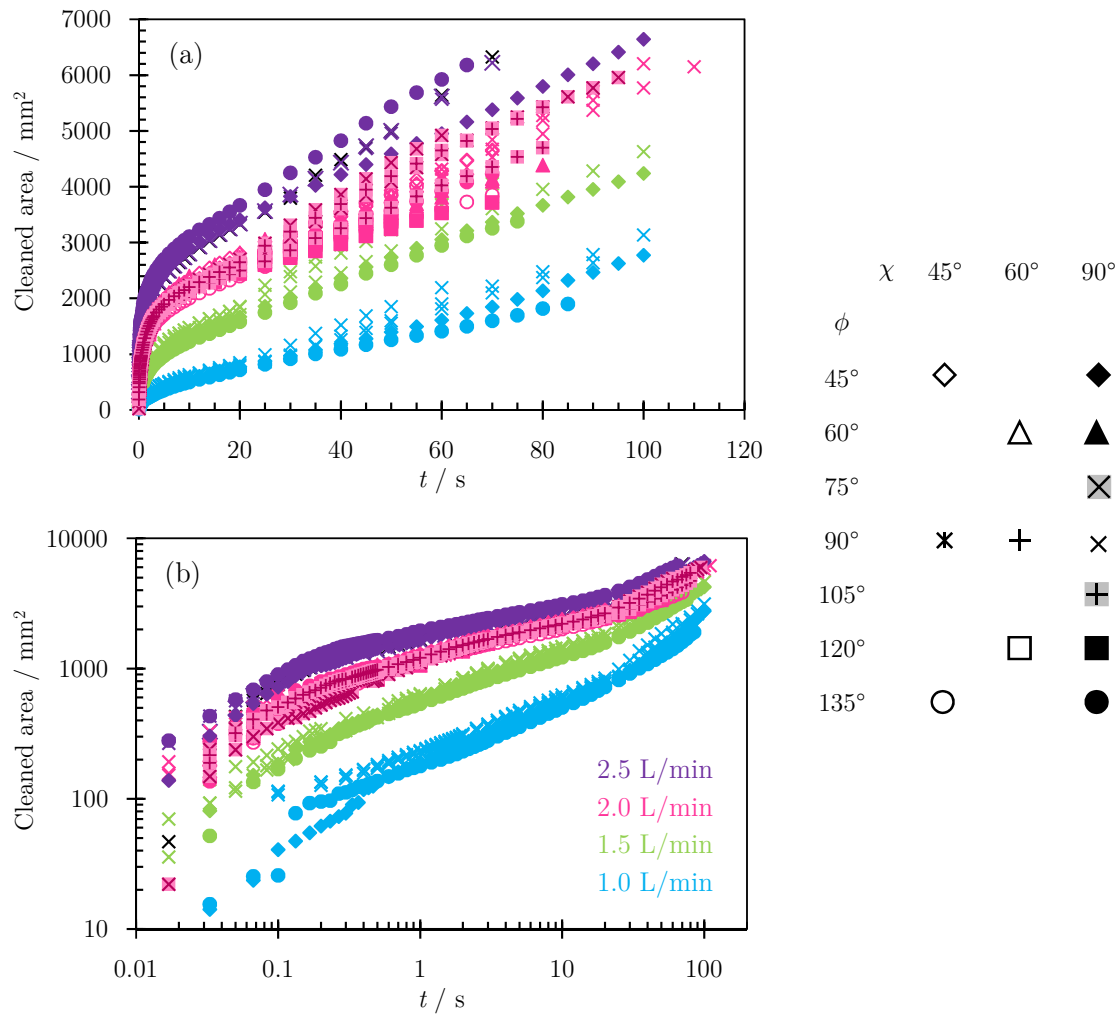


Figure 4.30: Evolution of the cleaned area over time, plotted on a (a) linear and (b) \log_{10} scale. Colour is used to indicate the jet flow rate and the symbols indicate jet orientation. Repeats of a test are shown by the same symbol. The symbol size is greater than or equal to the uncertainty in the data.

Figure 4.31(a) shows an example of the curves fitted to data of a_θ against t to obtain an estimate of the cleaning rate, da_θ/dt . Equation 4.38 was used to obtain the corresponding value of M . Figure 4.31(b) shows a plot of M against radial distance, a_θ for the cleaning data and r for the hydrodynamic model, showing how the experimental data are compared with Wilson *et al.* (2012) hydrodynamic model (Equations 2.3, 2.7 and 2.10 combined), to obtain an estimate of $Q_{\theta, \text{equiv}}$.

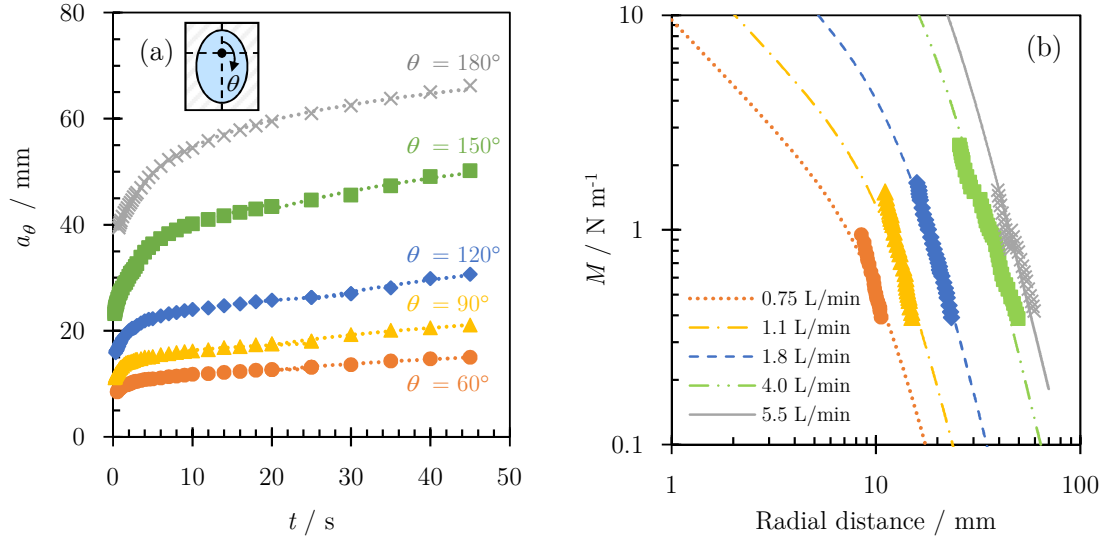


Figure 4.31: Data from an inclined jet cleaning test ($Q = 2.0 \text{ L min}^{-1}$, $\phi = 45^\circ$, $\chi = 90^\circ$, $\phi_{\text{overall}}^* = 45^\circ$). Colour is used to indicate the azimuthal angle, θ . (a) Evolution of the cleaned radius over time in different θ directions and the curves fitted to obtain an estimate of a cleaning rate, da_θ/dt . (b) Equation 4.38 was used to obtain a values of M for the da_θ/dt data from (a) and the cleaning data were compared with the curves from the Wilson *et al.* (2012) hydrodynamic model to obtain estimates of the volumetric flow rate in each θ direction, $Q_{\theta,\text{equiv}}$.

Fitting the changing ellipse flow distribution model (CEM)

The CEM was fitted to the $Q_{\theta,\text{equiv}}$ data from the cleaning tests. The fit was quantified using the fitting parameter ψ (Equation 4.36) and the minimum value of ψ gave the optimal value of ω , the best fit. Figures 4.32(a) and (b) show the results for two data sets where the jet conditions are identical to the hydrodynamic test results shown in Figures 4.20 and 4.21, respectively. The KM result is shown for comparison and is recovered with the CEM when $\omega = 1$.

As with the hydrodynamic tests, the CEM was found to provide a better fit to the experimental data than the KM result. This could be expected as the CEM has a fitting parameter while the KM has none. Figure 4.33 shows the variation in ψ with ω for the different jet orientations studied. The optimal values of ω are given in Table 4.7 and shown in Figure 4.34. There was no consistent optimum in ω . The ω values appear to lie in a band between a parabolic lower bound and an upper bound of about 0.7. All the optimal ω values lay in the range $0.51 \leq \omega \leq 0.71$.

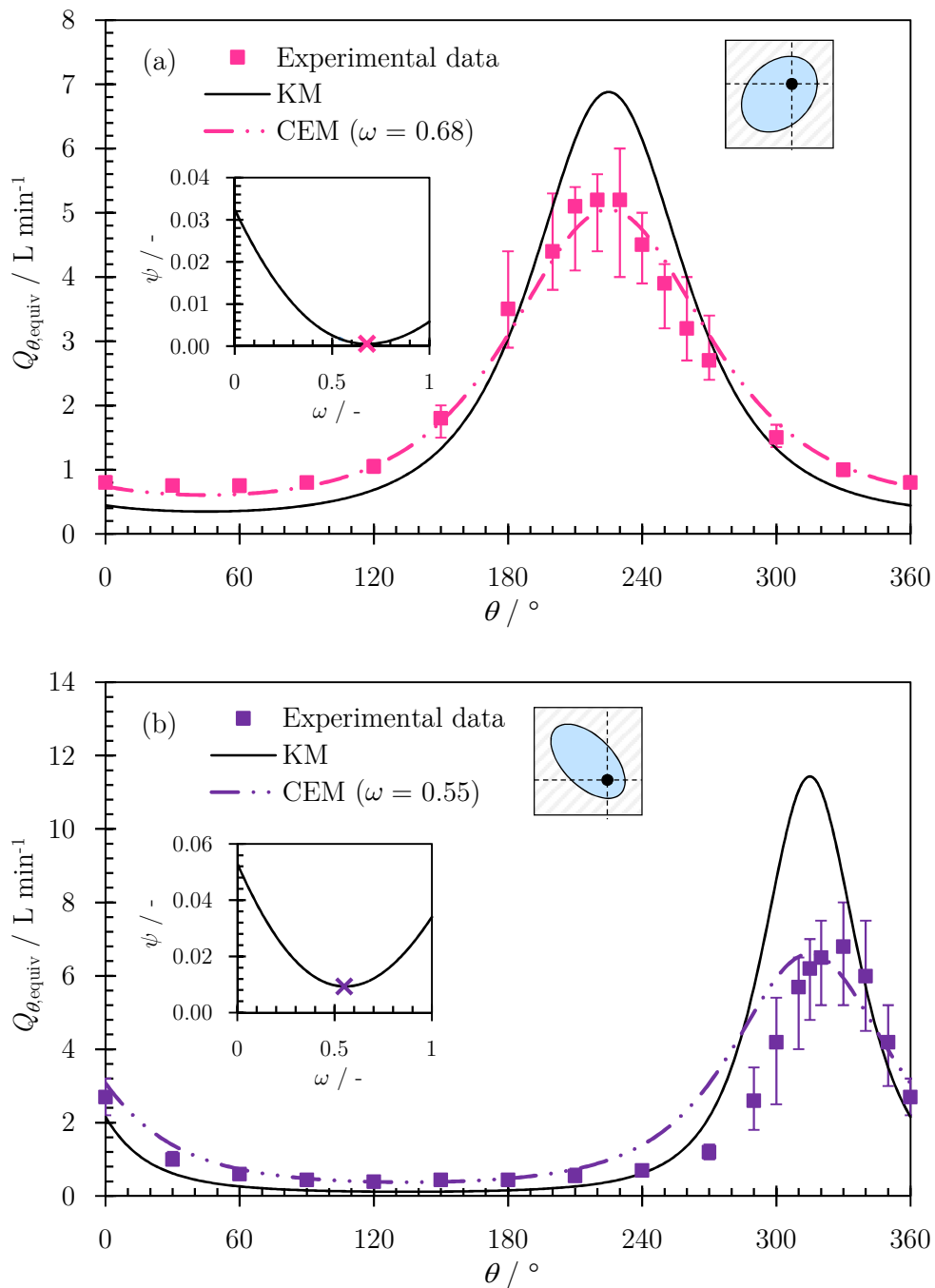


Figure 4.32: Fit of the CEM to $Q_{\theta, \text{equiv}}$ data from cleaning tests with a jet of $Q = 2.0 \text{ L min}^{-1}$: (a) $\phi = 60^\circ$, $\chi = 60^\circ$, $\phi_{\text{overall}}^* = 50.8^\circ$, and (b) $\phi = 135^\circ$, $\chi = 45^\circ$, $\phi_{\text{overall}}^* = 144.7^\circ$. The insets show the variation of the fitting parameter ψ with ω . The optimal value of ω (the best CEM fit to the data) is where ψ is a minimum.

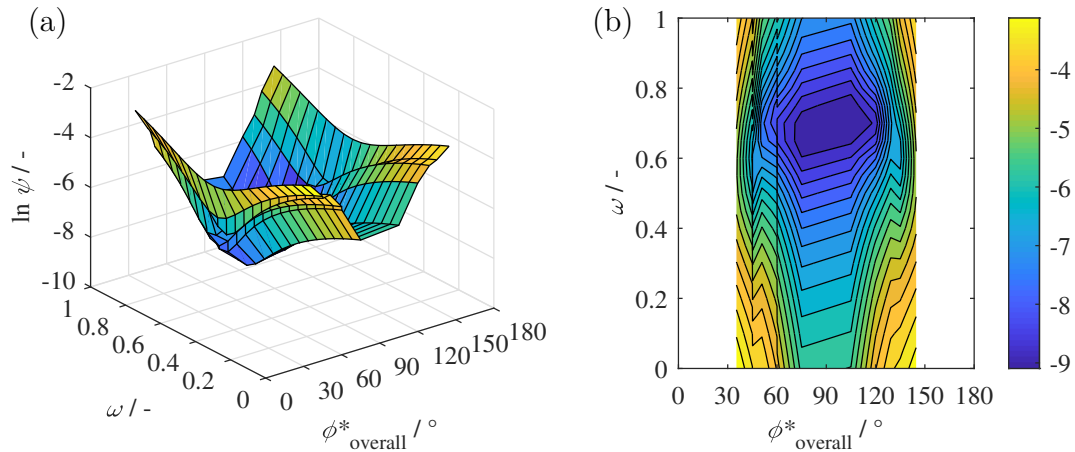


Figure 4.33: Variation of ψ (plotted as $\ln \psi$ for clarity) with ω across the different ϕ^*_{overall} values studied with $Q = 2.0 \text{ L min}^{-1}$, shown in (a) as a 3D plot and (b) as a 2D plot with the colour scale indicating the value of $\ln \psi$. Different combinations of ϕ and χ that have the same ϕ^*_{overall} value (but different θ^* values; Table 4.3) are plotted offset by $\phi^*_{\text{overall}} = 0.1^\circ$, giving the dark vertical streaks in (b).

Table 4.7: Optimal values of ω for the CEM fitted to experimental data from cleaning tests.

χ	90°	45°	60°	90°	90°
ϕ	$Q = 1.5 \text{ L min}^{-1}$	$Q = 2.0 \text{ L min}^{-1}$			$Q = 2.5 \text{ L min}^{-1}$
45°	0.54	0.56	-	0.61 ^a	0.57
60°	-	-	0.68	0.71 ^b	-
75°	-	-	-	0.67	-
90°	N/A	0.56 ^a	0.68 ^b	N/A	N/A
105°	-	-	-	0.71	-
120°	-	-	0.69	0.70	-
135°	0.51	0.55	-	0.61	0.60

^{a, b} Combinations of ϕ and χ that have the same ϕ^*_{overall} value (but different θ^* values; Table 4.3)

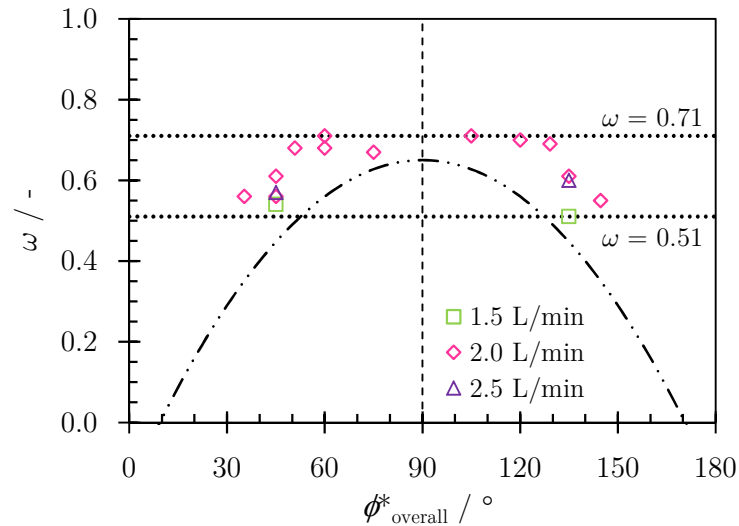


Figure 4.34: Optimal values of ω for the CEM fitted to experimental data from cleaning tests. Note that ω is undefined when $\phi_{\text{overall}}^* = 90^\circ$ (Equation 4.30). The parabolic lower bound is given by $\omega = -1 \times 10^{-4} (\phi_{\text{overall}}^* - 90^\circ) + 0.65$, where ϕ_{overall}^* is in degrees.

4.4.4 Review of data sets

Hydrodynamic and cleaning tests

Figure 4.35 shows a combined set of results from the hydrodynamic and cleaning tests, illustrative of the general trends observed across all jet flow rates and jet orientations studied. More hydrodynamic tests were conducted than cleaning tests. For cases where both hydrodynamic and cleaning tests were conducted, the data from both tests expressed as $Q_{\theta, \text{equiv}}$ are similar. The experimental data is described more closely by the CEM than the KM result.

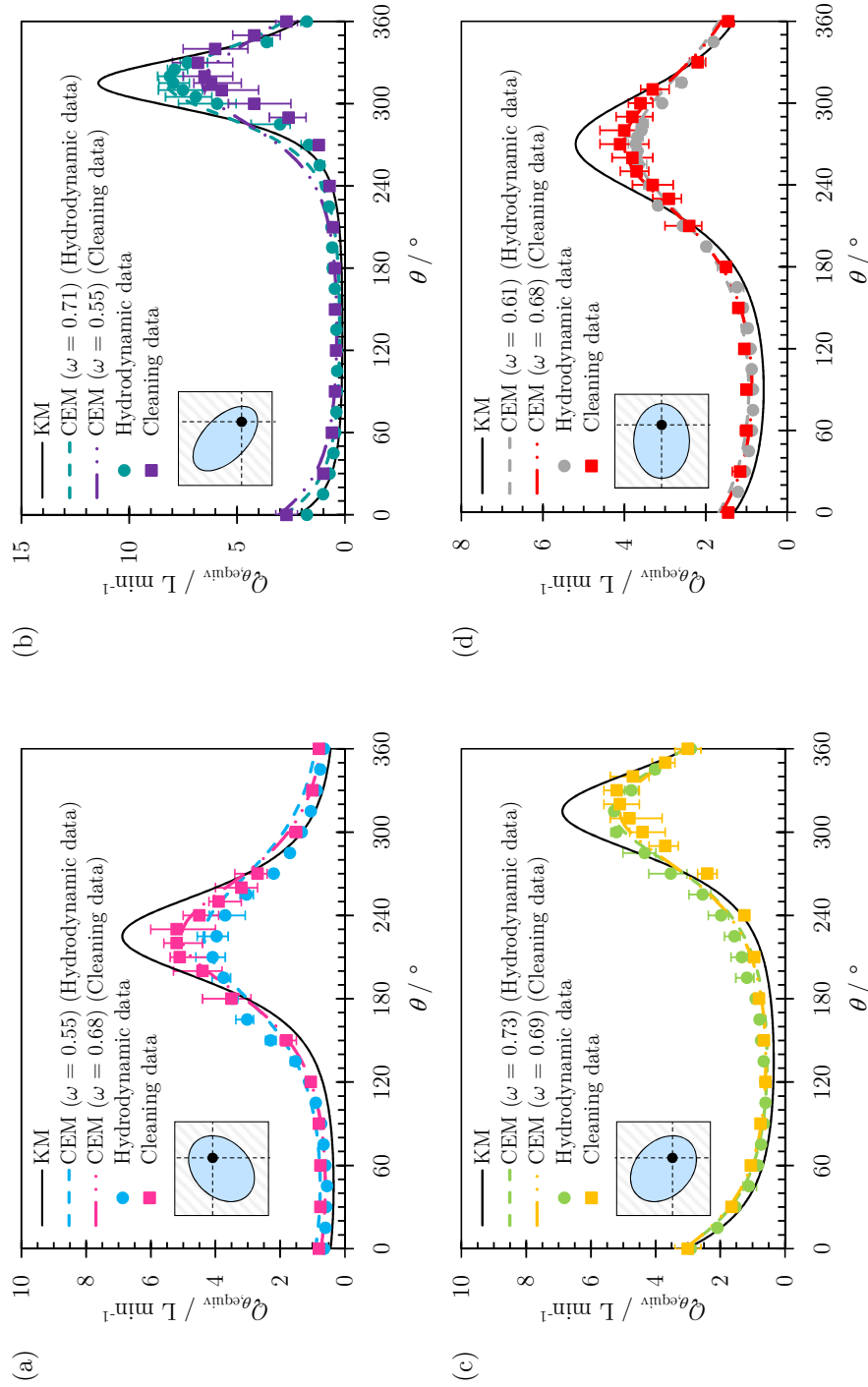


Figure 4.35: Combined results of the hydrodynamic and cleaning tests for $Q = 2.0 \text{ L min}^{-1}$ and (a) $\phi = 60^\circ$, $\chi = 60^\circ$, $\phi_{\text{overall}}^* = 50.8^\circ$ (Figures 4.20(a) and 4.32(a)), (b) $\phi = 135^\circ$, $\chi = 45^\circ$, $\phi_{\text{overall}}^* = 144.7^\circ$ (Figures 4.21(a) and 4.32(b)), (c) $\phi = 120^\circ$, $\chi = 60^\circ$, $\phi_{\text{overall}}^* = 129.2^\circ$ (Figure 4.17(c)), and (d) $\phi = 90^\circ$, $\chi = 60^\circ$, $\phi_{\text{overall}}^* = 60^\circ$ (Figure 4.17(a)). Optimal fits of the CEM to both hydrodynamic and cleaning tests are shown.

In Figure 4.36, the results from all the hydrodynamic and cleaning tests are plotted in the form of the distance of the source from the axis of the jet. There was more scatter in the data from the hydrodynamic tests (Figure 4.36(a)) than with the cleaning tests (Figure 4.36(b)), but a similar trend is evident. A line of best fit through the data from both sets of tests yielded

$$\frac{S_{\text{model}}}{r_0} = -0.8071 \phi_{\text{overall}}^* + 1.2522 \quad (4.39)$$

with ϕ_{overall}^* in radians. The regression coefficient, R^2 , was 0.9628.

This linear relationship between S_{model}/r_0 and ϕ_{overall}^* obtained with the CEM differs from the KM result, $S_{\text{model}}/r_0 = \cot \phi_{\text{overall}}^*$ (Equation 4.20).

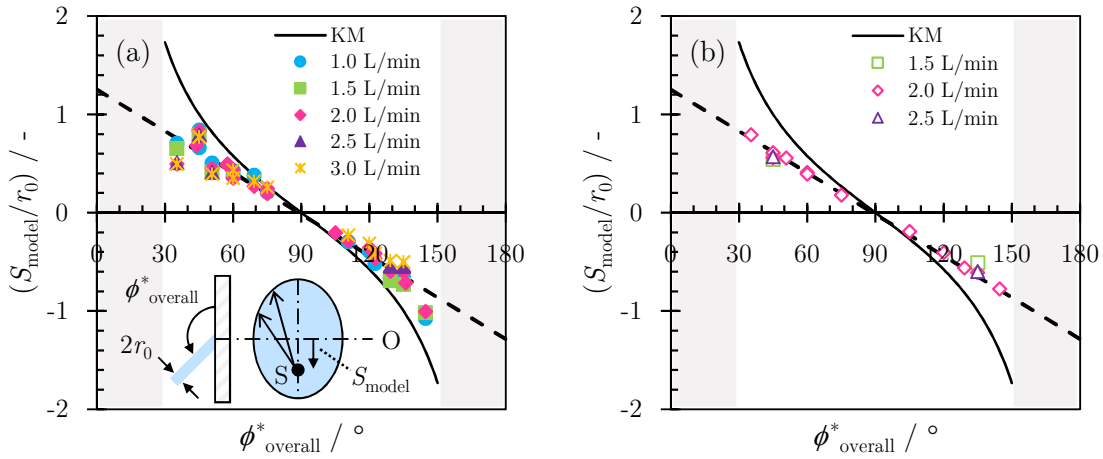


Figure 4.36: Distance of the source from the axis of the jet, S_{model} , scaled by the jet radius to give a non-dimensional term, S_{model}/r_0 , against the overall jet angle, ϕ_{overall}^* (Equation 4.7) for (a) hydrodynamic and (b) cleaning tests obtained with Equation 4.28 using the optimal value of ω from the CEM fits to the experimental data. The KM result (Equation 4.20) is shown by the solid black locus and the dashed line shows Equation 4.39. Only one jet radius ($r_0 = 1$ mm) was used in all the tests.

The flow distribution with the CEM corresponds to that of a jet with a modified angle, ϕ'_{overall} , instead of the jet angle from the geometric transformation, ϕ_{overall}^* . The value of ϕ'_{overall} is determined by ω (Equations 4.30 and 4.32). Figure 4.37 shows the data plotted as ϕ'_{overall} against ϕ_{overall}^* .

A line of best fit through the data from both the hydrodynamic and cleaning tests yielded

$$\phi'_{\text{overall}} = 0.715 \phi^*_{\text{overall}} + 0.4566 \quad (4.40)$$

with ϕ'_{overall} and ϕ^*_{overall} both in radians. The regression coefficient, R^2 , was 0.9758.

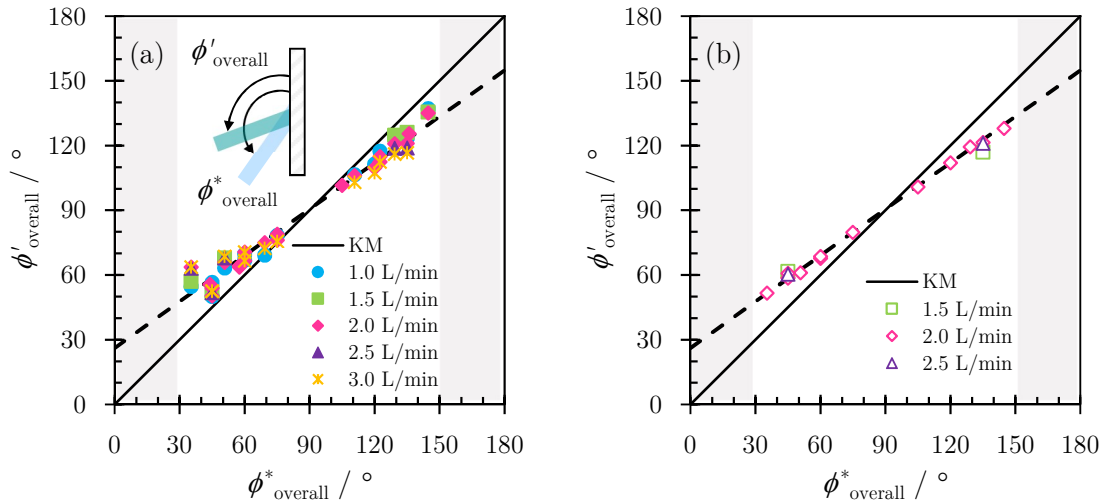


Figure 4.37: Relationship between the overall modified jet angle, ϕ'_{overall} , from the CEM and the overall jet angle, ϕ^*_{overall} , from the geometric transformation (Equation 4.7) for (a) hydrodynamic and (b) cleaning tests. ϕ'_{overall} was obtained from Equations 4.30 and 4.32 with the optimal value of ω from the CEM fits to the experimental data. The KM result (recovered when $\omega = 1$, giving $\phi'_{\text{overall}} = \phi^*_{\text{overall}}$) is shown by the solid black locus and the dashed line shows Equation 4.40.

Results in the literature

Baghel *et al.* (2020) investigated the heat transfer characteristics of liquids jets impinging obliquely on a uniformly heated horizontal plate. They obtained profiles for the Nusselt number (ratio of convective to conductive heat transfer) along the plane of jet impingement. The peak in the Nusselt number profile is taken to be the location of the source of the flow in the jet as it is assumed that at the source, there is no boundary layer in the liquid film, giving a maximum rate of convective heat transfer. Figure 4.38 shows their data, interpreted and plotted in the form of Figure 4.36, where S is the distance of the source from the axis of the jet.

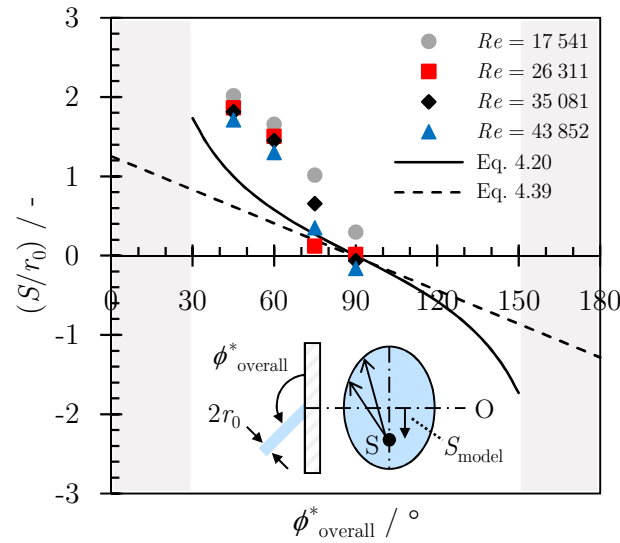


Figure 4.38: Data from Figure 12 of Baghel *et al.* (2020) interpreted and plotted in the form of Figure 4.36, showing the non-dimensional distance of the source from the axis of the jet for different jet angles and Reynolds numbers. The KM result (Equation 4.20) is shown by the solid black locus and the dashed line shows Equation 4.39.

The data from Baghel *et al.* (2020) differ from both the KM result and the values obtained in this work (Equation 4.39). Their values are consistently larger, by a factor of up to 2x. Their data also show variation in the location of the source with Re . This could be due to the uncertainties associated with heat transfer measurements, but also reflects the challenge in obtaining accurate experimental data for the location of the source of the flow.

Kate *et al.* (2007; 2008) reported data for inclined circular water jets impinging on a horizontal glass target. In the former paper they proposed a scaling relation that gives the location of the hydraulic jump (Equation 2.37) based on the work by Bohr *et al.* (1993), but did not compare this relation with their experimental data.

The Kate *et al.* (2007; 2008) data are compared with their scaling relation (Equation 2.37), the KM result (Equation 4.19) and the CEM result (Equation 4.31 with jet angle from Equation 4.40) in Figures 4.39, 4.40, 4.41 and 4.42.

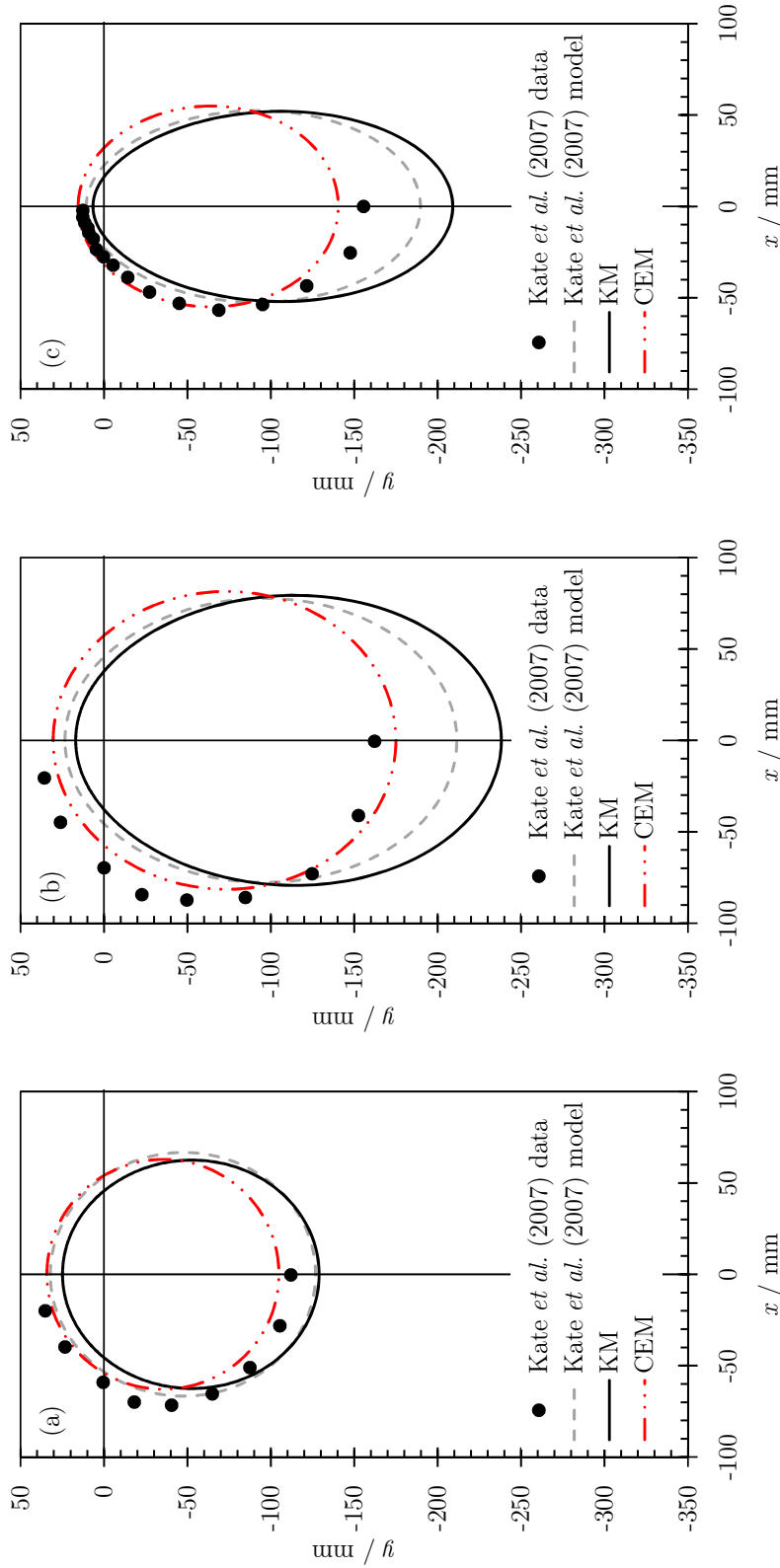


Figure 4.39: Location of the hydraulic jump reported by Kate *et al.* (2007) in their Figure 7 compared with their scaling relation (Equation 2.37), the KM result (Equation 4.19) and the CEM result (Equation 4.31 with jet angle from Equation 4.40).
 (a) $r_0 = 3.5 \text{ mm}$, $Q = 5.83 \times 10^{-5} \text{ m}^3 \text{ s}^{-1}$ (3.5 L min^{-1}), $Re = 10\,600$, $\phi_e = 60^\circ$, $\phi'_{\text{overall}} = 60^\circ$, $\phi^*_{\text{overall}} = 69^\circ$; (b) $r_0 = 4.35 \text{ mm}$, $Q = 8.33 \times 10^{-5} \text{ m}^3 \text{ s}^{-1}$ (5.0 L min^{-1}), $Re = 12\,200$, $\phi_e = 45^\circ$, $\phi'_{\text{overall}} = 45^\circ$, $\phi^*_{\text{overall}} = 58^\circ$; and (c) $r_0 = 3.25 \text{ mm}$, $Q = 5 \times 10^{-5} \text{ m}^3 \text{ s}^{-1}$ (3.0 L min^{-1}), $Re = 9\,800$, $\phi_e = 35^\circ$, $\phi'_{\text{overall}} = 35^\circ$, $\phi^*_{\text{overall}} = 51^\circ$.

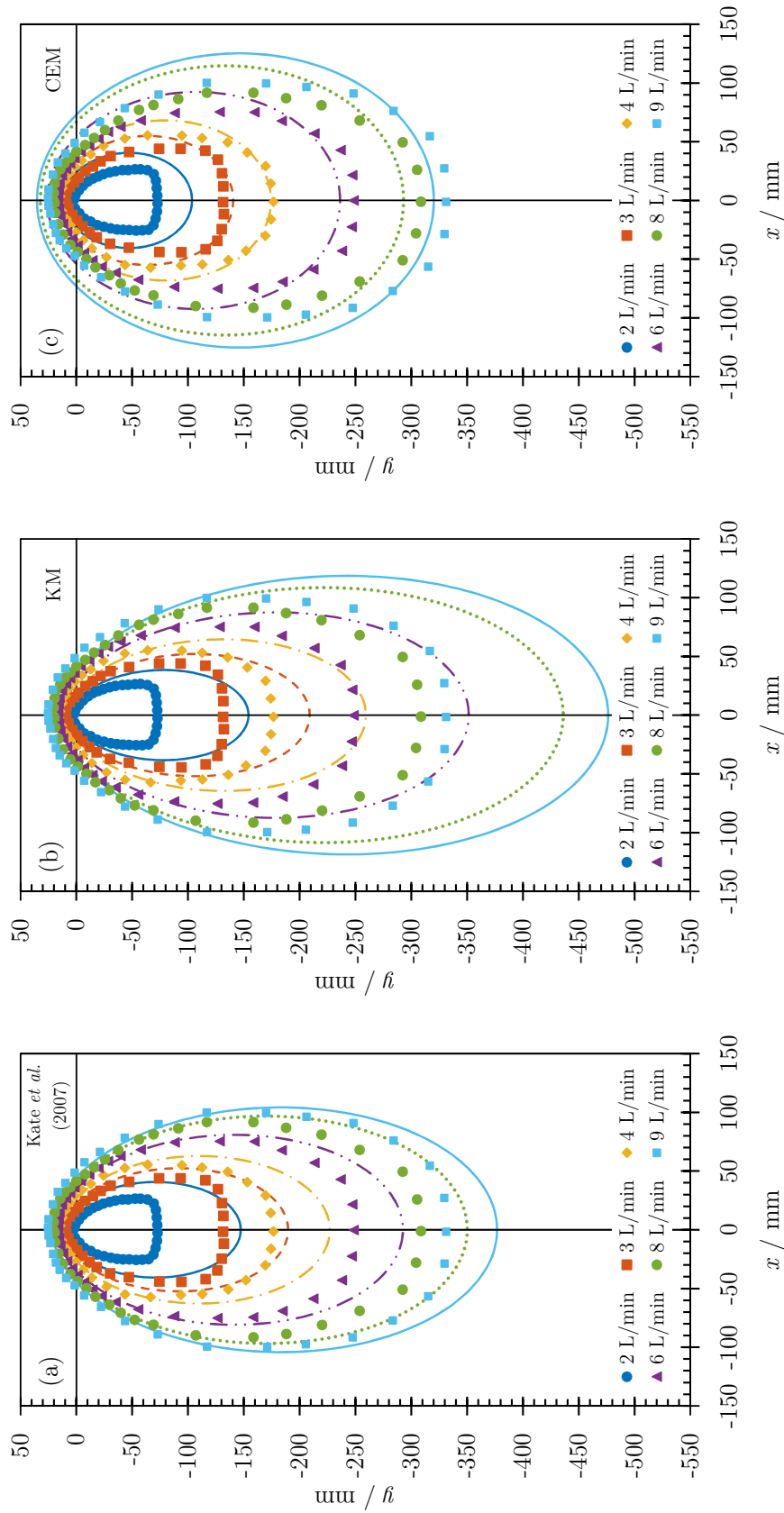


Figure 4.40: Location of the hydraulic jump reported by Kate *et al.* (2008) in their Figure 12 for $d_N = 6.5 \text{ mm}$, $\phi_e = 35^\circ$ and $6500 < Re < 29400$ compared with the (a) Kate *et al.* (2007) scaling relation (Equation 2.37), (b) KM result (Equation 4.19, $\phi_{\text{overall}}^* = 35^\circ$) and the CEM result (Equation 4.31 with jet angle from Equation 4.40, $\phi_{\text{overall}}^* = 51^\circ$).

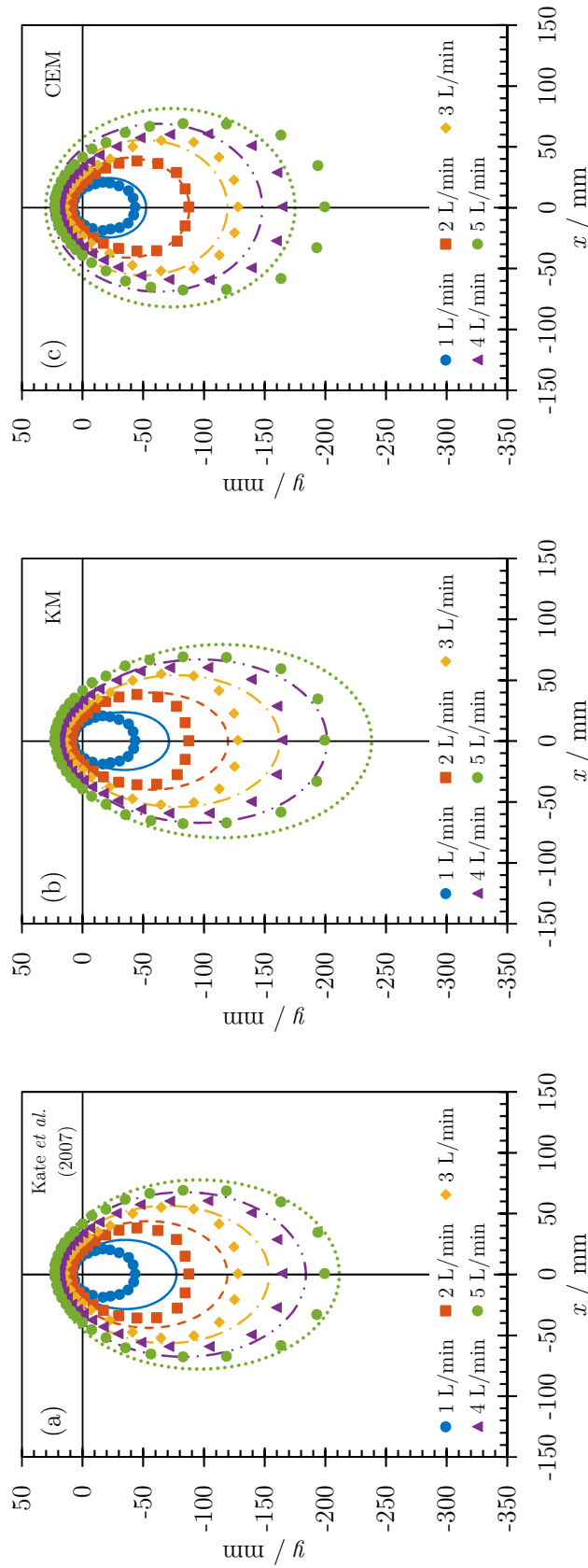


Figure 4.41: Location of the hydraulic jump reported by Kate *et al.* (2008) in their Figure 12 for $d_N = 6.5$ mm, $\phi_e = 45^\circ$ and $3300 < Re < 16300$ compared with the (a) Kate *et al.* (2007) scaling relation (Equation 2.37), (b) KM result (Equation 4.19, $\phi_{\text{overall}}^* = 45^\circ$) and the CEM result (Equation 4.40, $\phi_{\text{overall}}^* = 58^\circ$).

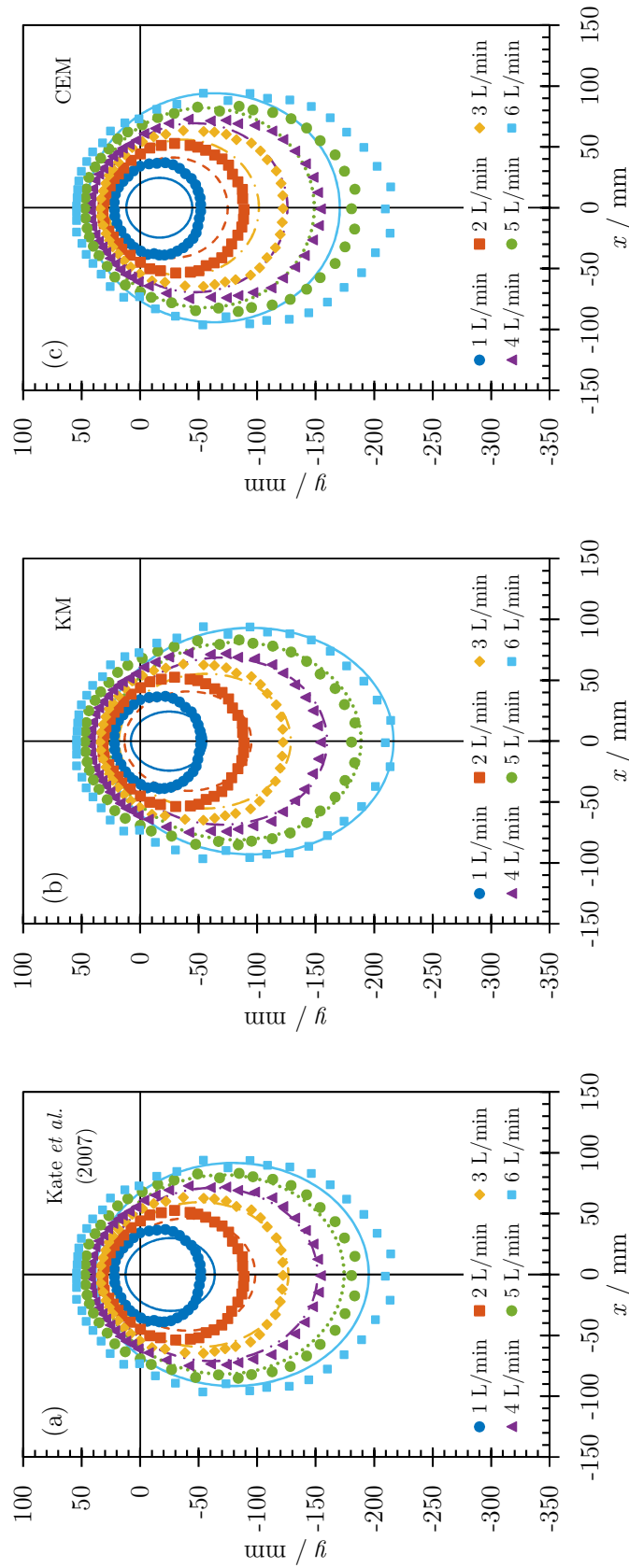


Figure 4.42: Location of the hydraulic jump reported by Kate *et al.* (2008) in their Figure 12 for $d_N = 6.4$ mm, $\phi_e = 55^\circ$ and $3300 < Re < 19900$ compared with the (a) Kate *et al.* (2007) scaling relation (Equation 2.37), (b) KM result (Equation 4.19, $\phi_{\text{overall}}^* = 55^\circ$) and the CEM result (Equation 4.31 with jet angle from Equation 4.40, $\phi_{\text{overall}}^* = 65^\circ$).

The results in Figure 4.39 show that the CEM gives better agreement to the Kate *et al.* (2007) experimental data the scaling relation or the KM.

In Figures 4.40, 4.41 and 4.42 with data from Kate *et al.* (2008), there is considerable variation between the experimental data and the predictions from all the models. None of the models provided a superior fit over the others.

The Kate *et al.* (2007; 2008) data are the steady state locations of the hydraulic jump formed by an inclined jet impinging on a horizontal target, where the hydraulic jump is surrounded by a thick film of liquid that pools on the target. The KM and CEM flow distributions are used with the Wilson *et al.* (2012) hydrodynamic model which considers the initial hydraulic jump formed when a jet impinges on a dry target, and are expected to predict a larger RFZ.

4.5 Conclusions

Kate *et al.* (2007) presented a geometric argument for the flow distribution of an inclined jet but this has been shown to overpredict the flow in the major flow region and underpredict the flow in the minor flow region. Three different flow distributions were developed as an alternative: the circular, moving stagnation point and changing ellipse models. The changing ellipse model was found to be the most effective model and was compared at length with experimental data from hydrodynamic and cleaning tests.

A geometric transformation was developed to describe jets inclined in both the horizontal and vertical planes by a single, overall jet angle, ϕ_{overall}^* , and jets of varying orientations were used in the tests. Attempts were made to obtain direct measurements of the local liquid flow rate, but this could not be achieved with the experimental setup available. The flow distribution was instead obtained from hydrodynamic tests, using the location of the hydraulic jump, and from cleaning tests. With the cleaning tests, the flow distribution was inferred based on the rate of cleaning of the probe soil, where the cleaning behaviour had been characterised using a normally impinging jet. The flow distributions obtained in the both the hydrodynamic and cleaning tests were consistent and they differed from the Kate *et al.* (2007) result. The heat transfer measurements of Baghel *et al.* (2020) also yielded a different trend in the location of the source of the flow.

The parameter of the changing ellipse model, ω , which gives the modified jet angle ϕ'_{overall} , is not predicted *a priori* so an empirical relationship was obtained for ϕ'_{overall} against ϕ^*_{overall} . The model was then compared with experimental data reported in the literature but it did not yield a superior fit over the Kate *et al.* (2007) result.

An estimate to the Wilson *et al.* (2012) hydrodynamic model was used in this work as it yielded simple analytical solutions. The Bhagat and Wilson (2016) hydrodynamic model provides a more accurate description of the flow in the liquid film when a jet impinges on a target, but is more complex and requires numerical calculations. Further work could be undertaken to revisit the data collected in this work using this hydrodynamic model. Significant changes to the overall trends and results are not expected.

The properties of the thin and fast moving films generated by impinging jets, such as the film thickness and velocity, are challenging to measure. Other direct measurements techniques such as particle image velocimetry (PIV), could enable a more accurate and complete set of experimental data on the liquid flow distribution to be obtained. Further work is required to elucidate the fundamental flow behaviour of an inclined jet impinging on a surface. It has thus far been assumed that there are no losses in the jet footprint due to the change in direction or wall friction. Full numerical simulations, which will be complex and computationally expensive, are required to provide further insight.

Chapter 5

Cleaning by intermittent jets

5.1 Introduction

This chapter reports a systematic study of the cleaning of soft solid soil layers in the absence of soaking effects, when a coherent water jet is applied intermittently. Such materials often pose challenges in cleaning and can require high water consumption or the use of chemicals: reducing either of these has immediate benefit for the sustainability of cleaning operations.

Fuchs *et al.* (2017) reported that cleaning by impinging jets can be enhanced while consuming less water by using intermittent jets, whereby the flow is repeatedly turned on and off, generating a series of regular accelerations. This is investigated here for a series of viscous soil layers, where the inertia in the jet is large enough to ensure that the footprint region is cleaned quickly and enhancement of cleaning in the radial flow zone (RFZ) is sought. Removal beyond the RFZ is not considered, as this is usually associated with a soil that does not pose problems in cleaning.

Different pulsing strategies can be compared in terms of a ratio of timescales, T , relating a characteristic timescale of the flow, t_{flow} , to the reaction or forcing timescale, t_{process} ,

$$T = \frac{t_{\text{flow}}}{t_{\text{process}}} \quad (5.1)$$

Slow processes, such as soaking to soften soiling layers (*e.g.* Yang *et al.*, 2019a; 2019b), constitute cases where $T \rightarrow 0$. Ultrasonic assisted cleaning represents an example with large T .

For an impinging jet, two values of t_{flow} can be identified. The first is that associated with jet breakup, giving a series of droplets. For the simplest case of breakup caused by the Plateau-Rayleigh instability with periodicity t_{breakup} , this gives

$$T = \frac{t_{\text{breakup}}}{t_{\text{process}}} = \frac{2.9}{t_{\text{process}}} \sqrt{\frac{\rho r_0^3}{\gamma}} \quad (5.2)$$

The second characteristic timescale is that associated with formation of the hydraulic jump (and establishment of the RFZ), t_{jump} , which can be estimated using the Wilson *et al.* (2012) hydrodynamic model (Equation 3.32), *viz.*

$$T = \frac{t_{\text{jump}}}{t_{\text{process}}} \approx \frac{0.0477 \rho Q}{t_{\text{process}} \gamma} \quad (5.3)$$

Figure 5.1 shows a range of jet behaviours. The intermittent jets used in this work result in regular spurts of the jet impinging on the target, giving a jet application profile of a series of rectangular pulses (Figure 5.1(b)). This represents an intermediate stage between the two limits of jet behaviour, namely a coherent continuous jet (Figure 5.1(a)), and complete jet breakup into discrete droplets (Figure 5.1(c)).



Figure 5.1: Schematic of different jet impingement conditions: (a) a coherent continuous jet, (b) a series of rectangular pulses, and (c) complete jet breakup into droplets.

For the water jets employed in this work ($r_0 = 1 \text{ mm}$, $\rho = 1000 \text{ kg m}^{-3}$, $\gamma = 0.073 \text{ N m}^{-1}$ and $Q = 2.0 \text{ L min}^{-1}$), the two characteristic timescales are comparable with $t_{\text{breakup}} \approx 11 \text{ ms}$ and $t_{\text{jump}} \approx 22 \text{ ms}$, corresponding to frequencies of 90 Hz and 45 Hz, respectively. t_{process} was taken to be the length of time for which the jet impinges on the target in each period, t_{on} , and $t_{\text{on}} = 630 \text{ ms}$ or 60 ms . This gives $T = 0.035$ or 0.37 for the jets, calculated by Equation 5.3. The Fuchs *et al.* (2017) study employed a similar water jet with $r_0 = 0.845 \text{ mm}$ and $Q \approx 2.5 \text{ L min}^{-1}$, giving $t_{\text{breakup}} \approx 8 \text{ ms}$ and $t_{\text{jump}} \approx 27 \text{ ms}$. The timescales were also similar, with $83 \text{ ms} \leq t_{\text{on}} \leq 1.5 \text{ s}$ and $0.018 \leq T \leq 0.33$.

The enhancement reported by Fuchs *et al.* (2017) was shown to be related to soaking effects, which introduces a chemical interaction timescale to the problem. The work reported in this chapter focused on cleaning layers free of soaking effects to investigate whether the hydrodynamics of an intermittent jet alone enhance cleaning.

Much of the work in this chapter has been published in the *Journal of Cleaner Production* (Volume 283, Article 124660) in 2021 as ‘Cleaning viscous soil layers off

walls by intermittent impinging jets' with co-author D. I. Wilson. The rheological tests were performed by Rubens Rosario Fernandes and the toothpaste particle size distributions were measured by Georgina Cuckston. The modified apparatus was commissioned by MEng students Justin Ng and Nene Yamasaki as part of their Chemical Engineering Tripos Part IIB research project, co-supervised by the author.

5.2 Materials and methods

5.2.1 Intermittent jet apparatus

Further modifications were made to the impinging jet apparatus described in Section 4.3.3. A schematic is shown in Figure 5.2.

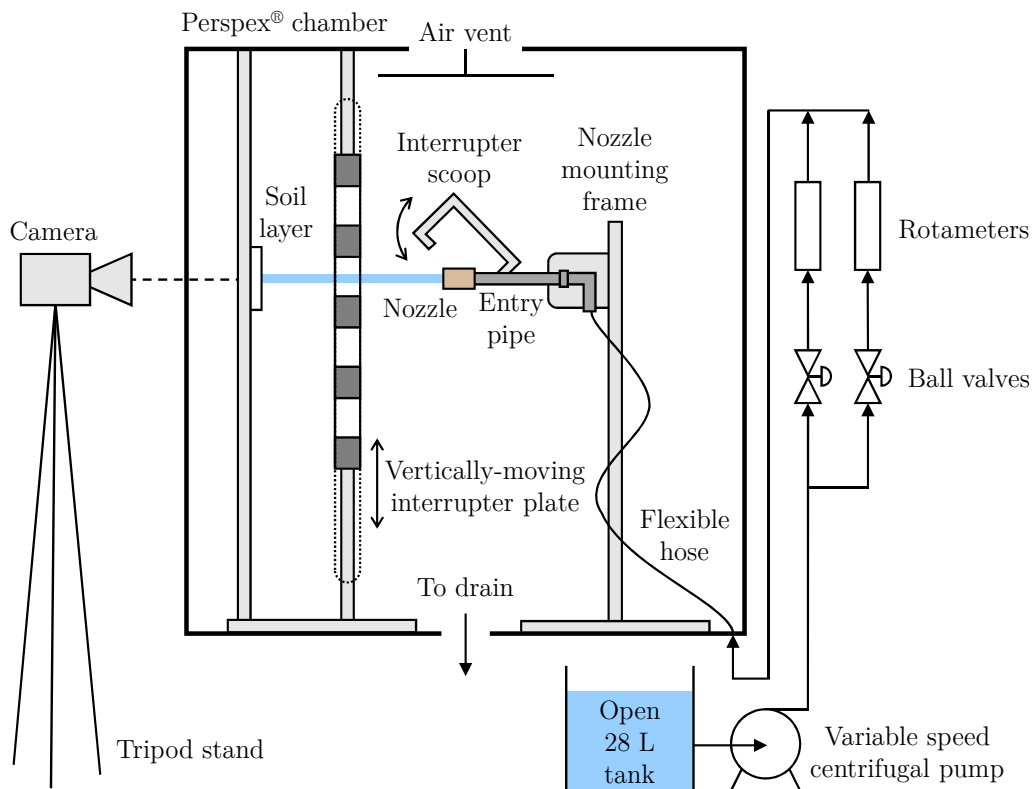


Figure 5.2: Schematic of the modified impinging jet apparatus.

Tests were performed at room temperature (20–22°C), using deionised water as the test liquid. The brass 55° convergent entry nozzle with bore diameter $d_N = 2$ mm was used. The pump speed was set to give a volumetric flow rate of $Q = 2.0$ L min⁻¹ through the nozzle, giving $U_0 = 10.6$ m s⁻¹, $Re = 21\,200$ and $We = 3\,100$. Under these conditions the jet dynamics lie in the first wind-induced regime (Lin and Reitz,

1998) (Table 2.2) with an expected breakup length (Grant and Middleman, 1966) (Equation 2.30) of 220 mm. The pump was allowed to run for at least 30 s before cleaning was started to ensure that a stable jet had formed. An interrupter scoop was placed over the end of the nozzle during this initial period to divert the jet away from the target. The deionised water was not recirculated. Normally impinging horizontal jets were used in all tests and the nozzle was located a horizontal distance of 105 mm from the vertical target to ensure that the jet was coherent.

To generate an intermittent jet, a Perspex[®] interrupter plate with external dimensions $360 \times 600 \times 5$ mm with slots and gaps of heights h_s and h_g , respectively, was located between the nozzle and target. A two-way variable speed motor moved the plate up or down to provide periodic disruption of the continuous horizontal jet, shown in Figure 5.3.

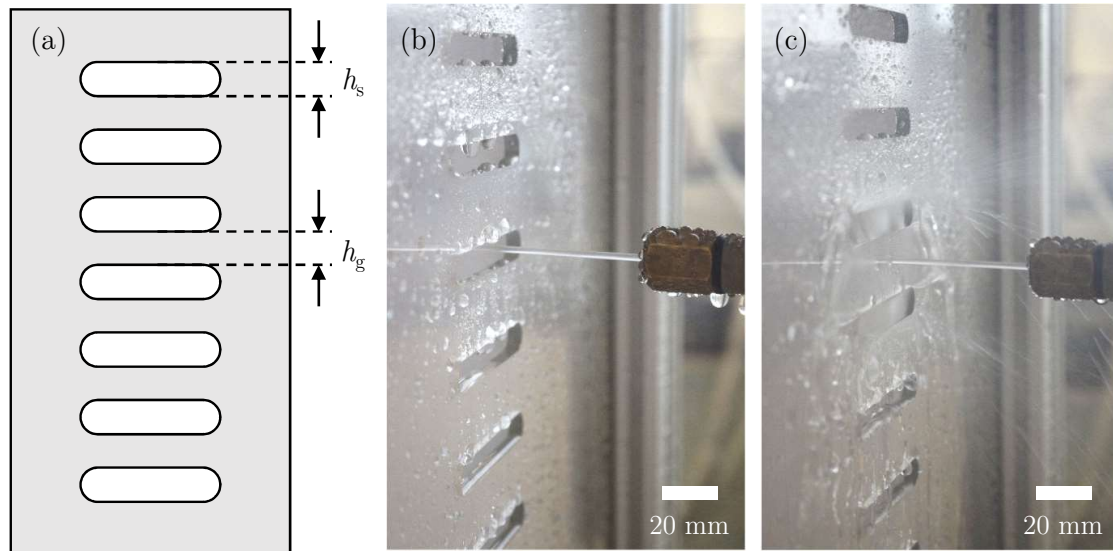


Figure 5.3: (a) Schematic of an interrupter plate; photographs showing the jet (b) passing through a slot in the plate, and (c) disrupted by the plate ($h_s = 9.5$ mm, $h_g = 20.5$ mm).

This method of generating an intermittent jet ensured that there was a stable jet with no acceleration or deceleration out of the nozzle. A range of jet interruption periods were investigated by using two different interrupter plates and various traverse speeds. Table 5.1 summarises the interrupter plate dimensions and the periods studied. t_{on} is the length of time the jet is imposed on the target in each period and t_{off} is the length of time the jet is interrupted from impinging on the target in each period. The T values are similar to those investigated by Fuchs *et al.* (2017): $T < 1$ so the jet is applied for longer than it takes to establish the RFZ and the response is expected to

be a combination of any enhancement associated with acceleration in addition to continuous cleaning behaviour.

Cut-off switches on the motor's belt drive ensured that the interrupter plate did not exceed the maximum travel on the frame. The traverse distance was limited to approximately 500 mm, so tests requiring longer durations required the motor direction to be reversed manually when the cut-off switch at either end was activated. Cleaning by a continuous jet was also performed to provide a control. The imaging and image analysis were carried out as described in Section 4.3.3.

Table 5.1: Key dimensions of the interrupter plates used and jet interruption periods studied.

h_s / mm	h_g / mm	Number of slots	Vertical traverse speed / mm s ⁻¹	Duty cycle ^a	Jet imposed, t_{on} / ms	Jet disrupted, t_{off} / ms	T / - (Eq. 5.3)	Periodicity ^b / Hz
9.5 ± 0.1	20.5 ± 0.1	16	15 ± 5	0.32	630 ± 10	1370 ± 10	0.035	0.5
9.5 ± 0.1	20.5 ± 0.1	16	155 ± 5	0.32	60 ± 10	130 ± 10	0.37	5.3
9.5 ± 0.1	5.4 ± 0.1	30	15 ± 5	0.64	630 ± 10	360 ± 10	0.035	1.0
9.5 ± 0.1	5.4 ± 0.1	30	155 ± 5	0.64	60 ± 10	35 ± 10	0.37	10.5

^a Duty cycle as defined by Fuchs *et al.* (2017), being the fraction of the cycle period in which the jet impinges on the target where the cycle period is given by $t_{\text{on}} + t_{\text{off}}$ and duty cycle = $t_{\text{on}} / (t_{\text{on}} + t_{\text{off}})$

^b Periodicity defined as $(t_{\text{on}} + t_{\text{off}})^{-1}$

5.2.2 Soil materials

Four soil materials, all examples of fast moving consumer goods (FMCG) products, were studied:

- (i) Petroleum jelly (Atom Scientific GPS5220, provided by APC Pure, UK), labelled PJ.
- (ii) Colgate[®] toothpaste (Cavity Protection Toothpaste Great Regular Flavour, Colgate-Palmolive, UK), labelled Colgate[®].
- (iii) Oral-B[®] toothpaste (Pro-Expert Strong Teeth Toothpaste, Procter & Gamble, UK), labelled Oral-B[®].
- (iv) Tomato ketchup (Classic Heinz Tomato Ketchup, Heinz, UK), labelled ketchup.

The four materials differed in terms of their rheology and interaction with water, and thus clean on different timescales, providing a range representative of different industrial materials. PJ, Colgate[®] and ketchup were found to be viscoplastic while the Oral-B[®] was thixotropic and exhibited complex rheological behaviour (Section 5.3.1). The PJ, being hydrophobic, did not interact with the cleaning liquid. Oral-B[®] and Colgate[®] are both suspensions with glycerol as the continuous phase, which soften on contact with water. The ketchup is a more dilute aqueous suspension and was readily dispersed in water.

The particle size distributions of the Oral-B[®] and Colgate[®] toothpastes were measured with a laser diffraction particle size analyser (Mastersizer 2000 with Hydro 2000MU sample dispersion unit, Malvern Instruments, UK). The toothpaste samples were dispersed in deionised water at a concentration of 0.05 wt% and 15 measurements were made on each sample. The light scattering patterns were analysed using Mie theory. For the analysis of the Oral-B[®] toothpaste, the optical properties of silica (refractive index 1.45, absorption 0.1) were used with a refractive index of 1.33 for the deionised water. For the analysis of the Colgate[®] toothpaste, the optical properties of calcium carbonate CaCO₃ (refractive index 1.69, absorption 0.1) were used with a refractive index of 1.31 for the deionised water as it had been heated to 50°C. The volume-based particle size distributions of the toothpastes are shown in Figure 5.4.

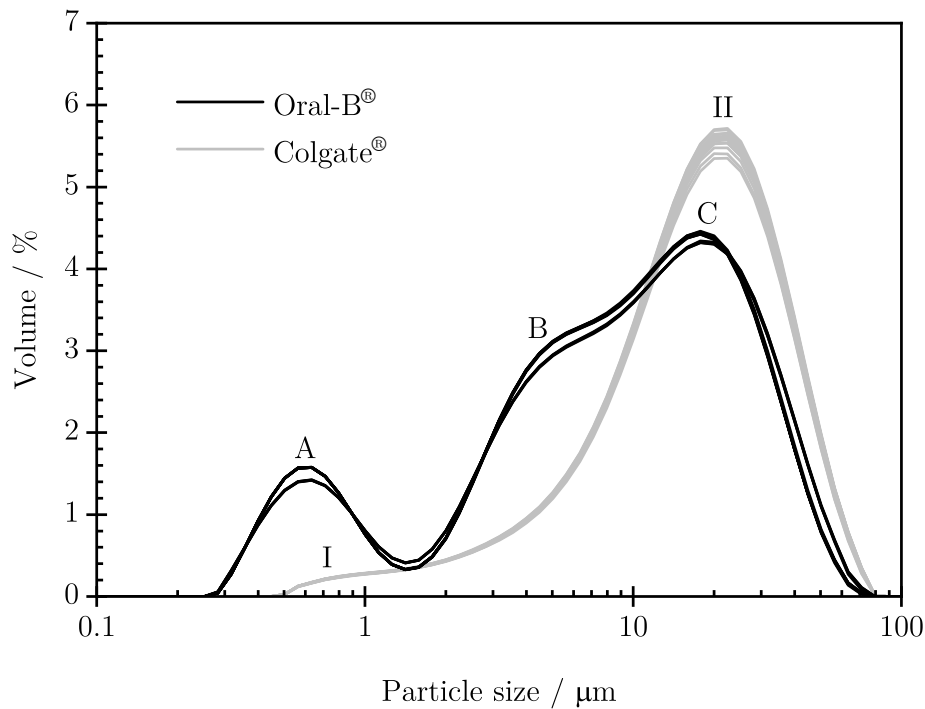


Figure 5.4: Volume-based particle size distributions of the Oral-B® and Colgate® toothpastes.

The Oral-B® toothpaste exhibited a trimodal particle size distribution with peaks at approximately 0.6, 4.5 and 20 μm , labelled A, B and C, respectively, on Figure 5.4. The Colgate® toothpaste distribution was a skewed unimodal one, with a long tail towards finer particles, labelled I, and a modal value of approximately 22 μm , labelled II. The particle size distribution of a suspension affects its rheological properties and thus its cleaning behaviour. Yang *et al.* (2019a) studied the effect of soaking Colgate® layers in water before cleaning by an impinging water jet. They reported a significant increase in the rate of cleaning over a timescale of minutes, where the rate of cleaning increased with soaking time.

The rheological properties of the petroleum jelly have been reported by Fernandes *et al.* (2019). The behaviour of the ketchup, Colgate® and Oral-B® was investigated on a controlled stress rheometer (Kinexus Lab+, Malvern Instruments, UK) using rough 40 mm diameter parallel plates with a 1 mm gap. Increasing steady shear stress ramps (increasing the shear stress at a rate of 10 Pa min^{-1}) were used to quantify the flow behaviour. Oscillatory shear stress sweeps (at a frequency of 1 Hz) provided insight into the nature of the material. The Oral-B® toothpaste was probed further by shear rate ramp testing.

5.2.3 Target plate preparation

A transparent Perspex[®] plate with dimensions $150 \times 150 \times 10$ mm (width \times height \times thickness) was used as the target. A centred square recess of side length 110 mm and depth 0.5 mm was machined into the plate and an area measuring 80×80 mm was marked out within the recess using tape. Soil layers were prepared by applying the soil to the recessed area and scraping excess soil away before removing the tape. This method enabled soil layers to be generated with consistent depth.

The plate was weighed before and after coating to determine the mass coverage of soil and the thickness of the soil layer, δ , was calculated knowing the density of the soil, measured by filling Petri dishes of known volume (25.4 mL) and weighing on a digital balance. The densities are reported in Table 5.2. After each test, the plate was cleaned with soap and warm deionised water, wiped with isopropyl alcohol, then allowed to dry before a new layer of soil was applied.

5.2.4 Cleaning

Cleaning of the tomato ketchup and toothpaste layers was performed immediately after coating to avoid drying artefacts. The petroleum jelly layers were left to rest for 30 minutes before cleaning to allow any residual stress from coating to dissipate (Fernandes *et al.*, 2019). The target plate was mounted vertically for the cleaning tests.

The jet impinges normally on a coated vertical wall and an approximately circular cleared region of radius a grows over time. For simple soils undergoing adhesive removal, a has been reported to grow as $t^{1/5}$ (*e.g.* Wilson *et al.*, 2014) but when the soil exhibits yield stress behaviour, a exhibits asymptotic behaviour as $M \rightarrow M_y$, where M_y is the momentum flow rate associated with yielding the soil (Glover *et al.*, 2016).

Three of the four soil materials studied in this work could be characterised as viscoplastic and the evolution of a was quantified using the cleaning model proposed by Fernandes *et al.* (2019) (Equation 2.68). Two of the three viscoplastic soils were a simple viscoplastic fluid for which Bingham parameters could be obtained. Their cleaning behaviour was compared to the viscous dissipation model for Bingham materials proposed by Fernandes and Wilson (2020) (Equation 2.69).

The effect of pulsing was established by comparing the cleaning behaviour for continuous and intermittent jets. The cleaned regions were observed to be approximately circular in all cases so the values of a reported are the radius of a circle with equal area to the cleaned region. In all tests, $a > r_0$ so the effect of intermittent jetting on cleaning in the footprint region is not considered.

5.3 Results and discussion

5.3.1 Soil layer rheology

Low amplitude oscillatory stress (LAOS) testing was used to establish the rheological behaviour of the soil materials and quantify their response to an imposed stress using appropriate constitutive equation parameters. The data are presented in terms of the elastic and viscous modulus, G' and G'' , respectively, in Figure 5.5 where τ_a is the amplitude of the imposed stress.

The ketchup and petroleum jelly both exhibit viscoplastic behaviour at low imposed stresses, with the response dominated by elasticity ($G' \gg G''$). At higher stresses, both G' and G'' decrease and are equal at some critical value of τ_a known as the crossover stress, τ_X . There are several measures and methods employed in the viscoplasticity literature to define the yield stress of a material, as discussed by Fernandes *et al.* (2019). In this work, τ_X is used to describe the transition between solid and fluid behaviour.

The Colgate[®] data also exhibit the G' and G'' crossover but both measures decrease steadily before τ_X , indicating that it is not a simple viscoplastic material. The values of τ_X , reported in Table 5.2, are comparable with values reported in the literature (*e.g.* ketchup, 26-30 Pa, Missaire *et al.*, 1990; toothpastes, 38-179 Pa, Ahuja *et al.*, 2018; petroleum jelly, 212 Pa, Fernandes *et al.*, 2019).

The G' values for ketchup, Colgate[®] and Oral-B[®] are all similar. Oral-B[®] exhibited noticeably different behaviour: at low stresses G' and G'' are approximately equal, and the strong decrease in G' at higher τ_a evident with the other materials is not observed. The τ_X value of 2 Pa is also noticeably smaller than all three other materials (26-250 Pa). The similarity in modulus values at low stresses and increases at higher stresses (and strain rates) indicate that the material is not viscoplastic.

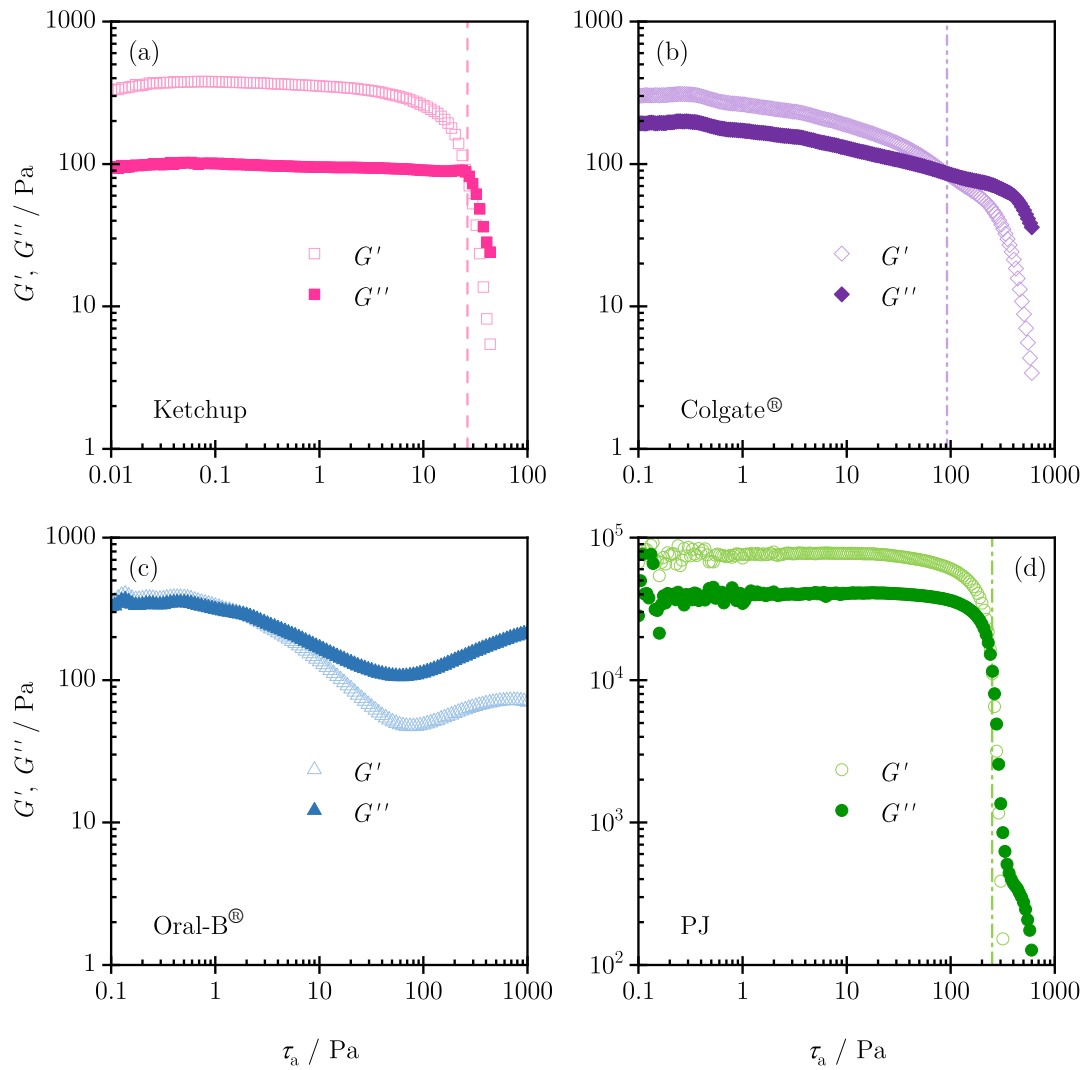


Figure 5.5: Oscillatory studies of soil material yielding behaviour. τ_a is the amplitude of the imposed oscillatory stress (frequency 1 Hz). (a) Ketchup, (b) Colgate®, (c) Oral-B®, and (d) PJ. Hollow symbols are used for G' and filled symbols are used for G'' . The vertical dashed lines on (a), (b) and (d) indicate the crossover stress τ_X . Note the different modulus scale on (d).

The flow (post yielding) behaviour was characterised by steady stress, τ , sweeps and the data are presented as the apparent viscosity, η_{app} , in Figure 5.6.

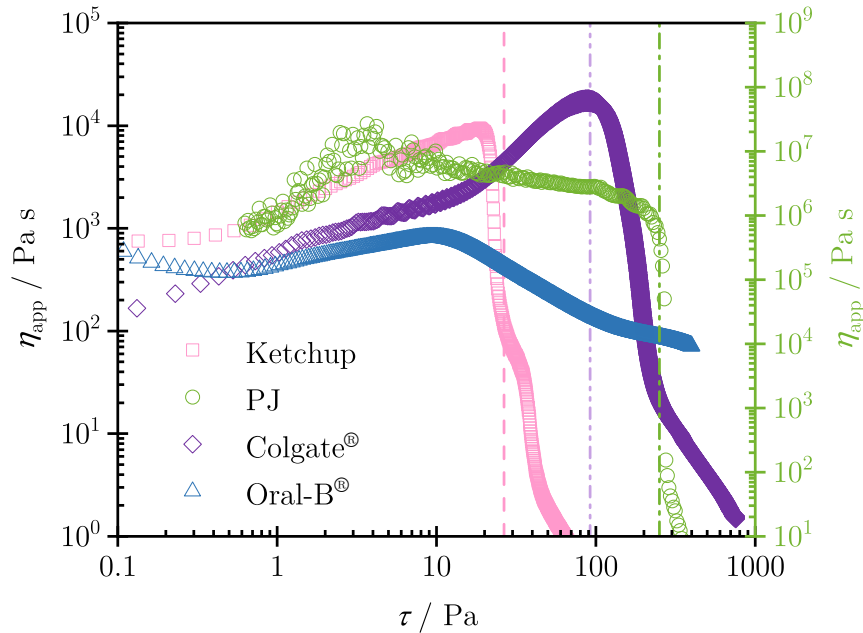


Figure 5.6: Flow behaviour of soil materials obtained from steady stress ramps. Note the different scale for the PJ data. Vertical dashed lines show τ_X values obtained in oscillatory stress testing (Figure 5.5) for PJ, ketchup and Colgate®.

The η_{app} values for PJ are much larger than the other materials, at $10^6 - 10^7$ Pa s for $\tau < \tau_X$. Both the ketchup and PJ exhibit a sharp decrease in η_{app} in the vicinity of τ_X , indicating a significant change in microstructure and deformation mode at this critical stress associated with viscoplasticity. The Colgate® also shows a sharp drop in η_{app} , but the value of τ_X obtained from Figure 5.5 is the stress where η_{app} exhibits a maximum. These features are not discussed further here: they provide further evidence that Colgate® is not a simple viscoplastic material. The Oral-B® behaviour again differs from the other three materials, as in oscillatory testing (Figure 5.5). At low stresses η_{app} is of similar order of magnitude to ketchup and Colgate® but above 10 Pa there is a more gradual decrease in η_{app} with increasing τ . Factors contributing to its different behaviour include the different particle size distribution (trimodal, facilitating good packing) and the liquid phase containing more glycerol than the Colgate® product.

The ketchup and PJ are simple viscoplastic materials that exhibit Bingham plastic behaviour. The Bingham parameters, the critical shear stress, τ_c , and the Bingham viscosity, μ_B , were obtained from the flow curves, shown in Figure 5.7, and are reported in Table 5.3.

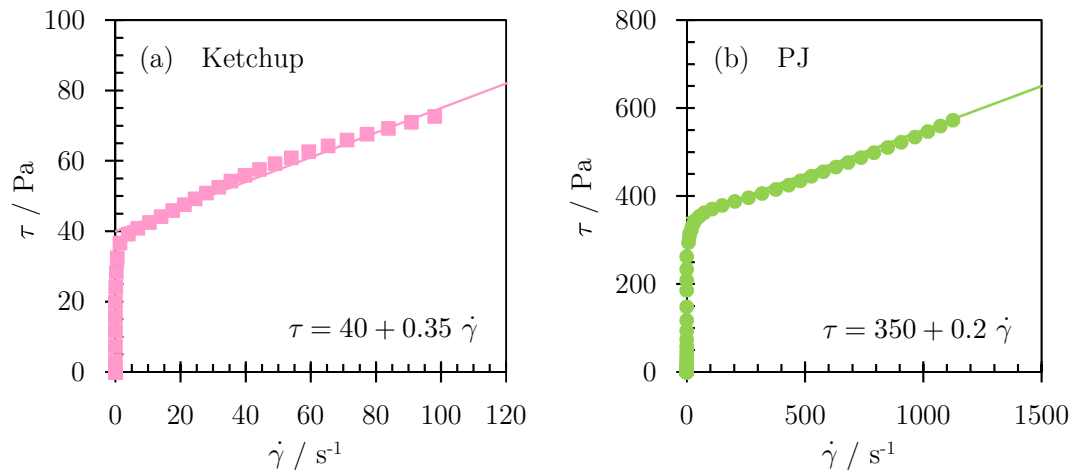


Figure 5.7: Shear stress as a function of shear rate obtained from steady stress ramps of (a) ketchup and (b) PJ. The lines show the Bingham fits ($\tau = \tau_c + \mu_B \dot{\gamma}$, where $\dot{\gamma}$ is the shear rate) used in the viscous dissipation model. The Bingham parameters are reported in Table 5.3

The Oral-B[®] behaviour was probed further by shear rate ramp testing, shown in Figure 5.8.

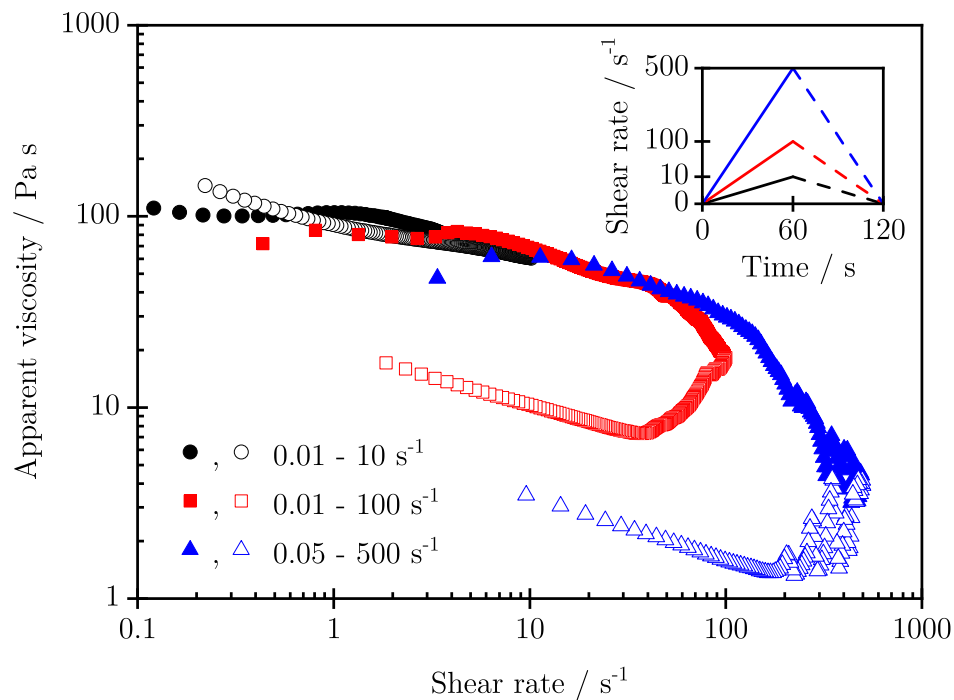


Figure 5.8: Shear rate ramps for the Oral-B[®] toothpaste. Filled symbols indicate the increasing ramp and hollow symbols the decreasing ramp. The inset shows the shear rate ramps performed (note the y-axis is not to scale).

The outward and return flow curves were similar when the maximum shear rate was 10 s^{-1} : increasing the shear rate to 100 s^{-1} (and 500 s^{-1}) resulted in much lower apparent viscosity on the return leg, indicating significant thixotropy of the material. In all cases, the apparent viscosity measured for further cycles of increasing and decreasing shear rate ramps were similar to the values from the first decreasing shear rate ramp, indicating that the material microstructure had been modified from its initial, stored, state. The restoration behaviour of the material (*e.g.* the response to decreased stress or recovery when the imposed stress is set to zero) was not investigated as this condition does not arise for the material at the cleaning front.

5.3.2 Continuous jet cleaning

Each material was subjected to cleaning by a continuous jet to characterise the cleaning behaviour. The cleaned regions were approximately circular and did not extend beyond the RFZ. Repeats were carried out to determine the reproducibility of the tests and Figure 5.9 shows examples of the cleaning profiles obtained.

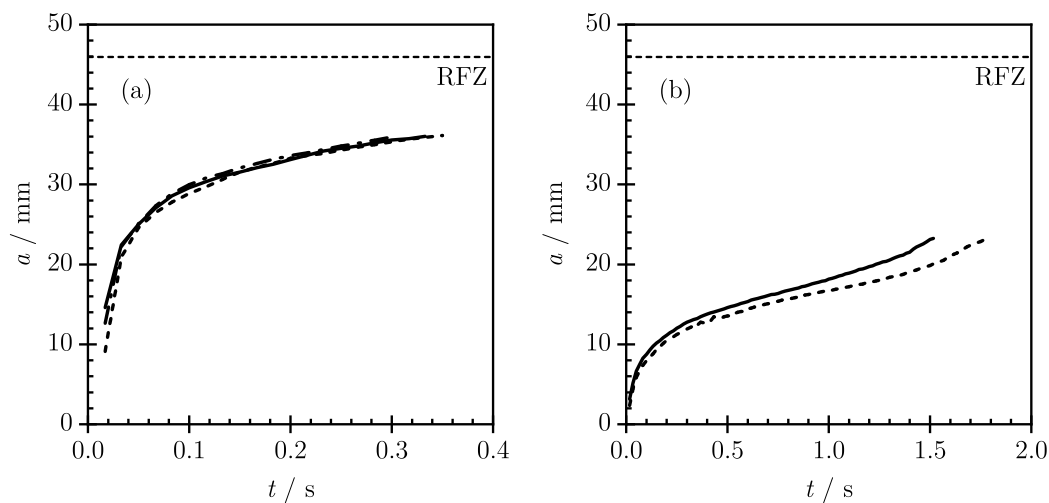


Figure 5.9: Example of the reproducibility of the continuous jet cleaning tests: cleaning of (a) ketchup and (b) Colgate[®] layers. Solid and dashed lines indicate different tests. The horizontal dashed line marked RFZ shows the location of the hydraulic jump observed with uncoated surfaces.

The cleaning of ketchup, PJ and Oral-B[®] layers were found to be reproducible, each giving cleaning profiles of similar reproducibility to that shown in Figure 5.9(a). The

difference in the cleaning profiles of Colgate® layers in Figure 5.9(b) was attributed to the fingering (preferential removal) of the soil layer, illustrated in Figure 5.10.

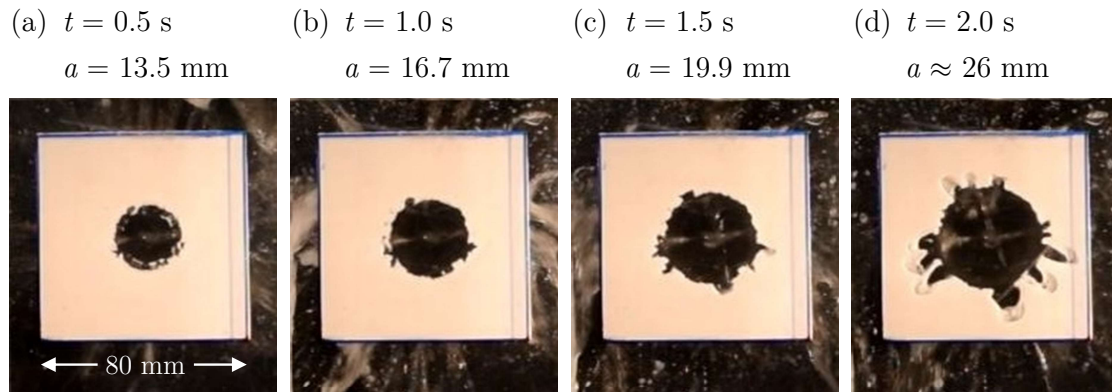


Figure 5.10: Cleaning of a Colgate® toothpaste soil layer by a continuous jet showing fingering and peeling. t is the time elapsed after jet impingement and a is the average cleaned radius.

Fingering was also reported in a study of this material by Yang *et al.* (2019a). The fingering mechanism is not considered further here: the patterns were random and were attributed to differences in adhesion to the substrate. Further work is required in order to determine the effect of the substrate properties on cleaning. The soil removal mode is determined by the balance between the adhesion of the soil to the substrate and the cohesive strength of the soil. In the limit, a slip-promoting substrate would promote peeling (adhesive removal) of the soil while a very rough surface would promote erosion of the soil.

The cleaning behaviour of the materials is compared in Figure 5.11. The profiles show that the ketchup, which had the lowest yield stress, was removed most quickly. The first image was taken 17 ms after the jet impinged on the target: for comparison, the time taken to form the hydraulic jump on an uncoated surface under these jet conditions was $t_{\text{jump}} = 22$ ms. The Colgate® toothpaste and PJ were removed at a similar rate initially, but their behaviour deviated after 1 s. The rate of cleaning of Colgate® increased after point F, which is when fingering of the soil layer was first observed.

In contrast, the PJ approached a limiting value asymptotically, with $a \rightarrow 25.2$ mm. Asymptotic cleaning behaviour is associated with the material having a yield stress and has been reported for PJ and other hydrophobic materials (*e.g.* Fernandes *et al.*, 2019). The hydrophobic nature of the PJ means that the yield behaviour is not

affected by contact with water, unlike toothpastes which weaken on soaking (Yang *et al.*, 2019a).

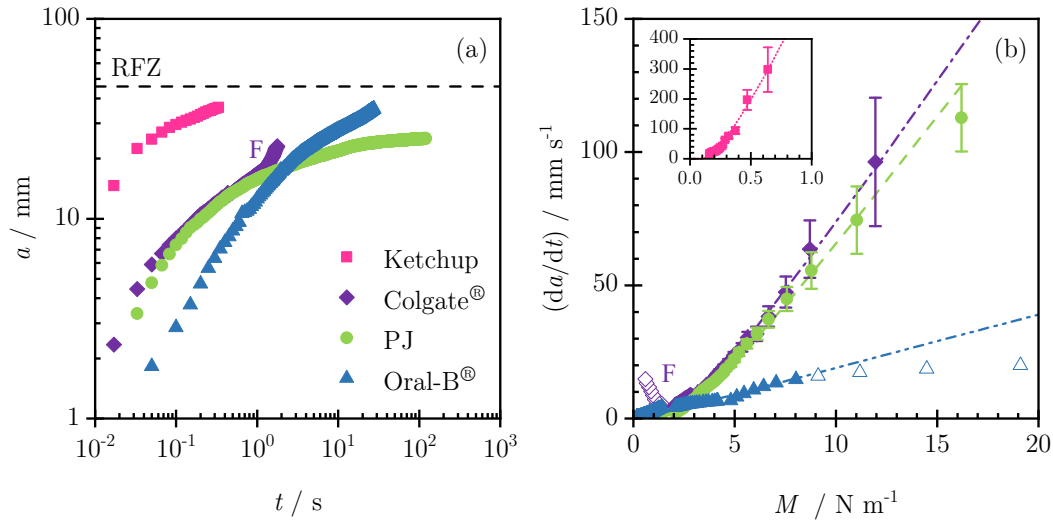


Figure 5.11: Cleaning by continuous jet impingement. (a) Evolution of the average cleaned radius, a (note \log_{10} scales). Horizontal dashed line marked RFZ shows the location of the hydraulic jump observed with uncoated surfaces. Label F indicates fingering of the Colgate® soil layer. Symbol size greater than or equal to the uncertainty in measurement. (b) Cleaning rate data, plotted in the form of Equation 2.68: M calculated using the Bhagat and Wilson (2016) model (Equations 2.20, 2.23 and 2.26 in Table 2.1) and da/dt extracted from curve fitting to the data in (a). Error bars show the estimated uncertainty in the gradient from the fitting and are omitted where the symbol size is greater than or equal to the estimated uncertainty. Dashed lines show the fit of the data to Equation 2.68 with parameters k' and M_y given in Table 5.2. Hollow symbols indicate data that were not used in the fitting.

The Oral-B® toothpaste profile exhibits a noticeable lag, of approximately 50 ms ($> 2t_{\text{jump}}$), before a measurable cleaned region appeared. Thereafter, the initial rate of cleaning was slower than the other three materials and was only comparable with the PJ as the latter entered its asymptotic regime. The differences in behaviour are very noticeable in Figure 5.11(b): the rates here were obtained by fitting polynomials or logarithmic trendlines to the data in Figure 5.11(a), with regression coefficients $R^2 > 0.99$, and differentiating the resulting expressions to estimate the gradient at the time at which datum was measured. The ketchup and PJ show very good agreement with Equation 2.68 and the model parameters k' and M_y obtained by fitting by eye are reported in Table 5.2. The Colgate® data collected after 1 s (labelled

F on the plots) are subject to fingering and were not considered in the model fitting; otherwise the model gave a good description of this material's behaviour.

The initial behaviour of the Oral-B® did not give good agreement with the model and the parameters in Table 5.2 are reported for completeness but with low confidence. These results indicate that the momentum-driven model does not give a good description of the removal of the thixotropic Oral-B® toothpaste. This result illustrates how knowledge of the soil rheology is needed to understand its cleaning behaviour: investigation of thixotropic and viscoelastic soils represent two topics for future investigation.

The values of k' and M_y show the expected trend, of a smaller M_y and larger k' for ketchup, consistent with its lower yield stress and apparent viscosity. The values for Colgate® and PJ are similar, even though the rheological parameters in Table 5.2 are quite different, again requiring further investigation.

Fernandes and Wilson (2020) proposed a viscous dissipation cleaning model for Bingham materials (Equation 2.69). The model requires the Bingham parameters, τ_c and μ_B , and has two fitting parameters, ϕ_{ramp} and δ_i . The ketchup and PJ exhibited Bingham plastic behaviour and the data were fitted to the model by eye to obtain values of $\overline{k'_B}$ (Equation 2.72) and $\overline{M_{y,B}}$ (Equation 2.73). The cleaning profiles are shown in Figure 5.12 and the model parameters are summarised in Table 5.3.

Fernandes and Wilson (2020) studied the cleaning of the same PJ but reported different rheological parameters as the material aged under storage ($\tau_c = 140$ Pa and $\mu_B = 1$ Pa s). The value of $\phi_{\text{ramp}} = 20^\circ$ obtained in this work for the PJ lies in the range reported by Fernandes and Wilson, $15^\circ \leq \phi_{\text{ramp}} \leq 32^\circ$ across tests with different values of d_N , Q and δ (for $d_N = 2$ mm, $Q = 2.0$ L min⁻¹, $\delta = 0.39$ μm , they reported $\phi_{\text{ramp}} = 24^\circ$ and $\delta_i = 5$ μm). The value of $\phi_{\text{ramp}} = 45^\circ$ for the ketchup corresponds to total internal shear of the material as it is cleaned.

The model predictions for both materials were found to be sensitive to the value of the fitting parameter δ_i . The model fitted the data well at lower values of da/dt but did not provide a superior fit over Equation 2.68. The values of $\overline{k'_B}$ and $\overline{M_{y,B}}$ show the expected trend, of a smaller $\overline{M_{y,B}}$ and larger $\overline{k'_B}$ for ketchup, consistent with its lower yield stress and apparent viscosity. The values of $\overline{k'_B}$ and $\overline{M_{y,B}}$ for PJ were similar to the k' and M_y values obtained using the cleaning model proposed by

Fernandes *et al.* (2019) (Equation 2.68; Table 5.2), while the ketchup values were of similar order of magnitude.

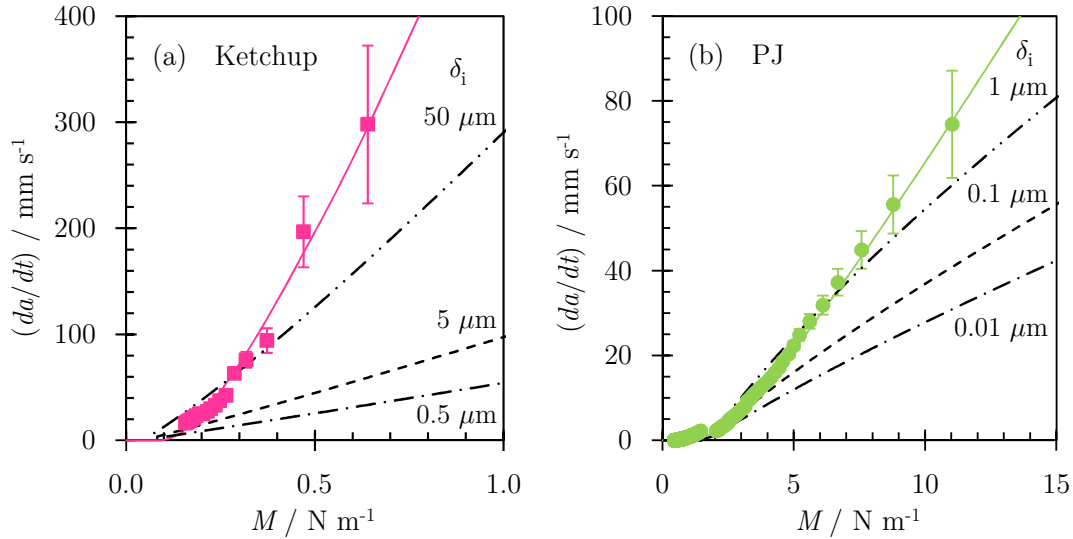


Figure 5.12: Cleaning profiles of (a) ketchup and (b) PJ fitted with Equation 2.68 from Figure 5.11(b) compared with the predictions from the Fernandes and Wilson (2020) viscous dissipation cleaning model for Bingham materials (Equation 2.69) for several values of δ_i .

The values of the cleaning rate constants obtained in this work are compared to those previously reported for the adhesive removal of soils by impinging water jets in Table 5.4. There is some variation in the values, arising from differences in the models and methods employed to evaluate M . The ketchup is cleaned quickly, with a similar cleaning rate constant to the paint studied by Wang *et al.* (2015). The toothpaste values are similar to those reported by Yang *et al.* (2019a), who also studied the effect of soaking (soaking increased k'). The petroleum jelly parameters (and those reported for a similar material by Fernandes *et al.*, 2019) are relatively large compared to other values reported in the literature, which is attributed to the variation in rheological characteristics (and composition) of different petroleum jellies.

The cleaning map of Fryer and Asteriadou (2009), Figure 2.3, classified soils in qualitative terms and did not propose a quantitative framework for comparing different soils. Table 5.4 represents one way of comparing different soils in measurable parameters, for cleaning by impinging jets.

Table 5.2: Soil layer properties and rheological parameters (Figures 5.5 and 5.6), and cleaning model parameters obtained by fitting Equation 2.68 to data in Figure 5.11(b).

Soil	Density	Mass coverage	Layer thickness, δ	Rheological parameters		Cleaning parameters	
	/ kg m ⁻³	/ g m ⁻²	/ mm	τ_w / Pa	η_{app} at τ_w / Pa s	k' / m s kg ⁻¹	M_y / N m ⁻¹
Ketchup	1 170 ± 10	735 ± 31	0.6 ± 0.1	26 ± 5	110 ± 10	0.8 ± 0.2	0.35 ± 0.05
Colgate®	1 390 ± 10	562 ± 31	0.4 ± 0.1	92 ± 5	18 000 ± 1 000	0.011 ± 0.002	4.0 ± 0.5
Oral-B®	1 440 ± 10	875 ± 31	0.6 ± 0.1	-	820 ^a	0.0020 ^b ± 0.0005	0.5 ^b ± 0.5
PJ	812 ± 13	360 ± 16	0.4 ± 0.1	250 ± 10	430 000 ± 10 000	0.010 ± 0.002	4.2 ± 0.5

^a Maximum value: τ_x not identified for this material

^b Data did not fit Equation 2.68 well

Table 5.3: Bingham material parameters (Figure 5.7) and cleaning model parameters for different fits of Equation 2.69 to the data, shown in Figure 5.12.

Soil	Bingham rheological parameters		Cleaning parameters			
	τ_c / Pa	μ_B / Pa s	ϕ_{ramp} / °	δ_i / μm	$\overline{k'_B}$ / m s kg ⁻¹	$\overline{M_{y,B}}$ / N m ⁻¹
Ketchup	40	0.35	45	0.5	0.05	0.021
PJ	350	0.2	20	5	0.09	0.021
				50	0.26	0.021
				0.01	0.004	2.0
			0.1	0.005	2.0	
			1	0.008	2.0	

Table 5.4: Comparison of cleaning rate parameters obtained in this work to results in the literature.

Soil	Substrate	$\delta / \mu\text{m}$	Temp / $^{\circ}\text{C}$	d_N / mm	Re	Jet orientation	$k' / \text{m s kg}^{-1}$	$M_y / \text{N m}^{-1}$	Model equation	Source								
Ketchup	Perspex [®]	600 ± 100	20 - 22	2	21 200	Horizontal	0.8	0.35	2.68	This work								
											0.26	0.021						
Acrylic paint	Glass	60 ± 10	20 ± 2	2	3 500 - 5 900	Horizontal	0.72	-	2.50	Wang <i>et al.</i> (2015)								
PVA (polyvinyl acetate) glue	Perspex [®]	70 ± 30	20 ± 1	2	11 000 - 32 000	Horizontal	0.21	-	2.50	Wilson <i>et al.</i> (2014)								
											120 \pm 30	20 \pm 1	2	11 000 - 32 000	Vertical	4.5×10^{-4}	-	2.50
											140 \pm 30	20 \pm 1	2	5 300 - 32 000	Horizontal	1.0×10^{-4}	-	2.50
											20 - 170	20	2	21 700	Horizontal	0.27×10^{-4} - 2.6×10^{-4}	-	2.53
Carbopol [®] 940 gel	Glass	~ 33	18 - 20	2	10 900 - 32 700	Inclined at 45 $^{\circ}$	1.3×10^{-4}	-	2.63	Bhagat <i>et al.</i> (2017)								
NIVEA [®] cream	Painted steel	2000	20	1	12 700	Inclined at 30 $^{\circ}$	0.02	-	2.65	Tuck <i>et al.</i> (2020)								
											4000	20	1 - 2	6 400 - 12 700	Inclined at 30 $^{\circ}$	0.02	-	2.50
											4000	20	1 - 2	9 200 - 18 400	Inclined at 30 $^{\circ}$	0.4	-	2.50
											8000	20	1 - 2	6 400 - 12 700	Inclined at 30 $^{\circ}$	8×10^{-4}	-	2.50
											8000	20	1 - 2	9 200 - 18 400	Inclined at 30 $^{\circ}$	0.05	-	2.50
											1000	20 - 22	2	10 600 - 26 500	Horizontal	0.02	2	2.68
Toothpaste (Oral-B [®])	Perspex [®]	600 ± 100	20 - 22	2	21 200	Horizontal	2×10^{-3a}	0.5 ^a	2.68	This work								

Toothpaste (Colgate®)	Glass	500	22 ± 2	2	21 200	Vertical	0.68×10^{-2} - 9.7×10^{-2}	0.047 - 1.2	2.66	Yang <i>et al.</i> (2019a)
	Perspex®	400 ± 100	20 - 22	2	21 200	Horizontal	1.1×10^{-2}	4.0	2.68	This work
Xanthan gum	Stainless steel	<80	20 ± 1	0.84 - 2.66	12 000 - 49 000	Horizontal	2×10^{-3}	-	2.50	Wilson <i>et al.</i> (2014)
			17 ± 4	0.39 - 3.30	6 800 - 57 000	Vertical	2×10^{-3}	-	2.50	
	11 ± 1^b g m ⁻²	22 ± 1.7	0.84 - 2.66	7 700 - 50 000	Vertical moving jet	2×10^{-3}	-	2.59	2.59	Wilson <i>et al.</i> (2015)
Dried suspension	PMMA		17 ± 4	1.69 - 2.66	27 000 - 43 000	Vertical	2.2×10^{-3} - 5.3×10^{-3}	-	2.50	
		175 ± 10	Ambient	0.25 - 2	4 975 - 39 000	Horizontal	1.8×10^{-5}	-	2.47	Overmann <i>et al.</i> (2019)
		250 ± 30	20 ± 1	2	11 000 - 32 000	Horizontal	6.7×10^{-6}	-	2.50	Wilson <i>et al.</i> (2014)
Petroleum jelly	Glass		24 ± 1			Horizontal	1.5×10^{-5}	-		
			30 ± 1			Vertical	5.7×10^{-5}	-		
			40 ± 1			Horizontal	6.3×10^{-4}	-		
Perspex®	250	300 ± 30	20 ± 1	2	11 000 - 32 000	Vertical	3.3×10^{-3}	-		
		322 ± 50 - 409 ± 50	18 - 20	2	21 800	Inclined at various angles	1.4×10^{-7}	-		
		140 - 1860	20	2	21 700	Horizontal	0.027	-	2.63	Bhagat <i>et al.</i> (2017)
Feldung Damkjær <i>et al.</i> (2017)	250		20 ± 2	2	26 000 - 32 000	Horizontal	7.7×10^{-7} - 2.6×10^{-4}	-	2.53	Glover <i>et al.</i> (2016)
				3.8 - 5.5	93 000 - 167 000	Long jets	3.4×10^{-5}	-	2.54	
						Horizontal	5.8×10^{-6}	-	2.55	
Fernandes <i>et al.</i> (2019)	400 ± 100	130 - 1490	20	2 - 4	6 500 - 37 000	Horizontal	0.07×10^{-3} - 8×10^{-3}	1.3 - 24	2.68	
			20 - 22	2	21 200	Horizontal	10×10^{-3}	4.2	2.68	This work
							2.0	2.69		

^a Data did not fit Equation 2.68 well

^b Thickness not reported - mass coverage quoted

5.3.3 Intermittent jet cleaning

Figure 5.13(a) shows an example of a cleaning profile obtained with an intermittent jet (Oral-B[®] toothpaste, $t_{\text{on}} = 60$ ms, $t_{\text{off}} = 130$ ms). The short stationary plateaus show periods when the jet is diverted from the target by the solid sections in the interrupter plate. The long stationary plateau between $t = 3$ s and $t = 4$ s corresponds to a delay where the motor direction was reversed manually using its two-way switch. The stationary plateaus were removed manually to yield the cleaning profile in terms of water contact time, yielding Figure 5.13(b). It was noticeable that removal stopped when the jet was not in contact with the soil, showing that the soil removal was dominated by mechanical action of the liquid.

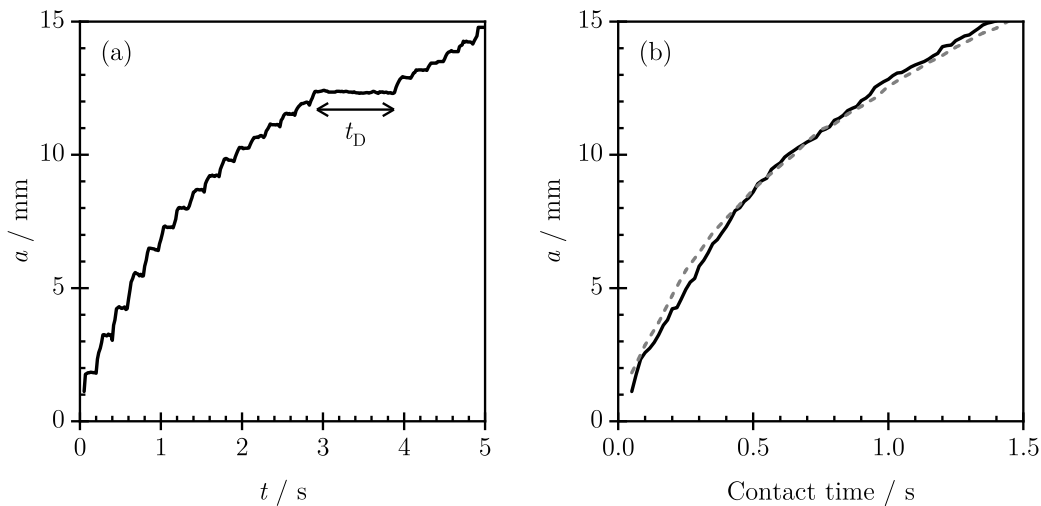


Figure 5.13: Cleaning of Oral-B[®] layer, with $t_{\text{on}} = 60$ ms, $t_{\text{off}} = 130$ ms: (a) cleaned radius detected from images, and (b) after removal of the stationary plateaus. The dashed line shows the cleaning profile for a continuous jet (Figure 5.11(a)). The interval labelled t_D in (a) indicates where the motor direction was reversed manually using its two-way switch.

Similar agreement was obtained for other materials. Figure 5.14 presents the cleaning profiles for each soil material for each interruption strategy in Table 5.1, plotted in terms of the time in contact with the jet. The cleaning profiles obtained with the continuous jet (Figure 5.11(a)) are provided for comparison.

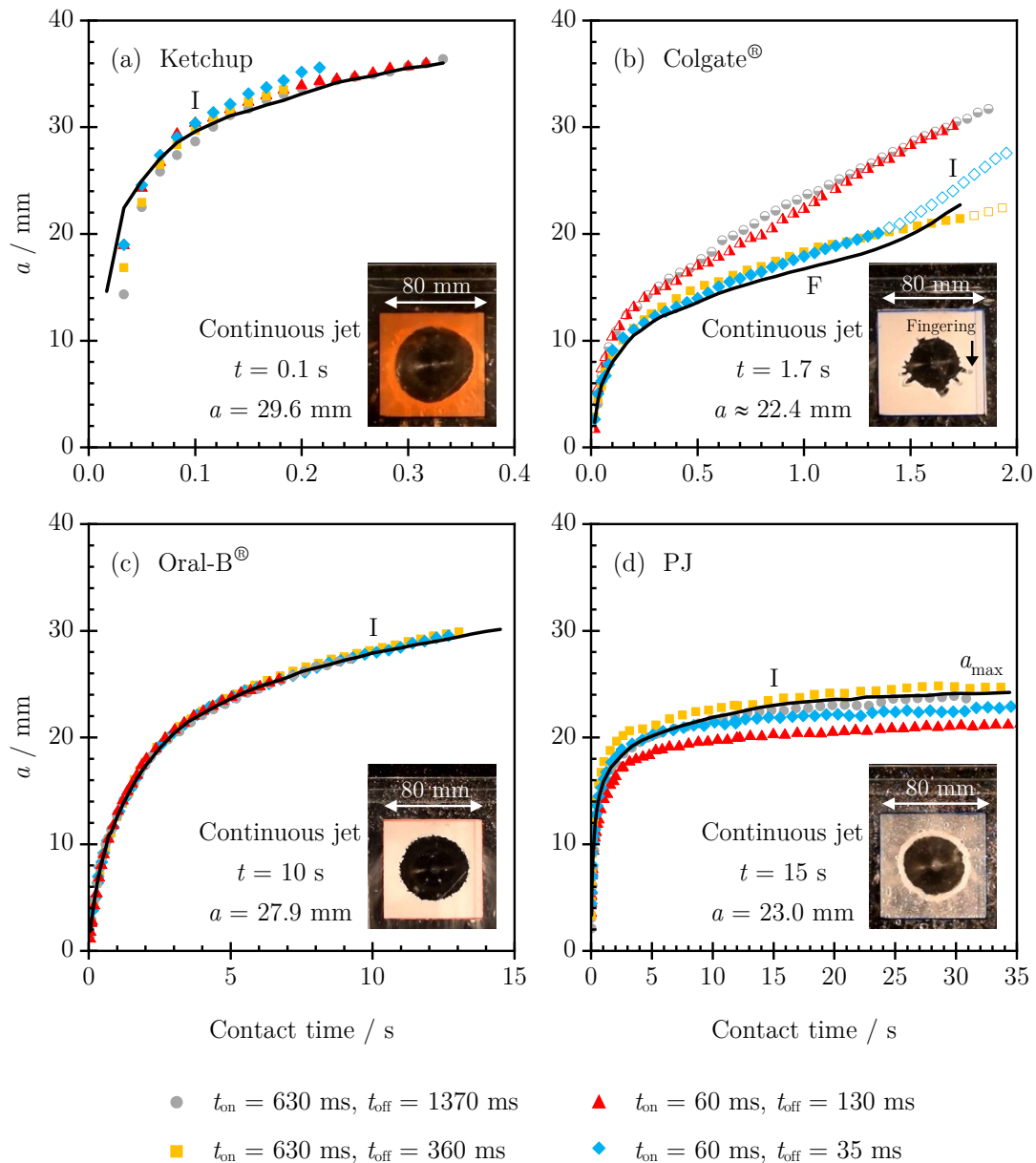


Figure 5.14: Cleaning profiles for each soil with the stationary plateaus removed. A reduced number of data points are plotted and error bars are omitted for clarity. The uncertainties in the measurements are approximately $a \pm 1$ mm and $t \pm 0.02$ s. The solid line indicates continuous jet cleaning. In (b), the half-shaded data points indicate tests where the area cleaned was not circular, and the label F and hollow data points indicate fingering. The label I indicates the time at which the inset image was taken.

There was no statistically significant effect of interrupting the jet for ketchup and Oral-B[®]. The cleared regions were approximately circular and dislodged material was conveyed away from the cleaning front in the liquid film. The initial delay in removal

observed with the Oral-B[®] toothpaste (Figure 5.11(a)) will include a contribution from cleaning in the jet footprint region of order 1 - 2 jet diameters: no change in this delay was observed for the different pulsing conditions.

The Colgate[®] profiles in Figure 5.14(b) exhibit variation, associated with fingering and peeling of the soil layer. There was no consistent effect of the intermittent jets on fingering and peeling behaviour, but it is noticeable that the cases with the shorter duty cycle (and therefore longer periods of time for soaking effects) gave non-circular cleaned areas and overall faster removal rates. Soaking of material below the point of impingement by liquid draining down the target is expected to weaken the material and thus promote its removal, which would result in asymmetric cleaning behaviour.

Intermittent pulsing had little effect on PJ removal, with the exception of the case where $t_{\text{on}} = 60$ ms, $t_{\text{off}} = 130$ ms with $T = 0.37$. This difference is attributed to the heterogeneous nature of the PJ, which made it difficult to prepare soil layers with consistent thickness. The photograph in Figure 5.14(d) shows that the petroleum jelly displaced by the liquid film accumulated in a berm at the cleaning front. The shape of this berm and the approach to an asymptotic extent of removal (labelled a_{max}) have been discussed by Fernandes *et al.* (2019) and Fernandes and Wilson (2020). There was no noticeable change in the berm shape with different contact times.

Figure 5.14 shows that for these cohesive soil layers, there was no advantage in subjecting the soil to intermittent jetting. For these non-interacting cohesive soil layers, cleaning was dominated by the mechanical action of the liquid film. The size of the cleaned regions were larger than the jet footprint, *i.e.* $a/r_0 > 2$, where the dynamics of the liquid film are governed by wall friction and waves rather than impulse. The effect of pulsing on wave formation was not quantified, partly because there was no noticeable effect on cleaning.

5.3.4 Reconciliation with results in the literature

The findings in this work are now related to those of Fuchs *et al.* (2017). They did not report any enhancement in the cleaning of a starch-based soil applied with a mass coverage of 40 ± 7 g m⁻², which is an order of magnitude smaller than the layers studied here (layer thicknesses were not reported). They reported enhancement for a xanthan gum soil with a lower coverage of 10 ± 1 g m⁻². The area they considered for cleaning extended well beyond the RFZ into the region in which the flow takes

the form of a falling film. Inspection of one of their cleaning profiles, reproduced in Figure 5.15, showed that there was an initial, rapid stage of cleaning, lasting less than a minute, followed by little further removal until 7 minutes had elapsed. The removal rate then increased ten-fold. The initial stage is consistent with cleaning in the RFZ and the later behaviour is consistent with soaking-induced weakening of the soil beyond the RFZ, introducing a delay into the onset of cleaning in this region. Their measures are dominated by cleaning in the falling film region: the wall shear stress and momentum imposed by a falling film will be affected by wave formation, which is expected to be enhanced by the periodic jetting.

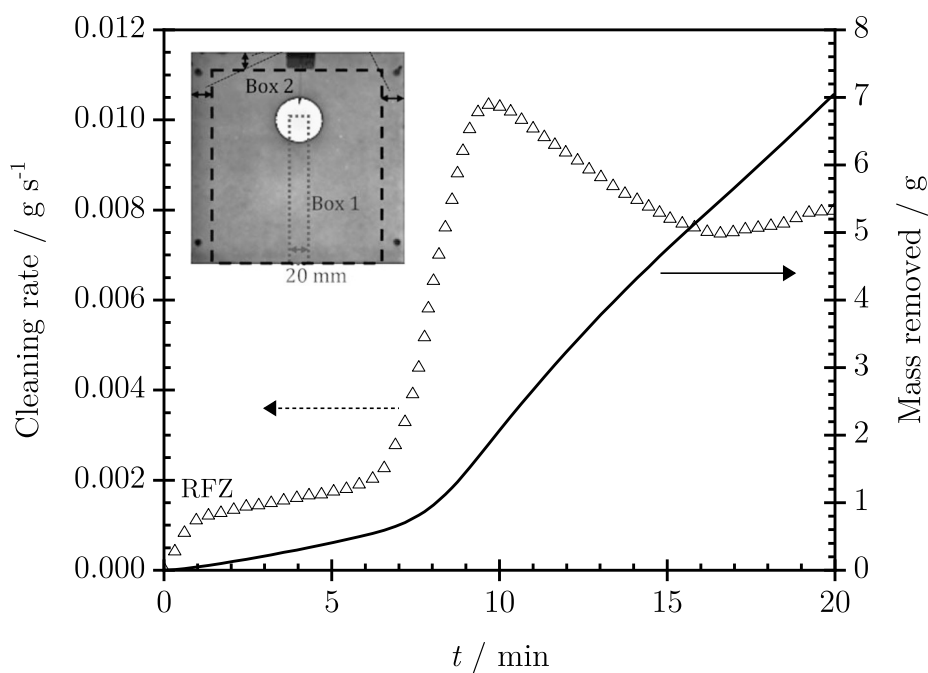


Figure 5.15: Example cleaning profile from Fuchs *et al.* (2017). Cleaning rate data reproduced from Figure 4 in their paper: the cumulative mass removed was obtained by integrating the cleaning rate data. Label RFZ indicates the time at which the RFZ region was cleaned. The inset is Figure 3(d) from their paper, showing the two regions (Box 1 and Box 2) they used to evaluate cleaning.

Yang *et al.* (2019a) reported a study of the cleaning of the Colgate[®] toothpaste employed in this work by continuous water jets, and considered removal in the region below the RFZ as well as in the RFZ. They showed that soaking over a period of several minutes gave rise to faster cleaning in both regions. This is consistent with Fuchs *et al.*'s observations for their xanthan gum soils. Little enhancement was observed for the starch-based soil which had a higher mass coverage than the

xanthan gum. This could be due to soaking taking longer to have an effect on the soil removal.

Yang *et al.* (2019b) investigated the effect of intermittent jetting on alkaline cleaning of egg yolk soil layers in laboratory tests and in an industrial tank. Intermittent jetting improved the rate of cleaning per unit volume of cleaning agent (or effective contact time) by up to 50% as the period between bursts provided additional time for the diffusion of the alkaline solution into the soil layer. However, the enhancement varied with position on the tank wall, reflecting the differences in hydrodynamic conditions and therefore the balance between soaking and mechanical force effects.

Ultimately the cleaning behaviour is determined by the rheology of the soil and its interaction with the cleaning agent. In the RFZ, for all the soils considered here, the timescale for cleaning within the RFZ was shorter than the characteristic time for soaking or other effects, so there was no effect of intermittent jetting. Fuchs *et al.* focused on the draining film region, with longer cleaning timescales, so T differs. The studies are therefore consistent: this work confirms that intermittent jets do not offer any advantages in cleaning within the RFZ.

5.4 Conclusions

The use of intermittent impinging jets to remove viscous soil layers was investigated for four different layers of materials using a novel jet interrupter apparatus which allowed the two timescales (the length of time that the jet was applied and the period between bursts) to be varied independently. The metric used to assess cleaning was the clearing of soil within the radial flow zone around the point of jet impingement. The period of jet application was similar to the time taken for the liquid to form a steady flow pattern in this zone.

Of the four soil materials studied, three were viscoplastic (tomato ketchup, petroleum jelly and Colgate[®] toothpaste), with different yield stresses and miscibility with water. The tomato ketchup, with a lower yield stress, was removed quickly and soaking effects were not observed. The petroleum jelly was immiscible with water so is not subject to soaking effects and its high yield stress resulted in limited removal, with no removal in the draining film zone. The Colgate[®] toothpaste exhibited peeling and fingering behaviour while the Oral-B[®] toothpaste exhibited complex rheological behaviour.

The cleaning behaviour of the three viscoplastic soils were described well by the viscoplastic removal model of Fernandes *et al.* (2019), while the delay in cleaning and slow initial removal rate of the Oral-B® was not consistent with the model. The tomato ketchup and petroleum jelly exhibited Bingham plastic behaviour and their cleaning behaviour was described reasonably well by the Fernandes and Wilson (2020) viscous dissipation theory for Bingham materials.

No consistent enhancement of cleaning performance was observed with intermittent jetting over cleaning by a continuous jet for any of the materials studied. This can be reconciled to the enhancement reported in previous studies by noting that those studies focused on the wall region below the impingement point and beyond the radial flow zone, where soaking effects and waves play an important role.

For layers that are sensitive to soaking, intermittent jetting could be used initially to wet the layer with liquid, maintaining it in a wet state, enabling soaking to take place while minimising the use of cleaning liquid. After a given soaking time, once the soil has weakened, cleaning by continuous jets could be used to minimise the production downtime required for cleaning.

The intermittent jets used in this work were a series of regular bursts, generated by periodically disrupting the impingement of a continuous coherent jet onto the target. One avenue for further work would be the investigation of the effect of intermittent jetting resulting from jet breakup, where a coherent jet breaks up into droplets and the droplets impact the target, resulting in the combined effects of splatter from jet breakup and intermittent application on cleaning.

Chapter 6

Conclusions and future work

This chapter summarises the key findings of this thesis and identifies work for further investigation.

6.1 Conclusions

The three questions to be answered in this work were:

- I. How does jet length and wall curvature affect the flow pattern generated by a normally impinging liquid jet and thus its cleaning performance, and are the existing hydrodynamic models able to capture these effects?*

Horizontal jets of different lengths, diameters and flow rates impinging normally on a vertical target were investigated. For a given jet diameter and flow rate, jet breakup occurred as the jet length increased. The amount of liquid lost to splatter was measured, but it was not possible to distinguish splatter from jet breakup and splatter from the rebound of liquid droplets off the target. The amount of liquid lost to splatter could not be predicted *a priori* but the experimental data showed good agreement with a correlation proposed by Bhunia and Lienhard (1994) to predict the onset of splattering, defined as the point where more than 5% of the liquid is lost to splatter. The existing hydrodynamic models were able to describe the liquid flow pattern once splatter had been accounted for. Splatter reduces the flow rate delivered by the jet to the target, giving an effective flow rate. Jets of the same diameter with a similar effective flow rate were found to give similar cleaning rates.

To investigate wall curvature, tests were carried out with horizontal coherent jets impinging normally on concave curved walls, the internal surfaces of horizontal and vertical cylinders. Wall curvature was found to have little effect on the hydrodynamics and cleaning behaviour of the jets. The curvatures studied in this work were larger than those likely to be encountered in many manufacturing applications, so concave wall curvature is not expected to present a challenge in the modelling of jet behaviour.

II. What is the liquid flow distribution in the film when a jet impinges at an angle to the target surface? How accurate is the existing Kate et al. (2007) model for the liquid flow distribution which has been used by previous workers and can this be improved?

A geometric transformation was developed to describe jets inclined in both the horizontal and vertical planes by a single, overall jet angle. The liquid flow distribution in inclined liquid jets could not be measured directly but was instead obtained by two separate means, namely hydrodynamic and cleaning tests. Hydrodynamic tests were carried out to determine the shape of the hydraulic jump. With the cleaning tests, the liquid flow distribution in inclined jets was determined in an inverse calculation as the cleaning of the test material by normally impinging jets had first been characterised.

The flow distribution obtained in the both the hydrodynamic and cleaning tests were consistent, differing from the Kate *et al.* (2007) model which overpredicts the liquid flow in the major flow direction and underpredicts the flow in the minor flow direction. The best of the three alternative flow distribution models developed, the changing ellipse model, was compared at length with the experimental data. It does not give an *a priori* prediction of the liquid flow distribution, but was able to provide a better fit to the experimental data, though this could be expected as it has one fitting parameter while the Kate *et al.* model has none.

When compared to the results reported in the literature for the location of the hydraulic jump, the changing ellipse model did not provide a superior fit over the Kate *et al.* flow distribution. Inferring the location of the source of the flow from heat transfer measurements reported in the literature did not resolve the question as the values differed from those obtained in this work and the Kate *et al.* flow distribution.

III. Does intermittent application of a liquid jet rather than continuous application allow the consumption of cleaning liquid to be reduced?

Cleaning by intermittent jets was investigated by using a moving interrupter plate to periodically disrupt the impingement of a continuous water jet. Cleaning was only considered in the radial flow zone, to investigate the effect of the additional impulse and waves generated there by the repeated impact of the jet during intermittent application. The time taken for the hydraulic jump to be established was shorter than the length of time for which the jet impinged on the target in each period.

Intermittent jetting was not found to give any consistent enhancement of cleaning performance over cleaning by a continuous jet for the four materials studied (petroleum jelly, tomato ketchup and two toothpastes). These observations differed to the enhancement previously reported by other workers (Fuchs *et al.*, 2017; Yang *et al.*, 2019a; Yang *et al.*, 2019b), where cleaning below the radial flow zone was considered. The reported enhancement was related to soaking of the soil as soaking increases the cleaning rate. Intermittent application of the jets could therefore be useful to reduce the consumption of cleaning liquid in cases where the soil layers are sensitive to soaking.

These three questions address particular issues which arise in transferring knowledge and experimental results gained with well-defined configurations (*e.g.* a coherent jet impinging normally onto a vertical surface) to those typical of industrial and other applications, illustrated in Figure 1.2. Developing this understanding further will require identification of the dominant phenomena for the application involved, as these are complex problems which give rise to series of related fluid flow problems. For example, at a very oblique impingement angle the jet could rebound off a non-wetting soil, while at extended jet lengths the jet will take the form of a series of liquid droplets. On top of this, the jet behaviour will depend on the nozzle design and whether it is rotating or static.

6.2 Future work

This work has provided insights into several aspects of cleaning by impinging water jets. Cleaning is, however, a complex process, with a large number of parameters needed to define the problem. Investigations often need to be done by examining each aspect separately to provide a better fundamental understanding, as has been done in this work. This introduces the challenge of bringing together all the different aspects that have been investigated, as results are often presented in a fragmented manner in the literature, as well as understanding the interaction between them.

Jet length (breakup and splatter), wall curvature, jet angle and intermittent application were investigated independently. Further work is needed to understand the interaction of these different aspects, such as how wall curvature and jet angle affects the splatter of long jets. Convergent entry nozzles were used in this work, so another avenue for further work would be to investigate the effect of the nozzle type and design.

The liquid flow distribution in an inclined jet was obtained through indirect methods in this work. Further work remains to enable the liquid flow distribution in an inclined jet to be predicted *a priori*. This would require developing methods for direct *in situ* measurements of the local flow rate, velocity and liquid film thickness in the radial flow zone, to provide more accurate data.

Rotary jets used in industrial jet cleaning systems not only give rise to obliquely impinging jets, but also to moving nozzles and curved jet trajectories. The effect of nozzle rotation on the jet dynamics has not been investigated. Piping, fitting connections and other protuberances in process tanks and vessels also give rise to areas of convex wall curvature where soil could accumulate, or shadow areas that do not receive direct contact from liquid delivered by the nozzle, and these need to be accounted for.

Most cleaning studies have focused on the use of thin layers of model soils but there is a need to understand how the thickness of the soil layer affects its cleaning. Other considerations include how the rheology of the soil, the nature of the target surface and the soil-surface interaction affect cleaning. These are examples of the many factors that need to be considered for cleaning.

Bhagat *et al.* (2017) presented a modelling approach which could be used to systematically design impinging liquid jet cleaning systems. The findings from this work could be incorporated into their approach, such as how a change in the liquid flow distribution in an inclined jet affects the shape of the cleaned region for a moving nozzle.

Ultimately, bringing together the knowledge about how each parameter affects cleaning would enable a full plant scale simulation tool to be developed, with input parameters such as the geometry of the system and the nature of the soil material. This would allow cleaning systems and cleaning protocols to be designed and optimised *in silico*, minimising the need for tests to be carried out and thus reducing the time and resources required, improving the overall sustainability.

While this work had focused on impinging liquid jets for cleaning applications, the insights gained into the hydrodynamics can be transferred to other fields where jets are used such as heat transfer, de-icing of aircraft wings and coating flows.

References

- AHUJA, A., LUISI, G. and POTANIN, A. (2018). Rheological measurements for prediction of pumping and squeezing pressures of toothpaste. *J. Non-Newton. Fluid Mech.*, **258**, 1–9.
- ALVAREZ, N., DAUFIN, G. and GÉSAN-GUIZIOU, G. (2010). Recommendations for rationalizing cleaning-in-place in the dairy industry: Case study of an ultra-high temperature heat exchanger. *J. Dairy Sci.*, **93**, 808–821.
- ALVAREZ, N., GÉSAN-GUIZIOU, G. and DAUFIN, G. (2007). The role of surface tension of re-used caustic soda on the cleaning efficiency in dairy plants. *Int. Dairy J.*, **17**, 403–411.
- AOUAD, W., LANDEL, J. R., DALZIEL, S. B., DAVIDSON, J. F. and WILSON, D. I. (2016). Particle image velocimetry and modelling of horizontal coherent liquid jets impinging on and draining down a vertical wall. *Exp. Therm. Fluid Sci.*, **74**, 429–443.
- ASKARIZADEH, H., AHMADIKIA, H., EHRENPREIS, C., KNEER, R., PISHEVAR, A. and ROHLFSM, W. (2019). Role of gravity and capillary waves in the origin of circular hydraulic jumps. *Phys. Rev. Fluids*, **4**, 114002.
- AZUMA, T. and HOSHINO, T. (1984). The radial flow of a thin liquid film: 3rd report, velocity profile. *Bull. JSME*, **27**, 2755–2762.
- BAGHEL, K., SRIDHARAN, A. and MURALLIDHARAN, J. S. (2020). Experimental and numerical study of inclined free surface liquid jet impingement. *Int. J. Therm. Sci.*, **154**, 106389.
- BELTAOS, S. (1976). Oblique impingement of circular turbulent jets. *J. Hydraul. Res.*, **14**, 17–36.
- BHAGAT, R. K. (2019). *Flow fields created by impinging liquid jets and applications in cleaning*. Ph.D. thesis, University of Cambridge.
- BHAGAT, R. K., JHA, N. K., LINDEN, P. F. and WILSON, D. I. (2018). On the origin of the circular hydraulic jump in a thin liquid film. *J. Fluid Mech.*, **851**, R5.
- BHAGAT, R. K. and LINDEN, P. F. (2020). The circular capillary jump. *J. Fluid Mech.*, **896**, A25.

- BHAGAT, R. K., PERERA, A. M. and WILSON, D. I. (2017). Cleaning vessel walls by moving water jets: Simple models and supporting experiments. *Food Bioprod. Process.*, **102**, 31–54.
- BHAGAT, R. K. and WILSON, D. I. (2016). Flow in the thin film created by a coherent turbulent water jet impinging on a vertical wall. *Chem. Eng. Sci.*, **152**, 606–623.
- BHUNIA, S. K. and LIENHARD, J. H. (1994). Splattering during turbulent liquid jet impingement on solid targets. *J. Fluids Eng.*, **116**, 338–344.
- BOHR, T., DIMON, P. and PUTKARADZE, V. (1993). Shallow-water approach to the circular hydraulic jump. *J. Fluid Mech.*, **254**, 635–648.
- BOHR, T. and SCHEICHL, B. (2021). Surface tension and energy conservation in a moving fluid. *Phys. Rev. Fluids*, **6**, L052001.
- BRITISH ELECTRICITY INTERNATIONAL (1992). *Modern Power Station Practice (Third Edition) Volume E - Chemistry & Metallurgy*. Pergamon.
- BUSH, J. W. M. and ARISTOFF, J. M. (2003). The influence of surface tension on the circular hydraulic jump. *J. Fluid Mech.*, **489**, 229–238.
- BUTTON, E. C., DAVIDSON, J. F., JAMESON, G. J. and SADER, J. E. (2010). Water bells formed on the underside of a horizontal plate. part 2. theory. *J. Fluid Mech.*, **649**, 45–68.
- DINGKREVE, M., FAZILATI, M., DENN, M. M. and BONN, D. (2018). Carbopol: From a simple to a thixotropic yield stress fluid. *J. Rheol.*, **62**, 773–780.
- DUCHESNE, A., ANDERSEN, A. and BOHR, T. (2019). Surface tension and the origin of the circular hydraulic jump in a thin liquid film. *Phys. Rev. Fluids*, **4**, 084001 1–7.
- EGGERS, J. and VILLERMAUX, E. (2008). Physics of liquid jets. *Rep. Prog. Phys.*, **71**, 036601.
- EIDE, M. H., HOMLEID, J. P. and MATTSSON, B. (2003). Life cycle assessment (LCA) of cleaning-in-place processes in dairies. *Lebensm.-Wiss. U.-Technol.*, **36**, 303–317.
- EPSTEIN, N. (1983). Thinking about heat transfer fouling: A 5×5 matrix. *Heat Transf. Eng.*, **4**, 43–56.

- ERRICO, M. (1986). *A study of the interaction of liquid jets with solid surfaces*. Ph.D. thesis, University of California, San Diego.
- EUROPEAN COMMISSION (2015). EudraLex - Volume 4 - Good Manufacturing Practice (GMP) guidelines. Annex 15: Qualification and Validation. https://ec.europa.eu/health/documents/eudralex/vol-4_en, accessed September 2021.
- FELDUNG DAMKJÆR, N., ADLER-NISSEN, J., JENSEN, B. B. B. and WILSON, D. I. (2017). Flow pattern and cleaning performance of a stationary liquid jet operating at conditions relevant for industrial tank cleaning. *Food Bioprod. Process.*, **101**, 145–156.
- FERNANDES, R. R. (2021). *Cleaning viscoplastic soil layers from flat surfaces using impinging water jets*. Ph.D. thesis, University of Cambridge.
- FERNANDES, R. R., OEVERMANN, D. and WILSON, D. I. (2019). Cleaning insoluble viscoplastic soil layers using static and moving coherent impinging water jets. *Chem. Eng. Sci.*, **207**, 752–768.
- FERNANDES, R. R. and WILSON, D. I. (2020). Modelling the cleaning of viscoplastic layers by impinging coherent turbulent water jets. *J. Non-Newton. Fluid Mech.*, **282**, 104314.
- FOOD STANDARDS AGENCY (2017). *Review of Food Withdrawal and Recall Processes: Data Analysis of FSA Food Alerts 2013 - 2016*. Technical report, Analytics Unit Science, Evidence and Research Division.
- FÖSTE, H., SCHÖLER, M., MAJSCHAK, J.-P., AUGUSTIN, W. and SCHOLL, S. (2013). Modeling and validation of the mechanism of pulsed flow cleaning. *Heat Tran. Eng.*, **34**, 753–760.
- FRYER, P. J. and ASTERIADOU, K. (2009). A prototype cleaning map: A classification of industrial cleaning processes. *Trends Food Sci. Technol.*, **20**, 255–262.
- FUCHS, E., HELBIG, M., PFISTER, M. and MAJSCHAK, J.-P. (2017). Erhöhung der Reinigungseffizienz bei der Cleaning-in-Place-Reinigung durch diskontinuierliche Flüssigkeitsstrahlen. *Chem. Ing. Tech.*, **89**, 1072–1082.
- FUCHS, E., KÖHLER, H. and MAJSCHAK, J.-P. (2019a). Measurement of the impact force and pressure of water jets under the influence of jet break-up. *Chem. Ing. Tech.*, **91**, 1–13.

- FUCHS, E., KRICKE, S., SCHÖHL, E. and MAJSCHAK, J.-P. (2019b). Effect of industrial scale standoff distance on water jet break-up, cleaning and forces imposed on soil layers. *Food Bioprod. Process.*, **113**, 129–141.
- GÉSAN-GUIZIOU, G., SOBÁŇKA, A. P., OMONT, S., FROELICH, D., RABILLER-BAUDRY, M., THUEUX, F., BEUDON, D., TREGRET, L., BUSON, C. and AUFFRET, D. (2019). Life cycle assessment of a milk protein fractionation process: Contribution of the production and the cleaning stages at unit process level. *Sep. Purif. Technol.*, **224**, 591–610.
- GILLHAM, C. R., FRYER, P. J., HASTING, A. P. M. and WILSON, D. I. (2000). Enhanced cleaning of whey protein fouling deposits using pulsed flows. *J. Food Eng.*, **46**, 199–209.
- GLOVER, H. W., BRASS, T., BHAGAT, R. K., DAVIDSON, J. F., PRATT, L. and WILSON, D. I. (2016). Cleaning of complex soil layers on vertical walls by fixed and moving impinging liquid jets. *J. Food Eng.*, **178**, 95–109.
- GRANT, R. P. and MIDDLEMAN, S. (1966). Newtonian jet stability. *AIChE J.*, **2**, 669–678.
- HARTLEY, D. E. and MURGATROYD, W. (1964). Criteria for the break-up of thin liquid layers flowing isothermally over solid surfaces. *Int. J. Heat Mass Transfer*, **7**, 1003–1015.
- JALIL, A. and RAJARATNAM, N. (2006). Oblique impingement of circular water jets on a plane boundary. *J. Hydraul. Res.*, **44**, 807–814.
- JOHNSON, C. G. and GRAY, J. M. N. T. (2011). Granular jets and hydraulic jumps on an inclined plane. *J. Fluid Mech.*, **675**, 87–116.
- JOPPA, M. (2020). *Experimentell unterstützte Entwicklung eines Basismodells für die quantitative Vorhersage der Strahlreinigung in der Lebensmittelindustrie mithilfe numerischer Strömungssimulation*. Ph.D. thesis, Technische Universität Dresden.
- JOPPA, M., KÖHLER, H., KRICKE, S., MAJSCHAK, J.-P., FRÖHLICH, J. and RÜDIGER, F. (2019). Simulation of jet cleaning: Diffusion model for swellable soils. *Food Bioprod. Process.*, **113**, 168–176.
- KATE, R. P., DAS, P. K. and CHAKRABORTY, S. (2007). Hydraulic jumps due to oblique impingement of circular liquid jets on a flat horizontal surface. *J. Fluid Mech.*, **573**, 247–263.

- KATE, R. P., DAS, P. K. and CHAKRABORTY, S. (2008). An investigation on non-circular hydraulic jumps formed due to obliquely impinging circular liquid jets. *Exp. Therm. Fluid Sci.*, **32**, 1429–1439.
- KAYE, P. L., PICKLES, C. S. J., FIELD, J. E. and JULIAN, K. S. (1995). Investigation of erosion processes as cleaning mechanisms in the removal of thin deposited soils. *Wear*, **186–187**, 413–420.
- KERN, D. Q. and SEATON, R. E. (1959). A theoretical analysis of thermal surface fouling. *British Chem. Eng.*, **4**, 258–262.
- KIBAR, A. (2018). Experimental and numerical investigation on a liquid jet impinging on a vertical superhydrophobic surface: spreading and reflection. *Prog. Comput. Fluid Dyn.*, **18**, 150–163.
- KIM, H., CHOI, H., KIM, D., CHUNG, J., KIM, H. and LEE, K. (2020). Experimental study on splash phenomena of liquid jet impinging on a vertical wall. *Exp. Therm. Fluid Sci.*, **116**, 110111.
- KÖHLER, H. (2018). *Methode zur Untersuchung, Modellierung und Optimierung von Reinigungsprozessen mit kohärentem Flüssigkeitsstrahl*. Ph.D. thesis, Technische Universität Dresden.
- LANDEL, J. R. and WILSON, D. I. (2021). The fluid mechanics of cleaning and decontamination of surfaces. *Annu. Rev. Fluid Mech.*, **53**, 147–171.
- LEROUX, S., DUMOUCHEL, C. and LEDOUX, M. (1996). The stability curve of newtonian liquid jets. *At. Sprays*, **6**, 623–647.
- LIENHARD, J. H., LIU, X. and GABOUR, L. A. (1992). Splattering and heat transfer during impingement of a turbulent liquid jet. *J. Heat Transfer*, **114**, 362–372.
- LIN, S. P. and REITZ, R. D. (1998). Drop and spray formation from a liquid jet. *Annu. Rev. Fluid Mech.*, **30**, 85–105.
- MCCARTHY, M. J. and MALLOY, N. A. (1974). Review of stability of liquid jets and the influence of nozzle design. *Chem. Eng. J.*, **7**, 1–20.
- MERTENS, K., PUTKARADZE, V. and VOROBIEFF, P. (2005). Morphology of a stream flowing down an inclined plane. part 1. braiding. *J. Fluid Mech.*, **531**, 49–58.

- MISSAIRE, F., QIU, C.-G. and RAO, M. A. (1990). Yield stress of structured and unstructured food suspensions. *J. Texture Stud.*, **21**, 479–490.
- MITCHELL, B. R., KLEWICKI, J., SHWAERY, G., KORKOLIS, Y. P. and KINSEY, B. L. (2018). On the comparison between a liquid jet and a droplet train. In *Proceedings of the ASME 2018 13th International Manufacturing Science and Engineering Conference. Volume 4: Processes*, Texas, USA: College Station.
- MITCHELL, B. R., KLEWICKI, J. C., KORKOLIS, Y. P. and KINSEY, B. L. (2019). Normal impact force of rayleigh jets. *Phys. Rev. Fluids*, **4**, 113603.
- MODCAD WORKSHOP (2021). The Roadmapping of Quantitative Understanding and Modelling of Cleaning and Decontamination Workshop, 20-22 April 2021. <https://www.modcad.org/>, accessed September 2021.
- MORISON, K. R. and THORPE, R. J. (2002). Liquid distribution from cleaning-in-place sprayballs. *Food Bioprod. Process.*, **80**, 270–275.
- MÜLLER-STEINHAGEN, H., MALAYERI, M. R. and WATKINSON, A. P. (2005). Fouling of heat exchangers - new approaches to solve an old problem. *Heat Transf. Eng.*, **26**, 1–4.
- NUSSELT, W. (1916). Die Oberflächenkondensation des Wasserdampfes. *Z. Ver. Dtsch. Ing.*, **60**, 541–546 569–575.
- OEVERMANN, D., BHAGAT, R. K., FERNANDES, R. R. and WILSON, D. I. (2019). Quantitative modelling of the erosive removal of a thin soil deposit by impinging liquid jets. *Wear*, **422–423**, 27–34.
- PETTIGREW, L., BLOMENHOFER, V., HUBERT, S., GROß, F. and DELGADO, A. (2015). Optimisation of water usage in a brewery clean-in-place system using reference nets. *J. Clean. Prod.*, **87**, 583–593.
- QUARINI, J. (2002). Ice-pigging to reduce and remove fouling and to achieve clean-in-place. *Appl. Therm. Eng.*, **22**, 747–753.
- RAYLEIGH, L. (1879a). On the capillary phenomenon of jets. *Proc. R. Soc. London*, **29**, 71–97.
- RAYLEIGH, L. (1879b). On the instability of jets. *Proc. London Math. Soc.*, **10**, 4–13.

- RAYLEIGH, L. (1914). On the theory of long waves and bores, *proc. R. Soc. Lond. A*, **90**, 324–328.
- REITZ, R. D. and BRACCO, F. (1986). Chapter 10: Mechanisms of breakup of round liquid jets. In *Encyclopaedia of Fluid Mechanics*, Houston (Texas), USA: Gulf Publishing Company, pp. 233–249.
- RODGERS, A. J. (2019). *A hydrodynamic study on the soil removal mechanisms of liquid jets and sprays*. Ph.D. thesis, University of Leeds.
- SABERI, A., MAHPEYKAR, M. R. and TEYMOURTASH, A. R. (2019). Experimental measurement of radius of circular hydraulic jumps: Effect of radius of convex target plate. *Flow Meas. Instrum.*, **65**, 274–279.
- SABERI, A., TEYMOURTASH, A. R. and MAHPEYKAR, M. R. (2020). Experimental and numerical study of circular hydraulic jumps on convex and flat target plates. *Eur. J. Mech. B Fluids*, **80**, 32–41.
- SINNER, H. (1959). *The Sinner Circle "TACT", Sinner's Cleaning Philosophy*. Henkel.
- TAMIME, A. Y. (2009). *Cleaning-in-place: dairy, food and beverage operations*. John Wiley & Sons.
- TAYLOR, G. (1960). Formation of thin flat sheets of water. *Proc. R. Soc. Lond. A*, **259**, 1–17.
- TUCK, J. P., ALBERINI, F., WARD, D., GORE, B. and FRYER, P. J. (2020). Cleaning of thick viscoplastic surface deposits using an impinging jet: Effect of process variables. *J. Food Eng.*, **266**, 109699.
- UTH, T. and DESHPANDE, V. S. (2013). Unsteady penetration of a target by a liquid jet. *Proc. Natl. Acad. Sci.*, **110**, 20028–20033.
- VAN ASSELT, A. J., VISSERS, M. M. M., SMIT, F. and DE JONG, P. (2005). In-line control of fouling. In *6th International Conference on Heat Exchanger Fouling and Cleaning - Challenges and Opportunities*, Kloster Irsee, Germany.
- WANG, T. (2014). *Flow and cleaning behaviour of coherent liquid jets impinging on vertical walls*. Ph.D. thesis, University of Cambridge.
- WANG, T., DAVIDSON, J. F. and WILSON, D. I. (2013a). Effect of surfactant on flow patterns and draining films created by a static horizontal liquid jet impinging on a vertical surface at low flow rates. *Chem. Eng. Sci.*, **88**, 79–94.

- WANG, T., DAVIDSON, J. F. and WILSON, D. I. (2015). Flow patterns and cleaning behaviour of horizontal liquid jets impinging on angled walls. *Food Bioprod. Process.*, **93**, 333–342.
- WANG, T., FARIA, D., STEVENS, L. J., TAN, J. S. C., DAVIDSON, J. F. and WILSON, D. I. (2013b). Flow patterns and draining films created by horizontal and inclined coherent water jets impinging on vertical walls. *Chem. Eng. Sci.*, **102**, 585–601.
- WANG, Y. and KHAYAT, R. E. (2019). The role of gravity in the prediction of the circular hydraulic jump radius for high-viscosity liquids. *J. Fluid Mech.*, **862**, 128–161.
- WASSENBURG, J. R., STEPHAN, P. and GAMBARYAN-ROISMAN, T. (2019). The influence of splattering on the development of the wall film after horizontal jet impingement onto a vertical wall. *Exp. Fluids.*, **60**, 173.
- WATSON, E. J. (1964). The radial spread of a liquid jet over a horizontal plane. *J. Fluid Mech.*, **20**, 481.
- WERNER, R., BOLLWEIN, B., PETERSEN, R., TIPPMANN, J. and BECKER, T. (2017). Pulsatile jet cleaning of filter cloths contaminated with yeast cells. *Chem. Eng. Technol.*, **40**, 450–458.
- WILSON, D. I. (2005). Challenges in cleaning: Recent developments and future prospects. *Heat Transf. Eng.*, **26**, 51–59.
- WILSON, D. I. (2018). Fouling during food processing - progress in tackling this inconvenient truth. *Current Opinion in Food Science*, **23**, 105–112.
- WILSON, D. I., ATKINSON, P., KÖHLER, H., MAUERMANN, M., STOYE, H., SUDDABY, K., WANG, T., DAVIDSON, J. F. and MAJSCHAK, J.-P. (2014). Cleaning of soft-solid soil layers on vertical and horizontal surfaces by stationary coherent impinging liquid jets. *Chem. Eng. Sci.*, **109**, 183–196.
- WILSON, D. I. and CHEW, Y. M. J. (eds.) (2014). *Fouling & Cleaning in Food Processing 2014 - Green Cleaning*. University of Cambridge: Department of Chemical Engineering and Biotechnology.
- WILSON, D. I., KÖHLER, H., CAI, L., MAJSCHAK, J.-P. and DAVIDSON, J. F. (2015). Cleaning of a model food soil from horizontal plates by a moving vertical water jet. *Chem. Eng. Sci.*, **123**, 450–459.

- WILSON, D. I., LE, B. L., DAO, H. D. A., LAI, K. Y., MORISON, K. R. and DAVIDSON, J. F. (2012). Surface flow and drainage films created by horizontal impinging liquid jets. *Chem. Eng. Sci.*, **68**, 449–460.
- YANG, J. (2018). *Novel Strategies for Cleaning-in-Place Operations*. Ph.D. thesis, Technical University of Denmark.
- YANG, J., BHAGAT, R. K., FERNANDES, R. R., NORDKVIST, M., GERNAEY, K. V., KRÜHNE, U. and WILSON, D. I. (2019a). Cleaning of toothpaste from vessel walls by impinging liquid jets and their falling films: Quantitative modelling of soaking effects. *Chem. Eng. Sci.*, **208**, 115148.
- YANG, J., KJELLBERG, K., JENSEN, B. B. B., NORDKVIST, M., GERNAEY, K. V. and KRÜHNE, U. (2019b). Investigation of the cleaning of egg yolk deposits from tank surfaces using continuous and pulsed flows. *Food Bioprod. Process.*, **113**, 154–167.
- YECKEL, A. and MIDDLEMAN, S. (1987). Removal of a viscous film from a rigid plane surface by an impinging liquid jet. *Chem. Eng. Comm.*, **50**, 165–175.
- YECKEL, A., MIDDLEMAN, S. and KLUMB, L. A. (1990). The removal of thin liquid films from periodically grooved surfaces by an impinging jet. *Chem. Eng. Comm.*, **96**, 69–79.
- YECKEL, A., STRONG, L. and MIDDLEMAN, S. (1994). Viscous film flow in the stagnation region of the jet impinging on planar surface. *AIChE J.*, **40**, 1611–1617.
- ZHAN, Y., KUWATA, Y., MARUYAMA, K., OKAWA, T., ENOKI, K., AOYAGI, M. and TAKATA, T. (2020). Effects of surface tension and viscosity on liquid jet breakup. *Exp. Therm. Fluid Sci.*, **112**, 109953.
- ZHAN, Y., KUWATA, Y., OKAWA, T., AOYAGI, M. and TAKATA, T. (2021). Experimental study on secondary droplets produced during liquid jet impingement onto a horizontal solid surface. *Exp. Therm. Fluid Sci.*, **120**, 110249.
- ZHAN, Y., OYA, N., ENOKI, K., OKAWA, T., AOYAGI, M. and TAKATA, T. (2018). Droplet generation during liquid jet impingement onto a horizontal plate. *Exp. Therm. Fluid Sci.*, **98**, 86–94.